FABRICATION OF MESOPOROUS NICKEL OXIDE BASED THIN FILM ELECTRODES AND THEIR ELECTROCHEMICAL PROPERTIES

A DISSERTATION SUBMITTED TO
THE GRADUATE SCHOOL OF ENGINEERING AND SCIENCE
OF BILKENT UNIVERSITY
IN PARTIAL FULFILLMENT OF THE REQUIREMENTS FOR
THE DEGREE OF
DOCTOR OF PHILOSOPHY
IN
CHEMISTRY

By

Assel Amirzhanova Katırcı

January 2025

FABRICATION OF MESOPOROUS NICKEL OXIDE BASED THIN FILM ELECTRODES AND THEIR ELECTROCHEMICAL PROPERTIES

By Assel Amirzhanova Katırcı

January 2025

We certify that we have read this dissertation and that, in our opinion, it is fully adequate, in scope and quality, as a dissertation for the degree of Doctor of Philosophy.

_____

Prof. Ömer Dağ
Advisor

_____

Assoc. Prof. Ferdi Karadaş

_____

Assoc. Prof. Emre Büküşoğlu

_____

Prof. Mehmet Kadri Aydınol

_____

Assoc. Prof. Burak Ülgüt

Approved for the Graduate School of Engineering and Science:

_____

Orhan Arıkan
Director of the Graduate School

ABSTRACT

FABRICATION OF MESOPOROUS NICKEL OXIDE BASED THIN FILM ELECTRODES AND THEIR ELECTROCHEMICAL PROPERTIES

Assel Amirzhanova Katırcı
Ph.D. in Chemistry
Advisor: Ömer Dağ
January 2025

In this thesis, robust electroactive mesoporous $Ni_{1-x}Mn_xO$ thin-film electrodes were synthesized on FTO and graphite rod substrates. Molten salt-assisted self-assembly (MASA) synthesis method was employed to produce uniform thin films. The synthesis started with preparing ethanol solutions, containing various molar ratios of $[Mn(H_2O)_4](NO_3)_2$ and $[Ni(H_2O)_6](NO_3)_2$ (between 1.0 to 0.1 Ni(II)/Mn(II) ratio) and surfactants ($C_{12}H_{25}(OCH_2CH_2)_{10}OH$, $C_{12}E_{10}$ and $C_{16}H_{33}N(CH_3)_3Br$, CTAB). Then, these solutions are coated over conductive substrates to obtain the salt-surfactant lyotropic liquid crystalline (LLC) mesophase. The thin mesophase is calcined in order to produce mesoporous $Ni_{1-x}Mn_xO$ thin-films on the FTO or graphite. The thin-films form solid solutions with the x value of up to 0.7. The $Ni_{1-x}Mn_xO$ thin-films transform to $NiMnO_3$, Mn_3O_4, and Mn_2O_3 phases at increased Mn ratios and annealing temperatures. The films are mesoporous and were confirmed by N_2 adsorption-desorption analysis and typical type IV isotherms characteristic for mesoporous materials. Pore sizes varied from 2.8 to 17.6 nm from Ni-rich to Mn-rich oxides. The surface area reaches to 211 m^2/g in $Ni_{0.9}Mn_1O$, while the pure NiO has a BET surface area of 164 m^2/g at 350 ºC calcination temperature.

The FTO and graphite-coated electrodes (FTO-$Ni_{1-x}Mn_xO$ and G-$Ni_{1-x}Mn_xO$) display high charge capacities, but the FTO coated electrodes are unstable and undergo to degradation over extended time of usage. In the first few CV cycles of the FTO-based electrodes, they show an increased capacity, however, decline in further cycles. On the other hand, graphite-based electrodes show better stability and high charge capacity. Origin for increasing charge capacity with cycling is attributed to a transformation of the metal oxides to metal hydroxides. Thus, the electrochemical CV cycling of both pure NiO and $Ni_{1-x}Mn_xO$ electrodes results in a structural change into a

$NiO(core)/Ni(OH)_2(shell)$ or $Ni_{1-x}Mn_xO(core)/Ni(OH)_2(shell)$ configurations. The shell thickness is ranged from 2.0 nm (pure NiO) to 1.1 nm ($Ni_{0.9}Mn_{0.1}O$) at 350°C. Moreover, the shell thicknesses and charge capacities are affected by the pore-wall thicknesses, which increases with increasing annealing temperature. Despite these changes, the manganese addition improves the stability of the electrodes, but there is no improvements on the overpotential on oxygen evolution reaction (OER). Moreover, the annealing temperature reduces the charge capacity, whereas the OER performance remains the same.

By using the same MASA method, m-$NiO-SiO_2$ electrodes were synthesized using $[Ni(H_2O)_6](NO_3)_2$ and tetramethyl orthosilicate (TMOS) with CTAB and $C_{12}E_{10}$ surfactants at different Ni to TMOS ratios. Silica acts as hard template support for NiO, and the film is formed in good quality with bimodal pore size distribution. The sample pore size that was observed is 2.6 nm, which originates from the m-SiO_2 domains. The second pore system had also mesopores; the average pore size is 15 nm, calcined at 350 ^oC. That property helps better infiltration of electrolytes, which is advantageous during electrochemistry. During electrochemical analysis, silica is etched out in basic electrolyte. These electrodes, prepared on graphite substrate have specific surface area of around 130 m^2/g. The electrodes show an overpotential 381 mV in the CP experiment at 10 mA/cm^2 current density.

KEYWORDS: molten salt-assisted self-assembly, mesoporous materials, nickel manganese oxide, nickel hydroxide, charge-capacity, oxygen evolution electrocatalysis, mesoporous silica, hard templating, soft templating.

ÖZET

MEZO-GÖZENEKLİ NİKEL OKSİT YAPILI İNCE FİLM ELEKTROTLARIN ÜRETİMİ VE ELEKTROKİMYASAL ÖZELLİKLERİ

Assel Amirzhanova Katırcı
Kimya, Doktora

Tez Danışmanı: Ömer Dağ
Ocak 2025

Bu tezde, kararlı elektroaktif mezogözenekli $Ni_{1-x}Mn_xO$ ince film elektrotlar, FTO ve grafit çubukların üzerinde sentezlenmiştir. Bu amaçla, eriyik tuz destekli kendiliğinden-oluşma (MASA) sentez tekniği kullanılmıştır. Sentez süreci, çeşitli mol oranlarında $[Mn(H_2O)_4](NO_3)_2$ ve $[Ni(H_2O)_6](NO_3)_2$ tuzlarının (Ni(II)/Mn(II)) oranı 1.0 ile 0.1 arasında) ve $C_{12}H_{25}(OCH_2CH_2)_{10}OH$ ($C_{12}E_{10}$) ve $C_{16}H_{33}N(CH_3)_3Br$ (CTAB) yüzeyaktif maddelerin etanol içinde çözünmesi ile başlar. Daha sonra bu çözeltiler, iletken yüzeylere kaplanarak sıvı kristal arafazlar elde edilir. Tuz-yüzey aktif sıvı-kristal arafazların yakılması ile FTO ve grafit üzerine kaplı mezogözenekli $Ni_{1-x}Mn_xO$ ince filmler elde edilir. Bu ince filmler, x değeri 0.7'ye kadar katı-çözelti oluştururken, artan manganez oranı ve tavlama sıcaklığı bunları $NiMnO_3$, Mn_3O_4 ve Mn_2O_3 fazlarına dönüştürür. Hazırlanan bu filmler mezo-gözenekli yapıdadır. Dolayısıyla, azot tutma-bırakma tayini ölçümleri, mezogözenekli malzemeleri tanımlayan karakteristik tip IV izoterm eğrilerini verir. Gözenek boyutlarının, nikelce-zengin bileşiklerinden manganca- zengin bileşiklere gidildikçe, 2.8 nm den 17.6 nm'ye kadar arttığı gözlenmiştir. 350°C'de yakılmış $Ni_{0.9}Mn_{0.1}O$ in yüzey alanı 211 m^2/g'a kadar ulaşırken saf haldeki NiO'in BET yüzey alanı 165 m^2/gr olarak hesaplanmıştır.

FTO ve grafit kaplı elektrotlar (FTO-$Ni_{1-x}Mn_xO$ ve G-$Ni_{1-x}Mn_xO$), yüksek yük kapasitesi değerleri sergilemiş olsalar da uzun süreli kullanımda dayanıklı olmadıkları ve parçalandıkları gözlenmiştir. FTO tabanlı elektrotlar ilk birkaç devinimde kapasite artışı gösterirken, uzun süreli devinimlerde kapasitelerinde düşüş gözlemlenmiştir. Buna karşılık, grafit tabanlı elektrotlar daha yüksek dayanıklılığa ve yük kapasitesine (tutma özelliği) sahip olduğu gösterilmiştir. Elektrokimyasal testler, hem saf NiO hem de $Ni_{1-x}Mn_xO$'nun yapısal olarak NiO (çekirdek)/$Ni(OH)_2$ (kabuk) veya $Ni_{1-x}Mn_xO$ (çekirdek)/$Ni(OH)_2$ (kabuk) yapılarına dönüştüğünü ortaya koymuştur. Bu durumlarda, kabuk kalınlıkları 350°C'de saf NiO için 2.0 nm, $Ni_{0.9}Mn_{0.1}O$ için 1.1 nm arasında değişmektedir. Kabuk kalınlıkları ve yük kapasitesi, tavlama sıcaklığı ile artan gözenek

duvar kalınlığından etkilenir. Bu değişikliklere rağmen, mangan eklenmesi elektrotların dayanıklılığını artırmıştır. Ancak, bu ekleme elektrotların ek potansiyeline bir katkı sağlamamıştır. Ayrıca, tavlama sıcaklığı yük kapasitesini etkilerken, oksijen çıkma tepkimesine (OER) davranışı aynı kalmıştır.

Ayrıca, MASA yöntemi kullanılarak, $[Ni(H_2O)_6](NO_3)_2$ ve tetrametil ortosilikat (TMOS) ile CTAB ve $C_{12}E_{10}$ yüzey aktif maddeleri kullanılarak farklı nikel/silika oranlarında m-NiO-SiO_2 elektrotları sentezlenmiştir. Silika maddesi, NiO için bir sert-kalıp görevi görmüş ve sonuç olarak yüksek kalitede gözenekli yapılar elde edilmiştir. Silika gözenek boyutları yaklaşık 2.6 nm dir. 350°C'de yakılarak elde edilmiş malzemeler de gözlenen ikincil mezogözenekler yaklaşık 15 nm dir. Bu boyut özelliği elektrokimyasal tepkimelerde elektrolit çözeltilerinin daha iyi nüfuz etmesini sağlamıştır. Analiz sırasında, silika, alkali elektrolit içerisinde çözülerek uzaklaşır. Dolayısıyla grafit üzerinde hazırlanmış elektrotların da yüzey alanları 130 m^2/gr olarak hesaplanmıştır. Bu elektrotlar 10 mA/cm^2 akım yoğunluğunda gerçekleştirilen CP deneylerinde 381 mV ek potansiyel değeri gösterir.

Anahtar Kelimeler: eriyik tuz destekli kendiliğinden-oluşma, mezogözenekli malzemeler, nikel manganez oksit, nikel hidroksit, yük-kapasitesi, oksijen dönüşüm elektrokatalizi, mezogözenekli silika, sert kalıplama, yumuşak kalıplama.

ACKNOWLEDGEMENTS

First and foremost, I extend my deepest gratitude to my thesis supervisor, Prof. Ömer Dağ, for his unwavering patience, insightful guidance, and steadfast support throughout my master's and doctoral studies. His mentorship has been a cornerstone of my academic journey. I am also profoundly thankful to my Ph.D. thesis committee members, Assoc. Prof. Ferdi Karadas, Assoc. Prof. Emre Büküşoğlu, Prof. Mehmet Kadri Aydınol, and Assoc. Prof. Burak Ülgüt, for their invaluable feedback and constructive insights, which significantly enriched this thesis.

I would also like to express my heartfelt appreciation to the cherished members of the Dağ Research Group. A special thanks to Dr. Irmak Karakaya Durukan for her enduring friendship, inspiring collaborations, and boundless kindness over the years. My sincere gratitude goes to Dr. Işıl Ulu for her camaraderie, encouragement, and thoughtful support. I am equally thankful to Nesibe Akmanşen, whose genuine kindness and uplifting spirit have been a source of motivation. I also wish to acknowledge my wonderful former and current lab mates—Ezgi Topuzlu, Najeeb Khan, Hamid Ali Reza, Arda Altan, Gözde Ceran, Elif Nur Adalı, Murtacan Öz, Pamir Göksu, Muamer Yaman, Tuluhan Olcayto Çolak and Doruk Ergöçmen —whose contributions and camaraderie have made the lab a vibrant and collaborative environment.

To my beloved family, words cannot fully express my gratitude. To my parents, Karlayash and Amangeldy, for their unwavering love and support that has been the foundation of all my achievements. To my dear sisters, Assem, Amira, and Amina, whose encouragement and warmth have been a constant source of strength. I am equally thankful to my extended family—my aunts, uncles, and cousins—who have always surrounded me with love and positivity. I want to thank my dear Uncle Yestay Kalguzhin for always being there for me and my sisters and always respecting and loving us and our life decisions. I would like to dedicate special acknowledgment to my dear aunt, who also became my second mother, Zakaz Bektasova, who sadly passed away due to COVID-19. Her love, support, and belief in me will always inspire me.

I am deeply grateful to my husband, Dr. Gökberk Katırcı, whose steadfast support, love, and encouragement have been invaluable throughout this journey. I can not imagine my academic journey without his presence and support. I also warmly thank my new family, including my brother-in-law Berkay, our dear companion Layka,

and my mother-in-law Jülide, for their kindness and care, which have made me feel truly at home. A special mention goes to my husband's late grandparents, Hamdi and Selma Türkmen, whom I had the honor of meeting in the summer of 2021. Their hospitality, warmth, and kindness left a lasting impression on me. Though they passed away in 2022, I hold their memory with profound respect and gratitude.

Lastly, I want to express my gratitude to my wonderful circle of friends Dinara Alikhnaova, Nazerke Ualiyeva, Kuandyk Klimenov, Koray Yavuz, Asli Yavuz, Eliza Sopubekova, Ulviyya Quliyeva. Special thanks to Ayşe Erdali, Emre Ece, my Taekwondo friends, and many others who have made this journey memorable with their laughter, friendship, and unwavering encouragement.

To everyone who has contributed to my academic and personal growth, thank you from the bottom of my heart.

To my dear parents, Amangeldy and Karlygash…….

Contents

LIST OF FIGURES

LIST OF TABLES

List of Abbreviations

LC -liquid Crystal;

LLC - lyotropic liquid crystal;

MASA - molten-salt assisted self-assembly;

OER - oxygen evolution reaction;

mCP- multistep chronopotentiometry;

mCA - multistep chronoamperometry;

GCD - galvanostatic charge discharge;

XRD - X-ray Diffraction;

POM- Polarized Optical Microscopy;

SEM - Scanning Electron Microscopy;

TEM - ransmission Electron Microscopy;

EDX - Energy Dispersive X-ray Spectroscopy;

XPS - X-ray Photoelectron Spectroscopy;

ATR-FTIR - Attenuated Total Reflection Fourier-Transform Infrared;

BET - Brunauer, Emmett, and Teller;

PDF - Powder Diffraction File

WE - Working Electrode

RE - Reference Electrode

CE - Counter Electrode

FTO - Fluorine doped Tin Oxide

Chapter 1

1 INTRODUCTION

1.1 Mesoporous Nickel Oxide and Nickel Oxide Nanoparticles

Nanostructured materials offer high surface to volume ratios thus giving a material with unique transport properties and altered physical properties due to quantum confinement effects. For the same reason, those materials, namely transition metal oxides, can be used as electrocatalysts for water oxidation, oxygen reduction reactions, photovoltaics, photocatalysts, supercapacitors, lithium-ion batteries etc.[1][2], [3][4], [5], [6], [7], [8], [9], [10]. Especially, nickel oxide nanoparticles have gained a lot of attention due to its optical properties and wide band-gap, as it is considered to be a p-type semiconductor. For instance, its catalytic activity was first investigated on thermal decomposition of ammonium perchlorate[11]. In this work, the 10 nm particles have shown to a superior catalytic activity compared to bulk NiO, and supports the fact that nanoscale is important for catalytic performance[11], [12]. Nickel oxide has also been investigated for dielectric applications as transparent electrode[13]. Smaller particles size and high surface area provides capacitive properties as that depends on the electric double layer[13]. And optical properties can be tuned by calcination temperature as it affects the crystallite size as a result, controls the band-gap. Electrochromic properties of nickel oxide can be utilized in smart windows application[14]. The Ni^{2+} is oxidized to Ni^{3+} by applying certain potential, which makes NiO film switch from transparent (reduced form) to black (oxidized form)[14]. The coloration and discoloration of the NiO electrode on the Fluorine-Dopped Tin Oxide electrode (FTO) during the cyclic voltammetry experiment are represented in Figure 1.1[15], [16] .

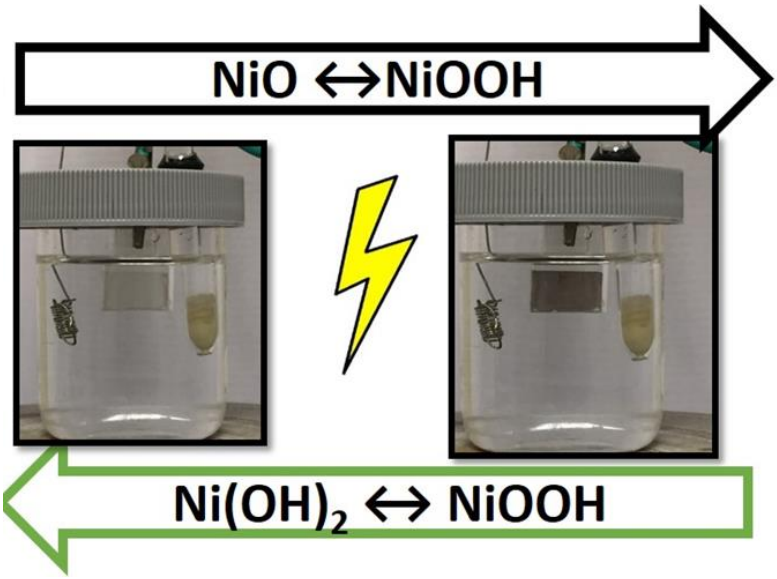

Figure 1.1. Schematic representation of NiO electrode during Cyclic Voltammetry experiment in basic media[15].

The coloration times were around 6 seconds for forward and reverse cycle and the efficiency was again explained by small particle size of nickel oxide, coated as a thin film by electrodeposition[14]. Electrochemical conductivity of NiO in the galvanic cell was investigated by Wang *et. al.* by combining NiO with Au nanoparticles, which shows that electrochromic properties of nickel oxide by combining with a second-row transition metal can be enhanced due to charge transfer between gold oxide and nickel oxide surface[17]. In another work, investigation on the optical properties of NiO, the stability of the film and life time of coloration and bleaching cycles were analyzed[18]. They found out that, in basic media, switching between dark and transparent phase can be conducted up to 500 cycles[18].

Electro-optical data of NiO thin films, synthesized by Garcia-Miquel *et. al.*, showed that the electrochromic response is getting better upon cycling[19]. This phenomenon is related with the formation of active surface on top of the NiO core, namely $Ni(OH)_2$/NiOOH active surfaces, upon cycling (cyclic voltammetry)[20]. Therefore, the properties of NiO are highly dictated by active surface species, which are $Ni(OH)_2$ and NiOOH species. There are several works on synthesis and characterization of nickel hydroxide and its electrochemical properties[21].

Several methods have been developed to synthesize nickel oxide with a desired morphology. For instance, the nanocrystalline NiO has been successfully fabricated by sol-gel and homogeneous precipitation method[22]. Homogeneous precipitation method produces NiO particles as small as 2 nm in size which makes that route of

synthesis more successful compared to sol-gel method that produces 19 nm nanoparticles[22]. Another synthesis route that was widely implemented is the hydrothermal synthesis, where precursor species were nickel chloride, ammonia, and glucose[23]. Due to spherical hollow structure and small size of nickel oxide nanoparticles, it can be used as electrode material in energy storage[23]. Pseudocapacitive performance of mesoporous NiO that was synthesized by homogeneous precipitation and microwave assisted heating method were also tested [24]. This work shows that the synthesis and fabrication routs highly control the properties of the end product. As synthesized porous NiO showed high specific capacitance and extraordinary electrochemical stability[24]. Therefore, it is important to develop alternative synthesis methods to elucidate what NiO may offer.

1.2 Hard and Soft Templating Synthesis Methods

There are several synthesis methods of mesoporous materials, but generally they are classified by two types, hard- and soft-templating[25]. Soft-templating method was first introduced by Kresge *et.al* in 1992 by using surfactants in a polymerizing media of silicate. Later, it is modified to make many other materials, such as TiO_2, Al_2O_3, SiO_2 and metal titanates with pore sizes around 14 nm[26]. These porous materials have thick channel walls with an extremely high thermal stability[26]. Thermal decomposition of oxalate precursor has been also used to fabricate mesoporous metal oxides[27]. This method of synthesis has a lot of advantages such as low cost, environmentally friendly, and has been employed to synthesize iron oxide, nickel oxide, manganese oxide, $NiFe_2O_4$ and $CoFe_2O_4$ [27]. Another soft templating route to obtain porous materials is a ligand assisted liquid crystal templating[28]. Using that method, porous niobium dioxide has been synthesized[28]. Moreover, sol-gel method is also one of the most popular routes to obtain mesoporous materials. One of the first examples is the synthesis of mesoporous titania[29]. Titanium alkoxide and phosphate surfactants were utilized as the precursor and structure directing agents, respectively. The large surface area with an ordered porous structure has been obtained by using sol-gel synthesis[29].

Schematics for both hard and soft templating synthesis of mesoporous materials are given in Figure 1.2[30].

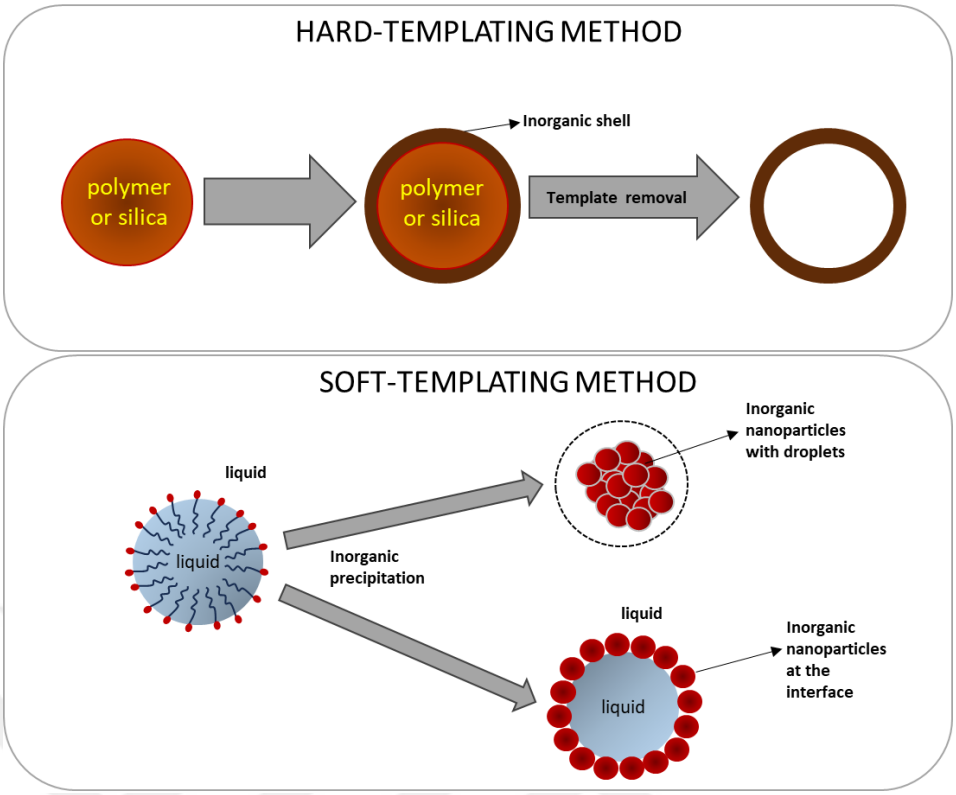

Figure 1.2. Schematic representation of hard and soft templating[30].

Evaporation-induced self-assembly (EISA) method has been developed to fabricate mesoporous silicon dioxide films, where poly(ethylene oxide)-b-polystyrene (PEO-b-PS) diblock copolymers were used as a template while TMOS was used as a silica precursor[31]. EISA methods has many advantages, but one of the main drawbacks is that it does not provide material with desired pore regularity, that is why hard templating has also been widely used[32]. The main idea of hard-templating, that is also called nano-casting, the precursor solution is infiltrated into the porous template and after a thermal treatment, the template is removed by etching with mostly acid or base, and the resulted material is reverse replica of the hard template[32][33].

Generally, commercial hard templates are used for making porous oxides, for example commercial silica framework SBA-15 is used to fabricate chromium oxide[34]. Then the silica template was removed by etching in HF[34]. Similarly, the mesoporous magnesium oxide has been synthesized[35]. Mesoporous carbon aerogel was also used as a hard template and magnesium nitrate as a manganese precursor[35]. The carbon template was removed by calcination at 600 ^{o}C for 8 hours and the resulted material had a surface area of 150 m^2/g[35]. Later, more transition metal oxides were fabricated using nano-casting, for instance cobalt oxide was synthesized using again

mesoporous silica, like KIT-6 and SBA-15[36]. The template was later removed by treatment with a mix of hydrogen peroxide and nitric acid[36].

In this work, the molten salt-assisted self-assembly (MASA) method that was developed by Dag *et al.* will be used to synthesize mesoporous metal oxide[37].

1.3 Lyotropic Liquid Crystal (LLC) Templating: Molten Salt Assisted Self Assembly (MASA) Method.

Lyotropic liquid crystalline mesophase are usually formed by surfactant molecules with hydrophobic and hydrophilic ends. For the formation of LLC phases, the mixture contains at least two components, solvent and surfactant molecules. The LLC phase is very sensitive to the amount of solvent and surfactant and also temperature. At specific solvent/surfactant ratio range, an LLC mesophase can be formed[38][39].

Salt-surfactant LLC (SS-LLC) mesophase that is consisting of a transition metal salt and surfactant was discovered by Dag *et al*[40]. These SS-LLC mesophases were formed by homogeneously mixing of a non-ionic oligo(ethylene oxide) surfactant and transition metal nitrate hexahydrate salt. By changing the salt to surfactant ratio, structure of the SS-LLC phases has been controlled [40].

The LLC phase is characterized by small-angle X-Ray diffraction technique, and d-spacing is calculated by using Braggs law that is shown in Equation 1.1[41].

$$n\lambda = 2d\ \sin\theta \quad \textbf{Equation 1.1}$$

n is an integer and is equal to 1

λ is a wavelength that is equal to 1.5405 Å

d is spacing of the unit cell in Å

θ is the measured half-angle in ^{o}

The SS-LLC phase is quite sensitive to the counter anions of the salts, so the mesophase may not be stable due to presence highly concentrated charged species (salt ions), for this reason extra charged surfactant, like CTAB or SDS have been introduced

to the mesophase. CTAB helps to stabilize the mesophase by interacting with non-ionic surfactants, and could accommodate large amounts of salts[42]. Confining salt species in a nano-space, among micellar domains, significantly decreases the melting point of the salt, that is how MASA method was developed to synthesize mesoporous transition metal oxides, metal cobaltites, metal phosphates, pyrophosphates and lithium metal oxides[43][20], [44], [42][45]. **T**he mesophase consists of metal salts and surfactants, where the salt species are any transition metal salt, like ($[Co(H_2O)_6](NO_3)_2$, $[Ni(H_2O)_6](NO_3)_2$, $[Zn(H_2O)_6](NO_3)_2$, and $[Cd(H_2O)_4](NO_3)_2$). In the MASA process, a mixture of changed and non-ionic surfactants is used together, namely $C_{12}EO_{10}$-CTAB and $C_{12}EO_{10}$-SDS couples[40]. The salt concentration can be increased up to 8 mole salt/surfactant mole ratios in the two surfactants LLC mesophase, where the salt concentration is significantly larger compared to a single surfactant LLCs. This stability is brought up by two surfactants interacting together and allowing to accommodate larger amounts of salts into hydrophilic domains of the mesophase. Evaporation of the volatile solvent that can be water or alcohols, the mesophase remains stable at such high salt concentration. The stability of the mesophase could be controlled by simply changing the amount of CTAB or SDS in the media[46].

A schematic representation of the MASA method is displayed in Figure 1.3.

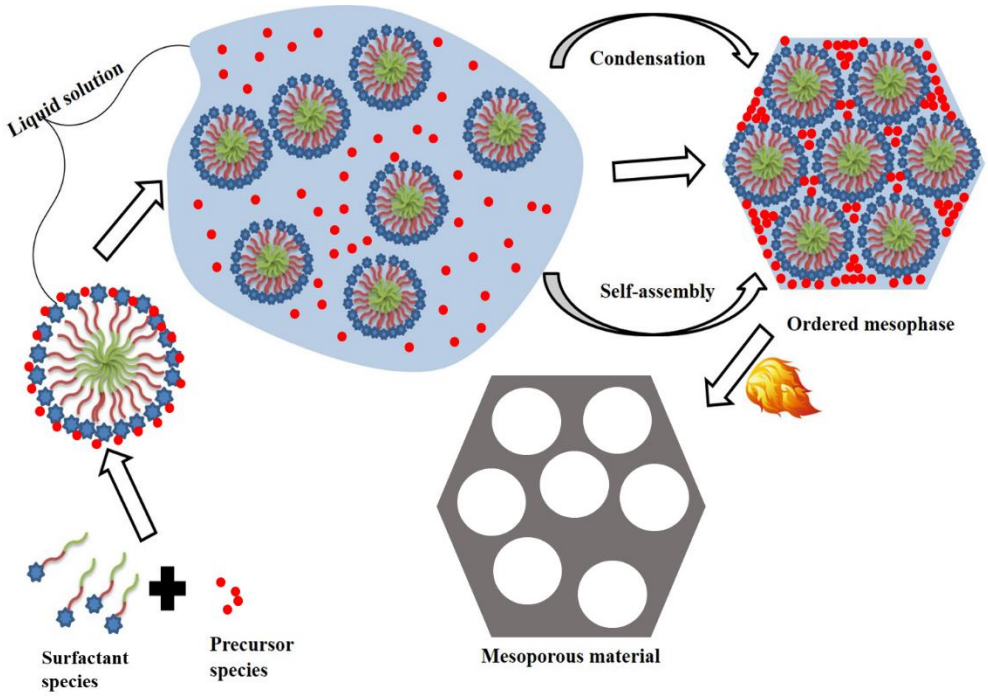

Figure 1.3. Schematic Representation of MASA method.

MASA was used to synthesize not only metal oxides but also the titanates like $Li_4Ti_5O_{12}$, $MnTiO_3$, $CoTiO_3$, $CdTiO_3$, Zn_2TiO_4, etc.[43] In the synthesis process, titania undergoes hydrolysis and condensation before the calcination and produce a very stable mesostructure. After calcination, the mesoporous titanate is produced with a high surface area. Note also that the MASA method can be adopted to synthesize other mesoporous materials with high surface area. Along with that, the method is considered to be one pot synthesis, very flexible and can be adopted to synthesize any transition metal oxide[20], [44].

1.4 Mesoporous Nickel Hydroxide and Nickel Hydroxide Nanoparticles.

Mesoporous nickel oxide is widely used in photocatalysis[47], electrocatalysis[48], [49] supercapacitors[50], [51], [52], [53], electrochromic devise[54] etc. There are many ways to synthesize mesoporous nickel hydroxide and nickel hydroxide nanoparticles. The most widely used ones are chemical precipitation, electrochemical precipitation, sol-gel synthesis, and hydrothermal or solvothermal methods [55]. The least common methods are microwave assisted, sonochemical, and solid state-synthesis[56].

There are two known structures of nickel hydroxide, α-and β-$Ni(OH)_2$[55]. The α-$Ni(OH)_2$ generally can be synthesized via chemical precipitation or electrochemical deposition[55]. Chemical precipitation is just a one-step method, where a solution of any Ni(II) salt is mixed with a base (NaOH or KOH), and when pH is high enough, the nickel hydroxide precipitate is formed. The best way to synthesize the β-$Ni(OH)_2$ is chemical aging of the α-$Ni(OH)_2$ in an alkaline media by dehydrating it or by simply heating it[56][57], [58].

The XRD patterns of nickel hydroxides, both α-and β-$Ni(OH)_2$, are given in Figure 1.4[56]. The β-$Ni(OH)_2$ is isostructural to brucite, manganese hydroxide, and it has less surface coverage[59]. While the α-$Ni(OH)_2$ has a larger layer-layer distance and is more hydrated with higher surface coverage. It consists of layers of β phase that are connected by water molecules[59]. Those water molecules are not fixed between the $Ni(OH)_2$ layers and have freedom to rotate that is why the water generally is omitted from the formula[59]. The α-$Ni(OH)_2$ is considered to be electrochemically more

active , compared to β phase, and the reason behind that is their structure[60]. Bode *et. al.* proposed the electrochemical reactions that can explain the behavior of nickel hydroxide electrodes during electrochemical oxidation, see Figure 1.5.[55][58].

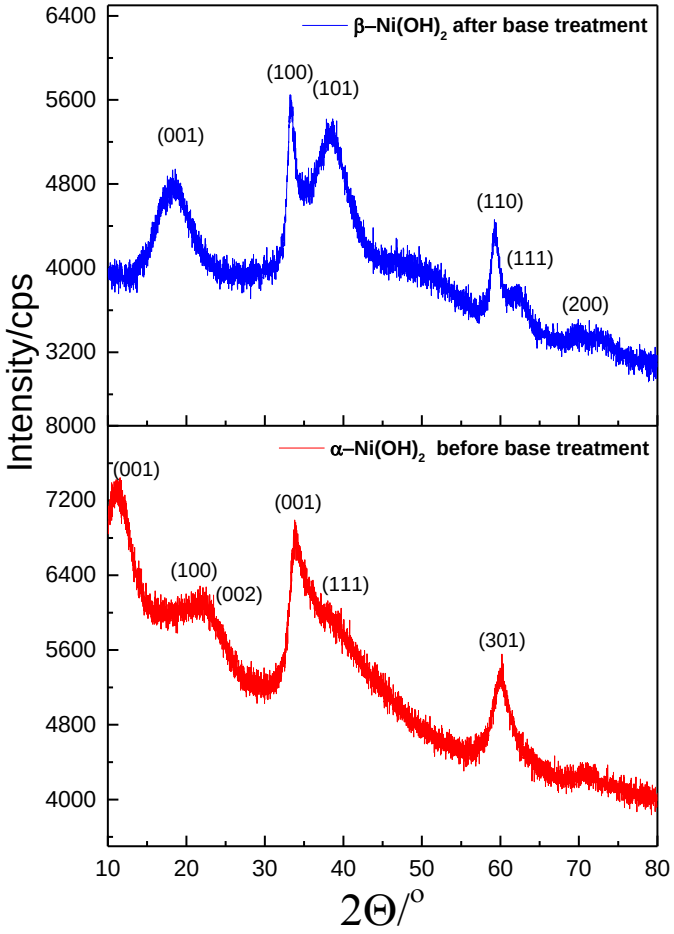

Figure 1.4. X-ray diffraction patterns of $Ni(OH)_2$ films: (Top) β-$Ni(OH)_2$ and (bottom)α-$Ni(OH)_2$ [56].

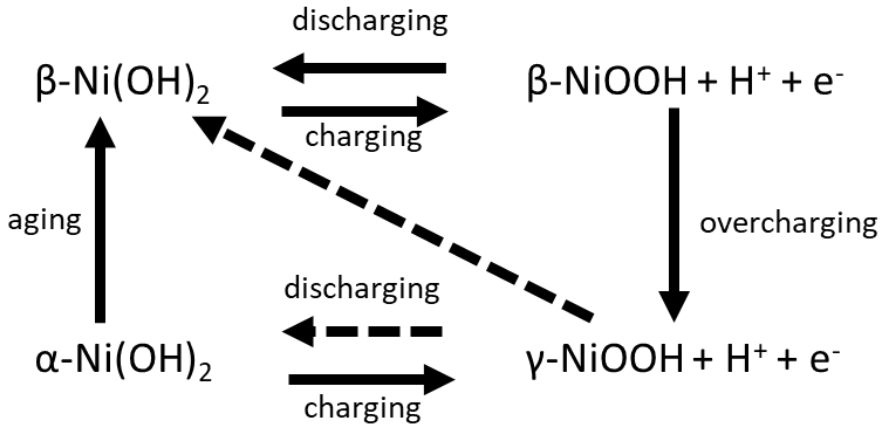

Figure 1.5. A general scheme of the chemical and electrochemical processes that occur at a nickel hydroxide battery electrode[55],[56].

As shown in the scheme in Figure 1.5, the oxidized phases are β- and γ-NiOOH and the reduced phases are α- and β-$Ni(OH)_2$[56]. These schematics generally represent the nickel hydroxide battery electrode behavior, and it is going to be used to characterize nickel oxide electrodes and to explain the electrochemical process in this study.

1.5 Mixed Mesoporous Nickel Manganese Oxides/Hydroxides and Nanoparticles: Synthesis, Characterization, and Electrochemical Properties

Water oxidation catalysts are essential in the renewable energy industry[61]. Manganese-based transition metal oxides got much attention because they are low-cost, earth-abundant with a tunable morphology and large potential window [62], [63], [64]. Among all of the methods of synthesis of Mn-based oxide electrodes, hydrothermal method is the most common because it requires high temperatures, so it's beneficial in terms of time and cost[65], [66], Fukuzumi *et al.* reported the work on $NiMnO_3$ as an efficient water oxidation catalyst[67]. Nickel manganese mixed oxides were investigated at different manganese-to-nickel ratios. Compared to pure NiO and Mn_3O_4, the $NiMnO_3$ showed better photocatalytic activity towards oxygen evolution reaction with highest oxidation current[67], [63], In this study, tris(bipyridine)ruthenium (II) complex and peroxydisulfate(VI) ion have been used as photosensitizers and oxidants,

respectively[67]. Following this study, Yu *et al.* studied the electronic structure and photocatalytic properties of $MnNiO_3$ as a photocatalyst in a basic media[68]. This study shows that the $MnNiO_3$ has a suitable band-gap position for oxygen evolution reactions (OER) and hydrogen evolution reactions (HER). The Pourbaix diagram analysis shows that this composition is stable in alkaline media[68]. Other manganese nickel oxides like, $Ni_{1.5}Mn_{1.5}O_4$, $NiMn_2O_4$, and $MnNi_2O_4$ were synthesized at 800 ^oC using a hydrothermal method, where a surfactant is not required[69]. In this study, $Ni_{1.5}Mn_{1.5}O_4$ exhibits exceptionally high performance towards urea oxidation at 0.3 V vs Ag/AgCl (3.5 M KCl) reference electrode with a 7 mA/cm^2 current [69]. To show the effect of the morphology of the mixed nickel and manganese oxide electrodes, the Mn_2O_3 nanowires were fabricated via solvothermal synthesis without any calcination and templating[70]. One-dimensional nano-wires of Mn_2O_3 are dopped with Ni^{2+} and Co^{2+} ions, which create defects in the lattice, leaving room for oxygen vacancies and enhancing the electrocatalytic performance of doped oxide compared to pure one[70]. In every other work, the water oxidation reaction mostly occurs in basic media[68], [71], [72], [68], [73].

It was studied that nickel mixed with manganese makes lattice distortion in manganese oxide spinel structure, which enhances overall water splitting[74], [75]. Also, nickel oxide being in a 3+ oxidation state improves cycling stability during the galvanostatic charge-discharge experiment[76]. Here, Rajendiran *et al.* show the synthesis of a hierarchical nickel-dopped manganese iron carbonate[76]. Duraivel *et al*. investigated the synthesis of nickel manganese oxide electrodes at different nickel manganese ratios, with a Ni ratio of 20, 25. 50, 75, and 80 %, to evaluate the optimum composition for OER[75]. The nickel-rich compositions, namely $Ni_{0.75}Mn_{0.25}O$ and $Ni_{0.8}Mn0_{.2}O$, showed the best performance towards water oxidation with overpotentials of 250 and 140 mV at 10 mA/cm^2 current density, respectively[75]. However, Tafel slopes are not as low as in this thesis and are around 100 mV/dec[75]. In the previous study of the same research group, different nickel manganese hydroxides were synthesized by hydrothermal method for water oxidation[77]. Different mole ratios were tested and in chronopotentiometry experiment at 10 mA/cm^2 the lowest overpotentials that were observed 264 and 165 mV both for oxygen evolution and hydrogen evolution reactions [77], [78].

During the electrocatalytic process, transition metal oxides tend to convert to metal hydroxides, which are usually active sites in OER and in other electrochemical processes, like galvanic charge-discharge measurements (GCD), Tafel and chronoamperometry measurements (CA), chronopotentiometry (CP), cyclic voltammetry (CV), etc.[79], [80], [81], [82][83]. So, many studies are targeted at synthesizing metal hydroxide[79], [80], [81], [82], [83], [84]. Transition metal hydroxides are layered materials so, for example, mixed nickel manganese hydroxides are called NiMn layered double hydroxides[84]. Mixed double hydroxides are easily synthesized using methods like co-precipitation, electrodeposition, hydrothermal methods, etc[85], [86]. Latorre-Sanchez *et al.* showed the synthesis of Nickel manganese hydroxides using the nickel and manganese nitrates mixed in ethanol and keeping them at 65 ^{o}C while stirring for 3 days till obtained suspension sonicated and dried to obtain hydroxides[87]. NiMn hydroxides microspheres were also synthesized on hard template silica oxide by using salts suspensions in ethanol and stirring the mixture at room temperature for 1 hour[88]. High temperatures are not required in co-precipitation methods, but the hydrothermal methods do require elevated temperatures. For hydrothermal synthesis urea is widely utilized to make metal hydroxides[89], [90], [91], [92].Urea increases the pH of the solution above 90 ^{o}C and speeds up the precipitation of NiMn hydroxide with high crystallinity and yield[89]. Similar to urea, hexamethylenetetramine is also used for synthesizing NiMn hydroxides via a hydrothermal route[93].

Because of the unique layered structures consisting of the monolayer nanosheets of nickel manganese double hydroxides, they are seen as promising energy storage materials[94], [95], [96]. As manganese can exist in different oxidation states, it is also a promising electrode material and is a good candidate for nickel in the fabrication of layered double hydroxides[97], [98]. Replacement of Ni^{2+} species with Mn^{3+} ones improve the usage of Ni^{2+} due to electronegativities between two metal ions[97]. In the literature, there are some mechanisms proposed for the electrochemical process (charge-discharge, OER, etc.) of the nickel and manganese mixed hydroxides as a Faradic redox reaction (see Equations 1.2, 1.3, 1.4)[99].

$$Ni(OH)_2 + OH^- \leftrightarrow NiOOH + H_2O + e^- \qquad \textbf{Equation 1.2 [99]}$$

$$Mn(OH)_2 + OH^- \leftrightarrow MnOOH + H_2O + e^- \qquad \textbf{Equation 1.3 [99]}$$

$$MnOOH + OH^- \leftrightarrow MnO_2 + H_2O + e^- \quad \textbf{Equation 1.4} \text{ [99]}$$

The electrochemical analysis should be done in the basic electrolyte as the electrode material is dissolved in the acidic media, and the charge storage happens due to electrons moving between layers of the double hydroxide redox active sites [99].

Manganese oxide alone, has high theoretical specific capacity of 755 mA*h/g[100][78]. In the very first study of manganese oxide as an energy storage material by Goodenough *et al.*, where potassium permanganate and manganese diacetate were reacted to produce manganese dioxide. The reaction is given in Equation 1.5[101].

$$Mn^{7+} + 3/2Mn^{2+} \rightarrow 5/2Mn^{4+} \quad \textbf{Equation 1.5}$$

The capacity of MnO_2 showed ideal values in NaCl and KCl electrolytes.

Capacity values were calculated by charge (Q) that was measured via cyclic voltammogram experiments or from galvanostatic charge-discharge profiles, and the charge value is divided by a static load of the electrode (m) and potential window (ΔE) that was initially set for the measurement; the formula is given in Equation 1.6[102].

$$C = Q/(m\Delta E) \quad \textbf{Equation 1.6}$$

It was determined that specific capacity is quite sensitive to the surface area of the electrode[102]. Increasing the surface area increases the capacity [102].

As for the nickel manganese double oxides, it was already discussed that they are excellent water oxidation catalysts and similar to double NiMn hydroxides, they are also good energy storage electrodes [65][103], [104]. They have high theoretical capacity and a wide potential window, which makes them promising electrochemical capacitors [105], [106]. There are several studies that have shown the application of nickel manganese oxide as an energy storage material, for example Wu *et al.* showed the synthesis of nickel magnet binary oxides nanoparticles with the specific capacity of 285 F/g at 5 mV/s scan rate[107], [108]. In another work, mesoporous $NiMn_2O_4$ was synthesized via the sol-gel method and showed a specific capacity of 243 F/g at 5 mV/s scan rate, which is similar to Wu *et al*. work[107]. Another study showed even lower capacitance for $NiMn_2O_4$ that is 202 F/g at 0.5 mA/cm^2 current density[109]. In all of the above-mentioned studies, the sodium salt electrolytes were used[107], [108], [109].

The capacity value was significantly improved by replacing the electrolyte with a basic one, 2M KOH[104]. The maximum capacity reported was 460 F/g at a 5 mV/s scan rate[104]. In one of the recent publications of Ray *et al*., the capacity of synthesized Ni-Mn-Oxide electrodes reached almost 1200 F/g at 2 mV/s scan rate with stability up to 5000 cycles [103]. Also, that material showed excellent coulombic efficiency of 97% up to 3000 cycles[103].

1.6 Mesoporous Nickel Oxide and Nickel Oxide Nanoparticles on Silica Support and their Electrochemical Properties

Attard *et al.* reported the first example on synthesis of mesoporous silica using liquid crystalline mesophases[110]. Silica with pores of around 3 nm was synthesized[111]. This synthesis method is considered to be a soft templating method with high surfactant concentration, where the phase diagram of silica with surfactant and surfactant with water look similar[110]. The liquid crystalline templating method later opened a window for fabricating other mesoporous materials via soft templating path[110]. Earlier, Bogush *et al.* studied the kinetics of the formation of silica nanoparticles via condensation of silicon alkoxides[112]. In this study, authors showed that TEOS (tetraethoxyorthosilicate, $Si(OCH_2CH_3)_4$) undergoes hydrolysis and condensation reactions when NH_3 is added [112]. The silica molecular sieves, such as MCM-41 and HMS were synthesized using TEOS and charged surfactant quaternary ammonium salts and neutral primary amine[113]. The pore size of the as-synthesized mesoporous silica was about 3.5 nm with a maximum surface area of 1250 m^2/g[113].

The successfully synthesized mesoporous silica has been employed as a hard template to fabricate mesoporous transition metal oxides. Liu *et al.* have synthesized one of the first examples mesoporous nickel oxide by silica templating [114]. The mesoporous nickel oxide with a surface area of 530 m^2/g has been synthesized using nickel sulfate as the salt precursor and CTAB as a surfactant [114]. In 2006, Kim *et al*. have synthesized NiO and SiO_2 nanocomposites using spray pyrolysis, which produced smaller nickel oxide nanoparticles when silica was involved in the synthesis, while the pure nickel oxide particles always grow into large crystallites by increasing temperature[115].

SBA-15 is probably one of the most widely utilized silica templates for synthesizing mesoporous materials[116]. So mesoporous nickel oxide was synthesized by nano casting method using SBA 15, and the synthesis schematics is shown in Figure 1.6[116].

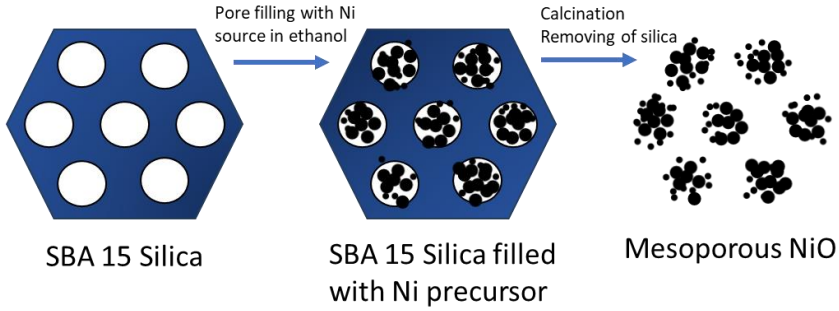

Figure 1.6. Schematics of the synthesis mesoporous NiO by using SBA-15[116].

In this synthesis, nickel nitrate hexahydrate, dissolved in ethanol, was used as a nickel source, and the SBA-15 powder was slowly added into the solution. The solution was stirred for 12 hours and dried for another 12 hours to obtain mesoporous nickel oxide powder on silica, after etching the silica template by sodium hydroxide solution[116].

Another method, which was employed to produce NiO nanoparticles using silica is microemulsion sol-gel synthesis[117]. The point of this study was to obtain different types of NiO compositions like pure nickel oxide, silica-coated nickel oxides, and nickel oxides inside of the silica matrix[117]. The study showed that NiO with silica shows a more uniform and smaller particle size compared to the pure NiO nanoparticles. If NiO-coated silica and NiO embedded in silica matrix are compared, the last one is more transparent in UV-visible and infrared regions[117]. Also, by tuning the surfactant, silica concentration, and calcination temperature, microemulsion sol-gel synthesis is considered to be advantageous in producing mesoporous nickel oxide with silica with different morphologies[117].

1.7 Fabrication of Ordered Mesoporous Nickel Oxide and α-, β - $Ni(OH)_2$

As has already been discussed, the method to synthesize mesoporous nickel oxide and nickel manganese mixed oxides is the molten salt-assisted self-assembly[20], [37], [43], [118], [119]. In this method, salt, non-ionic and charged surfactants are used

to create the LLC phase that can be calcined at elevated temperatures to obtain mesoporous metal oxide of the salt. MASA is an easy method and considered to be one pot synthesis. Though this method ensures high surface area, small particle size and large pore volume to the metal oxide, the main disadvantage compared to hard templating or nano-casting one [35] is that it does not produce ordered material but rather sponge like porous structure. For the optical characterization, ordered structures are more advantageous for measuring band gap for example[120]. Their ordered structure also provides advantages like easier structural characterization (XRD, SEM imaging, etc.)[121].

One way to synthesize ordered mesoporous nickel oxide could be electrochemical deposition from the dilute surfactant solution[122]. Mesoporous nickel hydroxide film was prepared by electrochemical deposition from diluted solution that contains surfactant templates by Tan *et al.* Lamellar structures were formed by using sodium dodecyl sulphate as a template together with triblock co-polymer (P123, $EO_{20}PO_{70}EO_{20}$, EO is ethylene oxide and PO is propylene oxide) and ethylene glycol. The electrodeposited mesoporous nickel oxide electrodes were obtained by washing with water and 2-propanol to remove the surfactant[122]. The end material was characterized by small angle XRD and shown that the nickel hydroxide film is quite uniform[122].

The XRD patterns can be indexed with a 2D hexagonal symmetry. It should be noted that $Ni(OH)_2$ was freshly electrodeposited from nickel nitrate and surfactant solution (plating solution), and it has a very regular structure. In order to obtain ordered mesoporous nickel oxide, the freshly deposited electrode can be calcined at high temperatures, assuming the end material is not going to lose its pore regularity after calcination. In the future work, this method will be utilized to synthesize mesoporous NiO for comparison.

1.8 Review of Electrochemical methods used in this study

Chronopotentiometry (CP) is a widely used technique in electrochemical experiments. In this technique, a constant current is applied to a system, and the voltage response is recorded[123]. This is achieved by employing special potentiostat devices in a traditional, wet electrochemical setup [123]. Lastly, the potential behavior is critical

for understanding the electrochemical reactions over time [123]. This method is widely used to test water oxidation reactions and obtain overpotentials at various current densities for OER[123].

Galvanostatic charge & discharge (GCD) is a sub-technique of chronopotentiometry is related to charge and discharge processes [124]. As the name implies, the direction (the sign) of the applied current leads to the charging of the electrochemical system [124]. This is widely used for battery research and analysis of different electrode materials that have high charge capacity as well [124]. Thus, the voltage behavior heavily depends on the electrochemical system (or the mesoporous transition metal oxide electrode in this thesis) and helps us to evaluate and characterize the electrodes [124]. On the other hand, the chronopotentiometric discharge process is the same as the charge process, where the direction or the sign of the current is opposite [124]. Therefore, it resembles a battery discharge[124].

Cyclic voltammetry (CV) is a very commonly used technique in traditional electrochemistry, where the potential/voltage is being swept at a constant rate and the current response is recorded. In this technique, the overall voltage window of the electrochemical system can be analyzed in detail, and the stability of the electrodes can be demonstrated over multiple cycles and scenarios [125]. Moreover, the current intensity over time can lead to conclusions regarding surface properties such as active site area, (double-layer) capacitance, and reaction kinetics[125].

Tafel equation is one of the well-known equations in electrochemistry[126]. It represents the overpotential (η) against the current density (*j*) to model/analyze reaction kinetics. The overall equation is given in Equation 1.7 [126].

$$\eta = a + b*\log(j) \quad \textbf{Equation 1.7 [126].}$$

In this equation, η is the overpotential in V (Volts), *j* is the current density (which is i/i_0), b is the Tafel slope (which includes parameters related to the charge transfer processes and temperature), and a is the intercept point at zero current [126]. Since it is a logarithmic equation, the plotting must have log-scale axes. Thus, the plot can be drawn by plotting η [126]. Tafel plot values provides information about the mechanism of the electrochemical reaction [126]. This plot is obtained from a

chronoamperometry (CA) experiment where voltage is given as an input and the current response is investigated [126].

Series resistance (R_s) measurement using electrochemical impedance spectroscopy (EIS) is a non-destructive, in-situ technique that is commonly used in battery research, electrochemical characterization, and similar fields[127], [128]. Fundamentally, it applies a sinusoidal excitation signal to the electrochemical system and analyzes the results[116][129]. Depending on the overall impedance, this excitation signal can be current or voltage[116]. If the current is applied, the voltage response is measured. Contrary, if the voltage is applied, the current response is analyzed[116]. The sinusoidal signal is applied at different frequencies, which range from kHz to mHz. The range selection depends on the studied system and electrochemical processes of interest[116] [129]. As a result, the excitation signal is applied over a log-based frequency range[116]. Thereafter, the response is analyzed for its linearity, causality, and reproducibility[116] [129]. All the data reported in this thesis are KK-compatible [129]. By doing EIS analysis, one can get critical parameters such as solution resistance, charge transfer resistance, double-layer capacitance, and diffusion processes [129]. These parameters can shed light on the electrode properties, which is the main focus point of this thesis [129]. Ohm's Law correlates between the potential and voltage relationship over a resistor. The Ohm's law is given in Equation 1.7[130].

$$V = I*R \quad \textbf{Equation 1.7} \text{ [130].}$$

In this formula, V is the voltage in V, I is the current in A, and R is the resistance in Ohms [130].

In this thesis, the mesoporous nickel manganese mixed oxides denoted as $Ni_{1-x}Mn_xO$ and nickel oxide on silica template denoted as m-NiO-SiO_2 electrodes are synthesized, and various structural characterization techniques with the above-mentioned electrochemistry analysis techniques will be implemented to characterize and analyze the properties of the NiO oxide-based electrodes.

Chapter 2

2 EXPERIMENTAL SECTION

2.1 Materials

Cetyltrimethylammonium bromide (CTAB), manganese nitrate tetrahydrate ($[Mn(OH_2)_4](NO_3)_2$), nickel nitrate hexahydrate ($[Ni(OH_2)_6](NO_3)_2$), 10 lauryl ether ($C_{12}E_{10}$), absolute ethanol, concentrated nitric acid (HNO_3), tetramethoxyorthosilicate, ($Si(OCH_3)_4$, TMOS), 1 M potassium hydroxide (KOH), lithium chloride (LiCl), lithium hydroxide (LIOH), deionized water, graphite rods, fluorine-dopped tin oxide (FTO).

2.2 Preparation of Ni(II) and Mn(II) Mixed Solutions

Ni(II) and Mn(II) mixed solutions are prepared by first dissolving a charged surfactant and metal salts (cetyltrimethylammonium bromide, CTAB), manganese nitrate tetrahydrate ($[Mn(OH_2)_4](NO_3)_2$) and nickel nitrate hexahydrate ($[Ni(OH_2)_6](NO_3)_2$) in 5 ml of ethanol and stirred with magnetic stirrer for 15 minutes to obtain clear solutions. Then a melted non-ionic surfactant (10 lauryl ether, $C_{12}E_{10}$) is added to the above solution and again stirred till clear solution is obtained. Note that the surfactants ratio was kept constant and only the Mn/Ni ratio was changed, keeping the total salts to surfactant ratio 10 to 1. Detailed composition information is provided in the Table 2.1.

Table 2.1. Compositions of the clear solutions, used for the preparation of mesoporous Ni_xMn_yO films, Ni salt rich compositions.

Ni(II)/Mn(II)/$C_{12}E_{10}$ Mole Ratio	Amount of $[Mn(OH_2)_4](NO_3)_2$ (g)	Amount of $[Ni(OH_2)_6](NO_3)_2$ (g)	Amount of CTAB (g)	Amount of $C_{12}E_{10}$ (g)	Amount of Ethanol (ml)
5:5:1	1.001	1.159	0.291	0.500	5
6:4:1	0.797	1.392	0.291	0.500	5
7:3:1	0.601	1.624	0.291	0.500	5
8:2:1	0.401	1.856	0.291	0.500	5
9:1:1	0.200	2.087	0.291	0.500	5
10:0:1	0	2.321	0.291	0.500	5

Table 2.1. provides Ni salt rich compositions. For better understanding the nickel and manganese mixed compositions, the manganese rich precursor solutions were also prepared and the compositions are tabulated in Table 2.2.

Table 2.2. Compositions of the clear solutions, used for the preparation of mesoporous Ni_xMn_yO films, Mn salt rich compositions.

Ni(II)/Mn(II)/$C_{12}E_{10}$ Mole Ratio	Amount of $[Mn(OH_2)_4](NO_3)_2$ (g)	Amount of $[Ni(OH_2)_6](NO_3)_2$ (g)	Amount of CTAB (g)	Amount of $C_{12}E_{10}$ (g)	Amount of Ethanol (ml)
4:6:1	1.201	0.928	0.291	0.500	5
3:7:1	1.401	0.696	0.291	0.500	5
2:8:1	1.602	0.464	0.291	0.500	5
1:9:1	1.795	0.232	0.291	0.500	5
0:10:1	1.994	0	0.291	0.500	5

As the amount of manganese is increased, the solutions become unstable, and eventually, brown precipitate forms. To avoid that issue, three drops of concentrated nitric acid are added. The reason why the above issue is not observed in the nickel-rich compositions is that the acidity provided by the nickel nitrate hexahydrate salt is sufficient to prevent any precipitation.

2.3 Preparation of Ni(II) and TMOS solutions and Fabrication of Mesopores Nickel Oxide Electrodes on Silica Support

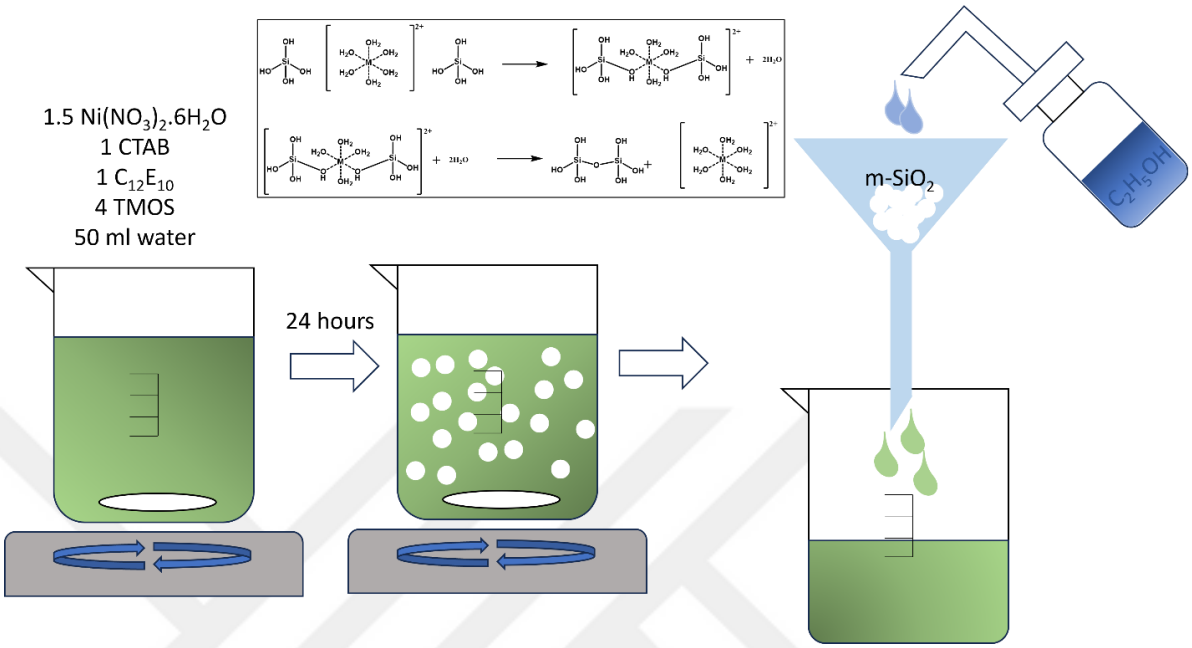

Figure 2.1. Synthesis Schematics of the mesoporous silica denoted as m-SiO_2.

In the synthesis schematics shown above, the nickel nitrate hexahydrate, CTAB, 10 lauryl ether, TMOS (tetramethoxyorthosilicate, $Si(OCH_3)_4$) and 50 ml of deionized water are mixed together in a 100 ml beaker and stirred over a magnetic stirrer till a homogeneous solution is obtained. After 24 hours of stirring, a cloudy precipitate started to appear in the solution. Later the solution is filtered washed with absolute ethanol and air dried to obtain mesoporous silica that later can be used as a template to synthesize mesoporous nickel oxide.

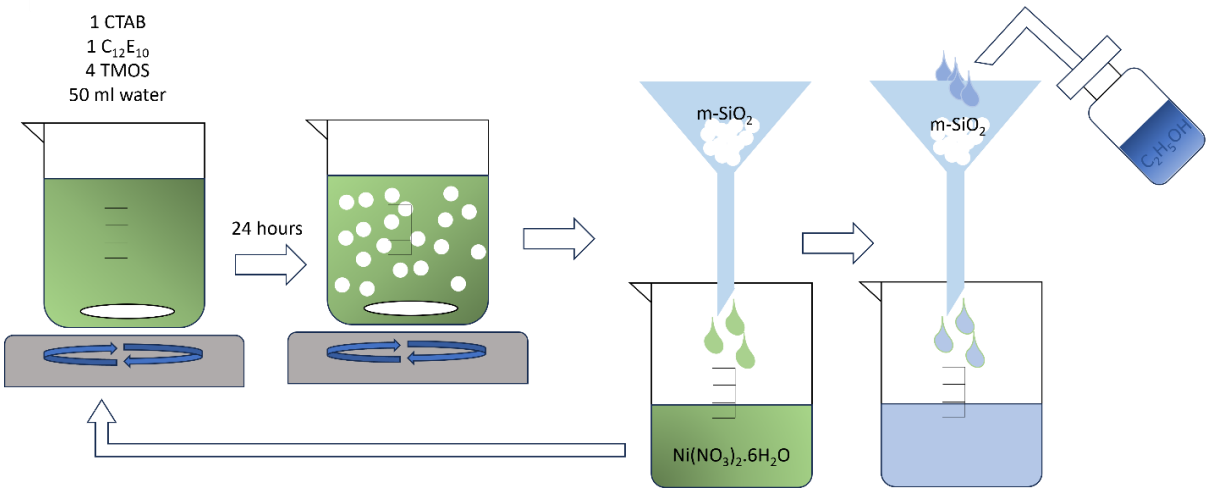

Figure 2.2. Synthesis Schematics of m-SiO_2 via reusing the filtrate.

As shown in Figure 2.2, the filtrate can be reused to synthesize more mesoporous silica oxide by adding precursors.

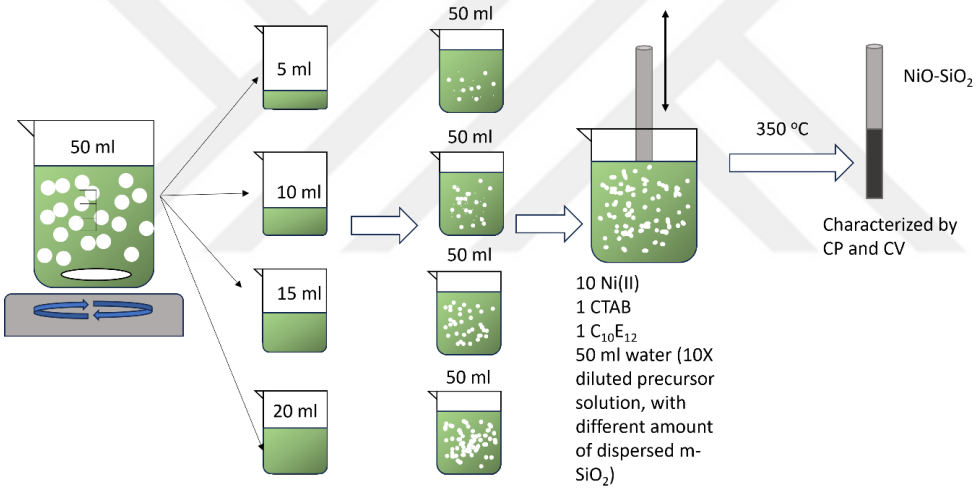

Figure 2.3. Synthesis schematics of the fabrication of mesoporous nickel oxide electrodes on graphite substrate, denoted as m-NiO using mesoporous silica at different amounts as a hard template.

For the detailed analysis of silica on structural compositions on mesoporous nickel oxide, different amounts of silica are used to synthesize NiO electrodes, as represented in Figure 2.3. The fully precipitated silica from the original solution was divided into 4 different parts with different concentrations of precipitated silica that were lately used for synthesizing mesoporous nickel oxide electrodes.

2.4 Preparation of Mesoporous Nickel Oxide (NiO) and Nickel Manganese Mixed Oxides ($Ni_{1-x}Mn_xO$).

Upon solution preparations, they were spread on the glass or fluorine-doped tin oxide (FTO) substrate by spin coating to obtain thin and by drop-casting to obtain thick LLC films. Spin-coating was done at 2000 rpm for 10 s that ensures immediate solvent evaporation and gelation. After calcination at 250 ^oC, the films are further annealed at higher temperatures, starting from 250 to 350 ^oC, with a 50 ^oC increments and keeping for 1 hour at each temperature. In the case of drop casting, drops of the precursor solution are spread on the glass substrate and kept at room temperature for 5-6 minutes to ensure gelation. After calcination, drop-casting produces thicker films, or monoliths. Spin-coated samples, on top of the FTO substrate, are used for electrochemical characterization, while the drop-casted ones are used for other characterizations, where large amount of sample is needed (like XRD and N_2-adsorption desorption measurements).

2.5 Preparation of the Electrodes for Electrochemical Characterization.

Above solutions are coated on top of the FTO glass by spin coating at 2000 rpm for 10 s. Then the coated samples are calcined at 250 ^oC, then annealed to 300 and to 350 ^oC for 1 hour at each temperature. The electrodes are used in electrochemical characterization in three-electrode systems in the basic electrolytes (1M KOH solution). The components of the electrochemical cell are working electrode (Ni_xMn_yO coated FTO), reference electrode (Ag/AgCl, in 4M KCl solution), and counter electrode (Pt wire). The cyclic voltammetry measurements were carried in various potential windows, at mostly 50 mV/s scan rate.

Electrodes on graphite substrate are prepared via diluting the original precursor solution 10 times and dip coating 1 cm length of graphite rode at a pulling speed of 10 cm/min, followed by calcination at high temperatures.

The schemes of three-electrode cells for electrochemical characterization are given in Figure 2.4.

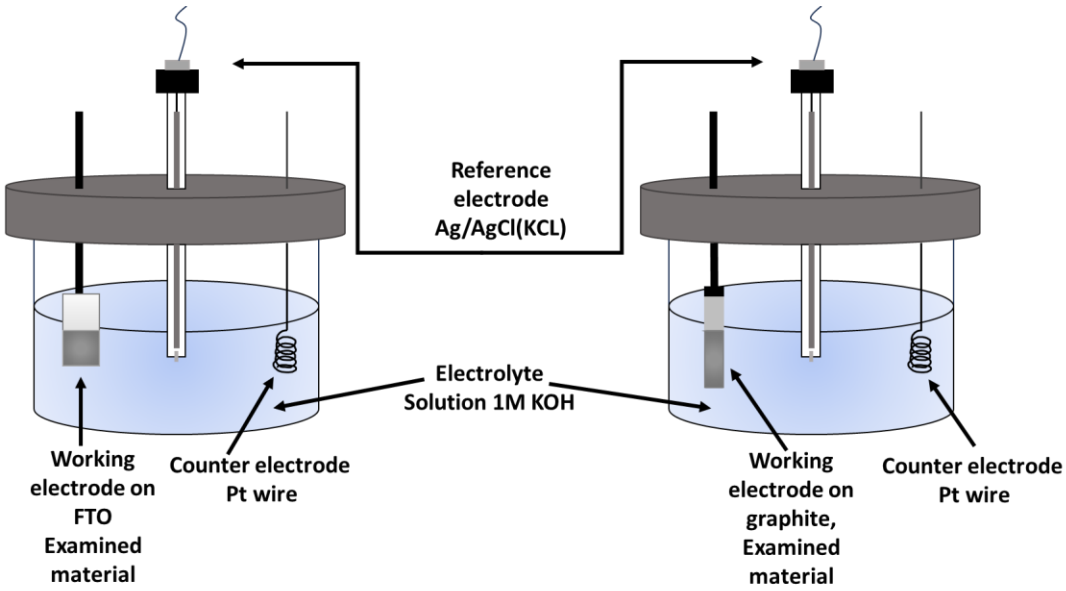

Figure 2.4. Schematic Representation of 3 electrodes, electrochemical cell for NiO based electrodes characterization.

2.6 Determination of Catalytic Load on Graphite Electrode

Catalytic load on the graphite electrode was determined by measuring the mass of the used precursor solution, diluted 10 times (see previous section). The schematic of catalytic load determination is given in Figure 2.5.

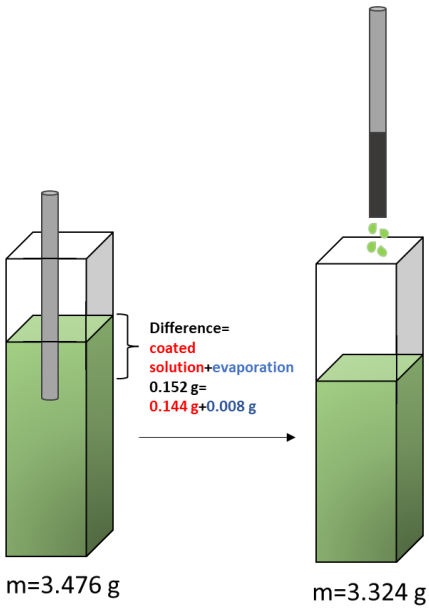

Figure 2.5. Schematic representation of the determination of catalytic load on graphite rod using change of the mass of the precursor solution.

10 times diluted initial precursor solution is poured in a UV cuvette. The mass of the UV cuvette is 1.879 g. The mass of the solution added is 1.597 g. The total mass is 3.476 g before dip coating. After dipping around 1 cm of 10 graphite rods into the solution, the mass of the cuvette decreased by 0.152 grams, 0.008 g of which is ethanol and evaporates during this process. So, 0.144 grams of solution is used to coat 10 graphite roads. As the amount of $Ni(NO_3)_2 \cdot 6H_2O$ is known in the initial precursor solution, it is calculated that $5.556*10^{-3}$ g of nickel nitrate was used for coating. After calcination of 10 graphites at 350 ^oC, the mass of the NiO coating becomes $1.427*10^{-3}$ g. Therefore, each electrode has a $1.427*10^{-4}$ g (or 0.143 mg) NiO coating(catalytic load on 1 single graphite rod).

2.7 Instrumentation

2.7.1 Powder X-Ray Diffraction (PXRD) Patterns

Rigaku Miniflex Difracometer operating at 30 kV/15 mA and Pananalytical X'Pertpro Multipurpose x-ray diffractometer, operating at 45 kV/40 mA with the K_α Cu X-Ray source (λ=1.54056 Å) are used for characterization of powder sample collected from drop-casting and spin-coated calcined samples scratched from the glass slides (wide angle) and fresh liquid crystalline phases that are prepared on glass or FTO substrates (small angle). The small-angle XRD patterns were measured between 1 and 5^o, 2θ, at a scan rate of 1 ^{o}/min. The wide-angle XRD patterns were measured between 10 to 80 ^{o}, 2θ, at a scan rate of 2 ^{o}/min. References for XRD patterns are taken from the JCPDS database (Joint Committee on Powder Diffraction Standards).

2.7.2 Polarized Optical Microscopy (POM) Images

ZEISS Axio Scope A1 polarizing optical microscope is used to collect POM images of the fresh or aged LLC mesophases.

2.7.3 N_2 (77.4 K) Adsorption-Desorption Measurements

Micrometerics Tristar 3000 automated gas adsorption analyzer in the range of 0.01 to 0.99 P/Po is used to obtain N_2-adsorption and desorption isotherms. Mesoporous transition metal oxide powders are scratched from the glass substrate, grinded thoroughly, and put into a vacuum of 35-40 mtorrs at 200 ^{o}C for at least 2 hours prior to the measurement to get rid of the volatile species and adsorbed water inside the pores for the accurate measurement. The surface area was calculated using the Brunauer-Emmett-Teller (BET) calculations using the first five points of the isotherms. Barrett-Joyner-Halenda (BJH) analysis is used to calculate pore size distribution.

2.7.4 Scanning Electron Microscopy (SEM) Images

FEI Quanta 200 F scanning electron microscope was used to make SEM images on the aluminum holder. The microscope operates at 15 keV beam energy and at high vacuum. Thoroughly grounded powder samples were put on the carbon tape on the aluminum SEM holder. Before the measurement, samples must be purged with dry air

to avoid contamination of the SEM chamber. The thickness of the film was investigated using a special vertical SEM holder where silicon wafer piece coated film was placed at 90 ^{o} angle.

2.7.5 Transmission Electron Microscopy (TEM) Images

FEI Technai G2 F30 microscope at an operating voltage of 200 kV is used to make high-resolution TEM images of mesopores transition metal oxide samples. The sample was prepared by diluting the original precursor solution 10 times and at a minimum spin rate of 500 rpm to make sure that the film obtained as thin as possible. after calcination, the film is carefully scratched from the glass substrate, thoroughly grounded using mortar, and diluted in absolute ethanol. The solution with powder in it was sonicated for at least 1 hour to ensure homogeneous powder dispersion, and after that, a few drops of the mixture were put on the TEM holder and dried under the powerful light source.

2.7.6 X-Ray Photoelectron Spectroscopy (XPS)

Thermo Scientific K_{α} photoelectron spectrometer equipped with Al Kα monochromatic source with the energy of 1486.68 eV at ultra-high vacuum conditions along with a flood gun for charge neutralization. Spot size is 400 µm. the XPS spectra were measured from the FTO and graphite rod surface by sticking them on XPS holder with conductive metal ribbon or copper tape. Charge shift was done with reference to C 1s scan (284.8 eV).

2.7.7 Electrochemistry Measurements

Gamry Instruments, Potentiostats PC14G750, and IFC5000-07565 were used to perform electrochemistry measurements, like Cyclic voltammetry (CV), Chrnopotentiometry (CP), Chronoamperometry (CA), Galvanostatic Charge-Discharge (GCD). All measurements were performed at 1 M KOH electrolyte. Ag/AgCl in 3.5 M KCl is the reference electrode (RE), Pt wire is a Counter electrode (CE), and the analyzed material is the working electrode (WE). Cyclic Voltammograms were recorded between -0.2 to 1 V potential window at 5 and 50 mV/s scan rate. Multistep Chronopotentiometry (mCP) was measured from 10 to 100 mA/cm^2 with 10 mA/cm^2

increment. Tafel slopes (A_t) were obtained from multistep chronoamperometry data (MCA) at a potential rage from 0.4 to 0.8 V with 0.02 V increment. GCD was measured at a potential window of 300 mV at current density of 0.1 mA/cm^2

Chapter 3

3 RESULTS AND DISCUSSION

3.1 Mesoporous Nickel Oxide Synthesis and Characterization

In our previous work, the mesoporous nickel oxide (denoted as m-NiO-n-XXX, where m stands for mesoporous, n is salt/surfactant ratio and XXX annealing temperature) was synthesized by using MASA method and described earlier [[20]. The m-NiO samples were characterized using PXRD, surface area analysis via N_2 adsorption-desorption measurement and Brunauer-Emmett-Teller (BET) calculations, imaging techniques (such as POM, SEM, and TEM), XPS, and electrochemical methods. The surface area, pore and pore-wall sizes can be tuned by changing the calcination/annealing temperature and salt to surfactant ratio. Once, the synthesis parameters were optimized, its electrochromic and electrocatalytic properties towards water oxidation were investigated[20]. The CVs, given in Figure 3.1, summarizes the electrochemical behavior of mesoporous nickel oxide[20].

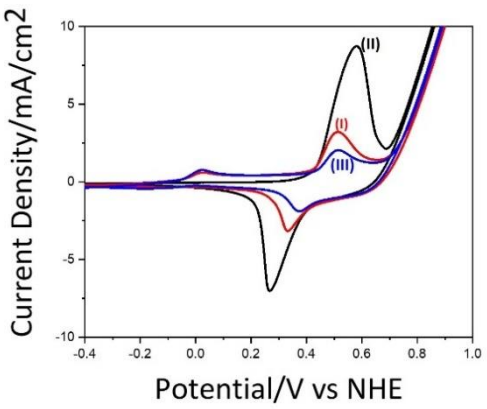

Figure 3.1. CV of m-NiO-10-400 (I) 1st, (II) 50th cycles, and (III) 1st cycle after annealing of (II).

Oxidation Peak around 0 V is attributed to to NiO oxidation. This assignment is based on the fact that it appears right after the calcination but disappears upon cycling, namely after 50 cycles. Moreover, the same oxidation peak reappears again after

annealing of the same electrode[20]. Another oxidation peak at a more positive potential is assigned to $Ni(OH)_2$ oxidation to NiOOH. Notice that the reverse cycling, NiOOH cannot be reduced back to NiO, rather to $Ni(OH)_2$, this can be explained by peak current density rising with each cycle and disappearing of NiO oxidation peak[20]. To summarize, NiO upon CV cycling, transforms to an active Ni(OH)2 on the NiO surface and is responsible for the water oxidation. It should be noted that, during the electrochemical process, color of the nickel oxide thin film changes from transparent ($Ni(OH)_2$) to black (NiOOH), indicating the electrochromic properties of the NiO thin films. The schematics of that transformation is shown in the Figure 3.2[20].

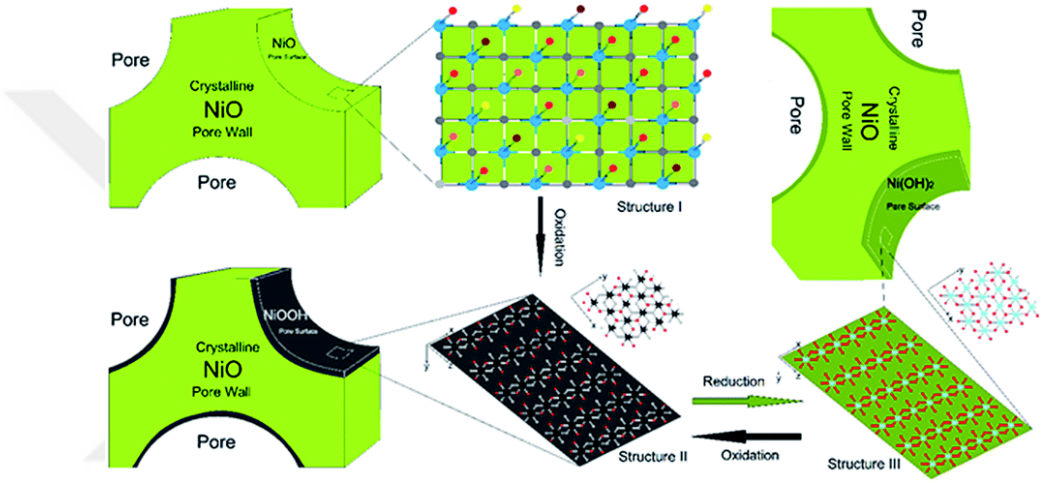

Figure 3.2. Schematic representation of mesoporous NiO before and after oxidation–reduction cycles with surface composition. Structure I: NiO surface and surface species; each color code indicates different species (such as OH, H_2O, etc.), structure II: NiOOH surface species, black atoms are Ni^{3+}, red spheres OH sites and gray O, and structure III: $Ni(OH)_2$ surface species, light blue Ni^{2+}, and red OH groups. Oxygen is coordinated to 6 Ni in NiO and 3 Ni in both NiOOH and $Ni(OH)_2$ (except surface oxygens)[20]. *Reproduced from Ref. [20] with permission from the Royal Society of Chemistry.*

The NiO to $Ni(OH)_2$ transformation occurs on the very top surface of the material. The XRD could not detect the formation of the nickel hydroxide layer, indicating either it is ultra-thin (a few nm) or amorphous. However, the XPS, being as a more sensitive surface technique, does provide information regarding this transformation (see Figure 3.3), as well as the cyclic voltammetry, see Figure 3.1[20].

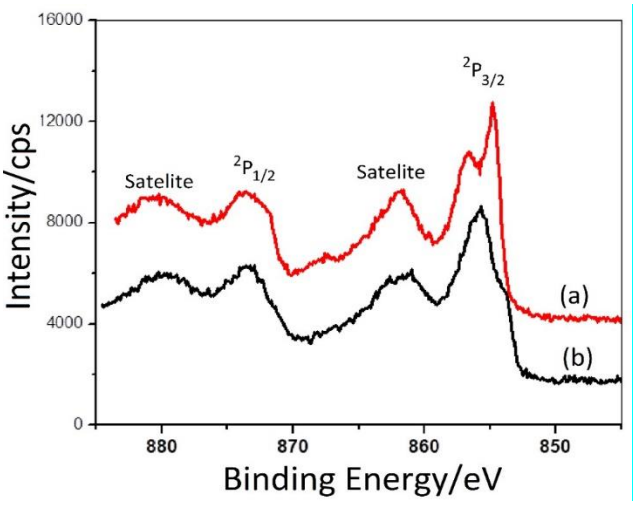

Figure 3.3. XPS spectra of the m-NiO (a) before and (b) after CV (1000 cycle).

Figure 3.3 shows the XPS spectra (Ni 2p region) of the m-NiO electrode before and after cyclic voltammetry experiment (1000 CVs). Before cycling, the peaks, observed at 854 and 856 eV, are assigned to different Ni(II) species, namely NiO and $Ni(OH)_2$, respectively. After electrochemical use, the peak around 854 eV loses its intensity and a new peak appears at 855.7 eV, that can be assigned to $Ni(OH)_2$/NiOOH species. Note that the nickel oxide peak doesn't completely disappears, indicating that only top surface in converted to hydroxide species[20].

The information that has been learned so far about nickel oxide, could be investigated further to evaluate what type of hydroxide species are forming on top of the oxide core. In literature, there are several known phases of nickel hydroxide, namely α-$Ni(OH)_2$ and β-$Ni(OH)_2$[56]. It is assumed that, with electrochemical use, initially the alpha phase is formed, and it is more active towards water oxidation, as peak currents are increasing with each cycle (see Figure3 4), however upon further cycling and in basic media, the peak current decays (Figure 3.5), indicating that alpha phase is transforming to less active β-$Ni(OH)_2$[56] or electrochemical degradation of the electrode. Previously, it was experimentally determined that upon aging α-$Ni(OH)_2$ in basic media, which is commonly used electrolyte 1M KOH, the phase transforms into β-$Ni(OH)_2$[20].

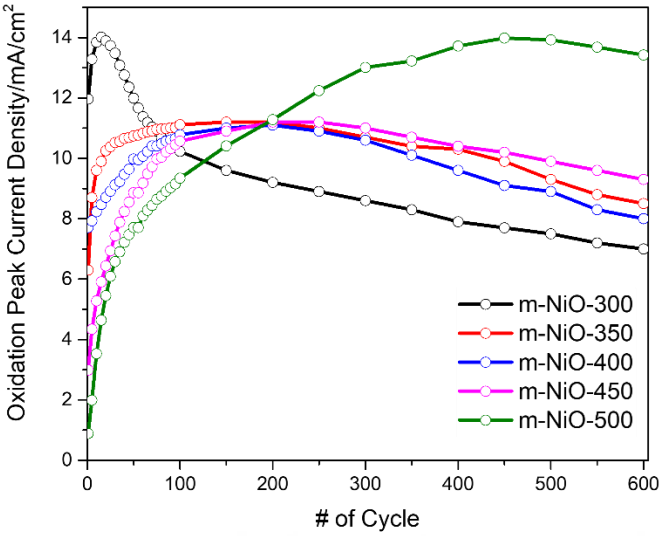

Figure 3.4. Overall change in peak current at around 0.6 V with cycling.

It should be noticed from Figure 3.4 that higher the calcination temperature, smaller the surface area, and bigger the crystallite size, the transformation of alpha phase to beta phase is slower, however at the end of the 600 cycles, the most crystalline electrode shows the highest current density[15]. The purpose of this work is to understand the kinetics of both α-$Ni(OH)_2$ and β-$Ni(OH)_2$ formation and understand the transformation mechanism by including another transition metal into the structure.

3.2 Characterization of Nickel and Manganese Salts-Surfactant LLC Mesophases

The freshly prepared solutions are drop-casted on the glass slides and analyzed by collecting small-angle XRD patterns (Figure 3.5). Total salt to surfactant ratio was kept 10 to 1, and amount of manganese precursor was varied from 1 to 9 with an increment of 1 by reducing nickel amount by the same amount.

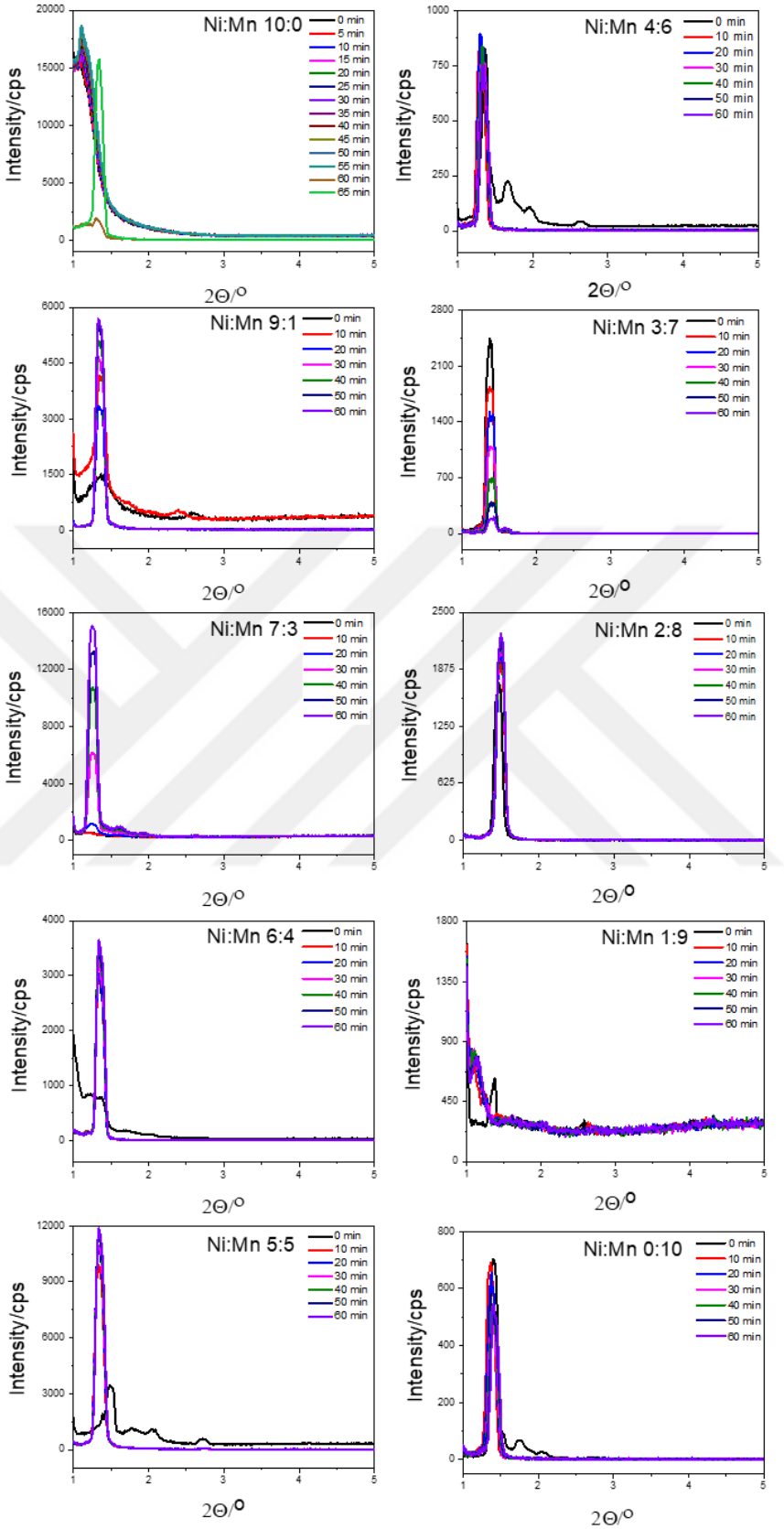

Figure 3.5. XRD patterns of Ni:Mn:$C_{12}E_{10}$ at different Ni to Mn mole ratio mesophases.

Figure 3.5 shows the small angle XRD patterns of the #Ni*Mn/1$C_{12}E_{10}$ samples. Upon drop-casting, they immediately form LLCs over the glass substrate (see the first diffraction patterns in Figure 3.5). With time, the diffraction line around 1.3°, 2θ, becomes more intense and shifts to a higher angle, indicating the evaporation of the volatile solvent and ordering of the mesophase. Increasing the amount of manganese salt stabilizes the mesophase, as no obvious diffraction line shift is observed after 30 minutes, however in the nickel salt rich mesophases the change in the diffraction line is more visible, diffraction line shifts from a smaller angle(~1.2°) to a higher angle (~1.4°) sharply from 55 to 65 mins. In the case of $Ni_{0.1}Mn_{0.9}$ composition, with aging a new diffraction line appears at smaller angles, which can be explained by changing the phase of the LLC.

Initially, the fresh mesophase displays diffraction lines that are visible even at higher angles, namely 1.34, 1.72, 1.79, 2.02, 2.27, 2.73 and 4.07 °, 2θ. Those diffraction lines are indexed to a 3D hexagonal mesophase and correspond to (101), (102), (003), (110), (103), (104) and (220) planes, respectively. Those indices were obtained from Equation 3.1 (see Figure 3.6.).

$$\frac{1}{d^2} = \frac{4}{3}\left(\frac{h^2+hk+k^2}{a^2}\right) + \frac{l^2}{c^2} \qquad \textbf{Equation 3.1}$$

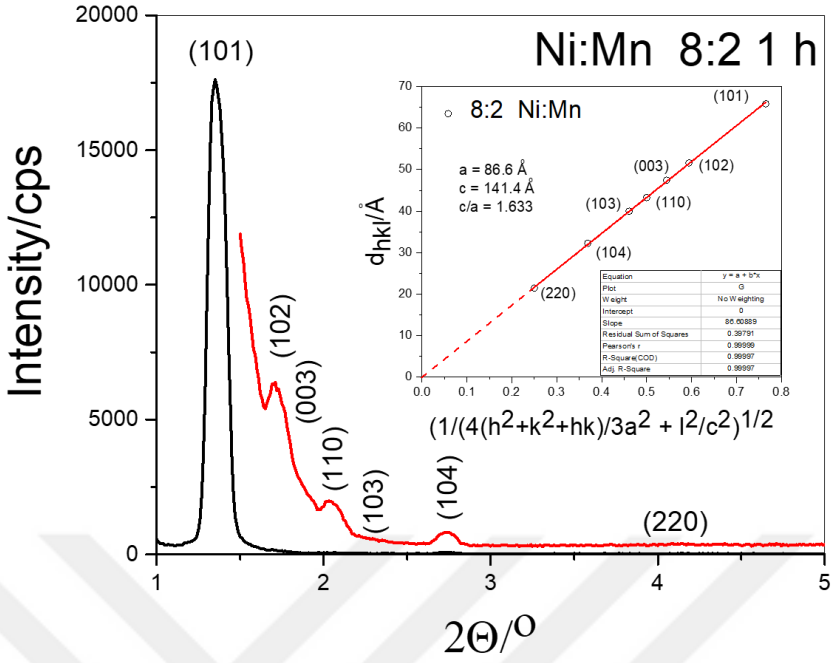

Figure 3.6. XRD pattern of Ni:Mn:$C_{12}E_{10}$ 8:2:1 mole ratio mesophase.

For the convenience, as the surfactant ratio does not change, the notation of the mesophase/oxide is going to be represented by following way, xNiyMn, where x and y the ratios of Ni and Mn, respectivel

After 1 hour of aging, diffraction lines after 1.5 ^{o} become less visible due to high intensity of the first line. However, if measurement starts after 1.5 ^{o}, the diffraction lines are visible.

Polarized optical microscope (POM) image of the Ni:Mn (8:2) sample is shown in Figure 3.7. Freshly spin-coated sample on the glass substrate gives a texture that is characteristic for the 3D hexagonal mesophase and supports the XRD data. This is well-known in the literature[40].

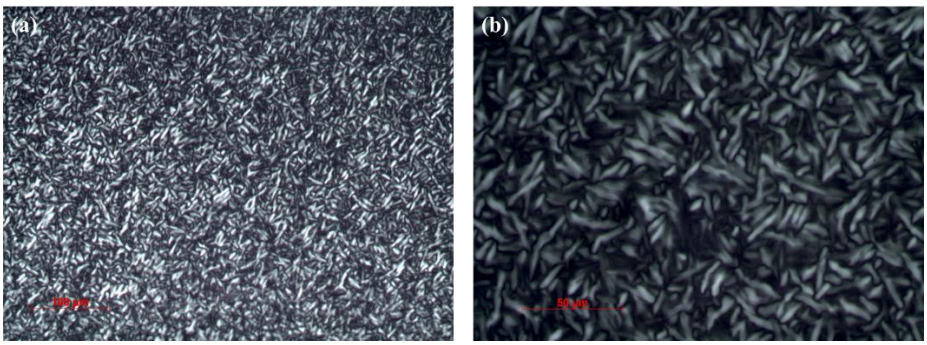

Figure 3.7. POM images of Ni:Mn (8:2) at (a) 100 and (b) 50 µm magnifications

With time, the mesophase stars to leach some of the salt out, and salt crystals appear in the POM image, however the texture is still present. Also, it should be noted that addition of Mn(II) salt increases stability of the mesophase. In the case of pure Ni salt, the crystallization takes around 10 minutes (see Figure 3.8).

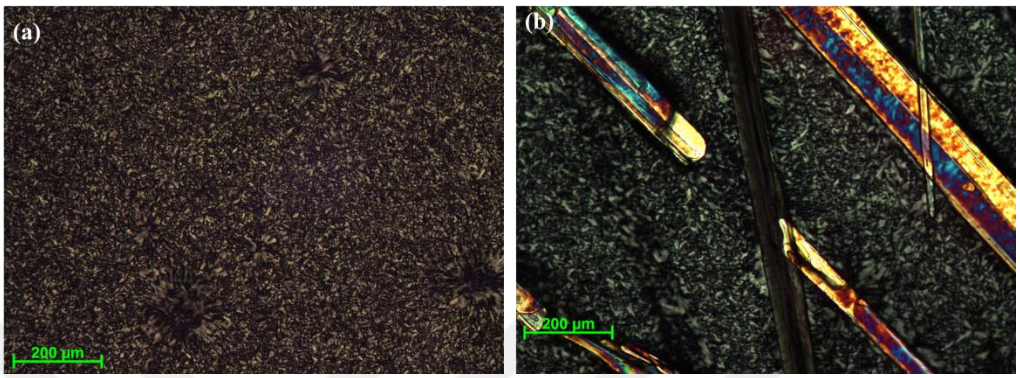

Figure 3.8. POM images of Ni:Mn (10:0) mesophase (a) fresh and (b) 10 minutes.

3.3 Structural Characterization of Mesoporous Mixed Oxides (m-$Ni_{1-x}Mn_xO$).

After the LLC characterization, the samples are calcined at 350 ^oC to obtain the mixed Ni and Mn oxides, denoted as m-$Ni_{1-x}Mn_xO$. The m-$Ni_{1-x}Mn_xO$ were characterized using XRD technique, and the particle sizes were calculated using Scheerer's equation given below (see Figure 3.9).

$$D = \frac{K\lambda}{\beta cos\theta} \qquad \textbf{Equation 3.2}$$

Where K is a shape factor, λ is x-ray wavelength (1.5405 Å), β is the fullwidth half maximum (FWHM) of the diffraction line, and θ is Bragg's diffraction angle[131].

The particle size gradually increases moving from high Mn concentration to a lower one (from 3.3 to 4.5 nm, respectively), indicating that the addition of manganese makes the product more robust to calcination at 350 ^oC. It was previously confirmed that the mesoporous manganese cobaltite resist to particle growth during calcination compared to mesoporous nickel cobaltite[44].

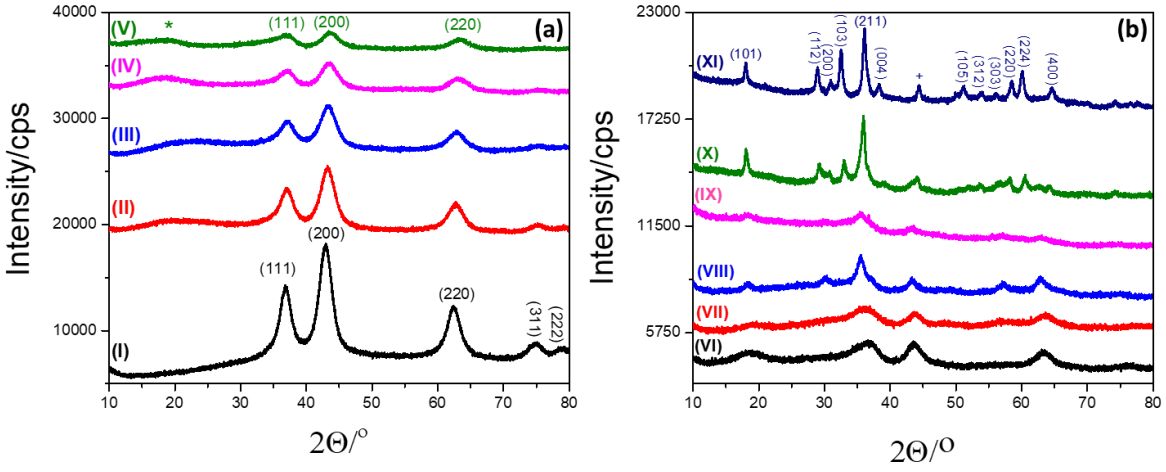

Figure 3.9. XRD patterns of (a) (I) NiO , (II) $Ni_{0.9}Mn_{0.1}O$, (III) $Ni_{0.8}Mn_{0.2}O$, (IV) $Ni_{0.7}Mn_{0.3}O$, (V) $Ni_{0.6}Mn_{0.4}O$, and (b) (VI) $Ni_{0.5}Mn_{0.5}O$, (VII) $Ni_{0.4}Mn_{0.6}O$, (VIII) $Ni_{0.3}Mn_{0.7}O$, (IX) $Ni_{0.2}Mn_{0.8}O$, (X) $Ni_{0.1}Mn_{0.9}O$, (XI) Mn_3O_4, calcined at 350 °C, * (101) plane of the Mn_3O_4 phase, + (200) plane of the NiO phase.

The diffraction lines on the Ni-rich site can be assigned to rock-salt NiO structure (PDF Card number – 00-044-1159), however slight shift is observed to a higher angle when the nickel content is decreased in the sample. Another diffraction line appears at around 18°, 2θ, in the case of m-$Ni_{0.5}Mn_{0.5}O$ sample, that might be assigned to MnO_2 formation. As shown in Figure 3.14, with increasing Mn amount, the diffraction lines due to the NiO (111) and (200) planes shift in opposite directions. As was mentioned, up to $Ni_{0.4}Mn_{0.6}O$, all compositions mimic a typical NiO unit cell (PDF card # - 00-047-1049), while after $Ni_{0.4}Mn_{0.6}O$, the diffraction lines can be indexed to the Mn_3O_4 unit cell (PDF card # - 00-024-0734). $NiMnO_3$, Mn_2O_3 phases appear at higher calcination temperatures (see further discussions).

To understand how the surface area and pore size distribution changes with addition of manganese to nickel oxide, the surface analysis has been performed. N_2 adsorption-desorption isotherms and pore size distribution plots of m-Ni_xMn_yO samples are shown in Figure 3.10.

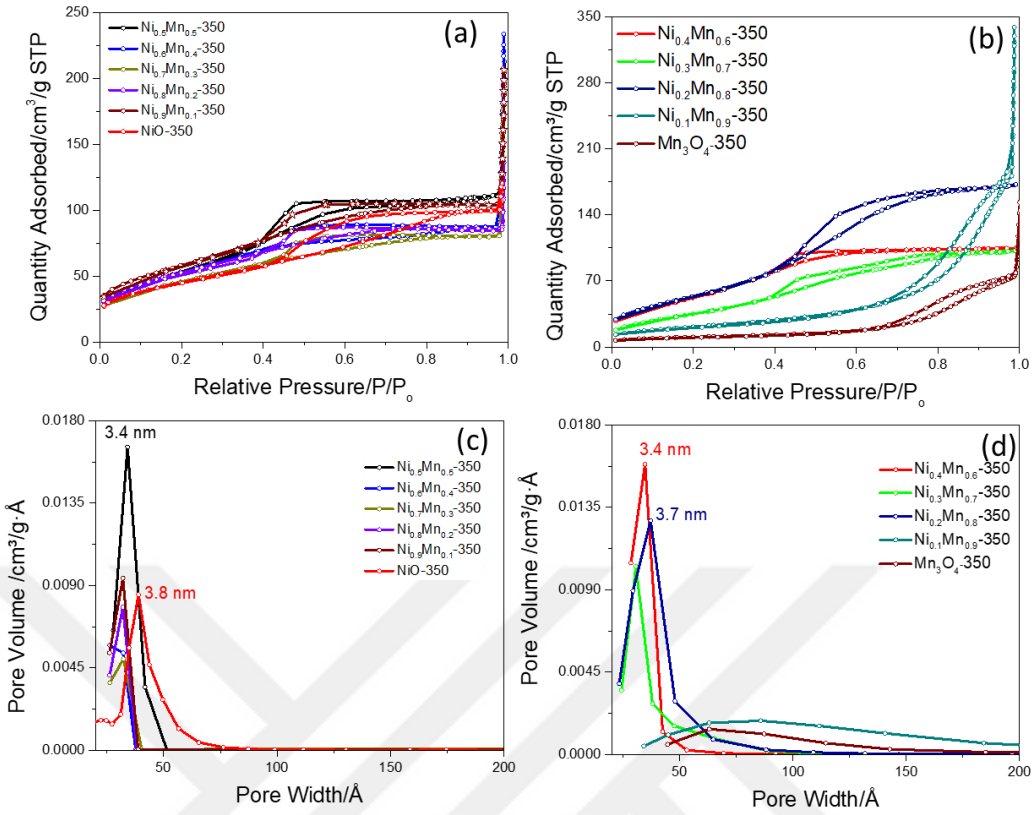

Figure 3.10. N_2(77 K) adsorption-desorption isotherms and pore size distribution plots (obtained from desorption branches) of the mesoporous Ni and Mn mixed oxides, calcined at 350 ^oC.

All isotherms are type IV and characteristic for the mesoporous materials[132]. The pore size distribution plots show that the $Ni_{0.5}Mn_{0.5}O$ and $Ni_{0.4}Mn_{0.6}O$ show the most uniform pore size distribution, with an average pore size of 3.4 nm, while the least uniform oxides are the Mn-rich oxides. From the pore size distribution plot, one can conclude that with increasing the Mn content, the pores get less uniform and the surface area decreases, see Table 3.1.

The average pore size decreases gradually moving from high Mn content oxide to pure NiO, so is the pore volume (see Table 3.1). The surface area follows the same trend and constituted a 191 m^2/g and 164 m^2/g for the $Ni_{0.5}Mn_{0.5}O$ and pure NiO, respectively. In the Mn rich site, the BET surface area drops from 196 to 38 m^2/g in the $Ni_{0.4}Mn_{0.6}O$ to pure MnO samples, respectively. The pore size follows the surface area, and it is 3.4 nm in the $Ni_{0.4}Mn_{0.6}O$ and 8.9 nm in the Mn_3O_4 sample. However, it does not follow any trend in the Ni-rich side, as the $Ni_{0.2}Mn_{0.8}O$ shows the highest surface

area of 201 m^2/g, and $Ni_{0.1}Mn_{0.9}O$ shows the highest pore volume and pore size of 0.511 cm^3/g and 17.6 nm, respectively.

Table 3.1. N_2(77 K) adsorption-desorption analysis data of $Ni_{1-x}Mn_xO$-350, S_{bet}[a] is BET surface area, V_P[b] is BJH pore volume, and D_P[c] is BJH pore size.

x of $Ni_{1-x}Mn_xO$ Samples	S_{BET}[a] (m^2/g)	V_P[b] (cm^3/g)	D_P[c] (nm)
0	164	0.175	4.1
0.1	211	0.292	4.7
0.2	192	0.171	2.8
0.3	167	0.247	5.5
0.4	193	30.317	6.0
0.5	195	0.341	5.1
0.6	196	0.191	3.4
0.7	131	0.168	3.6
0.8	201	0.278	3.7
0.9	78	0.511	17.6
1.0	38	0.117	8.9

As previously mentioned, at 350 ^oC, the nickel manganese oxides form a homogeneous mixture; there is no phase separation. To understand at which temperature the phase separation occurs or which phase forms at elevated temperatures, a temperature dependent analysis has been performed by recording their powder XRD patterns (see Figure 3.11 and 3.12 for all compositions, both Ni-rich and Mn-rich samples).

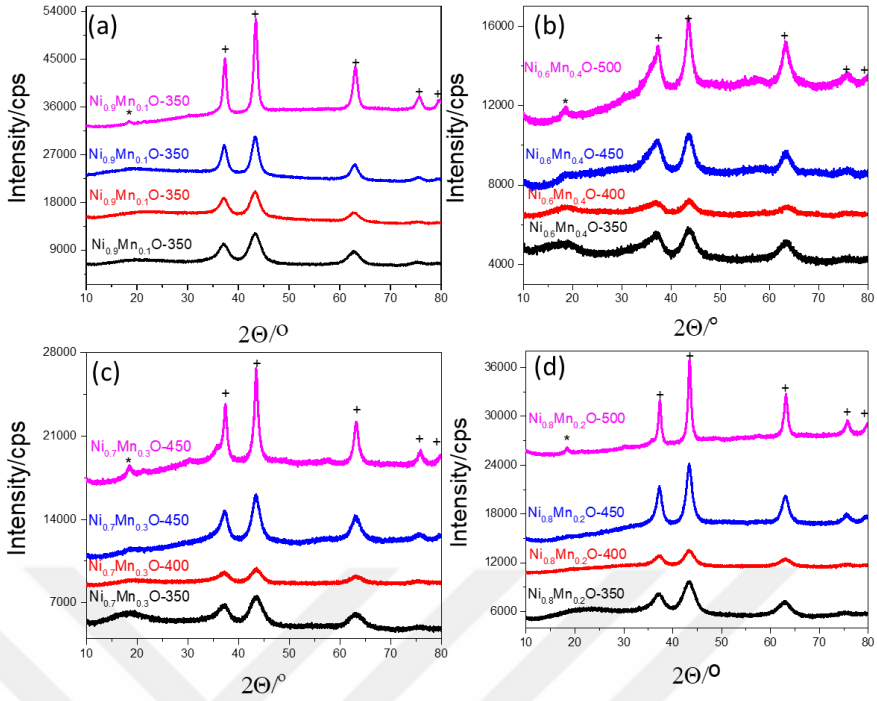

Figure 3.11. Temperature-dependent XRD patterns from 350 ºC to 500 ºC of (a) $Ni_{0.9}Mn_{0.1}O$, (b) $Ni_{0.8}Mn_{0.2}O$, (c) $Ni_{0.7}Mn_{0.3}O$, (d) $Ni_{0.6}Mn_{0.4}O$ (* diffraction line of Mn_3O_4 , + diffraction lines of NiO).

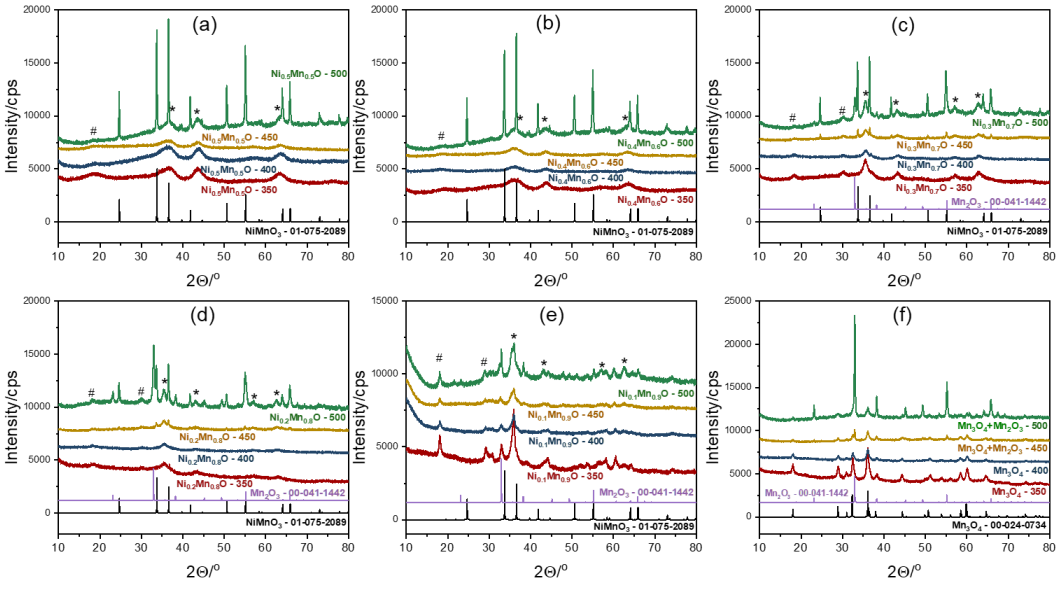

Figure 3.12. Temperature-dependent XRD patterns from 350 °C to 500 °C, # diffraction line of Mn_3O_4 , * diffraction lines of NiO, (a) $Ni_{0.5}Mn_{0.5}O$, (b) $Ni_{0.4}Mn_{0.6}O$, (c) $Ni_{0.3}Mn_{0.7}O$, (d) $Ni_{0.2}Mn_{0.8}O$, (e) $Ni_{0.1}Mn_{0.9}O$ and (f) Mn_3O_4.

In the figures above, the diffraction patterns of all compositions, calcined at 350, 400, 450, and 500 ^{o}C are given. It is shown in Figure 3.12 that for the $Ni_{0.9}Mn_{0.1}O$, $Ni_{0.8}Mn_{0.2}O$, $Ni_{0.7}Mn_{0.3}O$, and $Ni_{0.6}Mn_{0.4}O$ compositions, no visible phase separation occurs up to 500 ^{o}C. The structure remains the same and mimics the cubic NiO unit cell (PFD card # - 00-047-1049), except a diffraction line at 18.3^{o}, 2θ, that belong to (101) plane of Mn_3O_4 phase; it becomes more visible at 500 ^{o}C, in all above compositions. Once the amount of Mn is increased ($Ni_{0.5}Mn_{0.5}O$ and $Ni_{0.4}Mn_{0.6}O$) a clear phase separation is observed at 500 ^{o}C. However, the patterns cannot be indexed to any phase of manganese oxide, but rather to $NiMnO_3$ phase. This phase of nickel manganese oxide is phase separating from the rest, leaving NiO phase that might contain manganese oxide phase as well. Once, the amount of manganese is increased further (see Figure 3.12), at elevated temperatures, the new diffraction lines along with the $NiMnO_3$ phase appear and gets sharper once the amount of manganese is further increased. The new diffraction lines belong to Mn_2O_3, which is the phase of manganese oxide commonly observed at high temperatures (PDF card # - 00-041-1442). As already mentioned before, at lower temperatures, the Mn_3O_4 phase usually forms and remains up at 500 ^{o}C in the Mn-rich oxides. As for the pure manganese oxide, a smooth transition is observed from the Mn_3O_4 to Mn_2O_3 phase during annealing from 300 to 500 ^{o}C. .

The SEM images of the selected samples calcined at 350 and 500 ^{o}C are shown in Figures 3.13 and 3.14. The SEM images of all compositions display uniform film morphology. At high temperatures, the samples display large pores with crystalline pore walls. This is in good agreement with surface area analysis and powder XRD diffraction data. The manganese-rich samples show high crystallinity and separate particles. In the Ni-rich samples, at low calcination temperatures, pores are barely visible due to low crystallinity and small pore-size. In the $Ni_{0.8}Mn_{0.2}O$ sample, calcined at 500 ^{o}C, along with film formation separate particles are also observed. This may indicate a phase separation at high temperatures and is also in good agreement with the XRD data.

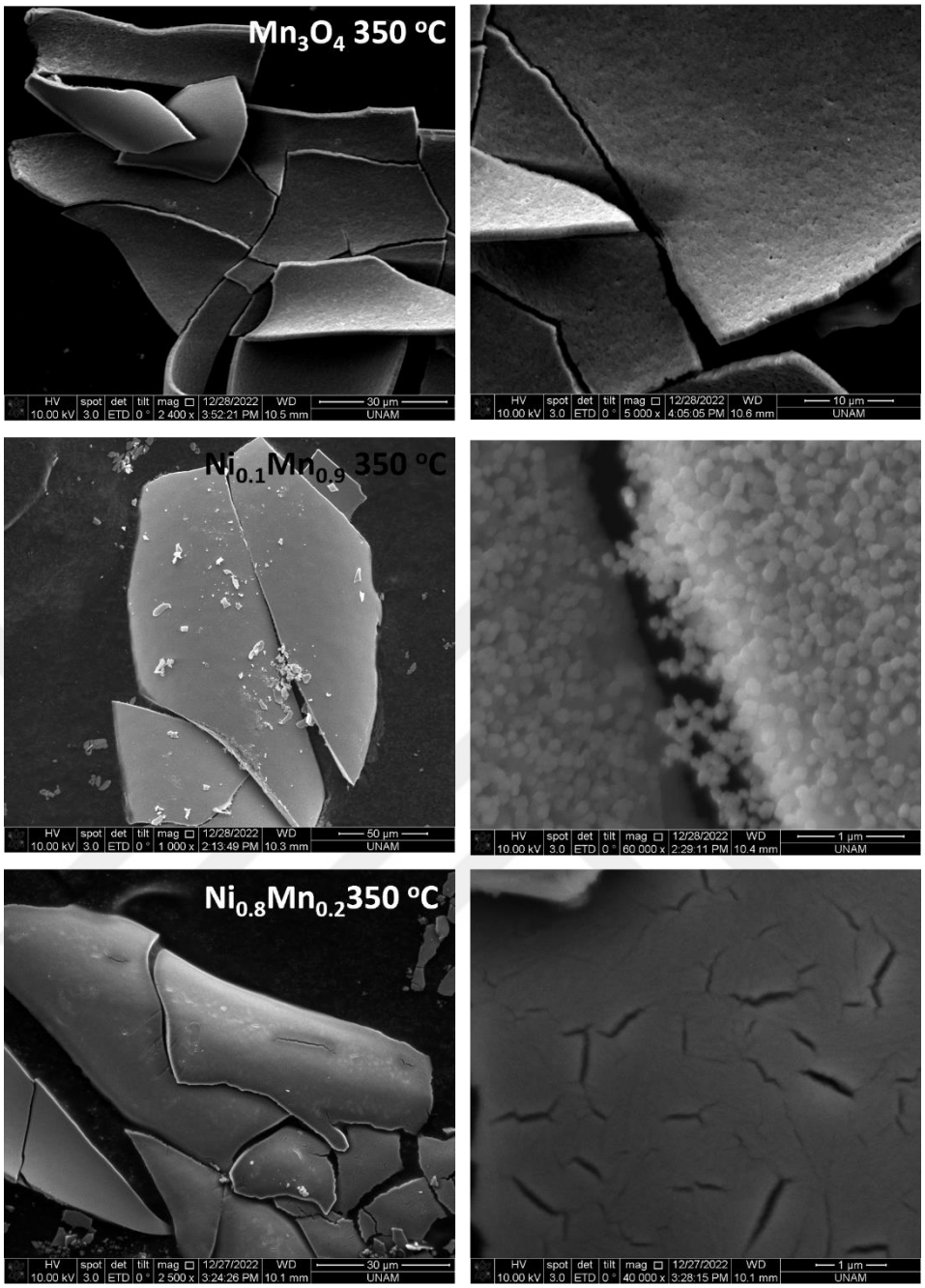

Figure 3.13. SEM images of Ni_0Mn_1O, $Ni_{0.1}Mn_{0.9}O$ and $Ni_{0.8}Mn_{0.2}O$, calcined at 350 ^oC, from top to bottom with a higher magnification on the right column.

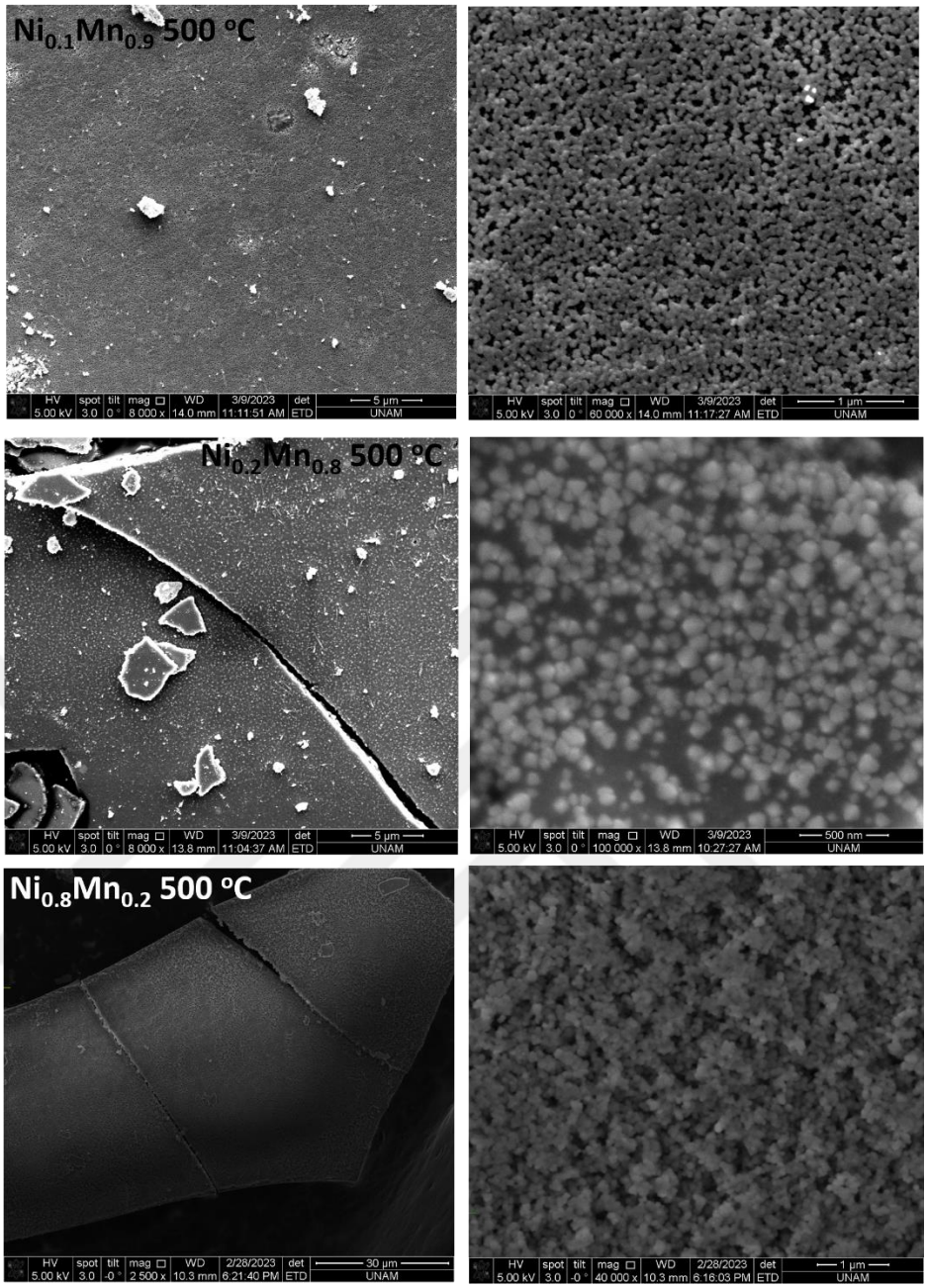

Figure 3.14. SEM images of $Ni_{0.1}Mn_{0.9}O$, $Ni_{0.2}Mn_{0.8}O$, and $Ni_{0.8}Mn_{0.2}O$, calcined at 500 ºC, from top to bottom with a higher magnification on the right column.

3.4 Electrochemical Characterization of Mesoporous Nickel and Manganese Mixed Oxides

The electrodes for electrochemical characterization were prepared by spin-coating (at 2000 rpm for 10 s) of the precursor solution on top of FTO substrates followed by calcination starting from 250 ºC up to 350 ºC for 1 hour at each

temperature. Each electrode was used in cyclic voltammetry experiment in 1M KOH electrolyte using three electrode system (see the experimental section).

The electrodes were cycled 120 times, to show how the manganese content in nickel oxide changes the electrochemical behavior of electrode over cycling (see Figure 3.15).

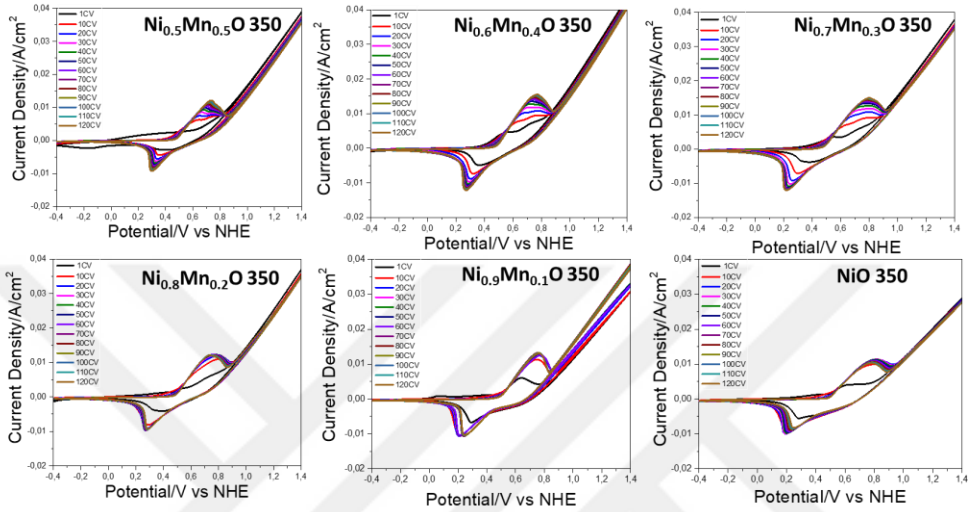

Figure 3.15. CVs of Ni and Mn mixed oxides electrodes, calcined at 350 °C (manganese content dependent), m-$Ni_{0.5}Mn_{0.5}O$, m-$Ni_{0.6}Mn_{0.4}O$, m-$Ni_{0.7}Mn_{0.3}O$, m-$Ni_{0.8}Mn_{0.2}O$, m-$Ni_{0.9}Mn_{0.1}O$, and m-NiO.

As shown in Figure 3.15, with increasing Mn concentration, the stability of the electrode also increases. The conversion of the top surface from NiO to $Ni(OH)_2$ slows down with increasing Mn in the electrodes, while in the case of pure NiO sample conversion is quite drastic, as also was previously confirmed[133].

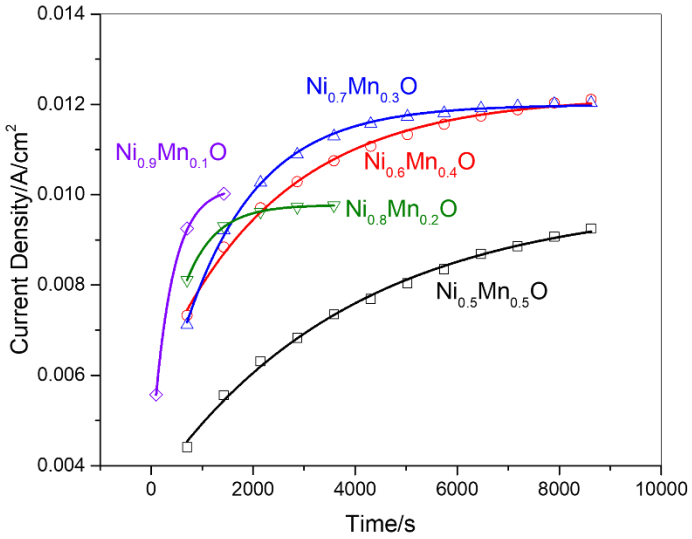

Figure 3.16. Oxidation Peak Current density vs time plots of the $Ni_{1-x}Mn_xO$ electrodes.

The plots of oxidation peak current density versus time are shown in Figure 3.16. From the plots, it is obvious that the electrode with lowest Mn ratio reaches to a plateau very quickly, compared to high ratio Mn samples, this might lead to a discussion about kinetics of NiO to $Ni(OH)_2$ conversion. As was previously mentioned, there are two phases of nickel hydroxide, α-$Ni(OH)_2$ and β-$Ni(OH)_2$. The alpha phase is more active towards water oxidation as it has higher surface coverage, however in the basic media, as was also previously discussed, the alpha phase transforms to the beta phase, that has less surface coverage and accordingly less active. Therefore, when the peak current rises with time and reaches a plateau, it means that α-$Ni(OH)_2$ fully formed, however if current density declines with time, it might mean that the alpha phase is transforming into the β-$Ni(OH)_2$ phase. However, from the plot above, it is not clear whether the beta phase is forming, as more data points are needed (120 CVs is not enough) to make reasonable discussion. For this reason, two extremes, $Ni_{0.5}Mn_{0.5}O$ and Ni_1Mn_0O, were chosen and cycled up to 600 CVs, and oxidation peak current density versus number of cycles was plotted, and shown in Figure 3.17, similarly to Figure 3.16.

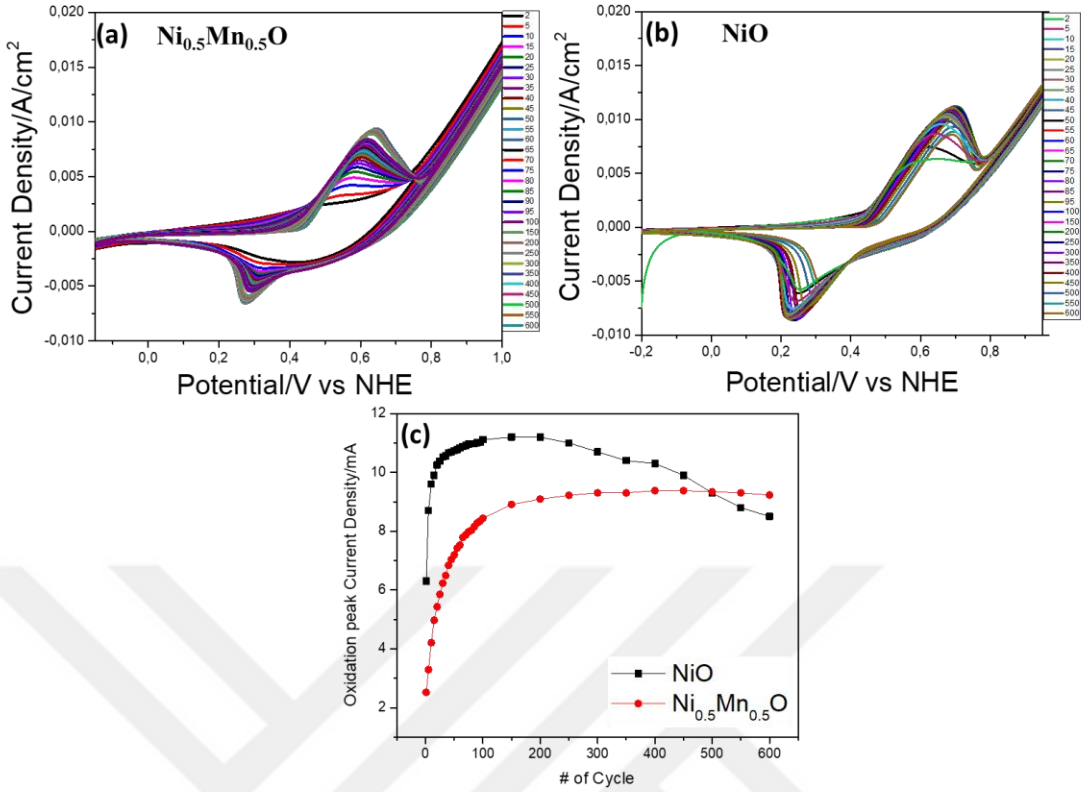

Figure 3.17. Cyclic Voltammograms (600 CVs) of (a) m-$Ni_{0.5}Mn_{0.5}O$ and (b) m-NiO electrodes, (c) the overall change in peak current around 0.6 V over cycling of m-$Ni_{0.5}Mn_{0.5}O$ and m-NiO calcined at 350 ^{o}C.

It should be noticed from Figure 3.17, that the m-$Ni_{0.5}Mn_{0.5}O$ electrode shows stability up to 600 cycles, while the pure m-NiO sample changes over time. From the shape of the curves (Figure 3.17 (c)), it is clear that the formation of least active β-$Ni(OH)_2$ phase is likely postponed and not observed in the case of manganese rich oxide. More cycles are needed to make relevant comparisons. However, in the case of pure m-NiO electrode, it reaches maximum capacity very quickly, and maximum current density of 11 mA/cm^2 was reached at around 150th CV, then it slowly decays showing that active alpha hydroxide phase is converting into a beta one, which has less surface coverage. Though initially m-$Ni_{0.5}Mn_{0.5}O$ did not possess a high capacity, at the end of 600 cycles, the electrode remains stable and more capacitive compared to the m-Ni_1Mn_0O electrode.

It is assumed that the NiO/$Ni(OH)_2$ transformation is occurring on the very top surface of the nickel oxide core, the XPS data has been collected for the electrodes before and after 120 CVs, and the data is shown in Figure 3.18.

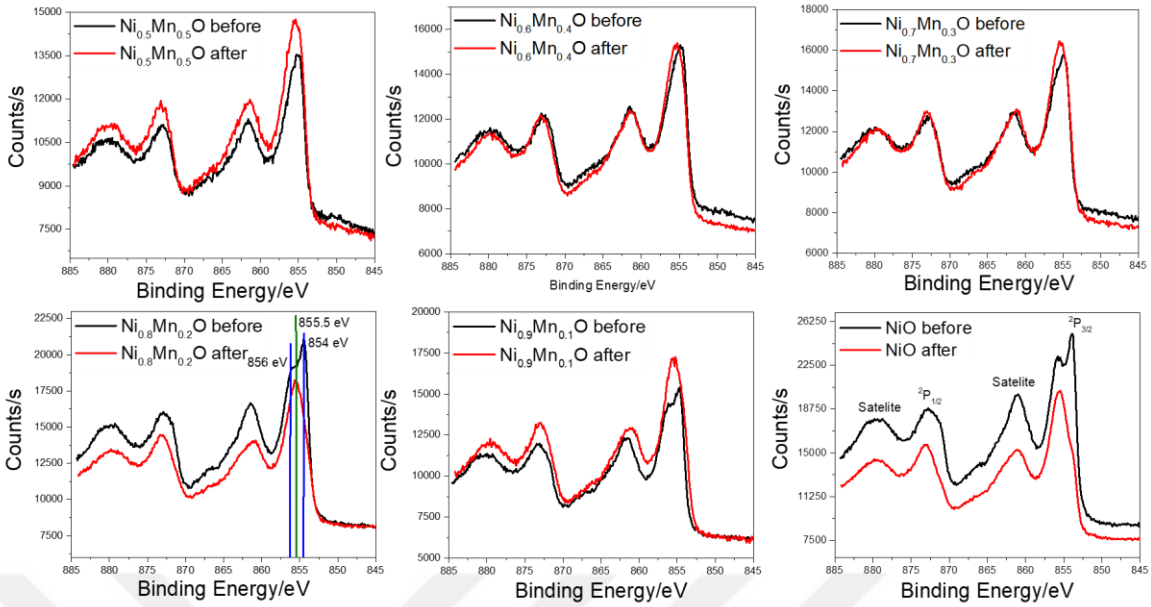

Figure 3.18. XPS spectra (Ni 2p) of the $Ni_{1-x}Mn_xO$ electrodes before and after 120 CVs. (black – before, red – after CVs), annealed at 350 ºC.

It is clear from the above spectra ofthe samples with low Mn and pure NiO electrodes, before the electro-catalytic use the spectra display Ni 2p peaks at 854 and 856 eV. Those peaks are assigned to different NiO species, however, after CVs, a new peak appears at 855.7 eV with a higher intensity, so it could be assigned to $Ni(OH)_2$/NiOOH surface species, but the peak at 854 eV does not completely disappear, meaning that NiO still remains and only very top surface is converted into nickel hydroxide[134]. The situation is slightly different in the case of high Mn content electrodes, as no obvious change occurs on the surface, meaning that Mn brings stability to the NiO electrode. This data also supports the electrochemical data, where the change in the peak current is slower in the case of m-$Ni_{0.5}Mn_{0.5}O$ electrode, compared to the pure NiO electrode.

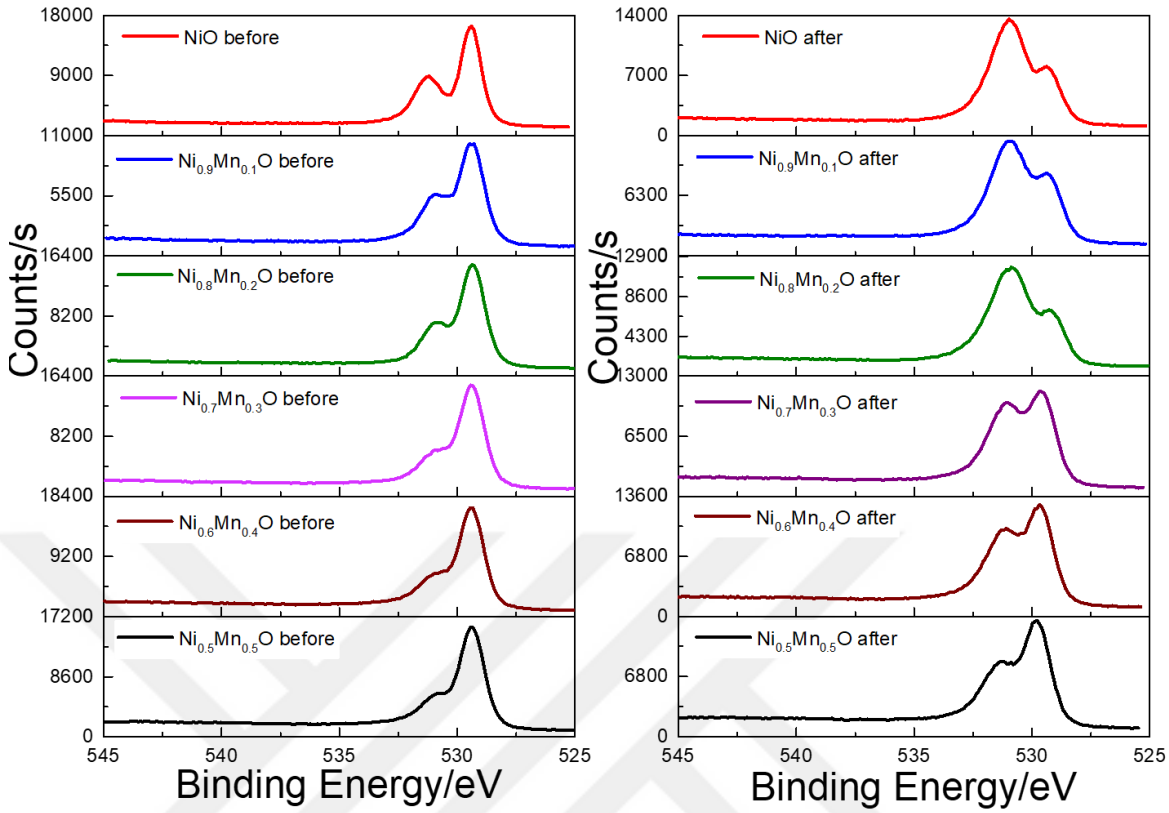

Figure 3.19. O 1s XPS spectra of the m-$Ni_{1-x}Mn_xO$ samples (a) fresh electrodes and (b) after 120 CVs.

However, the XPS spectra from O 1s region, brings us more information regarding the changes on the electrode surface, see Figure 3.19. The lower energy peaks belong to lattice oxygens of NiO/MnO, while the higher energy peaks are due to the hydroxide, aqua, and oxyhydroxide species. Before electrocatalytic use, in all compositions the surface is dominated by oxide species. After catalytic use, in the case of pure m-NiO and low Mn content electrodes, the surface becomes more dominant by hydroxide and oxyhydroxide species, indicating the formation of NiOOH and $Ni(OH)_2$ at the end of the cycling experiment. However, in the Mn-rich electrodes, the higher energy peak is not as intense as in the pure m-NiO, indicating that the formation of hydroxide surface is hindered, meaning that Mn brings stability to the nickel manganese oxide electrodes, which is in good agreement with electrochemical data.

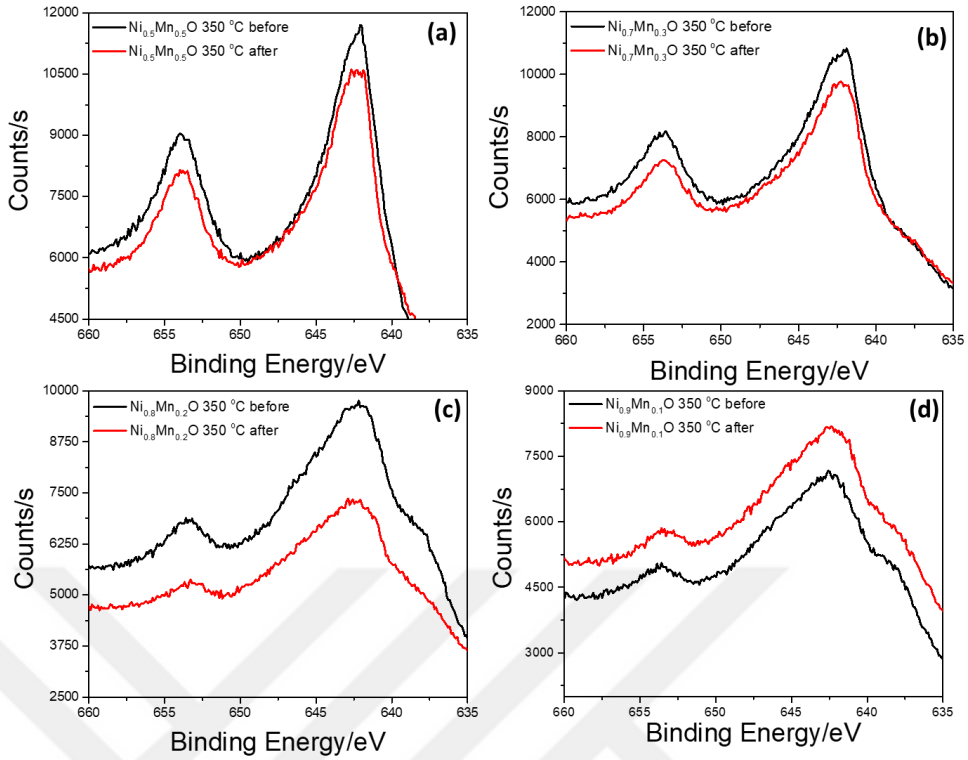

Figure 3.20. Mn 2p XPS spectra of the m-$Ni_{1-x}Mn_xO$ electrodes, calcined at 350 ºC (a) $Ni_{0.5}Mn_{0.5}O$, (b) $Ni_{0.7}Mn_{0.3}O$, (c) $Ni_{0.8}Mn_{0.2}O$ and (a) $Ni_{0.9}Mn_{0.1}O$ before (black) and after (red) 120 CVs.

Furthermore, the Mn 2p region is collected to look at the electrodes from the Mn side. Intensity of the Mn 2p peaks decrease after electrochemical tests. The decrease in the peak intensity enhances with increasing manganese in the m-$Ni_{1-x}Mn_xO$ electrodes, see Figure 3.20. Higher the amount of nickel in the nickel manganese oxide mixture, the broader the Mn 2p spectra look. This can be due to different manganese phases formed with nickel (see XRD patterns above). The 3s region is also checked for more information regarding the transformation on the surface of the electrode (see latter)[135], [136].

The potential window dependence measurements have also been performed to make relevant assumptions about the NiO/$Ni(OH)_2$ transformation, see Figure 3.21.

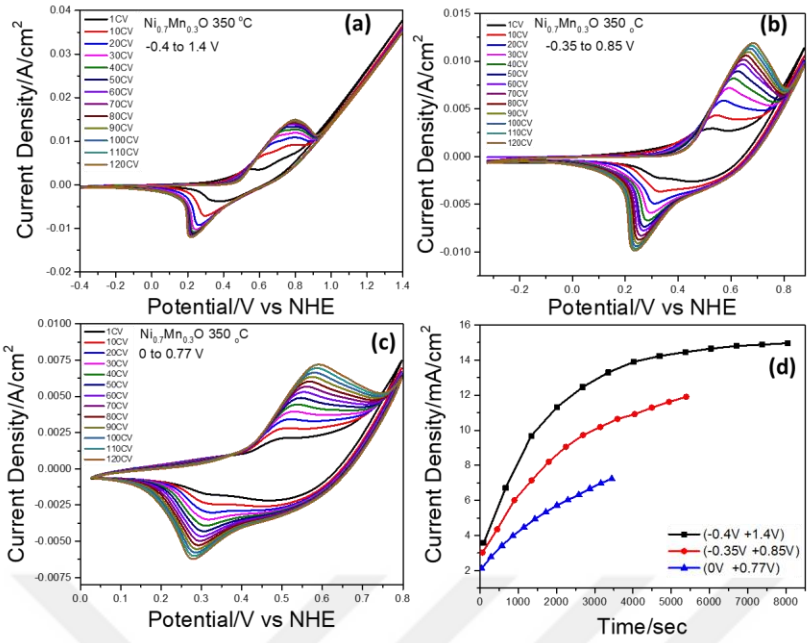

Figure 3.21. Potential window dependent CVs (a) -0.4 to 1.4 V, (b) -0.35 to 0.85 V, (c) 0 to 0.77 and (d) current density versus number of cycle plot of the $Ni_{0.7}Mn_{0.3}O$ electrodes.

As shown in Figure 3.21, each electrode has been used up to 120 cycles at different potential windows. From the peak current density versus number of cycles (that was converted into time) plot, it is clear that at a broader potential window, when cycles go up to water oxidation potentials, the formation of hydroxide surface species enhances and speeds up. The kinetics of transforming NiO into $Ni(OH)_2$ is way slower in the narrow potential window compared to the wide potential window.

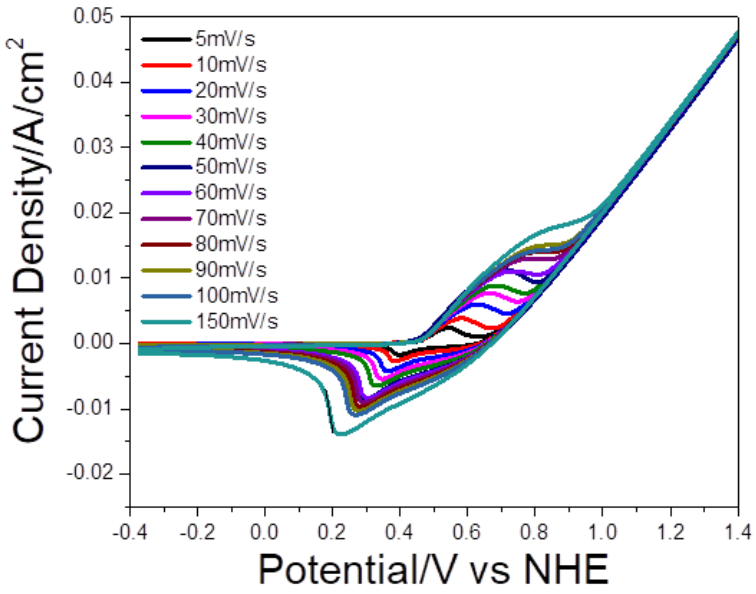

Figure 3.22. Scan rate dependent CVs of m-$Ni_{0.7}Mn_{0.3}O$ electrode, calcined at 350 ^oC.

Scan rate dependent CVs were also collected using freshly prepared m-$Ni_{0.7}Mn_{0.3}O$ electrode (see Figure 3.24). As the electrode was freshly prepared, and with every scan the peak current changes, this analysis may not give accurate data for the mechanism of the redox process. The scan rate analysis is useful when electrode reaches stability in terms of the current density. Later, the same test will be performed using the stabilized electrodes.

For further discussion, it would be wise to explain the purpose of mixing two different oxides together for better electrocatalytic performance. The pure manganese oxide tens to undergo disproportionation reaction (DR) during the electrochemical

process while the NiO loses its electrocatalytic activity in long OER, as shown in Figure 3.23.

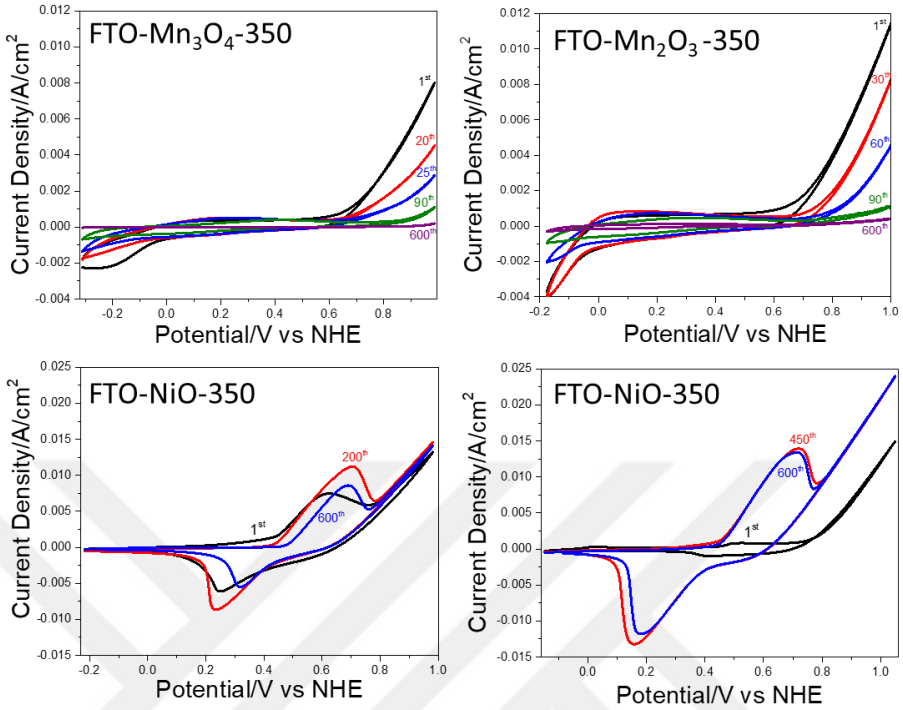

Figure 3.23. Cyclic Voltammograms recorded in 1M KOH at 50 mV/s scan rate of (above) Mn_3O_4 and Mn_2O_3 and (below) NiO calcined at 350 ^oC and 500 ^oC on FTO.

In case of pure manganese, the electrodes undergo DR as a result the peak current decays with cycling. During the CV in the water oxidation potentials, the manganese oxidizes to Mn(VI) that is unstable and undergoes to DR. In the DR, the Mn(VI) is converted to stable Mn(IV) (as MnO_2) and unstable Mn(VII) (MnO_4^{2-} ion). Reference 62 explains the process in detail.

As predicted from the XRD data, at 350 ^oC, the Mn_3O_4 phase forms, yet at 500 ^oC the Mn_2O_3 is the dominant phase with a trace amount of Mn_3O_4. The rate of electrode decomposition is different for both electrodes. The Mn_3O_4 decomposes much slower compared to Mn_2O_3 even though the Mn_2O_3 crystallites are much larger. After 50 cycles, the current density of the Mn_3O_4 electrode drops from 12.1 to 7.25 mA/cm^2, while in case of Mn_2O_3 the value drops from 7.99 to 1.41 mA/cm^2. This is a drastic change in such a short period. It should be noted that the Mn_3O_4 electrode reaches that current density only after 80 cycles and rest of the change is quite slow and steady. It should be concluded that, the phase of the manganese oxide and temperature that is calcined at does affect the electrochemical properties of the material.

Both Mn_3O_4 and Mn_2O_3 electrodes are unstable during the electrochemical process and lose their current density after 90th CV if it is cycled between -0.2 and 1 V potential window in the basic media, while the pure NiO nanoparticles and bulk phase (calcined at 500 ^oC) lose their activity after 200th and 450th cycles, respectively Increasing of the current density is attributed to the formation of the NiOOH on the surface of NiO and on the reverse cycle oxyhydroxide is converted into $Ni(OH)_2$, that is why current density rise is observed. This observation is consistent with the fact that larger crystallites transform relatively slower, because of reduced surface area.

If one compares the current density versus cycle numbers plots of the oxidation peak in the nickel oxide electrodes and water oxidation in manganese oxides ones, it is clear that manganese oxide, regardless of the phase (Mn_2O_3 or Mn_3O_4) are unstable in basic media (see Figure 3.24).

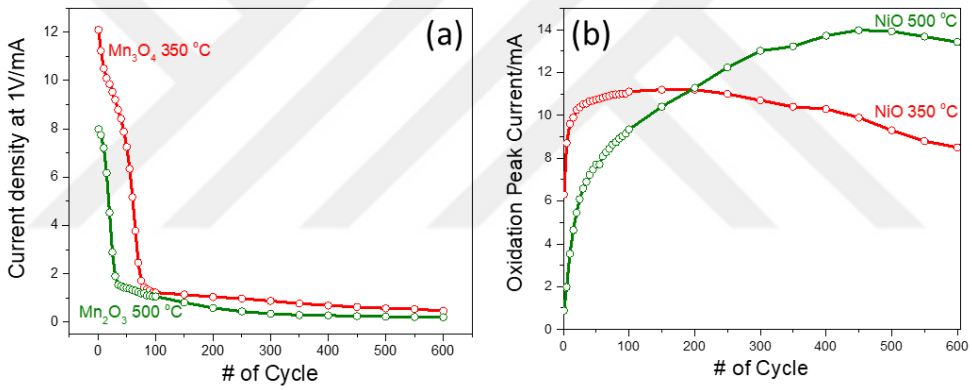

Figure 3.24. Plots of current versus cycle numbers (obtained from 600 CVs) of the FTO coated (a) Mn_3O_4 and (b) NiO electrodes.

If one looks at the current densities at 1V of manganese oxide electrodes, m-Mn_3O_4 electrode displays higher current density in the beginning of CVs due to higher surface area, while the Mn_2O_3 electrode, being more crystalline, displays lower current density. At the end of the cycling, both electrodes show very low currents due to the complete removal of the oxide from the FTO surface. Origin of this decomposition could be not only DR, but DR derived mechanical decomposition. However. the m-NiO electrode, calcined at 350 ^oC, displays higher current density in the first cycle compare to the electrode calcined at 500 ^oC, due to smaller particles size. But after 200th cycles, the more crystalline electrode shows a better electrocatalytic performance due to slow

transformation of the large NiO nanocrystals to $NiOOH/Ni(OH)_2$ on top of the NiO electrode.

As previously discussed, the electrodes were analyzed before and after electrochemical experiments, namely after 120 cyclic voltammograms (see Figure 3.18). A more detailed electrochemical analysis has also been carried out using all the electrodes of all compositions in longer electrochemical experiments, like 600 CVs and multistep chronopotentiometry (m-CP). The 600 CVs of the NiO, $Ni_{0.9}Mn_{0.1}O$, $Ni_{0.8}Mn_{0.2}O$, $Ni_{0.7}Mn_{0.3}O$, $Ni_{0.6}Mn_{0.1}O$ and $Ni_{0.5}Mn_{0.5}O$ (calcined at 350 ^oC) are given in Figures 3.25 and 3.26.

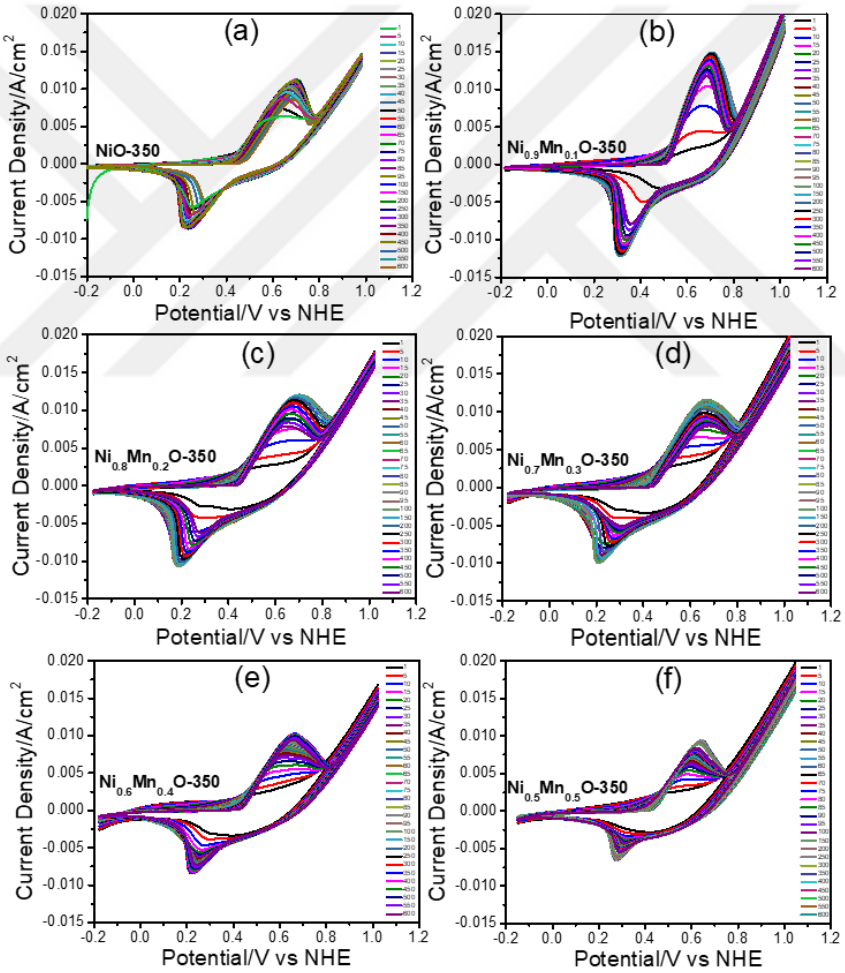

Figure 3.25. Selected CVs from 600 CV of the (a) NiO-350, and $Ni_{1-x}Mn_xO$-350, where x is (b) 0.1, (c) 0.2, (d) 0.3, (e) 0.4, and (f) 0.5.

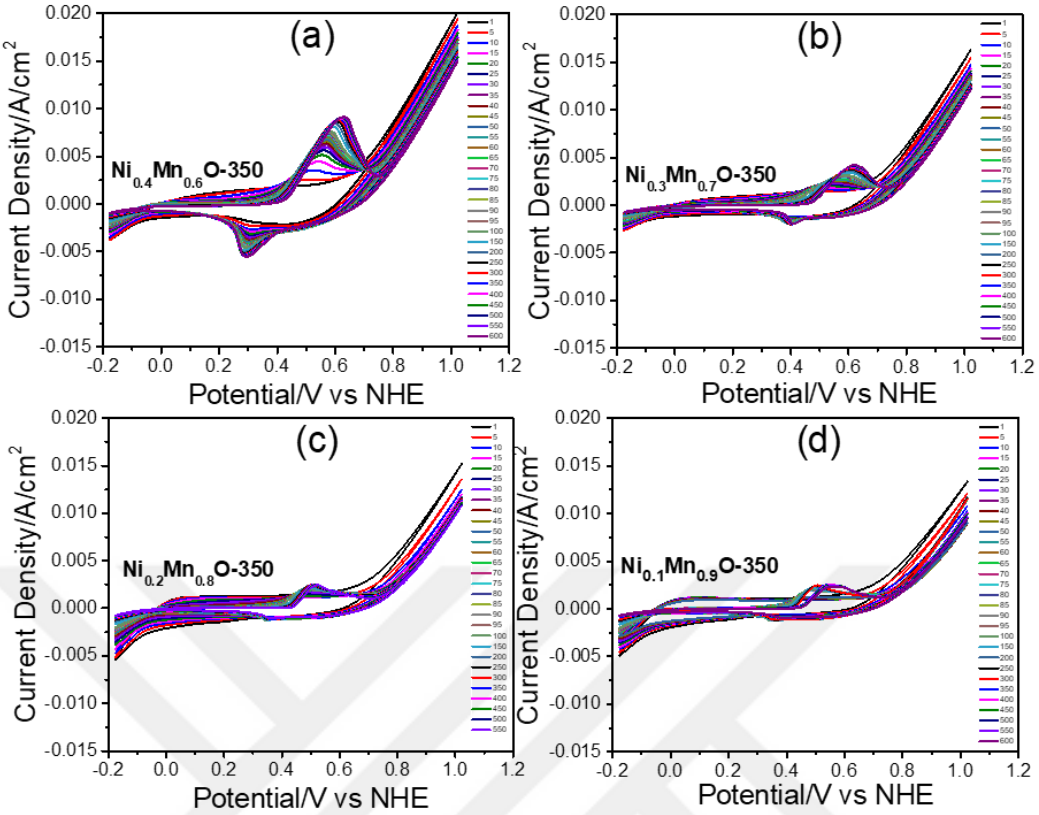

Figure 3.26. CVs of m-$Ni_{1-x}Mn_xO$ electrodes, calcined at 350 ^oC, namely the (a) m-$Ni_{0.4}Mn_{0.6}O$, (b) m-$Ni_{0.3}Mn_{0.7}O$, (c) m-$Ni_{0.2}Mn_{0.8}O$, and (d)m-$Ni_{0.1}Mn_{0.9}O$ electrodes.

As shown in the figures above, the increase of manganese content delays the formation of $Ni(OH)_2$ on top of the electrode. This can be explained by the fact that, the manganese oxide tends to disproportionate during electrochemical process[72], postponing the appearance of NiO surface. Larger the amount of manganese, longer it takes to disproportionate and formation of nickel hydroxide surface gets delayed as well. Another reason for the delay could be the stabilization of the $Ni(OH)_2$ surface due to synergic effect of manganese and nickel that needs further analysis to confirm. To understand the electrode behaviors, the oxidation peak current density maximum was taken from each CV and plotted versus cycle number, hence it becomes clearly visible at which point in time or cycle, the electrode decomposition and manganese disproportionation reaction occurs (see Figure 3.27).

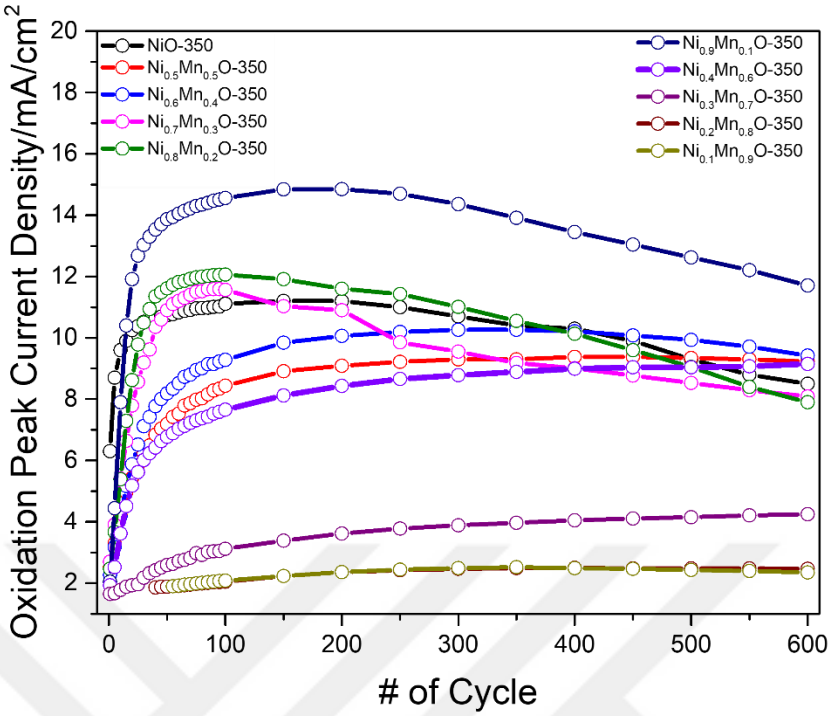

Figure 3.27. The overall change in peak current around 0.6 V over cycling of $Ni_xMn_{1-x}O$ calcined at 350 °C.

As shown in the plot above, the m-$Ni_{0.5}Mn_{0.5}O$, m-$Ni_{0.6}Mn_{0.4}O$ and m-$Ni_{0.4}Mn_{0.6}O$ electrodes do show the best stability with high current density during cycling. As for the Ni-rich side, due to low amount of Mn, the formation of $Ni(OH)_2$ is faster however, these electrodes are less stable and decompose in time.

According to the powder XRD temperature-dependent analysis (see Figure 3.11, 3.12), the homogenies $Ni_{1-x}Mn_xOs$ are formed without phase separation at 350 °C. At higher temperatures, the phase separation occurs and different phases like Mn_2O_3, $NiMnO_3$, Mn_3O_4 and NiO are formed. To understand the mechanism of manganese disproportionation mentioned above, the electrochemical analysis has been carried out using the electrodes, calcined at 500 °C. The 600 CVs of the $Ni_{0.5}Mn_{0.5}O$, $Ni_{0.9}Mn_{0.1}O$, $Ni_{0.8}Mn_{0.}O$, $Ni_{0.2}Mn_{0.8}O$, $Ni_{0.1}Mn_{0.9}O$, and Ni_0Mn_1O electrodes, calcined at 500 °C, are given in Figure 3.28.

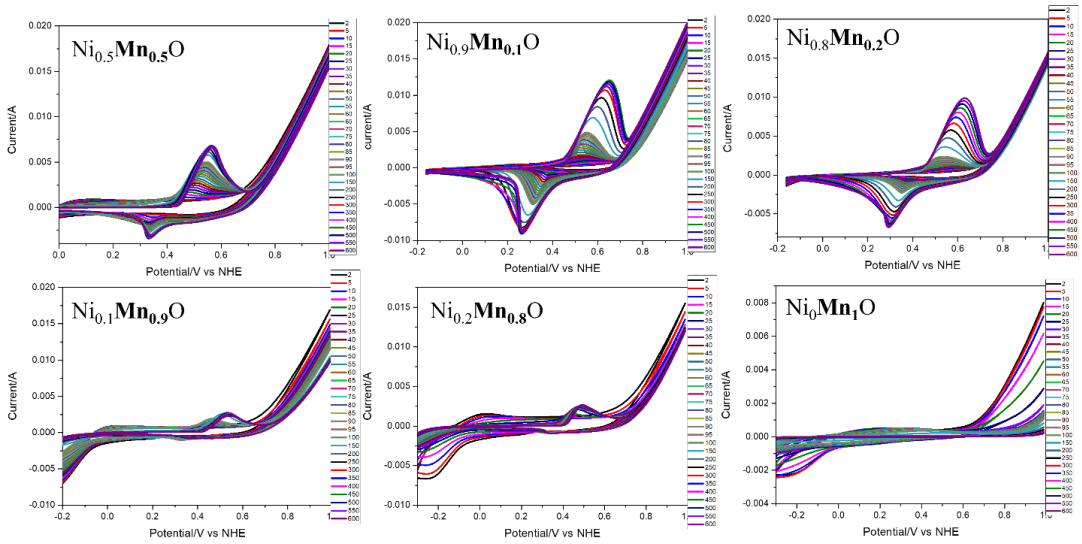

Figure 3.28. CVs of the $Ni_{1-x}Mn_xO$ electrodes, calcined at 500 ^oC, namely from left to right the m-$Ni_{0.5}Mn_{0.5}O$, m-$Ni_{0.8}Mn_{0.2}O$, m-$Ni_{0.9}Mn_{0.1}O$, m-$Ni_{0.1}Mn_{0.9}O$, m-$Ni_{0.2}Mn_{0.8}O$ and Ni_0Mn_1O electrodes.

From Cyclic voltammograms shown in Figure 3.28, it is shown that the higher the Ni concentration, the higher the current density; however, increasing manganese concentration increases the stability of the electrode during cycling. Hence, the oxidation peak current density versus cycle number has been plotted for the m-$Ni_{0.5}Mn_{0.5}O$, m-$Ni_{0.8}Mn_{0.2}O$, and m-$Ni_{0.9}Mn_{0.1}O$ electrodes (see Figure 3.29), because these particular compositions have prominent oxidation peak current from the first cycle.

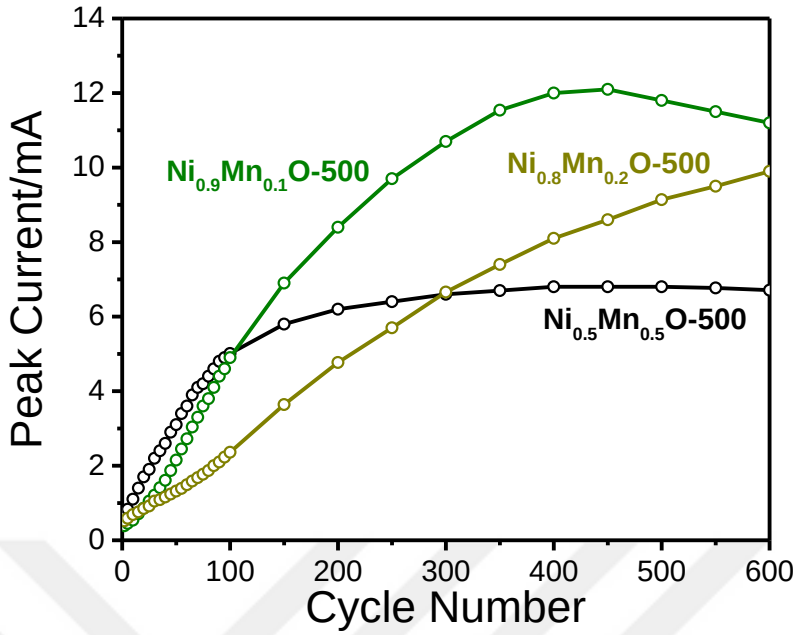

Figure 3.29. The overall change in peak current at around 0.6 V over cycling of the m-$Ni_{0.5}Mn_{0.5}O$, m-$Ni_{0.8}Mn_{0.2}O$, and m-$Ni_{0.9}Mn_{0.1}O$ electrodes, calcined at 500 ^{o}C.

Compared to the electrodes calcined at 350 ^{o}C, these electrodes reach to a maximum current density at a later time, as are more crystalline and have a low surface area, as well as they are more robust to change due to their crystallinity. Similarly, the m-$Ni_{0.5}Mn_{0.5}O$ electrode shows low stability, due to high manganese content; a high current density is reached quickly, but decays over time, while the $Ni_{0.8}Mn_{0.2}O$ electrode doesn't even reach to highest current density after 600 CVs. If one compares this datum with the data, obtained from the electrodes calcined at 350 ^{o}C, there is a clear difference; as 350 ^{o}C electrodes current density are more prone to decay with time, the electrodes calcined at 500 ^{o}C are more robust and more stable during electrolysis.

Though in the discussion above, it was stated that at 500 ^{o}C, the $Mn_2O_3$is formed as evidenced from the powder XRD data. However, it turned out that the calcination result varies from the substrate to substrate and on the FTO surface, the calcination is not as efficient as in the glass slides, meaning the same calcination product is not obtained on the FTO surface when it is calcination at 500 ^{o}C (see Figure 3.30).

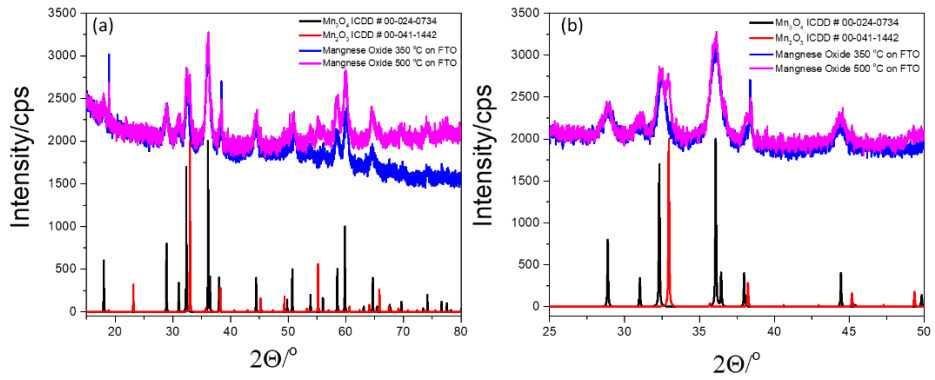

Figure 3.30. The XRD pattern of the Mn_3O_4 and Mn_2O_3 samples, obtained from FTO surface and corresponding references (PDF cards). (a) full XRD pattern, (b) XRD pattern focused on most intense line's region, 25-50°.

It is clear from the XRD patterns above that the transition from the Mn_3O_4 phase to Mn_2O_3 phase is not complete even at 500 °C; the Mn_3O_4 phase is still the dominant phase, only a small amount of Mn_2O_3 is formed (see Figure 3.30(b)). However, the powder samples, annealed at 500 °C, undergo complete transformation from Mn_3O_4 phase to Mn_2O_3 phase (see Figure 3.17 (d)). Thus, to have a relevant discussion about this issue, the experiment needs to be repeated, or a higher calcination temperature or longer calcination time needs to be applied for the FTO electrodes.

It is known that the electrodes change during electrochemical analysis, thus the structural analysis has been done for selected electrodes before and after 600 CVs. Regarding the stability and electrochemical performance, the m-$Ni_{0.5}Mn_{0.5}O$ electrode has been chosen for this analysis. It is known that at 500 °C, a phase separation occurs and different phases of manganese oxide and $NiMnO_3$ form at elevated temperatures. It is also known that the manganese oxides tend to disproportionate during electrolysis (compare the XRD data before and after) we will be able to determine which phase is decaying in the mixture. The XRD patterns of the m-$Ni_{0.5}Mn_{0.5}O$ electrode, calcined at 500 °C on FTO before and after 600 CV are shown in Figure 3.31.

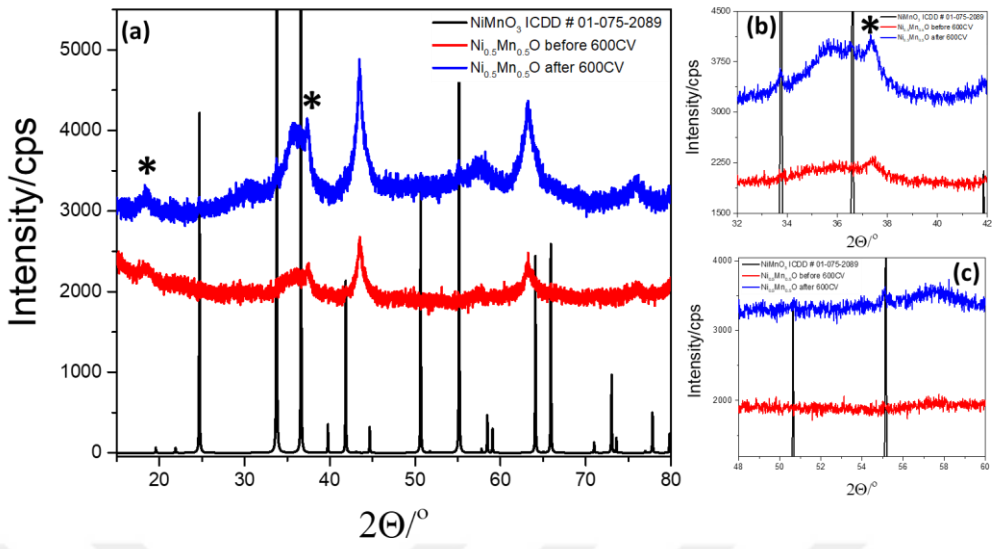

Figure 3.31. The XRD pattern of $NiMnO_3$ reference and m-$Ni_{0.5}Mn_{0.5}O$ calcined at 500 °C on FTO before (blue) and after (red) 600 CVs (a) overall XRD pattern, (b) and (c) focused regions (* shows the XRD lines of the Mn_3O_4 phase).

As previously mentioned, annealing of the sample on FTO is not efficient and the sharp crystalline lines are not observed in the XRD pattern (Figure 3.31(a)). However, the elimination of $NiMnO_3$ related lines is clearly observed after 600 CVs (see Figures 3.31(b) and (c)), as well as the lines belonging to Mn_3O_4 (marked with *) are also losing their intensity meaning that the disproportionation occurs in the mixture; both $NiMnO_3$ and Mn_3O_4 species undergo disproportionation reaction. To support this, a more crystalline electrode needs to be fabricated (calcined even at higher temperatures) and analyzed in the same way.

For the sake of reproducibility, the same experiment was repeated again, both at 350 and 500 °C, from the powder scratched from the FTO surface before and after 600 CVs. The XRD patterns are shown in Figure 3.32.

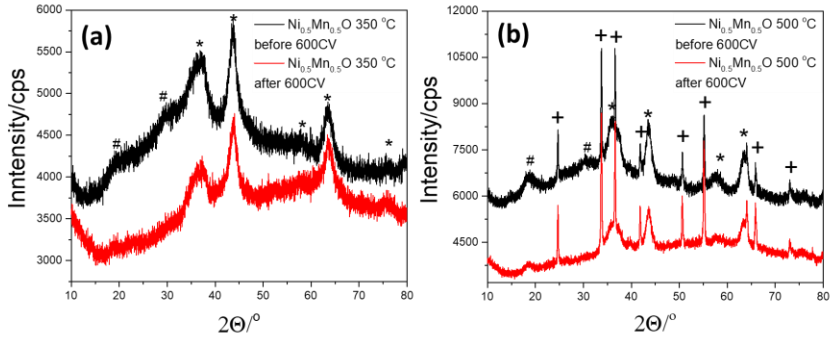

Figure 3.32. The XRD pattern of the m-$Ni_{0.5}Mn_{0.5}O$ sample, calcined at (a) 350 and (b) 500 °C on FTO before (black) and after (red) 600 CVs. # - Mn_3O_4, ICDD # -00-024-0734, *- NiO, ICDD # - 00-044-1159, +- $NiMnO_3$, ICDD – 01-075-2089.

Again, the diffraction lines that belong to the Mn_3O_4 phase lose their intensity due to manganese disproportionation reaction. However, the crystalline $NiMnO_3$ stays in the electrode after electrochemical experiment, indicating that the large crystallites of $NiMnO_3$ resist to degradation.

Similarly, XPS analysis has been done using the m-$Ni_{0.5}Mn_{0.5}O$ samples, calcined at 500 °C and 350 °C before and after 600 CVs. The spectra are shown in Figure 3.33.

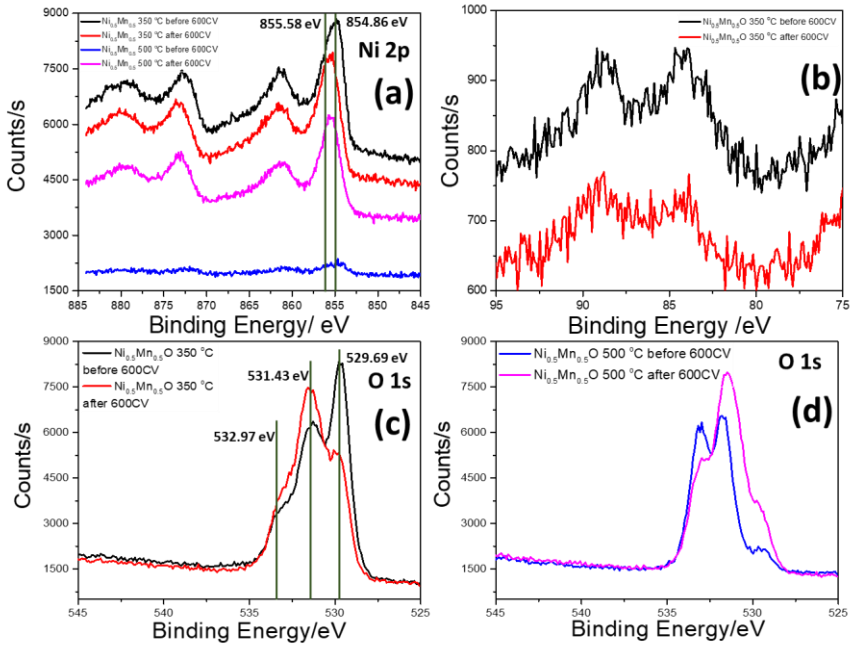

Figure 3.33. XPS spectra in the (a) Ni 2p, (b) Mn 3s, and (c) O 1s regions of the $Ni_{0.5}Mn_{05}O$-350, and (d) O 1s region of $Ni_{0.5}Mn_{05}O$-500 electrodes before and after 600 CVs.

Previously, the electrodes, calcined at 350 ^{o}C, have been analyzed by XPS (see Figure 3.21, 3.22), but the Mn 2p region did not provide sufficient information regarding to the disproportionation mechanism. The only change was in the Ni 2p and O 1s regions. The Mn 3s region has also been analyzed (see Figure 3.35 (b)); however, due to very low signal-to-noise ratio, it is hard to make a meaningful conclusion. One thing is clear that with usage, the amount of manganese decreases, as the related peaks are losing intensity. Especially, this is more obvious in the electrode, calcined at 500 ^{o}C. In the Ni2p region, before CV at 500 ^{o}C, the Ni signals are low in intensity but after CV they become more intense due to Mn removal from the surface and revealing the formation of nickel hydroxide surface.

From the Ni 2p spectra of the sample, calcined at 350 ^{o}C, it is found that the $^{2}P_{3/2}$ peak shifts from 854.86 to 855.58 eV after 600 CVs due to the formation of $Ni(OH)_2$ on top of the NiO core.

In the previous section, the XPS spectrum of the electrodes after 120 CV cycles was recorded and evaluated (see Figure 3.22). In this section, the same experiments was carried longer and the O 1s region was recorded once more; the spectrum looks quite different from the previous spectrum (compare Figures 3.22 and 3.33). Above spectra were recorded using the powder samples, scratched from FTO surface, while in previous section, it was recorded directly from the FTO surface. The lower energy peak belongs to lattice oxygens of NiO/MnO and appears at 529. 69 eV binding energy. With catalytic use, this peak loses intensity while the higher energy peaks (531.43 and 532. 97 eV) increase in intensity, and are due to the hydroxide and oxyhydroxide species. Before the electrocatalytic use, in all compositions, the surface is dominated by metal oxide species. However, after the catalytic use, in the case of pure m-NiO and low Mn content electrodes, the surface becomes predominantly hydroxide and oxyhydroxide, indicating the formation of NiOOH and $Ni(OH)_2$ on the electrode surface during the redox process. The electrode, prepared at 500 ^{o}C, has the same peaks at the same binding energies, however, the peak at around 531.43 eV is initially very intense, but it loses its intensity after cycling. Multiple peaks are observed due to different metal oxides, such as Mn_3O_4, and $NiMnO_3$. Low binding energy shoulder becomes more intense after usage probably due to hydroxide formation and manganese oxide disproportionation reaction that was previously confirmed.

EDX spectra and SEM images of the $Ni_{0.5}Mn_{05}O$-350 electrodes were collected directly from the FTO surface before and after 600 CVs to show the disproportionation reaction of the manganese species (Figure 3.34).

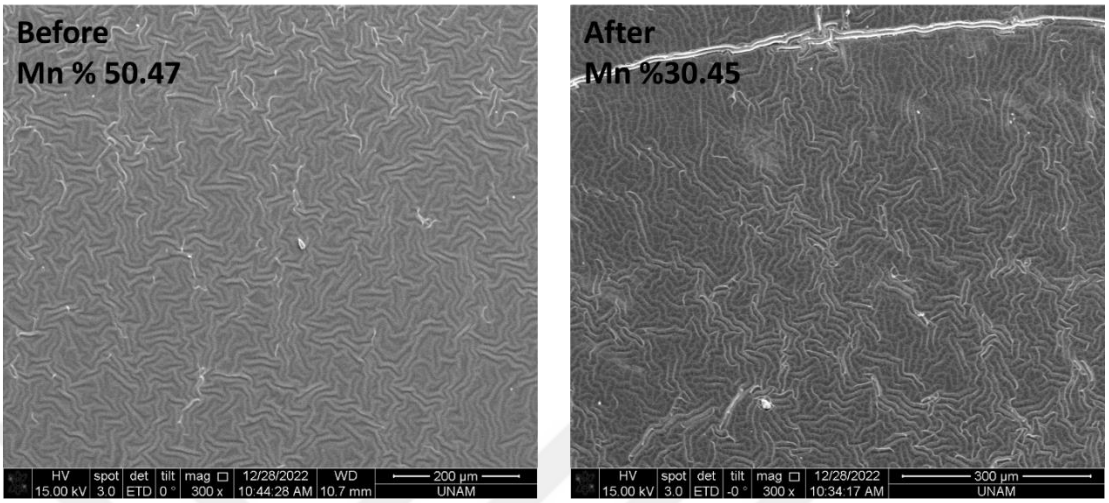

Figure 3.34. SEM images of the $Ni_{0.5}Mn_{05}O$ (calcined at350 ^{o}C) electrode, directly from FTO surface before and after 600 CVs. The Mn amount before and after catalytic use is given in the insets.

The SEM images above show that there is no change in the morphology of the electrode surface before and after usage, while the EDX analysis do confirm that after 600 cycles the amount of manganese drops drastically from 50 to 30 %. It should be noted that even after 600 CVs the manganese is still present in the electrode, so it does not undergo complete disproportionation reaction. Morphology of the FTO electrode surface is quite different from the samples, that were obtained by spin coating and calcining on the glass slide then scratched and imaged from the scraped powder on a carbon tape.

3.5 Effect of Series Resistance on the Overpotential of the Mesoporous Nickel and Manganese Mixed Oxides Electrodes

The multi-step CP (m-CP) analysis has been performed to understand the behavior of the electrodes towards oxygen evolution reaction (OER) at high current densities. The m-CP plots are shown in Figure 3.35, and series resistance and

overpotential at 1, 10, and 100 mA/cm^2 current densities of each electrode are given in Table 3.2.

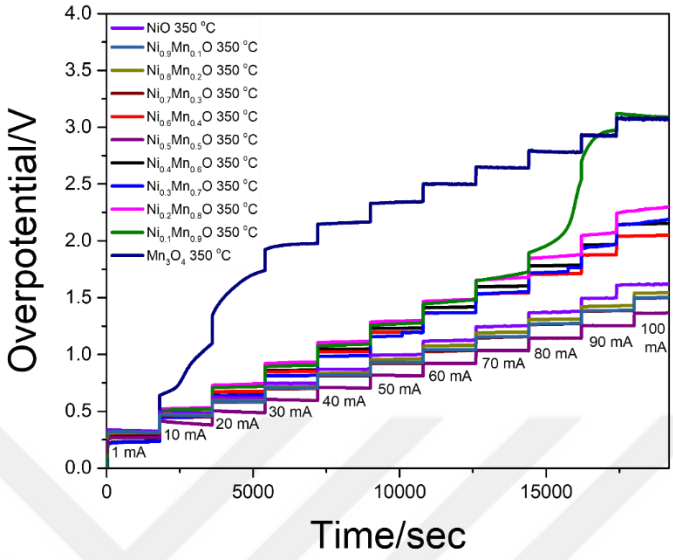

Figure 3.35. m-CP data of $Ni_{1-x}Mn_xO$ calcined at 350 °C, at current densities of 1 to 100 mA.

Table 3.2. Series resistance of each $Ni_xMn_{1-x}O$ electrode, calcined at 350 °C, before m-CP.

Oxide	Resistance Ohm	V at 1mA mV	V at 10 mA mV	V at 100 mA mV
NiO 350	~10.3	334	488	1623
$Ni_{0.9}Mn_{0.1}O$ 350	~9.9	311	461	1507
$Ni_{0.8}Mn_{0.2}O$ 350	~10.2	311	464	1552
$Ni_{0.7}Mn_{0.3}O$ 350	~9.6	304	452	1492
$Ni_{0.6}Mn_{0.4}O$ 350	~14.6	281	489	2049
$Ni_{0.5}Mn_{0.5}O$ 350	~10.4	265	379	1362
$Ni_{0.4}Mn_{0.6}O$ 350	~15.8	238	469	2153
$Ni_{0.3}Mn_{0.7}O$ 350	~14.8	233	451	2188
$Ni_{0.2}Mn_{0.8}O$ 350	~12.7	281	532	2031
$Ni_{0.1}Mn_{0.9}O$ 350	~13.6	286	520	3089
$Ni_0Mn_{10}O$ 350	~14.9	296	1095	3073

From the graph and table above, it is shown that the overpotential at any current density does partially depend on the series resistance of the electrode. Higher the resistance higher the overpotential value. Also, it can be noted that the overpotential is not an intrinsic property and does depend on many experimental parameters as well as the properties of the material like crystallinity, porosity, thickness etc. The m-$Ni_{0.5}Mn_{0.5}O$ electrode has the lowest overpotential at all current densities (see Figure 3.35), and does not change much within 30 minutes use at each current densities, showing that the electrode is stable and suitable for the OER. However, the m-$Ni_{0.1}Mn_{0.9}O$ and m-Mn_3O_4 electrodes showed sharp increases in their overpotential at 80 mA and 10 mA, respectively. This behavior indicates the disproportionation reaction of the manganese oxide. Clearly, the addition of Ni significantly postpones the disproportionation reaction or decomposition of the electrodes due to the synergic effects of both metals. The synergistic effect is due to the higher electronegativity of the nickel, so introducing manganese into the system makes it more prone to get oxidized at higher potentials and enhancing the OER[137].

The overpotentials of $Ni_{0.5}Mn_{0.5}O$ electrode is given in the Table 3.3. The m-CP data of the electrodes, prepared at 500 ^oC, are shown in Figure 3.36, and corresponding series resistance data is in inset.

Table 3.3. Overpotential of the m- $Ni_{0.5}Mn_{0.5}O$ electrode calcined at 350 ^oC at current densities from 1 to 100 mA/cm^2.

$Ni_{0.5}Mn_{0.5}O$ 350 ^oC Current density	**Overpotential**
1 mA	265 mV
10 mA	380 mV
20 mA	489 mV
30 mA	597 mV
40 mA	705 mV
50 mA	813 mV
60 mA	924 mV
70 mA	1033 mV
80 mA	1146 mV
90 mA	1255 mV
100 mA	1365 mV

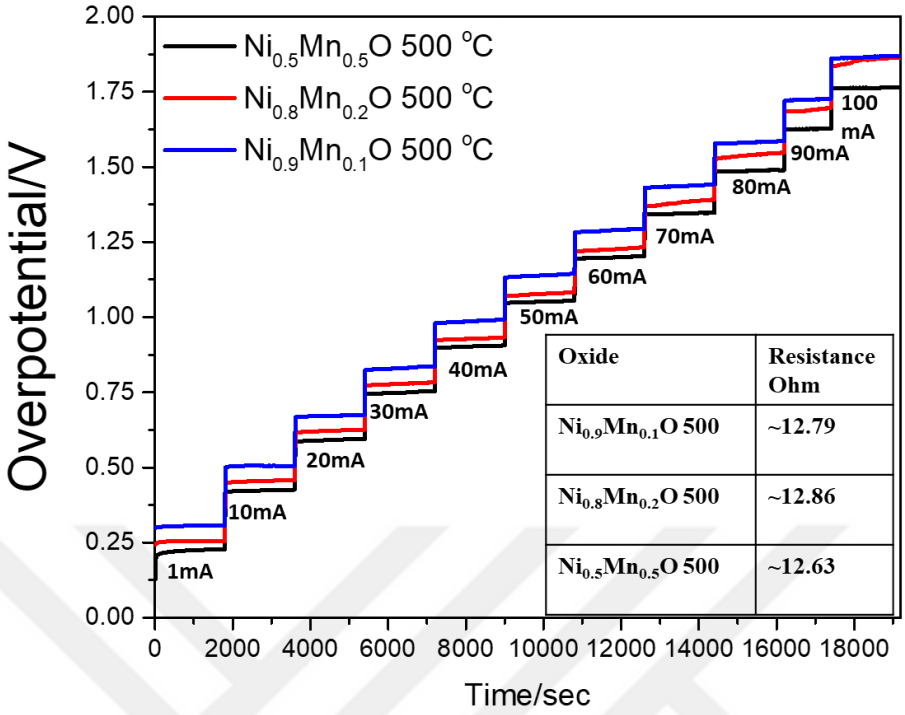

Figure 3.36. The m-CP data of the m-$Ni_{0.5}Mn_{0.5}O$, m-$Ni_{0.8}Mn_{0.2}O$ and m-$Ni_{0.9}Mn_{0.1}O$ electrodes, calcined at 500 ºC, at current densities from 1 to 100 mA/cm^2. Series resistance values are in the inset.

As an overall trend, the electrodes, prepared at elevated temperatures, are less resistive compared to the electrodes prepared at lower temperatures. Thus, it affects the overpotential that is also lower in general, though samples have lower surface area, seems like crystallinity rather than surface area benefits lower overpotential. m-$Ni_{0.5}Mn_{0.5}O$, has the lowest overpotential at all current densities.

To support the effect of the series resistance on overpotential, different sets of electrodes with the same compositions were prepared, and the m-CP experiment was performed again, however, with a more careful connection to ensure slightly lower resistance. Data is shown in Figure 3.37.

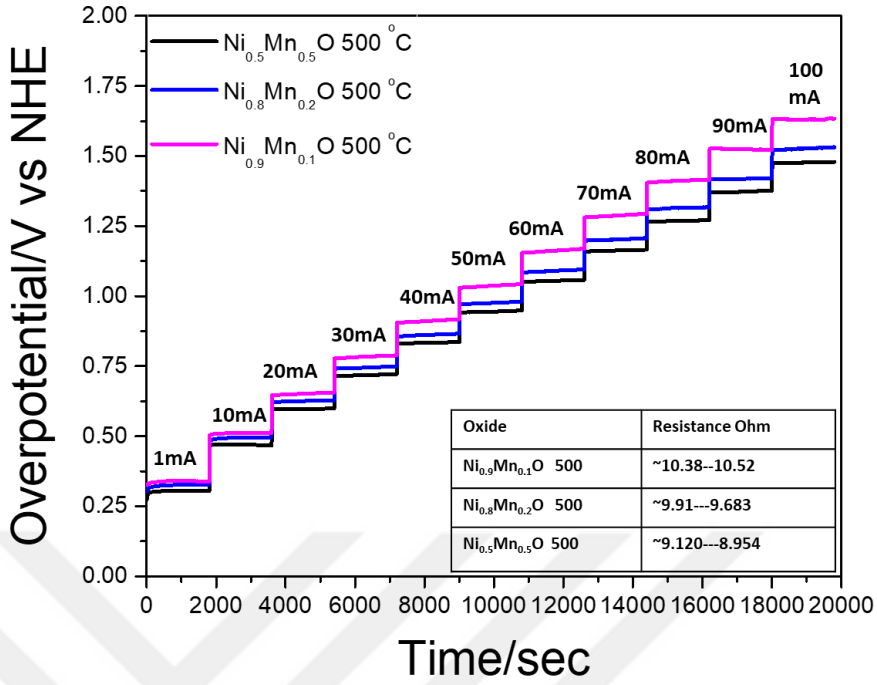

Figure 3.37. The m-CP data of the m-$Ni_{0.5}Mn_{0.5}O$, m-$Ni_{0.8}Mn_{0.2}O$ and m-$Ni_{0.9}Mn_{0.1}O$ electrodes, calcined at 500 ^{o}C, at current densities 1 to 100 mA/cm^2 (repeated). Series resistance values are given in the inset.

If Figures 3.36 and 3.37 are compared, it is clear that the plots in Figure 3.37 have lower overpotentials at higher current densities compared to Figure 3.36. Also, the m-$Ni_{0.5}Mn_{0.5}O$ electrode, annealed at 500 ^{o}C, displays the lowest overpotentials compared to the other electrodes.

The effect of the high temperature was investigated on the electrodes before and after m-CP using XPS technique. XPS spectra of the $Ni_{0.5}Mn_{0.5}O$, $Ni_{0.8}Mn_{0.2}O$, and $Ni_{0.9}Mn_{0.2}O$ samples, calcined at 500 ^{o}C , are shown in Figures 3.38, 3.39, and 3.40, respectively.

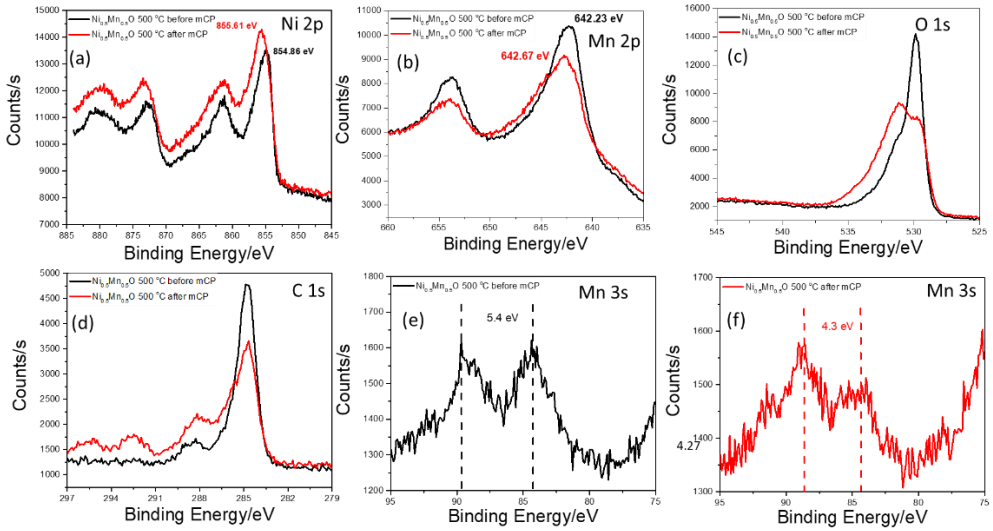

Figure 3.38. The XPS spectra of the m-$Ni_{0.5}Mn_{0.5}O$ electrodes before and after m-CP, calcined at 500 ºC: (a) Ni 2p, (b) Mn 2p, (c) O 1s, (d) C 1s, and Mn 3s (e) before and (f) after m-CP spectra.

Similarly, like in the case with samples that are calcined at 350 ºC, the electrodes, annealed at 500 ºC also show the disproportionation of manganese; As shown in the Mn 2p spectra, the intensity of the peaks decreased after electrochemical use.

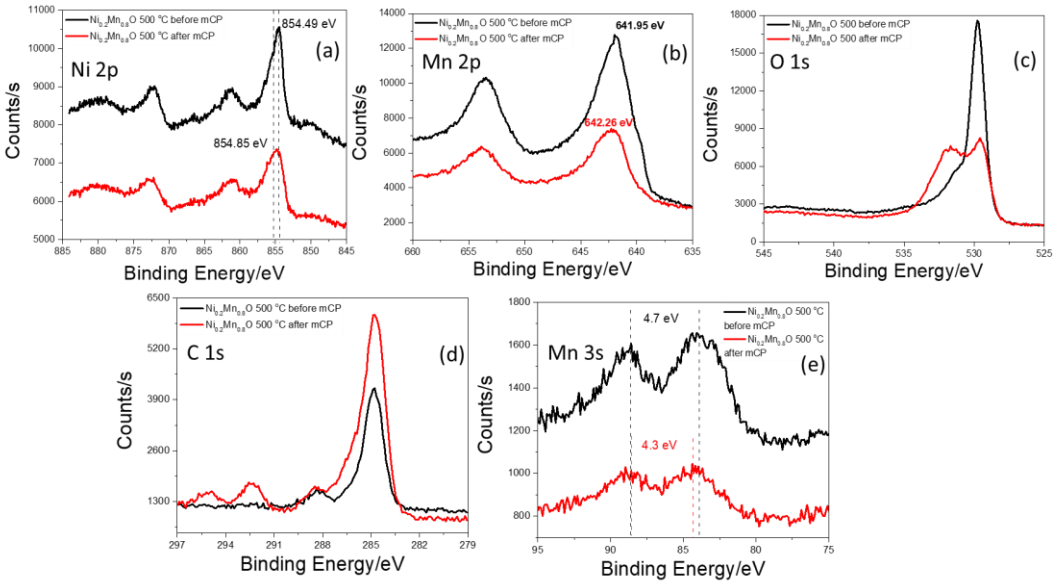

Figure 3.39. XPS spectra of the m-$Ni_{0.2}Mn_{0.8}O$ electrodes, calcined at 500 ºC, before and after m-CP in the (a) Ni 2p, (b) Mn 2p, (c) O 1s, (d) C 1s, and (e) Mn 3s regions.

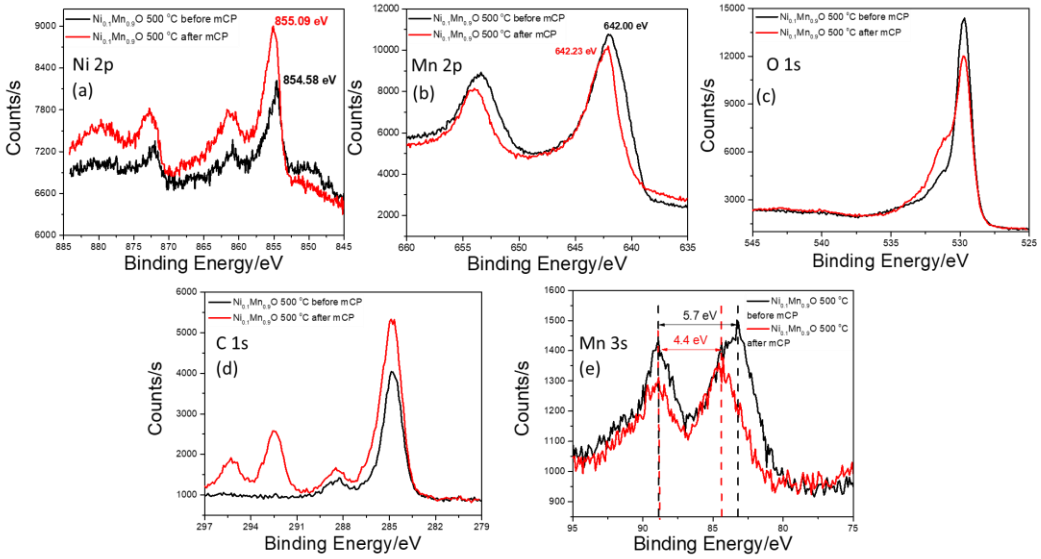

Figure 3.40. XPS spectra of the m-$Ni_{0.1}Mn_{0.9}O$ electrodes, annealed at 500 ^oC, before and after m-CP in the (a) Ni 2p, (b) Mn 2p, (c) O 1s, (d) C 1s, and (e) Mn 3s regions.

In the Ni 2p spectra in Figures 3.38 and 3.40, it is shown that the intensity of the main peak becomes more prominent and shifts to a higher binding energy (from 854.58 to 855.09 eV in case of m-$Ni_{0.1}Mn_{0.9}O$). This may be explained by the formation of the NiOOH/$Ni(OH)_2$ species on top of the electrode surface. Another factor could be the manganese disproportionation reaction that reduces the Mn amount on the surface, making nickel species more accessible and visible in the spectra. The Mn 3s region provides information on the manganese oxidation state, for example, in the case of m-$Ni_{0.5}Mn_{0.5}O$ (see Figure 3.38) the energy separation decreased from 5.4 to 4.7 eV, indicating that Mn^{3+} species dominated surface transforms into Mn^{4+} dominated surface that again supports the disproportionation reaction of the manganese species.

If one compares the m-$Ni_{0.1}Mn_{0.9}O$, m-$Ni_{0.2}Mn_{0.8}O$, m-$Ni_{0.5}Mn_{0.5}O$ samples, the O 1s spectra are quite different. In the Figures above, the higher energy peak on the O 1s spectrum is more prominent in Ni rich composition (m-$Ni_{0.5}Mn_{0.5}O$), while in the Mn rich oxide (m-$Ni_{0.1}Mn_{0.9}O$), the high binding energy peak is less intense. Considering that the peak was assigned to NiOOH and $Ni(OH)_2$ surface species, it is reasonable to assume that presence of manganese stabilizes the surface of NiO by preventing formation of hydroxide and oxyhydroxide species above.

In the C 1s spectra, there are extra peaks, observed due to presence of potassium ions. The reason for the potassium ion accumulation and its relation with Mn in the electrodes will be discussed further in later chapters. Another thing about the C 1s scan

is that the amount of carbonate species increases after electrochemical use; the data is supported by by FTIR data from the surface of FTO before and after m-CP (see Figure 3.41).

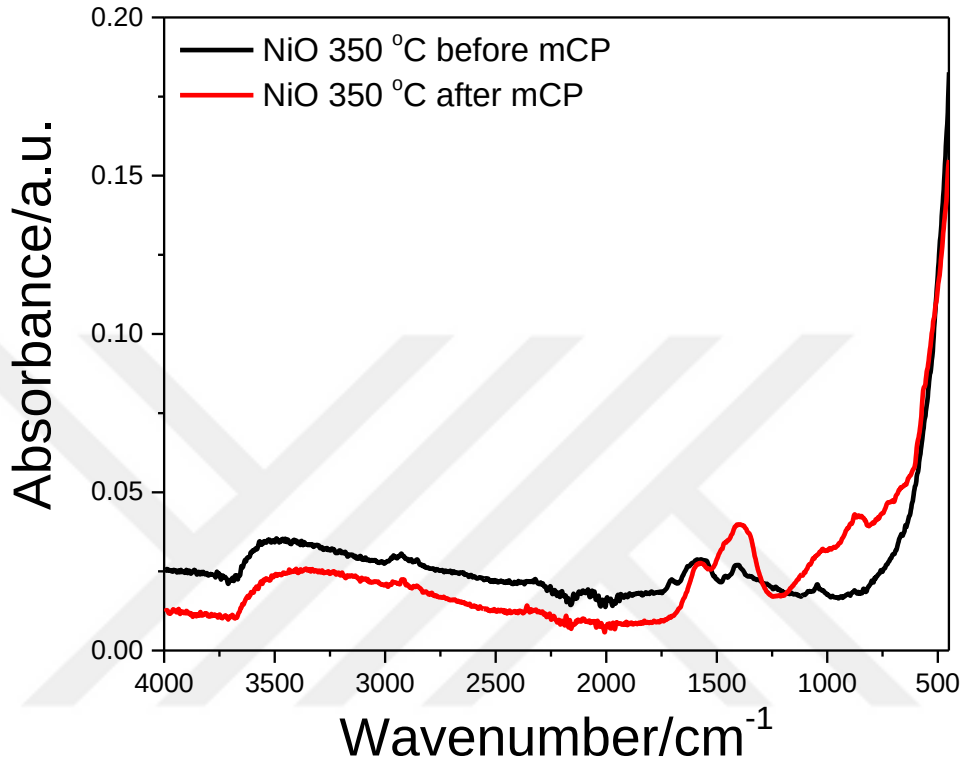

Figure 3.41. FTIR spectra of m-NiO electrode calcined ay 350 °C before and after m-CP.

The carbonate vibration region, namely the asymmetric stretching mode (v_3), observed in between 1400 and 1500 cm^{-1}, becomes more intense after electrocatalytic use, supporting the XPS C 1s data mentioned earlier.

The addition of Mn into the NiO system improves the water oxidation properties that have been discussed before by looking at CV plots. To confirm that, a 10 mA CP experiment of m-$Ni_{0.9}Mn_{0.1}O$ 350 °C and NiO 350 °C was performed for 12 hours both to check stability and water oxidation properties. The CP data is shown in Figure 3.42.

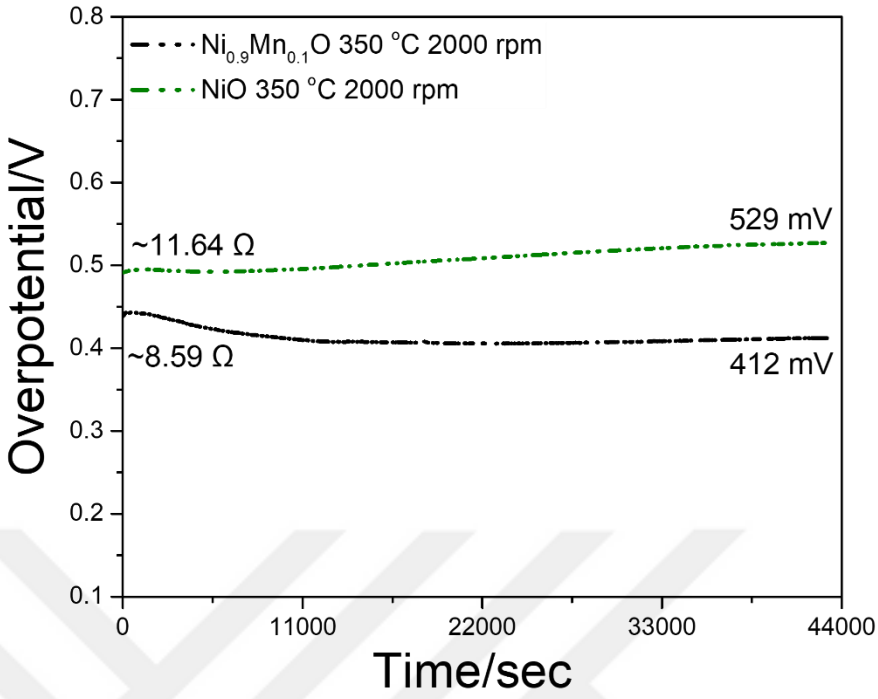

Figure 3.42. CP plots of the m-$Ni_{0.9}Mn_{0.1}O$ and m-NiO, calcined at 350 °C, at 10 mA/cm^2 current density.

The series resistance has a significant contribution to change in overpotential values, especially at high current densities. The series resistance between working electrode, produced from pure NiO and counter electrode is around 11.6 ohm, while the m-$Ni_{0.9}Mn_{0.1}O$ electrode system has a series resistance of 8.6 ohm. The overpotential of the last one is 412 mV, while the NiO shows 530 mV at 10 mA/cm^2 current density. The 118 mV extra overpotential in the NiO system originates from the IR loss that is 86 mV in the later electrode. So, addition of manganese to NiO improves both overpotential and stability of the electrode (see later).

Overpotentials of the m-NiO-500 electrodes, prepared at different spin rate, were measured at 10 mA/cm^2 (see Figure 3.43).

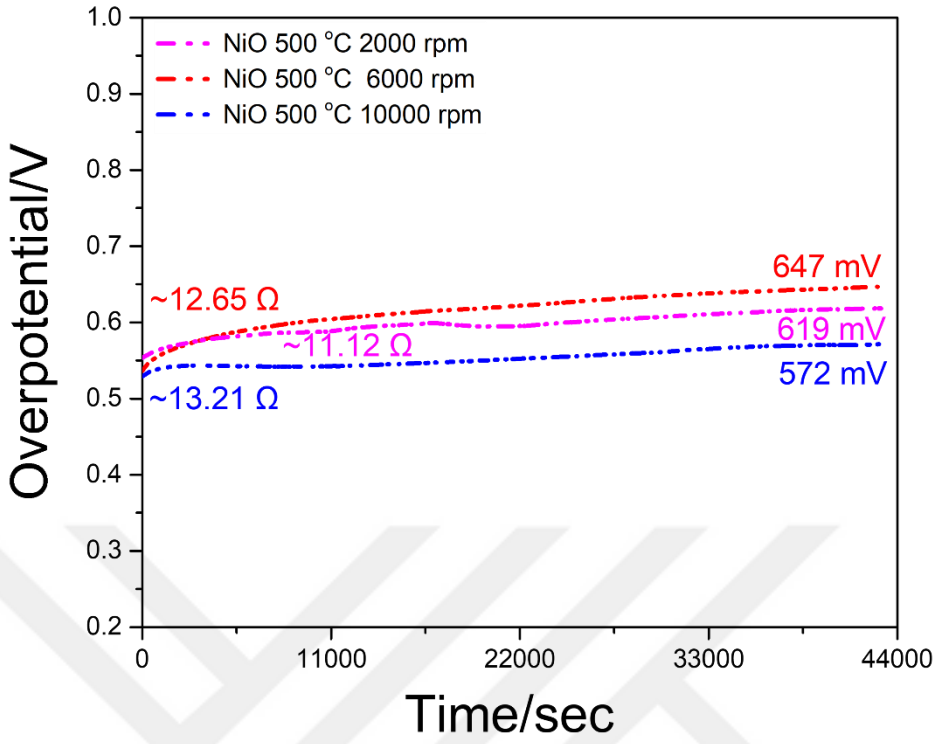

Figure 3.43. CP at 10 mA/cm^2 plot of the m-NiO electrodes, calcined at 500 °C, at different spin rates, thickness dependent.

The m-NiO electrodes, calcined at 500 °C, are also prepared at three different spin rates, namely 2000, 6000 and 10000 rpm. Note that increasing the spin coating rate produces thinner electrodes. Although the 10000-rpm sample has the highest resistance, it displayed the lowest overpotential, compared to the thicker electrodes. So, the series resistance is not the only parameter for the observed overpotential yet does have significant contribution at high current densities.

The electrode calcination temperature also affects the overpotentials. For example, Figure 3.44 displays CP curves at 10 mA/cm^2 of the m-$Ni_{0.9}Mn_{0.1}O$ electrodes, calcined at 350 and 500 °C. The electrode, calcined at lower temperature has lower resistance and lower overpotential, probably due to high surface area and homogeneous solid solution phase. The chronopotentiometry data given above shows that the m-$Ni_{0.9}Mn_{0.1}O$ composition is ideal for the further analysis.

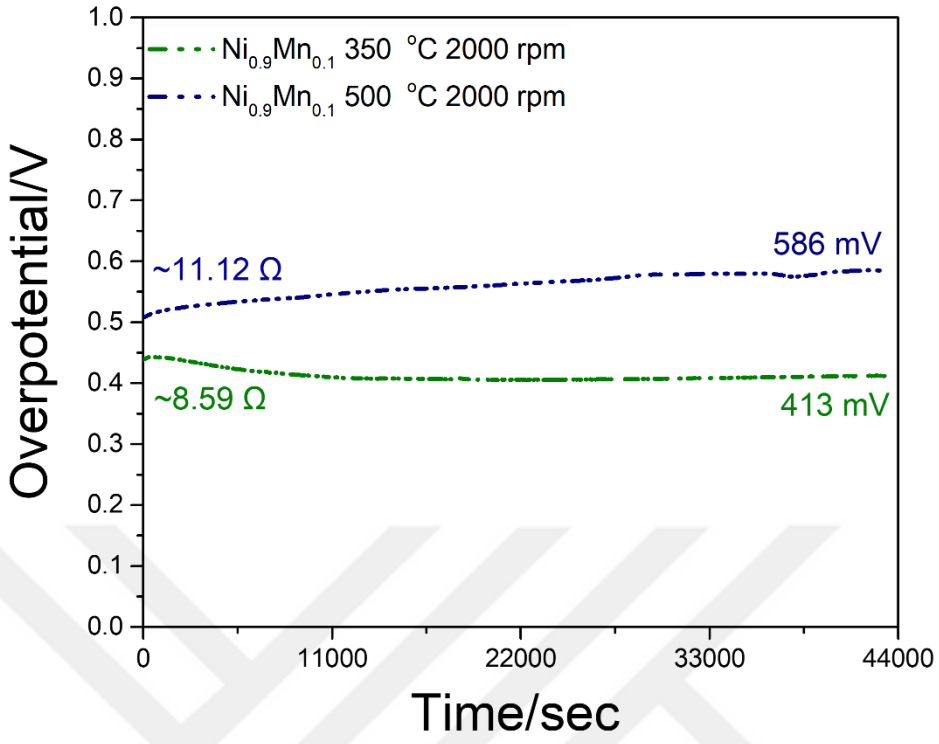

Figure 3.44. CP curves of m-$Ni_{0.9}Mn_{0.1}O$ electrodes, calcined at 350 and 500 ºC, at 10mA/cm^2 current density.

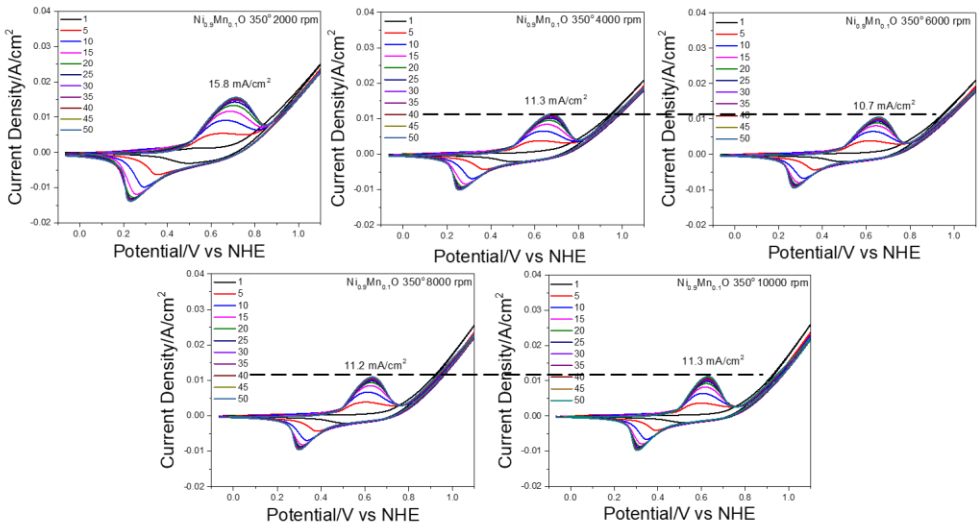

Figure 3.45. The thickness-dependent cyclic voltammograms of the m-Ni0.9Mn0.1O electrodes, prepared at different spin rates, 2000, 4000, 6000, and 10000 rpm (from left to right) and calcined at 350 ºC.

Figure 3.45 shows the 50 CVs, recorded at 50 mV/s scan rate of the m-$Ni_{0.9}Mn_{0.1}O$ electrodes in 1 M KOH electrolyte, from -0.2 to 1 V potential window. The m-$Ni_{0.9}Mn_{0.1}O$ electrodes were fabricated at different spin rates. The electrode

thickness will be provided in the later sections. However, it is clear from the Figure 3.44 , at all spin rates except 2000 rpm (the thickest electrode), the electrodes display the same oxidation peak current density of around 12 mA/cm^2 at 0.6 V. The possible explanation for this observation is that the only a part of the electrode surface is involved in the electrochemical process.

Since these electrodes have similar behavior during cycling, their stability was tested at 10 mA/cm^2 by performing a chronopotentiometry experiment for 12 hours. The CP data is shown in Figure 3.46. The resistance of the electrodes was also measured before and after CP, and these values are tabulated in Table 3.4.

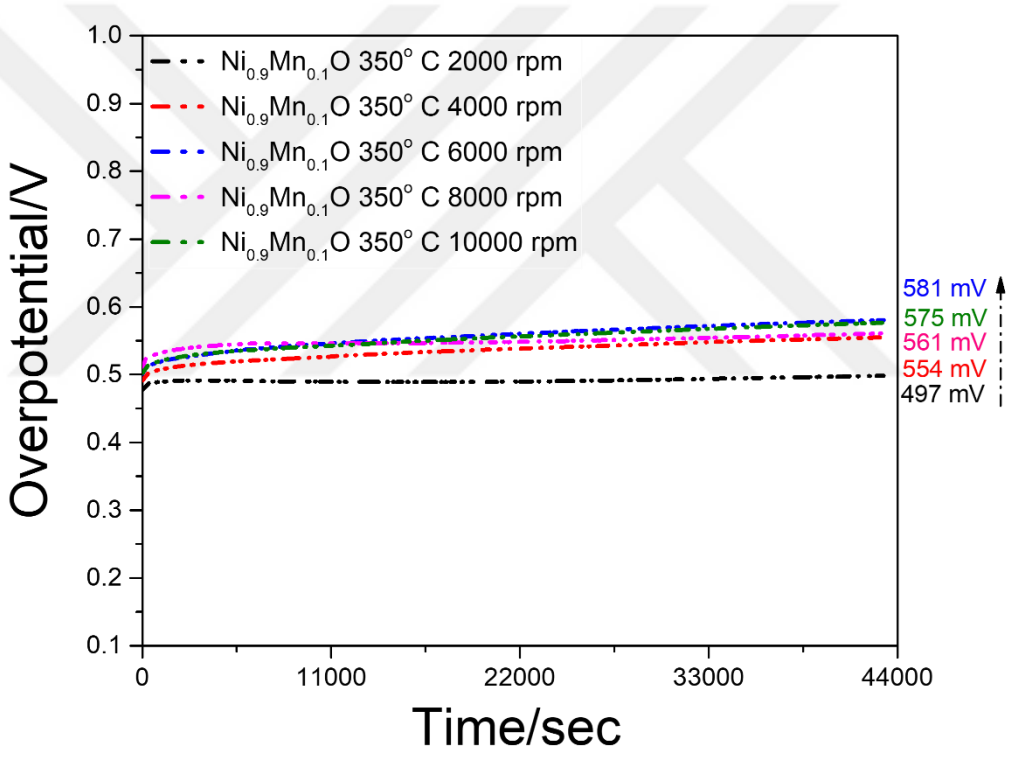

Figure 3.46. The thickness dependent 12 hours CP curves of the m-$Ni_{0.9}Mn_{0.1}O$ electrodes at 10 mA/cm^2 current density, prepared at different spin rates, 2000, 4000, 6000 and 10000 rpm and calcined at 350 ^oC.

Table 3.4. Series resistance and overpotential values of the m-$Ni_{0.9}Mn_{0.1}O$ electrodes, calcined at 350 ^oC, before and after 12 h CP experiment at 10 mA/cm^2 current density.

	Resistance (ohm) Before CP	**Resistance (ohm) After CP**	**Overpotential (mV) After CP**	**Corrected Overpotential (mV)**
2000 rpm	9.60	10.23	497	395
4000 rpm	9.86	10.14	554	453
6000 rpm	9.90	10.47	581	476
8000 rpm	12.30	12.13	571	450
10000 rpm	10.38	10.72	575	468

The electrode, prepared at 2000 rpm, has the lowest overpotential of 497 mV at the end of the CP experiment. Resistance of this electrode is also the lowest, it is 9.60 before and 10.23 ohm after CP experiment. That supports our previous assumptions that the series resistance has a contribution to the overpotential due to IR drop. Less resistive material is more conductive and has lower overpotentials as a result a better water oxidation property. The electrode, prepared at 4000 rpm, also displays comparatively low overpotential of 554 mV while the other samples have both higher overpotential values and higher resistance. It should also be noticed that almost in all cases, except 8000 rpm, the series resistance values increase and make the electrodes less active and less conductive.

To show that the electrodes, prepared at similar conditions and with similar compositions may require different overpotential values depending on the series resistance (how electrode was connected) and other unknown effects, three identical m-$Ni_{0.9}Mn_{0.1}O$ electrodes were prepared (at 2000 rpm and calcined at 350 ^oC) and used for 12 hours at 10 mA/cm^2 current density in the CP experiments(see Figure 3.47). Series resistance was also measured before and after the experiments, and tabulated in Table 3.5.

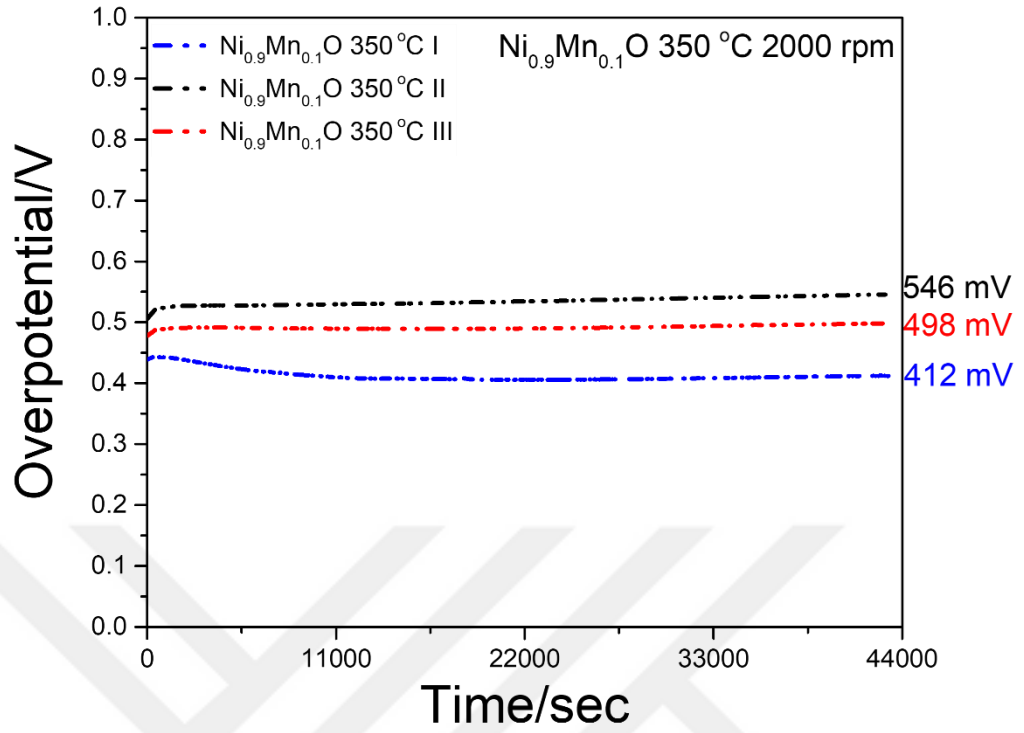

Figure 3.47. 12 hours CP curves of the m-$Ni_{0.9}Mn_{0.1}O$ electrode, calcined at 350 °C, at 10 mA/cm^2 current density with different series resistance values.

Table 3.5. Series resistance and overpotential values of the 3 different m-$Ni_{0.9}Mn_{0.1}O$ electrode (with three different resistance values), calcined at 350 °C, before and after 12 h CP experiments at 10 mA/cm^2 current density.

Sample	Resistance (ohm) Before CP	Resistance (ohm) After CP	Overpotential (mV) After CP	Corrected Overpotential (mV)
I	8.59	9.11	412	321
II	11.48	11.86	546	427
III	9.6	10.23	498	396

All the electrodes were connected intentionally in the way that they have different series resistance. For example, electrode I has the lowest resistance of 8.59 ohm while the electrode II has the highest resistance of 11.48 ohm. This data accords well with overpotential values (see Figure 3.46) as electrode I shows the lowest overpotential of 412 mV, while the other one shows the highest overpotential of 546 mV, but it is not the only parameter. This experiment is useful because, it shows that every electrode is different from each other even though they are prepared identical. It

also shows that, one should always repeat the same experiment several times before reporting the data of above measurements.

The m-$Ni_{0.9}Mn_{0.1}O$ electrodes at all thickness were also analyzed by using XPS technique, before and after 12 hours CP experiments. The XPS spectra in the Ni 2p, O 1s and C 1s regions are provided in Figure 3.48.

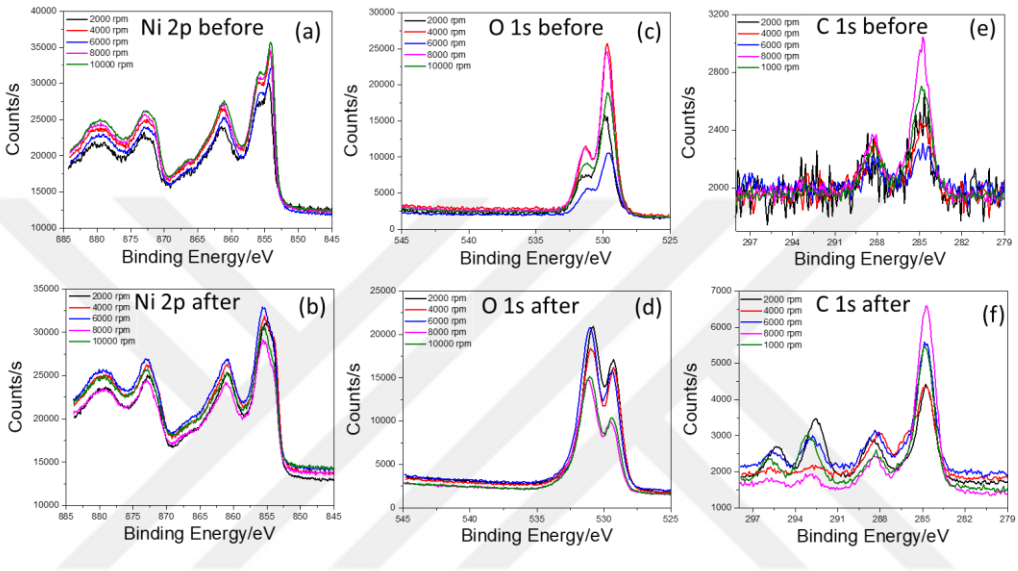

Figure 3.48. XPS spectra: (a) and (b) Ni 2p, (c) and (d) O 1s and (e) and (f) C 1 s regions of the m-$Ni_{0.9}Mn_{0.1}O$ electrodes, prepared at different spin rates (thickness dependent) and calcined at 300 ^{o}C, (a), (c), (e) before and (b), (d), (f) after 12 hours CP experiments at 10 mA/cm^2 current density.

Figures 3.48(a) and 3.48(b) show the Ni 2p region before and after 12 hours CP experiments. Before CP, the peaks at 854 and 856 eV are assigned to different Ni(II) species, NiO and $Ni(OH)_2$, respectively. After electrochemical use, the peak around 854 eV loses its intensity and a new peak appears at 855.7 eV, that can be assigned to $Ni(OH)_2$/NiOOH species. Notice that the nickel oxide peak doesn't completely disappears, indicating that only top surface is converted to hydroxide species.

As shown in the panels (c) and (d), the O1s region displays a peak at lower energy that belongs to the lattice oxygens of NiO/Mn_xO_z, and higher energy peaks due to the hydroxide and oxyhydroxide species. Before electrocatalytic use, in all compositions the surface is dominated by oxide species. After catalytic use, in all electrodes, the surface becomes predominantly hydroxide and oxyhydroxide, indicating the formation of NiOOH and $Ni(OH)_2$ at the end of the CP experiment. All the

electrodes show similar behavior both in the Ni 2p and O 1s regions. Lastly, C 1s region shows significant increase both in carbonates species and potassium after the catalytic use. The presence of potassium is over the electrode surface is due to the electrolyte (1 M KOH), used in GCD experiment. After the usage, though the surface of the electrode is thoroughly washed, some potassium remains and appears in the C 1s spectrum. More detailed explanation for the presence of potassium ions in the sample will be discussed in later chapters.

For better understanding electrode performance dependance on the thickness, the thinner electrodes were also fabricated by diluting the original precursor solution by 10, 20, 40 and 60 times and the electrodes were prepared at 2000 rpm and calcined at 350 ^{o}C for 1 hour. Their CVs are shown in the Figure 3.49.

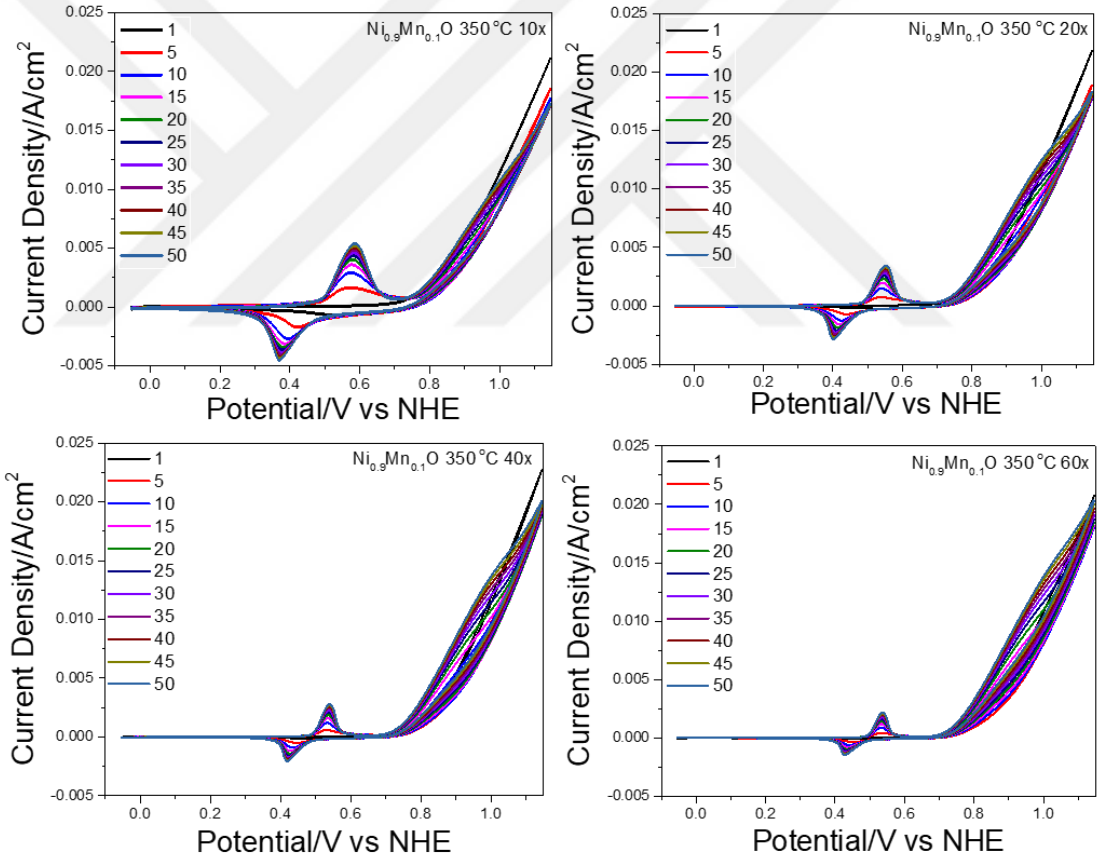

Figure 3.49. The thickness dependent 50 CVs of the m-$Ni_{0.9}Mn_{0.1}O$ electrodes, prepared at different dilutions (10, 20, 40, and 60 times) and calcined at 350 ^{o}C.

1 M KOH solution was used as an electrolyte, and each electrode was cycled 50 times at a potential window from -0.2 to 1 V at a scan rate of 50 mV/s. As shown in the Figures above, dilution has significant effect on thickness of the electrode as indicated in the oxidation peak current densities. The peak current drops from 5 mA in 10 times

diluted electrode to 2 mA in 60 times diluted electrode. Changing the spin rate was not effective and it was insignificant.

To compare these electrodes with the thicker ones, 1 hour CP experiment at 10 mA/cm^2 current density was performed along with a series resistance measurement. Bare FTO and FTO heated at 350 ^{o}C were also analyzed using CP measurement (see Figure 3.50).

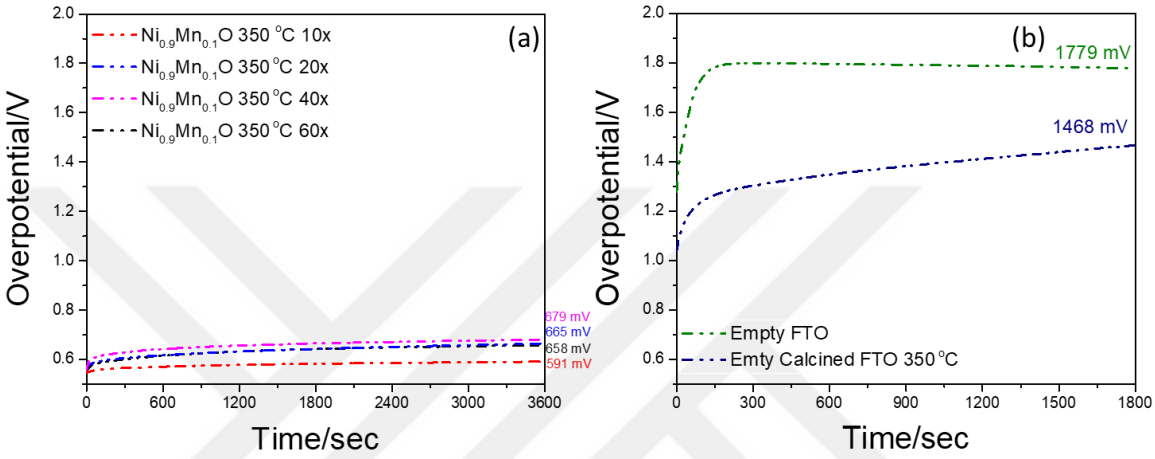

Figure 3.50. (a) Thickness dependent, 1 h CP curves (at 10 mA/cm^2 current density) of the m-$Ni_{0.9}Mn_{0.1}O$ electrodes, prepared using different dilutions and calcined at 350 ^{o}C, , (b) 30 mins CP curves at 10 mA/cm^2 of the bare FTO and heat treated bare FTO.

As shown in Figure 3.50(b), the bare FTO shows a huge overpotential of 1779 mV that slightly drops to 1468 mV in the heat treated FTO (Figure 3.50 (b)). For the dilution dependent electrodes (Figure 3.50 (a)), the 10 times diluted sample shows the lowest overpotential although, the series resistance (11.38 ohms) is not the lowest compared to the other electrodes (see Table 3.6), indicating that the series resistance has a contribution to the overpotential and its effect is only visible when identical electrodes are compared with each other. For example, the series resistance of bare FTO is comparable with the coated ones, but the overpotential is significantly larger. If different electrodes are analyzed, there are other factors that affect the overpotential, like the type of electrocatalyst, thickness of the electrode, and calcination temperature, etc.

Table 3.6. Series resistance values of the m-$Ni_{0.9}Mn_{0.1}O$ electrodes, calcined at 350 ^oC and bare FTO electrode before and after 10 mA CP experiment.

Electrodes	Resistance (ohm) Before CP	Resistance (ohm) After CP	Overpotential (mV)	Corrected Overpotential (mV)
10X	11.38	10.96	591	481
20X	10.96	10.91	665	556
40X	11.48	11.48	679	565
60X	11.50	10.62	658	552
Bare FTO	10.19	9.86	1779	1680
Bare FTO 350^o	10.86	10.47	1468	1363

To determine the thickness of the electrodes, the precursor solutions were also coated over a silicon wafer and the obtained films were imaged by scanning electron microscope. Figure 3.51 shows spin rate dependent images of the m-$Ni_{0.9}Mn_{0.1}O$ films, calcined at 350 ^oC.

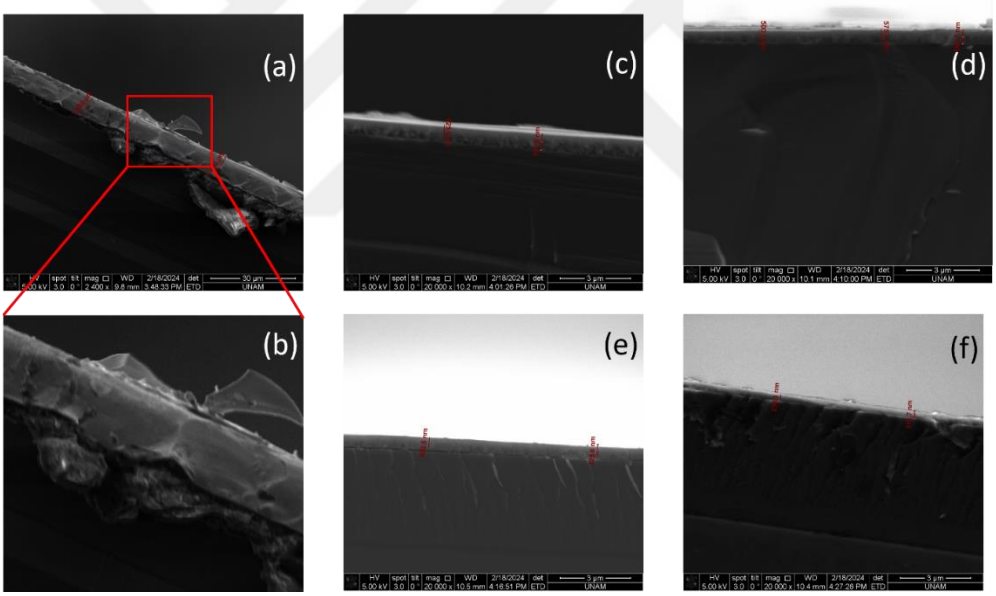

Figure 3.51. SEM images of the m-$Ni_{0.9}Mn_{0.1}O$ films, prepared at different spin rates of (a), (b) 2000 rpm, (c) 4000 rpm, (d) 6000 rpm, (e) 8000 rpm, (d) 10000 rpm, (thickness dependent) and calcined at 350 ^oC.

From the SEM images given above, it is clear that the thickness of the films varies with spin rate, but not drastically except the 2000 rpm one. For instance, thickness of the 2000 rpm film is around 5-7 µm, while the 4000, 6000, 8000 and 10000 rpm films are about 600, 550, 500, and 300 nm respectively. That supports previously shown cyclic voltammogram data where the current density is similar in all cases, except the 2000 rpm one.

That brings us to an important conclusion that, no matter what thickness of the sample is, only the particular surface is involved in electrochemical process, unless the sample is very thin, where all sample is accessible. So, basically, there is no need for very thick electrodes, but ultra-thin electrode is also not preferable reduced coverage of the FTO surface. Like for example in the very diluted samples that are shown in the Figure 3.52. The thickness of those electrodes is barely measurable.

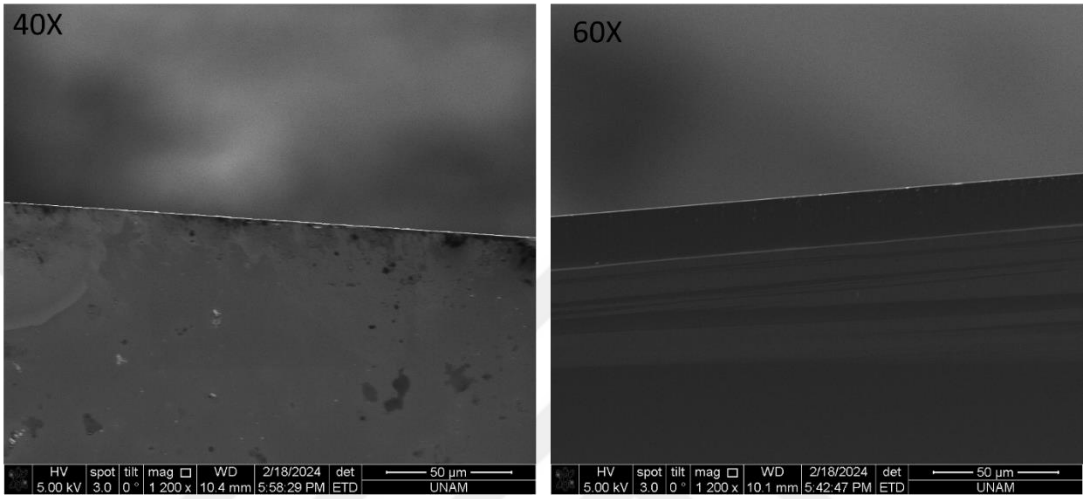

Figure 3.52. SEM images of m-$Ni_{0.9}Mn_{0.1}O$, calcined at 350 ^{o}C, prepared using 40x and 60x dilution, thickness dependent images.

The schematics provided in the Figure 3.53 represents the previously mentioned discussion.

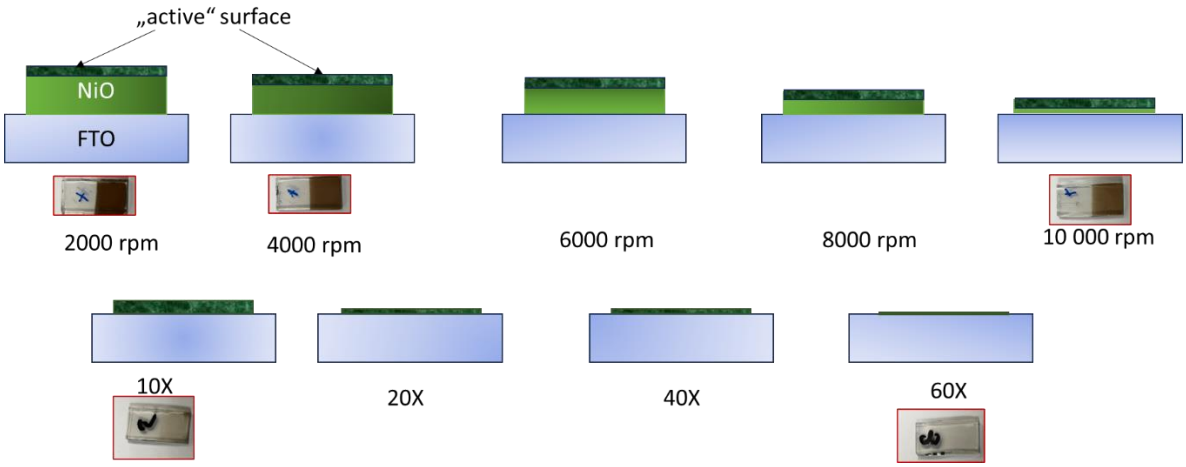

Figure 3.53. Schematic representation of active surface of the electrode, depending on the thickness.

When the electrode material is thick enough (top row Figure 3.53) not all surface is active in the electrochemical process. Most of the time, the electroactive surface is limited to a certain thickness and the rest acts like an extra substrate, that

might be good or bad in terms of resistance. Active surface is represented by dark green. That is why the same current density is observed in CVs at different spin rates. However, once the thickness of electrode is reduced drastically by dilution (bottom row Figure 3.53), the only active surface left is the whole surface of the sample due to very small thickness. That is why, the cyclic voltammograms show different oxidation current densities in the dilution dependent samples. Hence, there are some limitations in terms of active surface. Electrode should not be neither too thick nor too thin.

In all of the previous studies and experiments, only half of the FTO substrate was coated, and connection with the crocodile clip in the electrochemical cell was made with the uncoated part of the FTO. The reason was that FTO is a conductive surface while the mesoporous transition metal oxides are semiconductors so that may not be good for a proper connection. However, from recent experiments it was clear that the m-$Ni_{0.9}Mn_{0,1}O$ and m-NiO films are quite conductive materials as they show low resistance and low overpotential. Therefore, new set of electrodes were prepared from both m-$Ni_{0.9}Mn_{0,1}O$ and m-NiO samples at 350 ^oC where in one case only half of the substrate was coated and in the other case the whole surface of the FTO is covered with corresponding oxide. Both samples were prepared from 10 times diluted precursor solutions and spin coated at 2000 rpm. 1 hour 10 mA/cm^2 CP experiment was carried to compare the overpotentials (Figure 3.54). The series resistance values are also measured and tabulated in Table 3.7.

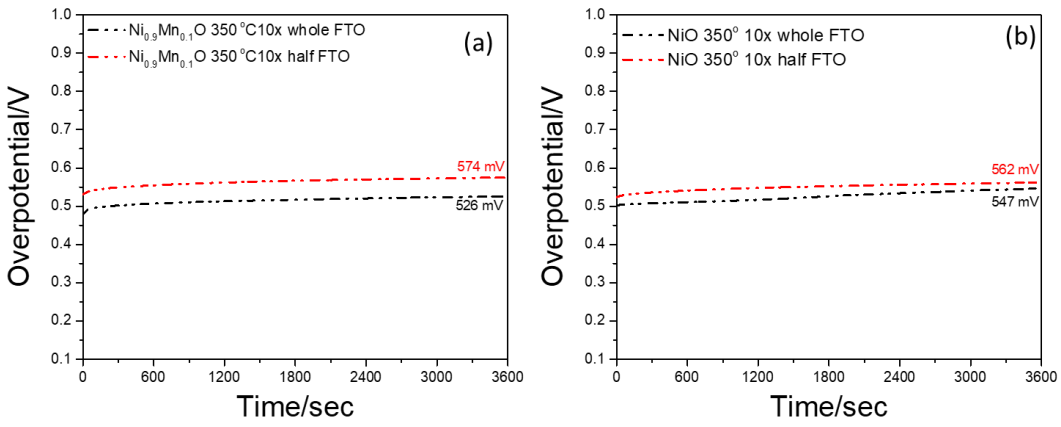

Figure 3.54. 1 h 10 mA CP of the (a) m-$Ni_{0.9}Mn_{0,1}O$ and (b) m-NiO electrodes, calcined at 350 ^oC, whole coated vs half coated FTO using 10x diluted solution at 2000 rpm spin rate.

Table 3.7. Series resistance of the m-$Ni_{0.9}Mn_{0.1}O$ and m-NiO electrodes, calcined at 350 °C before and after 1h 10 mA CP experiments.

	Resistance (ohm) Before CP	**Resistance (ohm) After CP**
$Ni_{0.9}Mn_{0.1}O$ 350 °C 10x whole FTO	10.42	10.76
$Ni_{0.9}Mn_{0.1}O$ 350 °C 10x half FTO	11.38	10.96
NiO 350 °C 10x whole FTO	10.33	10.23
NiO 350 °C 10x half FTO	10.75	10.15

In terms of the series resistance, all values are comparable. Yet, overpotential values are slightly lower for the whole coated FTO in both m-$Ni_{0.9}Mn_{0,1}O$ and m-NiO electrodes and dropped from 574 to 526 mV, and 562 to 543 mV, respectively. The coated electrode surface is twice large than the whole coated electrode the half-coated electrode, but the surface that is inserted into the electrolyte is the same in both cases, 1 cm^2.

To reduce both overpotential and series resistance and to test the theory that the whole coated substrate is better for water oxidation, new less resistive substrate is introduced, namely a graphite rod. Graphite is known to be more conductive than FTO. Same method was used to prepare the m-$Ni_{0.9}Mn_{0,1}O$ and m-NiO electrodes, but on graphite surface by dip coating using 10 times diluted precursor solution. 1 hour 10 mA CP data is given in Figure 3.55 and series resistance values are tabulated in Table 3.8.

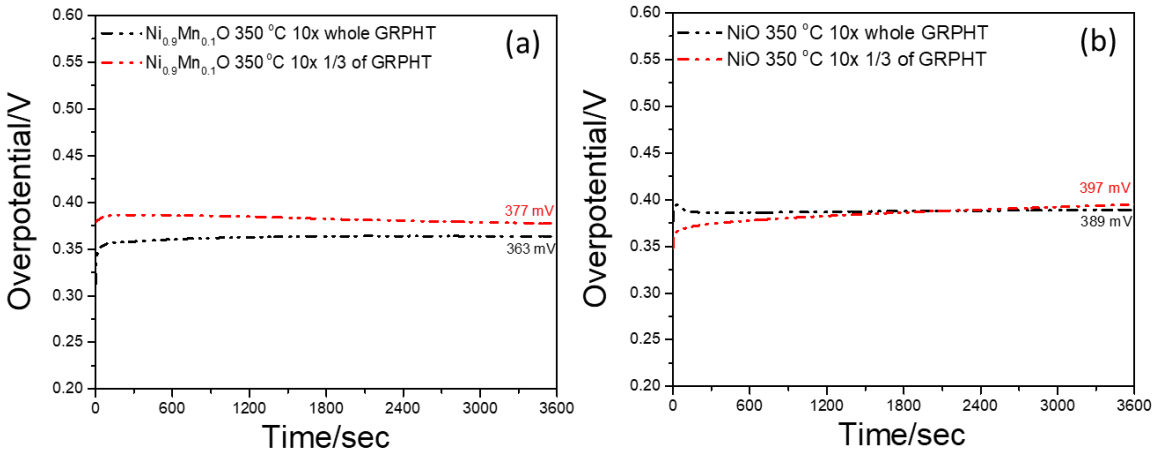

Figure 3.55. 1 h 10mA CP of the (a) m-$Ni_{0.9}Mn_{0.1}O$ and (b) m-NiO electrodes, calcined at 350 °C, whole graphite coated vs half graphite coated 10x dilution.

Table 3.8. Series resistance of the m-$Ni_{0.9}Mn_{0.1}O$ and m-NiO electrodes, calcined at 350 °C before and after 1h 10 mA CP on graphite substrate.

	Resistance (ohm) Before CP	**Resistance (ohm) After CP**
$Ni_{0.9}Mn_{0.1}O$ 350 °C 10x whole Graphite	2.61	1.46
$Ni_{0.9}Mn_{0.1}O$ 350 °C 10x 1/3 of Graphite	2.53	2.31
NiO 350 °C 10x whole Graphite	2.51	1.47
NiO 350 °C 10x 1/3 of Graphite	1.70	1.85

Similar to the FTO substrate, the whole coated graphite shows a lower overpotential of 363 and 389 mV for both m-$Ni_{0.9}Mn_{0.1}O$ and m-NiO electrodes. It should be noted that overpotential values are almost 200 mV lower than the FTO ones. Resistance values are 5-6 times lower than FTO. This is the advantage that the graphite substrate brings. In the following chapter, electrochemical characteristic of the m-$Ni_{0.9}Mn_{0.1}O$ and m-NiO on graphite substrate will be discussed.

3.6 Electrochemical Characterization of Mesoporous Nickel Oxide and Manganese Mixed Oxide Electrodes on the Graphite Substrate

The electrochemical characterization starts with the optimization of electrode thickness. The m-$Ni_{0.9}Mn_{0.1}O$ electrodes were prepared from 10x, 20x, 40x, and 60x diluted precursor solutions by dip coating method with a pulling speed of 10 cm/min and then calcined at 350 °C. First, to see the effect of the dilution on current density, 50 CVs were recorded at 50 mV/s scan rate from -0.2 to 1 V potential window in the electrolyte solution with a pH of 13.6 (see Figure 3.56).

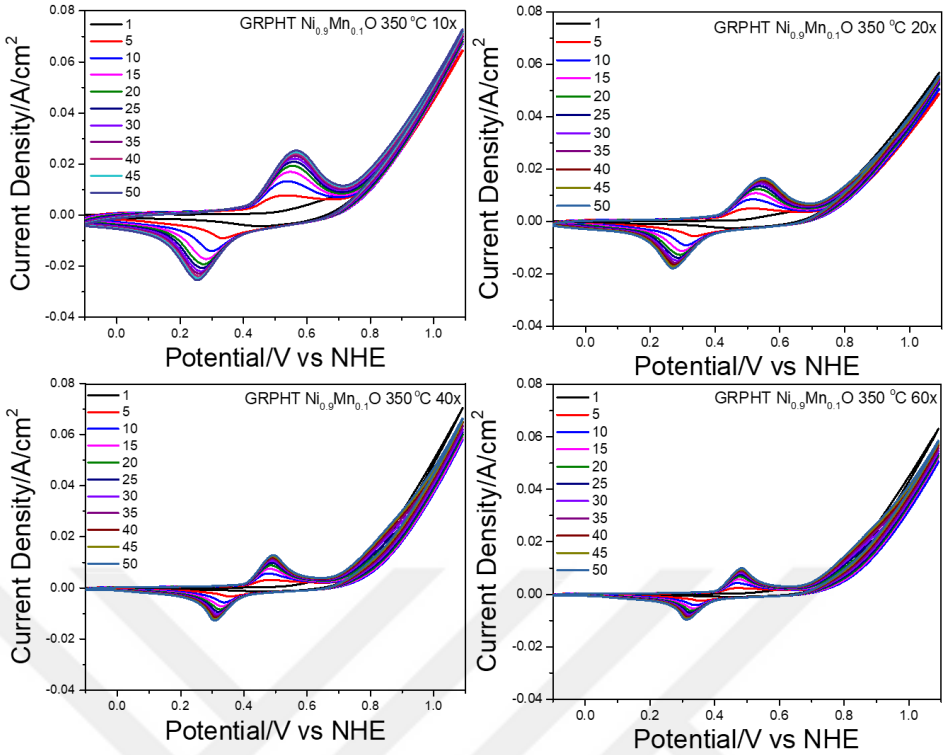

Figure 3.56. Thickness dependent (prepared at different dilutions) 50 CVs of the m-$Ni_{0.9}Mn_{0.1}O$ electrodes, coated on graphite substate and calcined at 350 °C.

Unlike spin rate dependance (FTO), the dilution shows us significant change in the oxidation peak current density as well as water oxidation side (around 1 V). The oxidation peak current density at 0.5 V decreased from 30 to 15 mA/cm^2 at 10x to 60x dilutions, respectively.

4 hours 10 mA CPs were also compared with the bare and heat-treated graphite (see Figure 3.57).

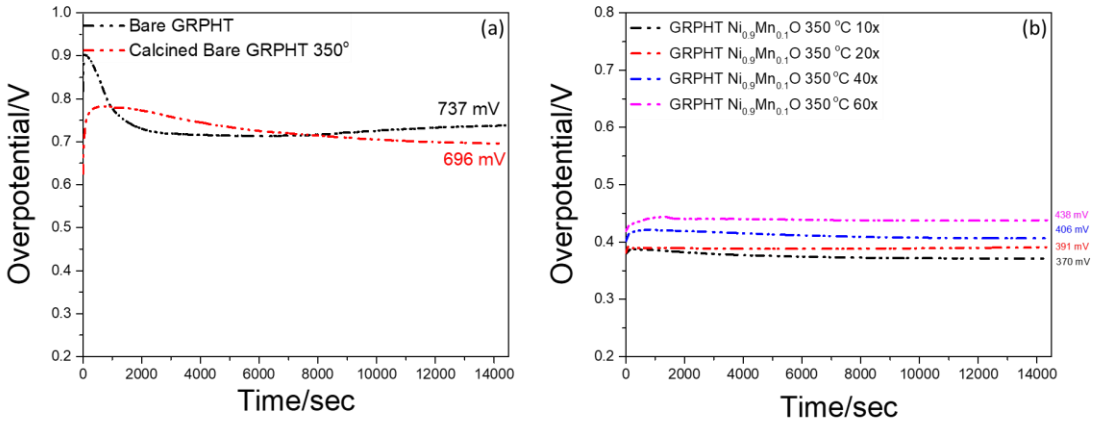

Figure 3.57. 4 hours 10 mA CP of (a) bare graphite and bare graphite calcined at 350 ^{o}C, and (b) the m-$Ni_{0.9}Mn_{0.1}O$ electrode, calcined at 350 ^{o}C, prepared at different dilutions, thickness dependent.

It is evident from Figure 3.57(a) that graphite is a better substrate than FTO, because even bare graphite shows a lower overpotential than that of the bare FTO. In case of the coated graphite, the electrode, made from10x diluted solution has the lowest overpotential of 370 mV as well as the lowest resistance of 2.5 ohms, while the electrode, made from 60x shows 2.7 ohms (see Table 3.9.) In general, the resistance of the cell gets lower with usage, that is the opposite in FTO case. Overpotential values also follow the dilution trend, the most diluted sample shows the highest overpotential value of 438 mV. Seems like the 10x dilution is the optimum one for further studies.

Table 3.9. Series resistance values before and after 10 mA CP of the m-$Ni_{0.9}Mn_{0.1}O$ electrodes, calcined at 350 ^{o}C and bare Graphite electrode.

	Resistance (ohm) Before CP	**Resistance (ohm) After CP**
10X	2.53	2.31
20X	2.91	2.84
40X	2.71	2.40
60X	2.71	2.49
Bare Graphite	3.11	3.49
Bare Graphite 350^{o}	2.68	2.32

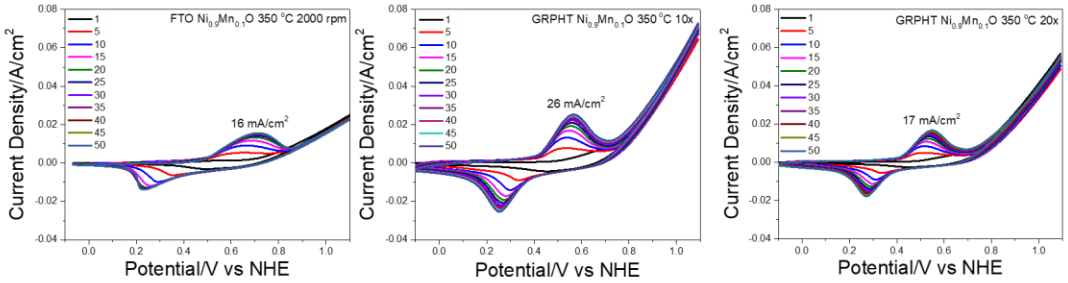

Figure 3.58. 50 Cyclic Voltammograms of the m-$Ni_{0.9}Mn_{0.1}O$ electrodes, calcined at 350 °C (from left to right), on (a) FTO substrate (2000 rpm, no dilution) and on graphite substrate using (b) 10x and (c) 20x diluted solutions.

The current densities of m-$Ni_{0.9}Mn_{0.1}O$ electrodes on graphite, coated using 10x and 20x diluted solutions 2000 rpm spin rate, were compared with the m-$Ni_{0.9}Mn_{0.1}O$ electrode coated on FTO with the same spin rate in Figure 3.58. Electrodes, prepared on graphite, at 50th cycle show slightly higher current density of around 20 mA/cm^2 at the oxidation peak maximum. The current density at water oxidation side, around 1 V, is significantly higher and 70 mA/cm^2 while the FTO coated electrode displays just 30 mA/cm^2 current density.

For further characterization, the same electrodes were tested in longer experiments. Figure 3.59 displays a selected group of CVs from a set 600 CVs. In long runs, the electrodes prepared on graphite display better stability, unlike the electrodes on FTO. Figures 3.60(a) and 3.60(b) show the oxidation peak current density at around 0.5 V vs number of cycles, and current density at 1 V vs number of cycle plots, respectively, of the m-$Ni_{0.9}Mn_{0.1}O$ electrodes on graphite substate, calcined at 350 °C.

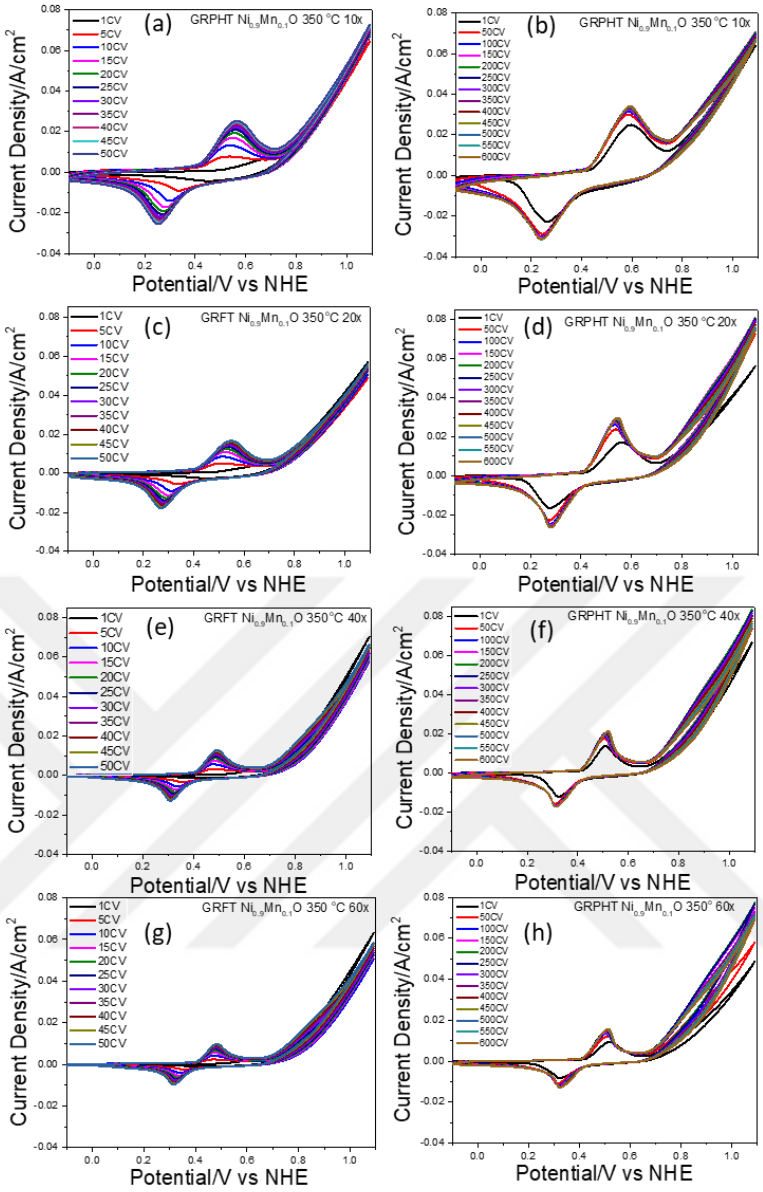

Figure 3.59. Thickness dependent (a), (c), (e), (g) 50 CVs and (b), (d), (f), (h) 600 CVs after 50 CVs (already used electrode) of m-$Ni_{0.9}Mn_{0.1}O$ on graphite substate, prepared from different dilutions and calcined at 350 ºC.

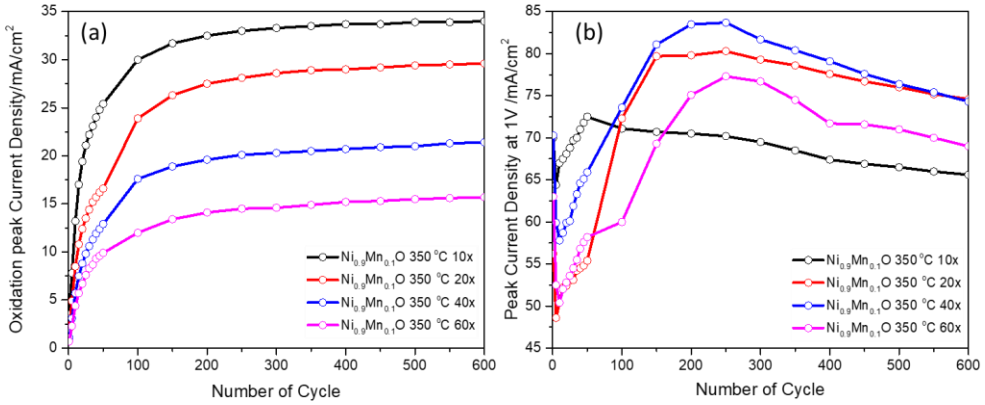

Figure 3.60. Thickness dependent (a) oxidation peak current density (around 0.5 V) vs number of cycles, and (b) current density at 1 V vs number of cycles of the m-$Ni_{0.9}Mn_{0.1}O$ electrode on graphite substate, prepared from different dilutions and calcined at 350 °C.

The plots given above clearly show the stability of the electrode on the graphite surface. After 600 cycles current density remains the same in all electrodes, and there is no decomposition of the electrodes. It should be noted that though 10x electrode shows the highest current density at 0.5 V, in the 1 V region it shows the lowest activity towards water oxidation in the later times. To better understand catalytic activity, first 4 hours 10 mA CP experiment was performed, followed by 12 hours CP to check the stability of the electrodes. The CP curves are given in the Figure 3.61.

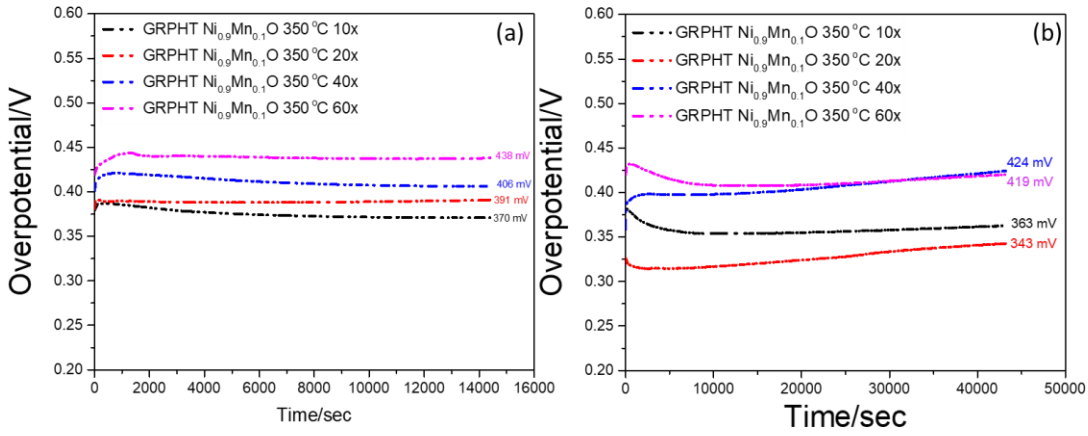

Figure 3.61. Thickness dependent (a) 4 hours 10 mA CP and (b) 12 hours 10 mA CP of the same electrodes (after 4 hours CP) of the m-$Ni_{0.9}Mn_{0.1}O$ electrodes on graphite substate, prepared from different dilutions and calcined at 350 °C.

As mentioned before, in the short experiment (Figure 3.61(a)), the 10x dilution electrode seems like the best electrode for the water oxidation, as it has the lowest

overpotential of 370 mV. In long run, after 12 hours (see Figure 3.61 (b)) this value is decreased to 363 mV, but 20x dilution shows even lower overpotential of 343 mV. Generally, the catalytic performance of the electrode with time is improved, and an overpotential decrease was observed in all electrodes after 12 hours at 10 mA CP.

If one compares the graphite coated $Ni_{0.5}Mn_{0.5}O$, $Ni_{0.9}Mn_{0.1}O$, and NiO electrodes with FTO ones (calcined at 350 ^{o}C and 500 ^{o}C), they are more robust and stable in the long electrochemical experiments. Figure 3.62 show the 600 CVs between -0.2 and 1V at scan rate 50 mV/s in 1 M KOH electrolyte. The main oxidation peak current density vs number of cycle plots are shown in Figure 3.63. From now on, the electrodes, prepared on graphite substrate are going to be denoted as G-$Ni_{1-x}Mn_xO$-XXX, where XXX is the calcination/annealing temperatures in Celcius and G stands for graphite.

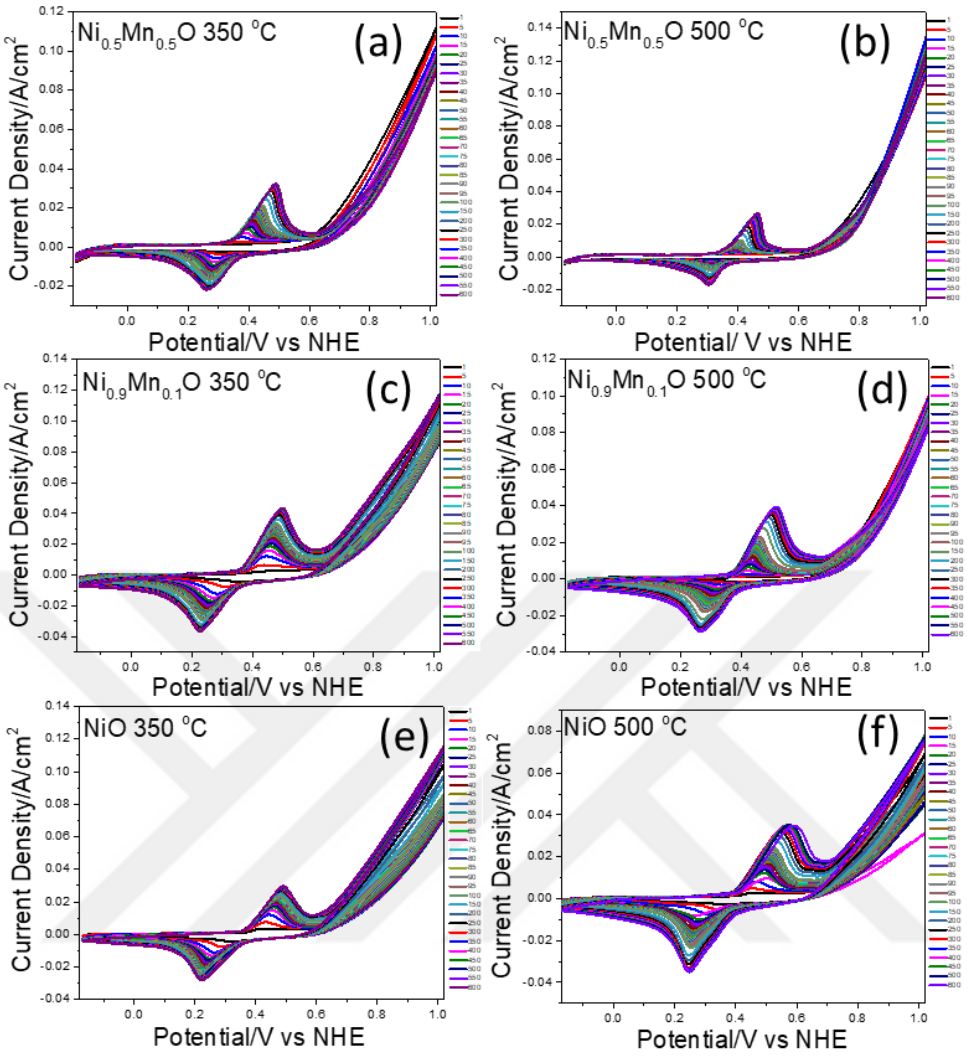

Figure 3.62. 600 CVs of the (a) G-$Ni_{0.5}Mn_{0.5}O$-350, (b) G-$Ni_{0.5}Mn_{0.5}O$-500, (c) G-$Ni_{0.9}Mn_{0.1}O$-350, (d) G-$Ni_{0.9}Mn_{0.1}O$-500, (e) G-NiO-350 and (f) G-NiO- 500 electrodes.

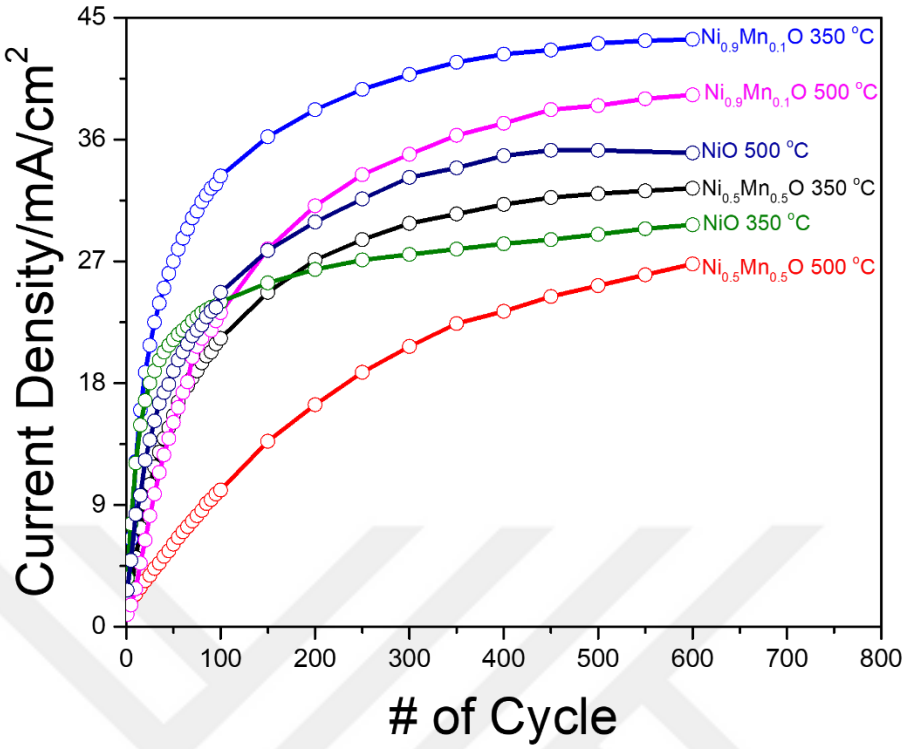

Figure 3.63. Current density vs number of CV cycles plots at 0.6 V (600 CVs) of the G-$Ni_{0.5}Mn_{0.5}O$, G-$Ni_{0.9}Mn_{0.1}O$, and G-NiO electrodes, calcined at 350 and 500 °C.

NiO on FTO loses its current density after the 50th cycle, which is not the case in the graphite electrodes. In the graphite case (see Figure 3.63 above), the current density at 0.6 V keeps increasing up to the 200th cycle and remains stable for the rest of the 400 CVs. For some reason, the decomposition kinetic of electrodes calcined at 350 °C is higher on FTO compared to graphite. The peak current of the $Ni_{0.5}Mn_{0.5}O$, $Ni_{0.9}Mn_{0.1}O$, and NiO electrodes reaches up to 32, 44, and 30 mA/cm^2 at 0.6 V, respectively. As was previously discussed, the higher the manganese content, the lower the oxidation current density on FTO (see previous chapters). An increase in the oxidation peak current at 0.6 V is assigned to the transformation of NiO to $Ni(OH)_2$/NiOOH species [20]. However, in the graphite case, the oxidation current densities of the $Ni_{0.5}Mn_{0.5}O$ and $Ni_{0.9}Mn_{0.1}O$ are comparable with the pure NiO and even become higher after cycling. It is related to the disproportionation of manganese oxide[72] and enhancing the surface of NiO as well, and increases the charge capacity of this electrode (see latter).

The 10 mA 12 hours CP experiments were also performed using the same electrodes, namely the G-$Ni_{0.5}Mn_{0.5}O$, G-$Ni_{0.9}Mn_{0.1}O$, and G-NiO electrodes (see Figure 3.64) and compared with FTO ones. The graphite electrodes show long-term stability and almost no change on their overpotential with cycling, that support the CV data.

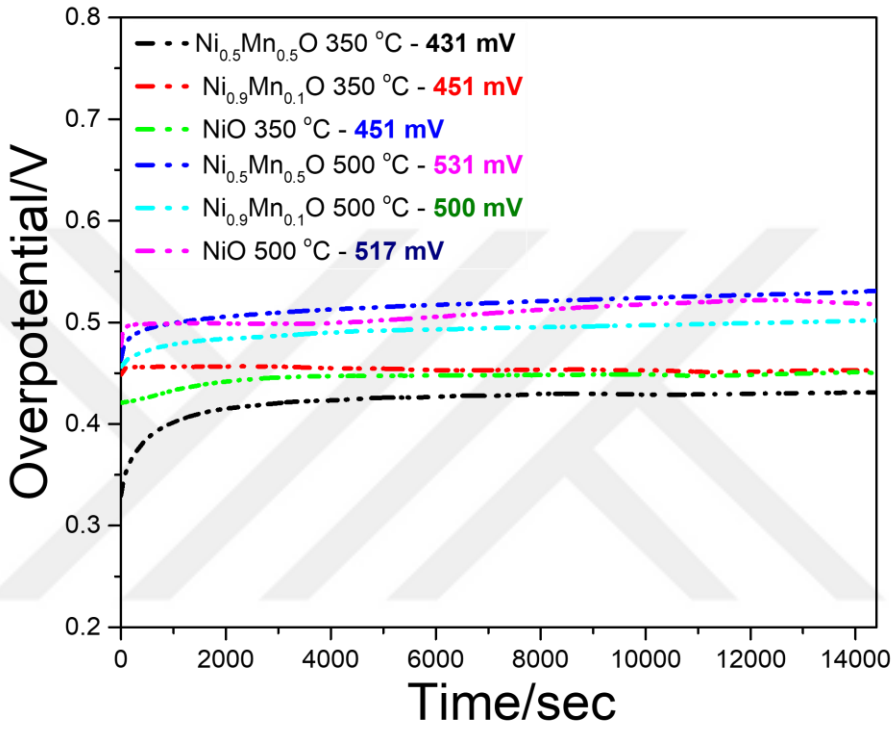

Figure 3.64. 12 hours 10 mA C of the $Ni_{0.5}Mn_{0.5}O$, $Ni_{0.9}Mn_{0.1}O$, and NiO electrodes, calcined at 350 and 500 ^{o}C.

Among all of the electrodes, the G-$Ni_{0.5}Mn_{0.5}O$-350 electrodes show the lowest overpotential of 431 mV, the highest one is observed from the G-NiO-500 electrode. That also supports our previous assumptions that binary mixtures of nickel and manganese oxides are better catalysts for water oxidation.

As graphite is a more suitable substrate for water oxidation, the m-CP experiment has been performed from 10 to 100 mA with a 10 mA increments for 30 min at each step. Series resistance was also recorded at each step, and later it was used for IR correction.

All overpotential values are tabulated in Table 3.10, and m-CP data of the G-$Ni_{1-x}Mn_xO$-XXX electrodes are shown in Figures 3.65 and 3.66.

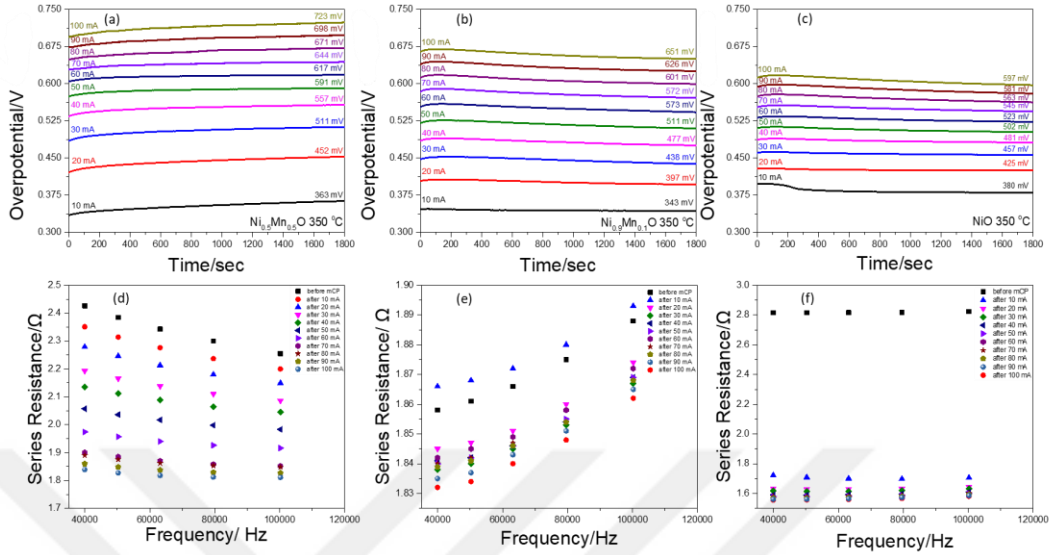

Figure 3.65. The m-CPs of the (a) G-$Ni_{0.5}Mn_{0.5}O$-350, (b) G-$Ni_{0.9}Mn_{0.1}O$-350, and (c) G-NiO-350 electrodes (numbers are overpotentials in mV at the end of each CP at each current densities, 10 to 100 mA/cm^2 with 10 mA increments, bottom to top). (d), (e) and (f) are corresponding series resistance value after each step.

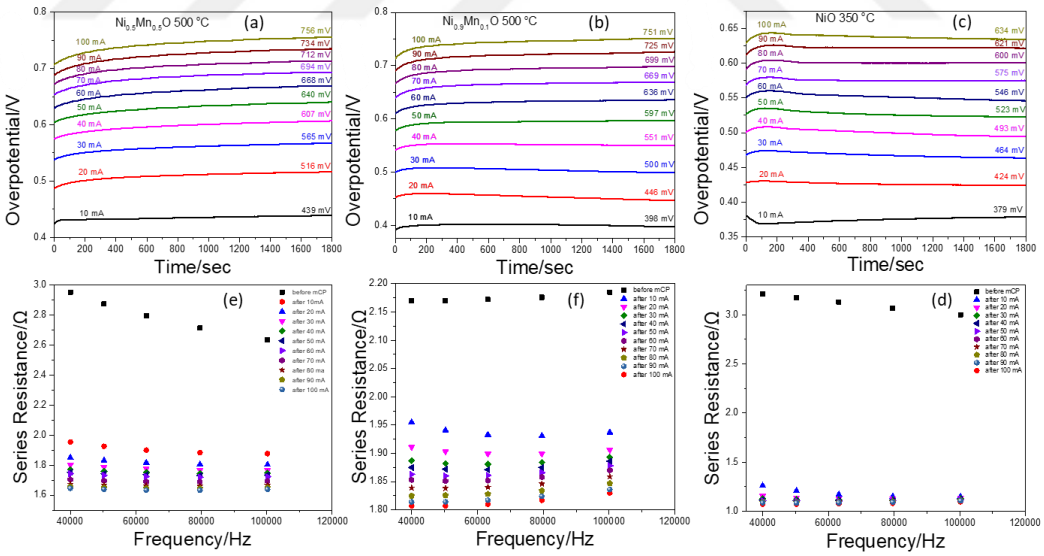

Figure 3.66. The m-CPs of the (a) G-$Ni_{0.5}Mn_{0.5}O$-500 (b) G-$Ni_{0.9}Mn_{0.1}O$-500, and (c) G-NiO-500 electrodes (numbers are overpotentials in mV at the end of each CP at each current densities, 10 to 100 mA/cm^2 with 10 mA increments, bottom to top). (d), (e) and (f) are corresponding series resistance value after each step.

Figures 3.65 and 3.66 show the m-CP curves of the G-$Ni_{0.5}Mn_{0.5}O$-350, G-$Ni_{0.9}Mn_{0.1}O$-350, G-NiO-350, G-$Ni_{0.5}Mn_{0.5}O$-500, G-$Ni_{0.9}Mn_{0.1}O$-500, and G-NiO-500

electrodes. The electrodes, calcined at 350 °C show slightly lower overpotentials than 500 °C due to higher surface area. In the G-$Ni_{0.5}Mn_{0.5}O$-350, the overpotential increases with time, while in the case of the G-$Ni_{0.9}Mn_{0.1}O$-350 and G-NiO-350 electrodes, the overpotentials decrease with time. The G-$Ni_{0.9}Mn_{0.1}O$-350 electrode shows the lowest overpotential at 10 mA of 343 mV before IR drop. It also has the lowest series resistance of 1.9 Ω. At the same current density, the G-$Ni_{0.5}Mn_{0.5}O$-350 and G-NiO-350 electrodes display overpotentials of 379 and 439 mV, respectively, and their resistance values are slightly higher as well, and 2.8 and 2.3 Ω, respectively. It was already mentioned in the previous chapters that resistance has some contribution to the overpotentials (IxR); the lower the resistance, lower the overpotential value. Compared to FTO electrodes, the series resistance also changes at each step, it drops in every step during the m-CP experiment, meaning that the electrode becomes more conductive and becomes better catalysts for water oxidation. For instance, the G-NiO-350 electrode shows the lowest overpotential at 100 mA of 597 mV and its resistance drops from 2.8 to 1.6 Ω. With IR compensation, the overpotential values further drop (see Table 3.10).

Table 3.10. Overpotentials (h), Series resistance (R_s), of $Ni_{1-x}Mn_xO$-350 and $Ni_{1-x}Mn_xO$-500 electrodes.[m]Measured from 2 h m-CP experiments, [c]calculated after IR compensation (R_s is the series resistance after m-CP).

Electrodes	**h_{10} (mV)[m]**	**h_{10} (mV)[c]**	**h_{100} (mV)[m]**	**h_{100} (mV)[c]**	**R_s (Ω)**
FTO-$Ni_{0.9}Mn_{0.1}O$-350	461	311	1984	484	15.00
FTO-$Ni_{0.8}Mn_{0.2}O$-350	455	308	1923	458	14.65
FTO-$Ni_{0.7}Mn_{0.3}O$-350	481	337	2001	566	14.35
FTO-$Ni_{0.6}Mn_{0.4}O$-350	489	342	2049	583	14.66
FTO-$Ni_{0.5}Mn_{0.5}O$-350	414	283	1723	413	13.10
FTO-$Ni_{0.4}Mn_{0.6}O$-350	469	311	2153	573	15.80
FTO-$Ni_{0.3}Mn_{0.7}O$-350	451	303	2188	709	14.79
FTO-$Ni_{0.2}Mn_{0.8}O$-350	532	405	2031	758	12.73
FTO-$Ni_{0.1}Mn_{0.9}O$-350	520	384	3089	1729	13.60
G-NiO-350	380	352	597	436	1.57
G-$Ni_{0.9}Mn_{0.1}O$-350	343	326	651	463	1.86
G-$Ni_{0.5}Mn_{0.5}O$-350	363	342	723	541	1.81
G-NiO-500	379	349	634	521	1.09
G-$Ni_{0.9}Mn_{0.1}O$-500	398	378	751	568	1.83
G-$Ni_{0.5}Mn_{0.5}O$-500	439	412	756	589	1.64

Notice that after IR compensation, the electrodes prepared on FTO substrate show lower overpotentials due to slightly lower Tafel slopes. In graphite-coated electrodes, the Tafel slope increases with increasing manganese content. Tafel slopes

obtained from the multi-step chronoamperometry (m-CA) experiment are shown in Figure 3.67.

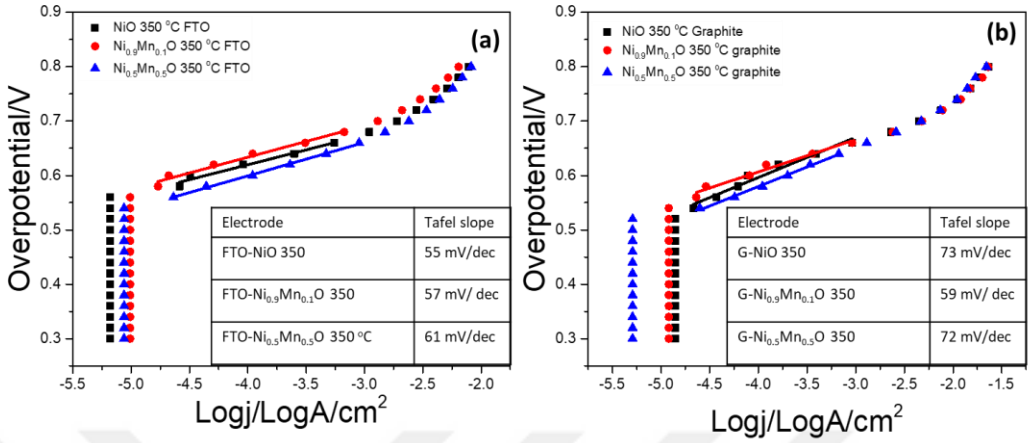

Figure 3.67. Tafel plots of electrodes (a) on FTO, (b) on graphite. In the inset, Tafel slope values are given.

The graphite electrodes have higher Tafel slopes of 73, 59 and 72 mV/dec for the G-NiO-350, G-$Ni_{0.9}Mn_{0.1}O$-350 and G-$Ni_{0.5}Mn_{0.5}O$-350 electrodes, respectively. It is the reason for the higher overpotential after IR compensation. The electrodes, prepared on FTO, have Tafel slopes of around 55-60 mV/dec.

From the chronopotentiometry experiment after IR compensations (see Table 3.10) between 10 and 30 mA/cm^2, there is a significant increase in overpotential, but between 30 and 100 mA/cm^2, it is not that large. From the series of resistance measurements, I have seen that the resistance value does not change much after 30mA/cm^2. After completing the mCP measurement, the graphite rod becomes completely wet due to the splashing of electrolytes because of the bubble of oxygen at higher currents. That is the reason why graphite electrodes are better OER catalysts at higher potential because part of the electrode that was out of the electrolyte but got splashed with electrolyte ensures better conductivity and lower overpotential.

3.7 Capacitive Properties of Pure Mesoporous Nickel Oxide, Optimization of Current and Potential Range.

The main property of the NiO electrodes is that, with the CV cycling experiment, the current density increases because of $Ni(OH)_2$ formation on the surface

of NiO. The NiO is converted to NiO/$Ni(OH)_2$ core-shell on the pore-walls. Current density increases with increasing $Ni(OH)_2$ amount, so the capacitive property of the NiO electrode is also investigated. Two NiO electrodes, calcined at 350 and 500 ^oC are analyzed using galvanostatic charge discharge (GCD) measurements after 2^{nd}, 200^{th}, and 600^{th} cycles (CVs were recorded at 50 mV/s scan rate). The GCD plots are given below and capacitance values are tabulated in Table 3.4. The CV scan rate was decreased down to 5 mV/s to determine the potential window for charge-discharge curves. Since, the main oxidation and reduction peaks are observed in between 0.2 and 0.55 V potential window, the GCD was recorded within this potential window. The charge discharge plots are given in Figures 3.68 and 3.69 and the capacity and specific capacitance values are tabulated in Tables 3.11 and 3.12 for NiO, calcined at 350 and 500 ^oC, respectively.

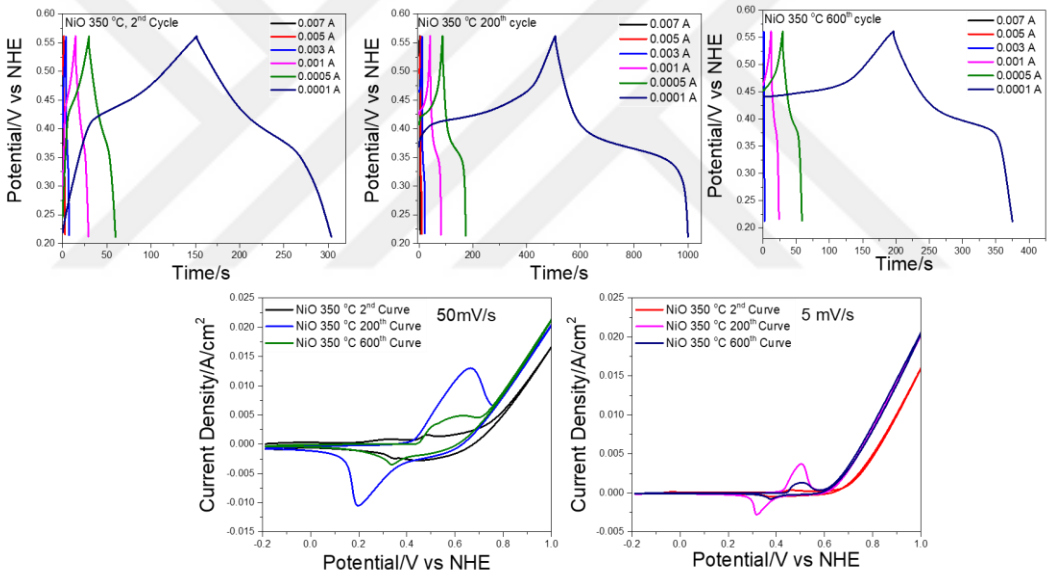

Figure 3.68. Charge-discharge curves at different current densities and at different cycle numbers, and CVs (2^{nd}, 200^{th}, and 600^{th} curves, top, left to right) at 50 and 5 mV/s (bottom, left to right) of the NiO electrode, calcined at 350 ^oC.

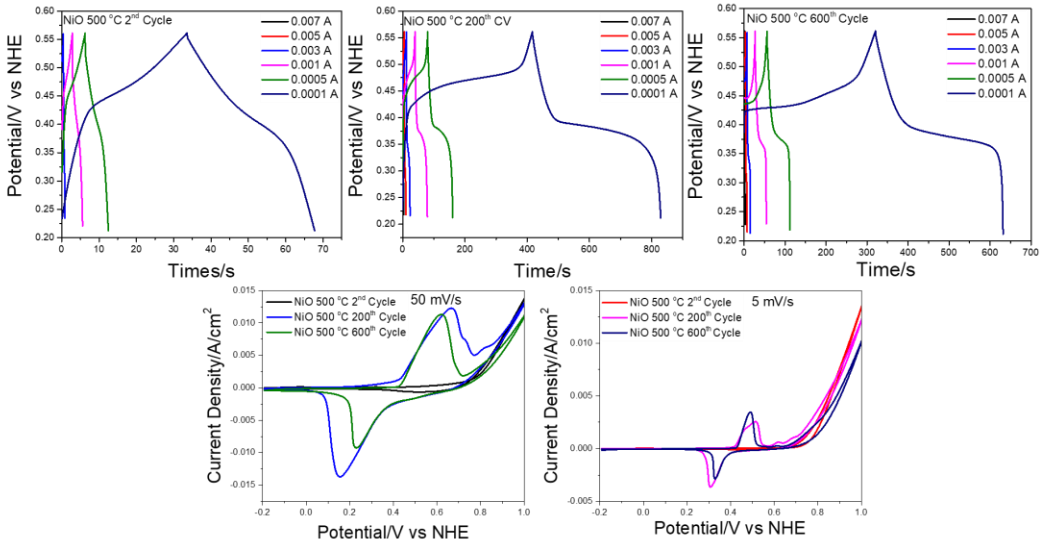

Figure 3.69. Charge-discharge curves at different current densities and at different cycle number, and CVs (2^{nd}, 200^{th}, and 600^{th} curves, top, left to right) at 50 and 5 mV/s (bottom, left to right) of the NiO electrode, calcined at 500 °C.

Table 3.11. Capacity and specific capacitance values of the NiO electrode, calcined at 350 °C.

Current Density (mA/cm^2)	**NiO 350 °C**					
	2^{nd} Cycle		200^{th} Cycle		600^{th} Cycle	
	Capacity (mA.s)	Specific capacitance (mF/cm^2)	Capacity (mA.s)	Specific capacitance (mF/cm^2)	Capacity (mA.s)	Specific capacitance (mF/cm^2)
7	2.67	7.63	13.91	39.74	0.0117	0.033
5	7.20	20.57	25.32	72.34	0.0173	0.049
3	10.87	31.06	32.28	92.23	3.49	9.97
1	14.47	41.34	40.25	115.00	11.86	33.89
0.5	14.80	42.28	42.70	122.00	14.33	40.94
0.1	14.92	42.63	48.53	138.66	17.24	49.26

Table 3.12. Capacity and specific capacitance values of the NiO electrode, calcined at 500 °C.

Current Density (mA/cm^2)	**NiO**					
	2^{nd} Cycle		200^{th} Cycle		600^{th} Cycle	
	Capacity (mA.s)	Specific capacitance (mF/cm^2)	Capacity (mA.s)	Specific capacitance (mF/cm^2)	Capacity (mA.s)	Specific capacitance (mF/cm^2)
7	0.0117	0.033	11.69	33.4	11.29	32.26
5	0.0173	0.049	25.01	71.48	18.08	51.66
3	1.39	3.97	34.71	99.17	22.48	64.23
1	2.76	7.89	39.02	111.49	26.80	76.57
0.5	3.09	8.83	39.67	113.34	27.58	78.80
0.1	3.31	9.46	40.21	114.88	30.05	85.86

From the CVs at first cycles, the NiO electrode, calcined at 350 °C, displays higher specific capacitance of 42.63 mF/cm^2 than the electrode, calcined at 500 °C, that has 9.46 mF/cm^2 specific capacitance at 0.1 mA /cm^2 current density. This is in a good agreement with the electrode surface area. At low temperature, the surface area is larger that is reflected in the initial current density. However, with time, even high temperature sample displays a high current density as the amount of nickel hydroxide build up on the pore-walls. After 200 CVs, the current densities are quite comparable with specific capacitance of 122 and 114 mF/cm^2 for the electrodes, calcined at 350 and 500 °C, respectively. At the very end, after 600^{th} cycle, the NiO electrode at 500 °C has a higher capacitance than the nickel oxide, calcined at 350 °C, the values are 85.86 and 49.26 mF/cm^2, respectively. These values are in good agreement with the current densities at peak maxima in the CVs.

3.8 Capacitive properties of NiO based thin film electrodes and its dependence on thickness of the electrode, calcination temperature and manganese content.

To better understand the electrocatalytic properties of the NiO-based thin film electrodes, the temperature-dependent GCD experiment has been performed using the NiO electrodes, prepared at 350, 400, 450, and 500 ºC. The GCD temperature-dependent data of the m-NiO electrodes are shown in Figure 3.70. Due to the unique nature of nickel oxide, the surface of the electrode always undergoes a chemical change that is reflected in the change of peak current of the oxidation and reduction peaks. During 600 cyclic voltammograms (between -0.2 and 1 V) the GCD curves were also recorded after every 50 CV cycles at a 0.1 mA/cm^2 current density. Pre and post treatment analysis has also been carried by using XPS data.

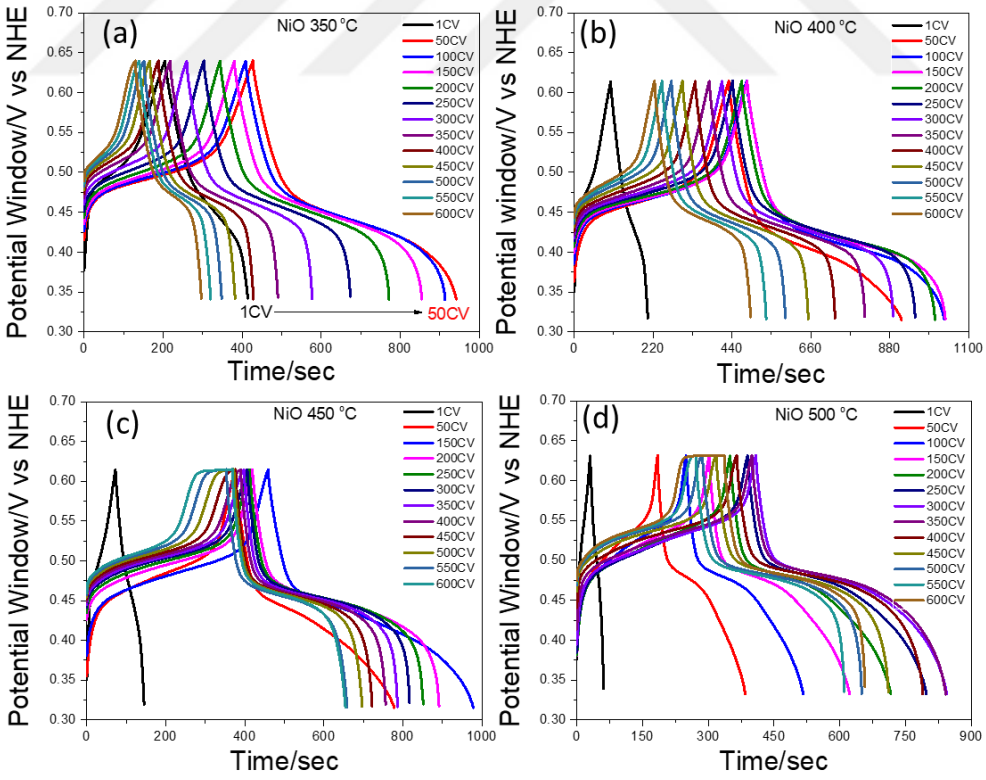

Figure 3.70. The GCD curves after each 50 CV cycles (from 1st to 600th CV) at 0.1 mA/cm^2 current density of the m-NiO electrodes, calcined at (a) 350, (b) 400, (c) 450 and (d) 500 ºC.

If one looks at the time scale, each electrode shows maximum capacity at different times, meaning that the annealing temperature does affect the capacitive properties of the NiO electrodes. Because, increasing annealing temperature decreases the surface area. Lower the surface area of the electrode means lower the capacity. The capacity and specific capacity values versus time plots obtained from the discharge data are shown in the Figure 3.71.

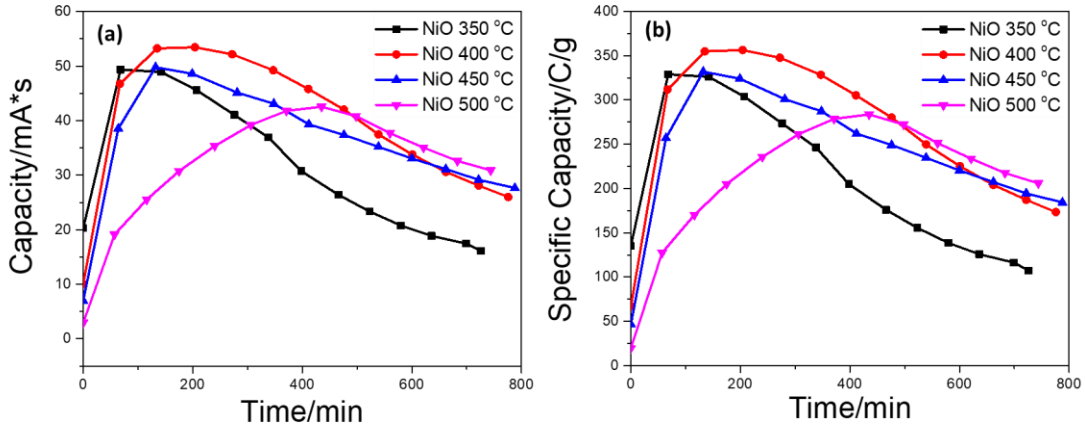

Figure 3.71. Annealing temperature dependent (a) capacity vs time and (b) specific capacity vs time plots of the m-NiO electrodes.

From the plots above, it is clear that within 100-150 minutes, the electrodes calcined at 350, 400 and 450 ^{o}C show their maximum capacity, while the 500 ^{o}C sample shows maximum capacity after 400 minutes. All the electrodes eventually show a decay in their capacity values, indicating the deactivation or decomposition of the electrode. The specific capacity was also calculated using the electrode weight, as of around 0.15 mg. Maximum capacity of around 350 C/g was calculated from the NiO electrode, calcined at 400 ^{o}C, at around 100 minutes. But the capacity gradually decays down to 170 C/g after 800 minutes.

Charge/discharge analysis has been performed after cyclic voltammetry experiment, at a scan rate of 5 mV/s. To compare whether the capacity value change with time is consistent with change in peak current density, the CVs from 1st to 600th CV (each 50th cycle) at 5 mV/s scan rate of the NiO electrodes (calcined at 350, 400, 450 and 500 ^{o}C) are shown in Figure 3.72. The peak current density versus cycle number plots of the same electrodes is shown in Figure 3.73.

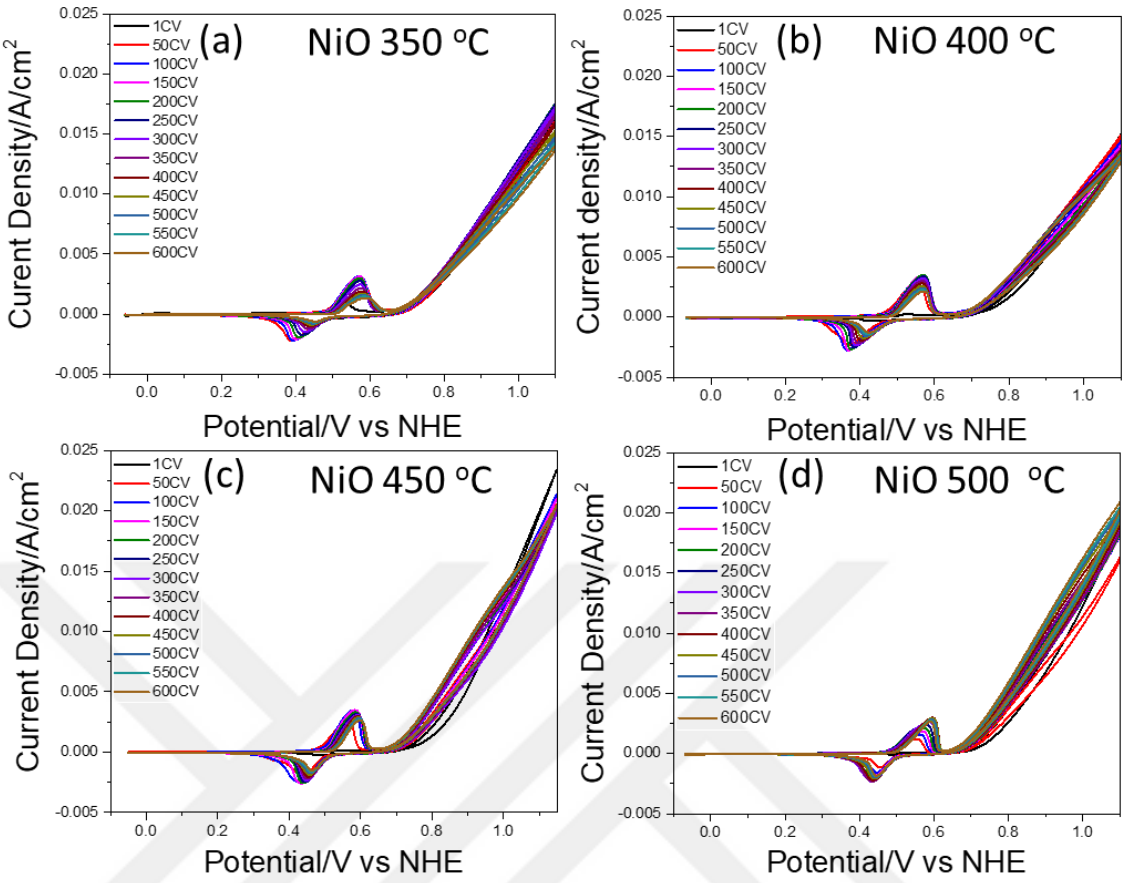

Figure 3.72. 600 cyclic voltammograms (each 50th curve) at 5 mV/s scan rate of the m-NiO electrodes, calcined at 350, 400, 450 and 500 °C.

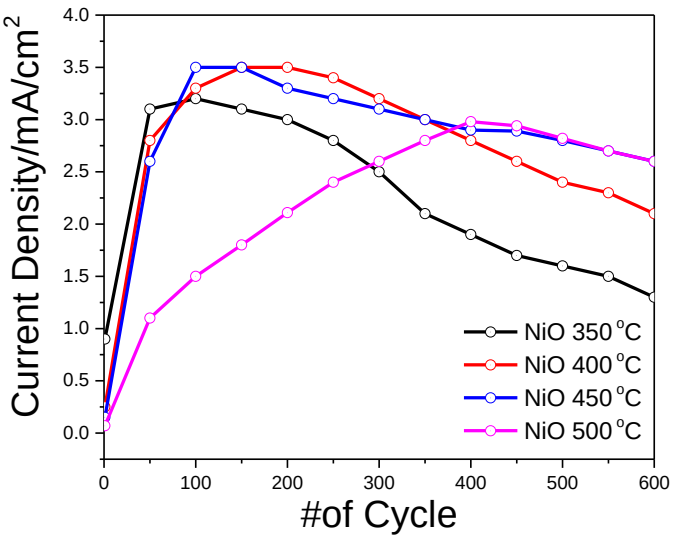

Figure 3.73. Oxidation peak current density vs # of cycle plot of the m-NiO electrodes, calcined at 350. 400, 450 and 500 °C.

Though the plot in Figure 3.73 is quite similar to the plot shown in Figure 3.71, the cyclic voltammetry does not fully follow the capacity data. The maximum peak current density for each electrode, calcined at 350, 400, 450 and 500 ^{o}C is reached after 100th, 150th, 150th and 400th cycles, respectively, while the maximum capacity is reached after 50th, 150th, 100th, and 350th cycles. The main conclusion that we can make from these results is that, though the peak current densities are valuable data to judge the behavior of the particular electrode, the area under the curve is more reliable, as it provides us with the whole charge that the material can store.

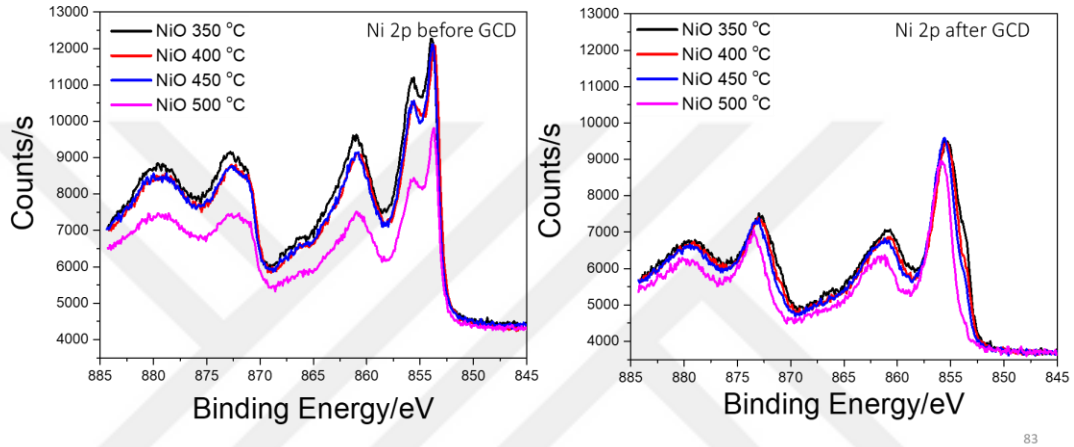

Figure 3.74. Ni 2p spectra of the m-NiO electrodes, before and after GCD.

Surface of the electrode was analyzed by XPS technique, and Ni 2p region before and after GCD experiment is given in Figure 3.74. Before the GCD experiment, the Ni 2p spectrum displays a typical NiO spectrum, two peaks in the $^{2}P_{3/2}$ region, the high binding energy peak (855.86 eV) belongs to $Ni(OH)_2$/NiOOH species while the low energy peak (853.89 eV) is assigned to NiO. However, after GCD measurements, all of the spectra show almost the same intensity, meaning that the surface species are similar and converted to $Ni(OH)_2$/NiOOH species. The intensity of the high energy peak increases, and the low energy peak diminishes by leaving only a small shoulder, indicating that only the top surface is converted to NiOOH and there are still NiO species underneath the surface. Only in the case of the 500 ^{o}C sample, the NiO peak completely disappears, supporting the fact that larger pore NiO (low surface area) produces more NiOOH species at the end of the 600 cycles due to the pore-size effect.

The XRD patterns do not display lines due to $Ni(OH)_2$ species, because either nickel hydroxide formed during the electrochemical process is amorphous or very

thin/small and not large enough to provide x-ray diffraction; particle size of the $Ni(OH)_2$ shell is smaller than diffraction limit that requires several unit-cells. TEM images of the NiO electrode, calcined at 500 ^oC, before and after 600 CVs is shown in Figure 3.75.

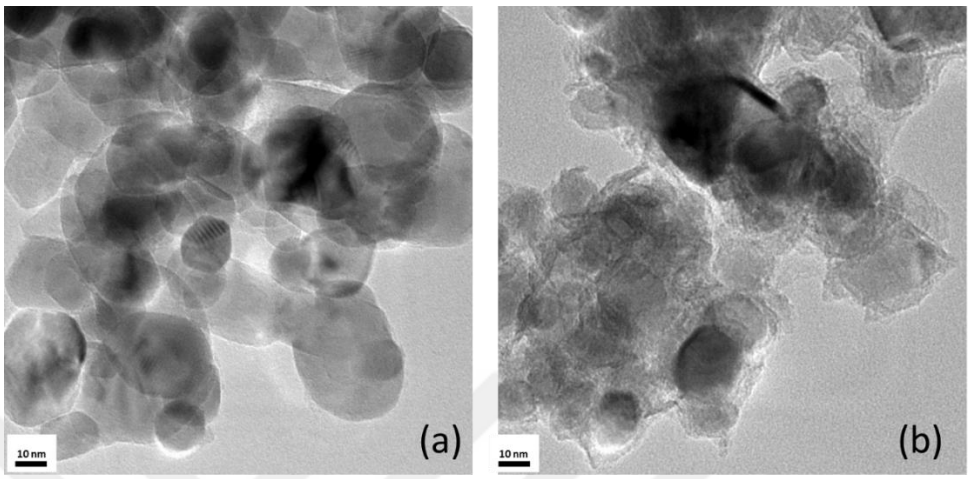

Figure 3.75. TEM images of the NiO electrode, calcined at 500 ^oC (a) before and (b) after 600 CVs.

From the TEM images above, before the electrochemical test, the NiO nanoparticles are crystalline and the NiO lattice fridges are visible. After 600 CV, the particles are covered with amorphous nickel hydroxide that changes the morphology of the particles.

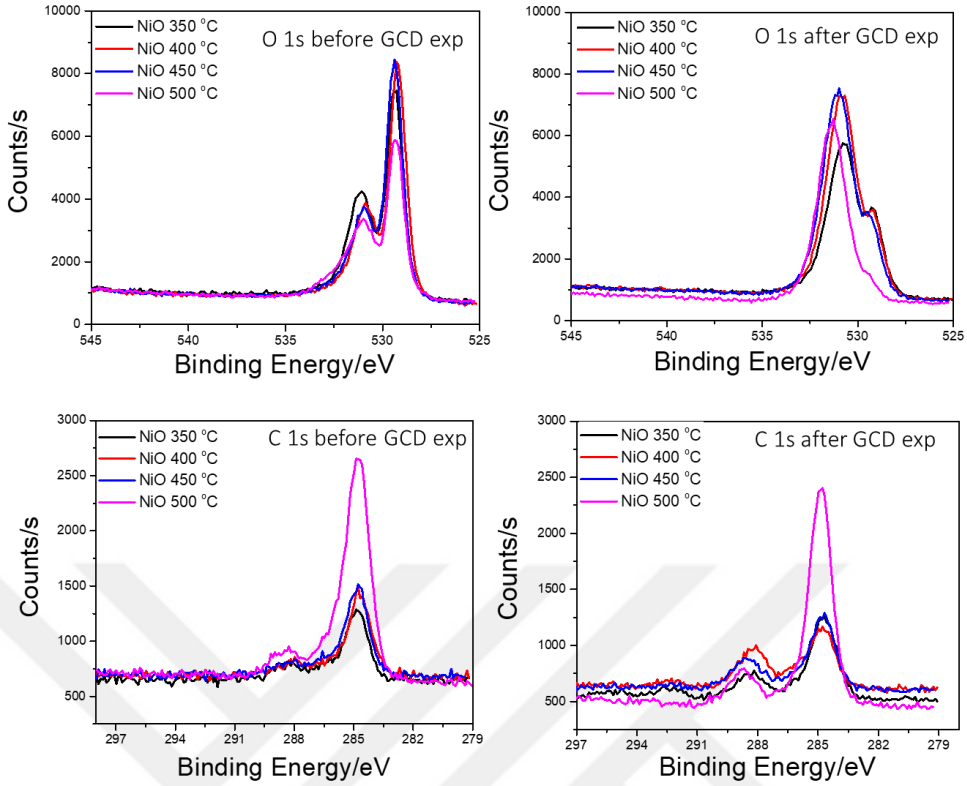

Figure 3.76. O 1s (top) and C 1s (bottom) spectra of the m-NiO electrodes, (left) before and (right) after GCD.

To support the above data, Figure 3.76 shows O 1s and C 1s spectra of the NiO electrodes at different temperatures. The oxygen 1s spectrum before GCD displays two peaks. Lower binding energy peak (at 529. 28 eV) is due to the lattice oxygens and belongs to NiO. Note that it also has higher intensity meaning that the surface is dominated by lattice oxygen species. After the GCD experiment, that peak loses its intensity and a higher binding energy peak at 531.03 eV becomes the dominant peak, indicating that the surface is converted into oxyhydroxides and hydroxides species. The low energy peak does not disappear completely that supports the fact that only the surface is converted to the hydroxides. The carbon 1s region almost does not show any change after usage of the electrode, except small peaks that appear between 290 and 295 eV due to potassium species. The potassium ions are present on the electrode surface, because the electrolyte used in GCD experiment is 1M KOH. After the usage, though the surface of the electrode is thoroughly washed, the trace amounts are still present and appears in the C 1s spectrum. K 2 p scan is shown in the Figure 3.77. Note also that the intense peak around 288 eV is due to C 1s of carbonate species.

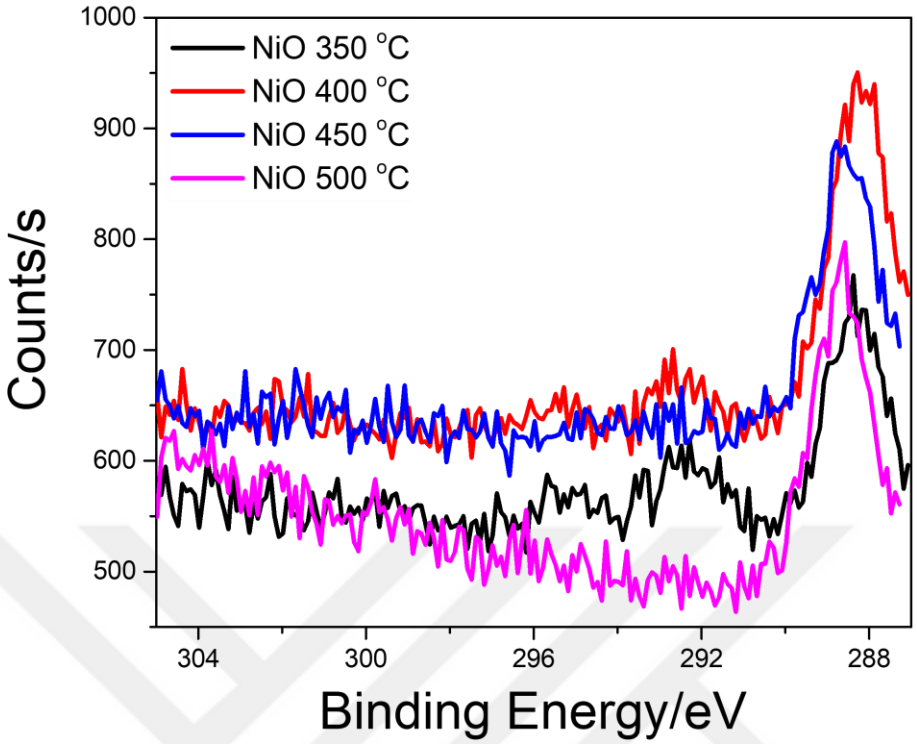

Figure 3.77. K 2p spectra of the m-NiO electrodes after GCD.

It is already established that only top surface of the m-NiO electrode is converted into nickel hydroxide and oxyhydroxide species. To support this assumption, the thickness dependent GCD measurements have also been performed. The GCD curves of the m-NiO electrodes, prepared at different spin rates and calcined at 350 ^{o}C, and capacity and specific capacity versus time plots are shown in Figures 3.78 and 3.79, respectively.

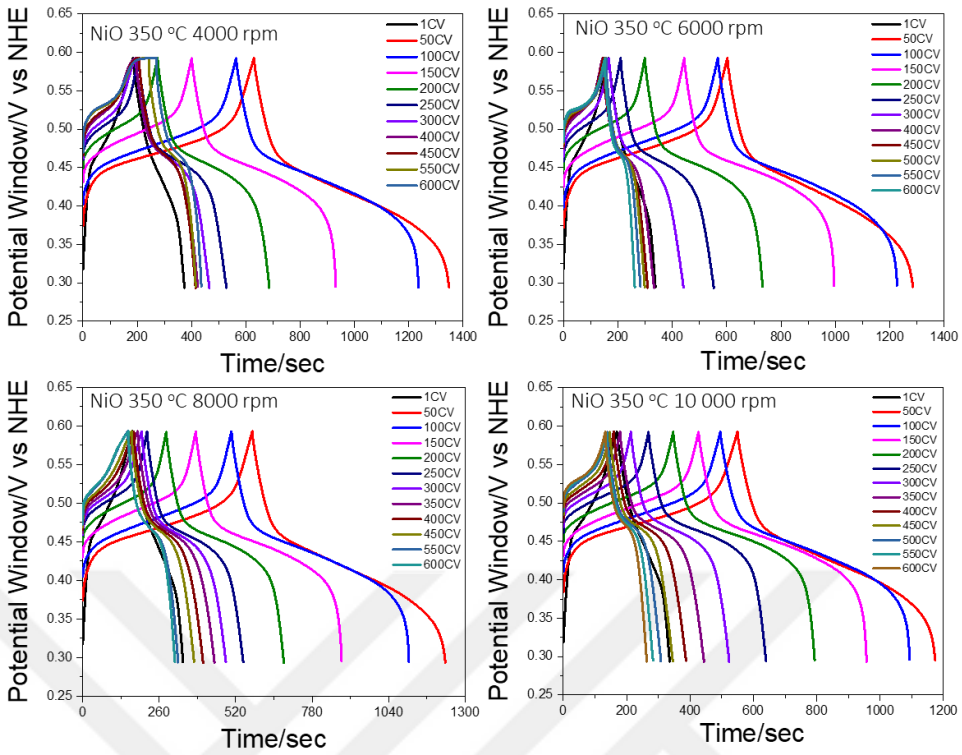

Figure 3.78. The GCD curves of the m-NiO electrodes, prepared at different spin rates (4000, 6000, 8000 and 10000 rpm) and calcined at 350 °C.

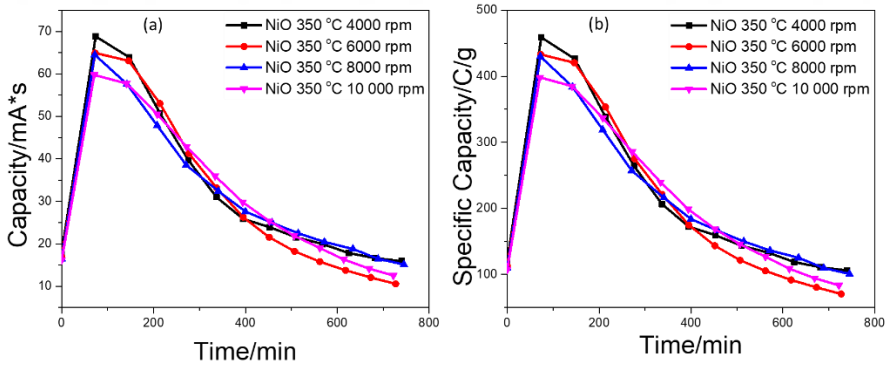

Figure 3.79. Thickness dependent (a) capacity vs time and (b) specific capacity vs time plots of the m-NiO electrodes, calcined at 350 °C.

he 4000-rpm coating makes the thickest film, while the 10000-rpm makes the thinnest film on top of the FTO substrate. From Figure 3.80, it is shown that all of the electrodes, reach their maximum capacity (around 60-70 mA*s) after 50 CVs. The maximum capacity values differ, but not drastically, for example at 4000 rpm the maximum capacity reached to 70 mA*s while in the case of 10000 rpm that value is 60 mA*s. At the end of 600 cycles, the capacities drop to 16 and 13 mA*s, respectively.

These values are quite similar to each other, and it supports the fact that only the top surface of the NiO electrode is getting converted into the $Ni(OH)_2$/NiOOH species.

Figure 3.80 displays the cyclic voltammograms, recorded at 5 mV/s, from 1st to 600th cycles of the same electrodes.

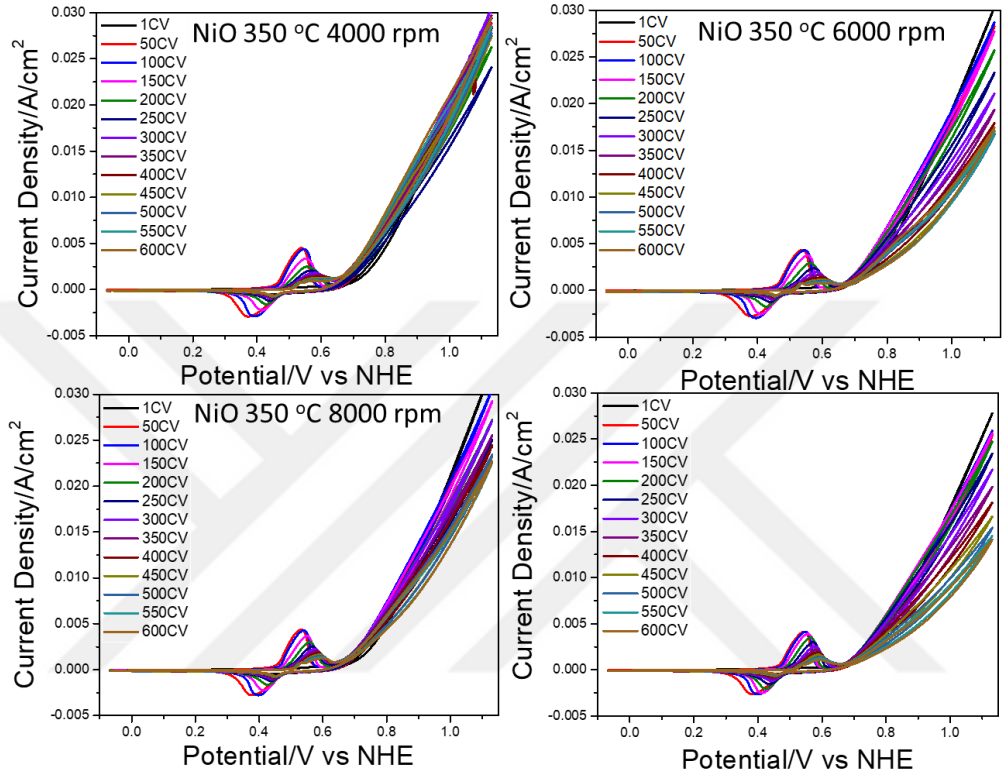

Figure 3.80. Thickness dependent 600 Cyclic Voltammograms (each 5th cycle) at 5 mV/s scan rate of the m-NiO electrode, calcined at 350 °C.

It is shown in above plots that all the electrodes exhibit high current densities at high potentials (water oxidation region), meaning they are active toward OER. The best stability during OER was shown in the 4000-rpm electrode. The 10000-rpm electrode is unstable and slowly loses its activity with 600 cycles. The current density gradually drops from 28 to 14 mA/cm^2 from 1st to 600th CV cycles.

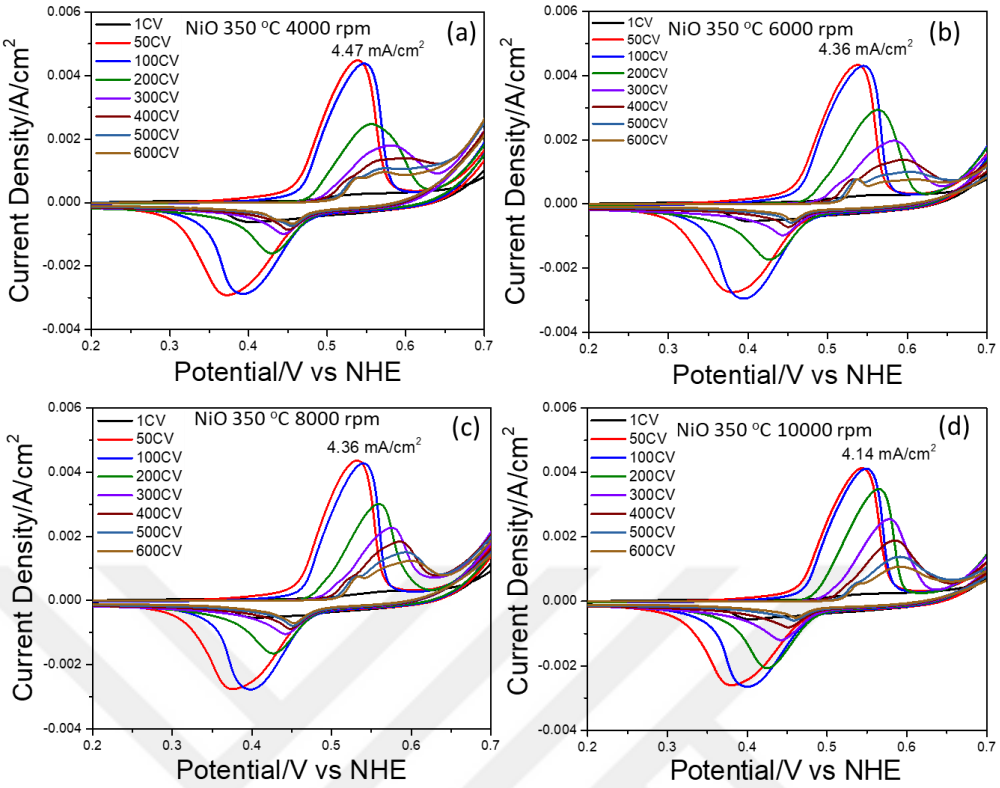

Figure 3.81. Thickness dependent 600 Cyclic Voltammograms (each 5th cycle) at 5mV/s scan rate (between 0.2 and 0.7 V) of the m-NiO electrodes, calcined at 350 ^{o}C.

Once, we have a closer look at the oxidation and reduction region of those electrodes, the change in oxidation peak current is almost the same in all spin rates. It gradually decreases with each cycle. Figure 3.81 shows the narrow potential window of 0.2-0.7 V CVs of the same electrodes. Once the current density gets decreasing, the better resolved oxidation peaks appear. After 400th cycle, instead of one broad oxidation peak, two peaks at 0.5 and 0.6 V are resolved. We previously assigned this peak to Ni^{2+} to Ni^{3+} or nickel hydroxide to nickel oxyhydroxide transformation. The second peak could be assigned to Ni^{3+} to Ni^{4+}. The appearance of NiO_2 is not clear yet as it is not stable, but it might also be layered material like nickel hydroxide. The fact that this peak may belong to unstable Ni^{4+}. It can be supported by the absence of a second peak in the reduction cycle.

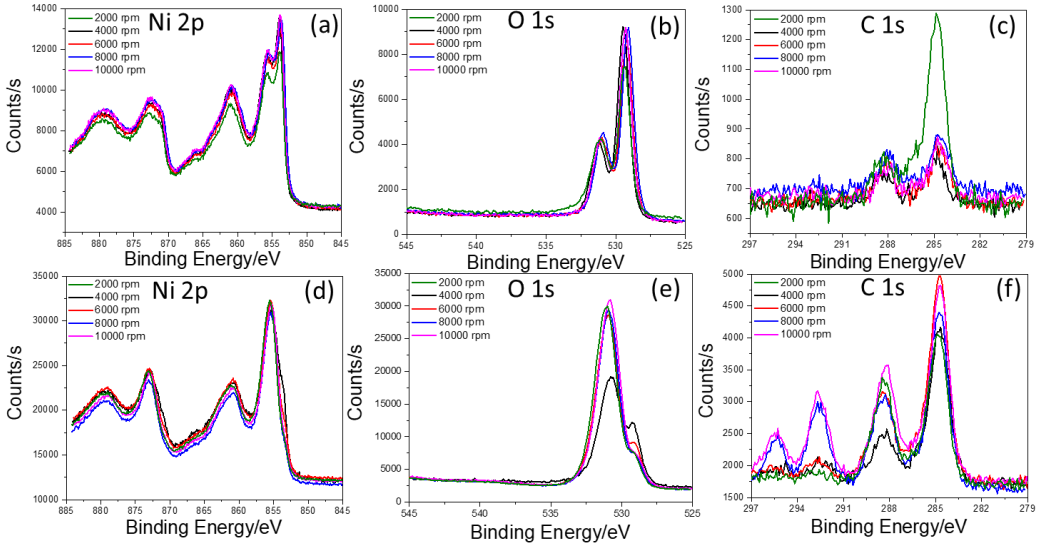

Figure 3.82. XPS spectra: (a), (d) Ni 2p, (b), (e) O 1s and (c), (f) C 1s regions of the m-NiO electrodes, prepared at different spin rates and calcined at 350 ^{o}C, (a), (b), (c) before and (d), (e), (f) after GCD.

Before exposing those electrodes to an electrochemical analysis, the XPS analysis has been done, and spectra are shown in Figure 3.82. Again, XPS data show that, all of the samples, though prepared at different spin rates, have identical spectra in the Ni 2p, O 1s and C 1s regions (see Figure 3.82 (a, b, c). To better understand the transformation that occurs on the surface, the post electrochemical XPS analysis has also been done (Figure 3.82 (d, e, f)). Before the GCD experiment, the Ni 2p spectrum displays typical NiO spectrum**.** After the catalytic use, the surface becomes hydroxide and oxyhydroxide dominant at the end of the GCD experiment. The C 1s scan shows significant increase both in carbonates species and potassium after the catalytic use. This is very similar to post electrochemical analysis mentioned in previous sections.

To check the effect of the electrode thickness on water oxidation 12 hours 10 mA CP experiment was carried along with series resistance measurement. Data is shown in Figure 3.83 and Table 3.13.

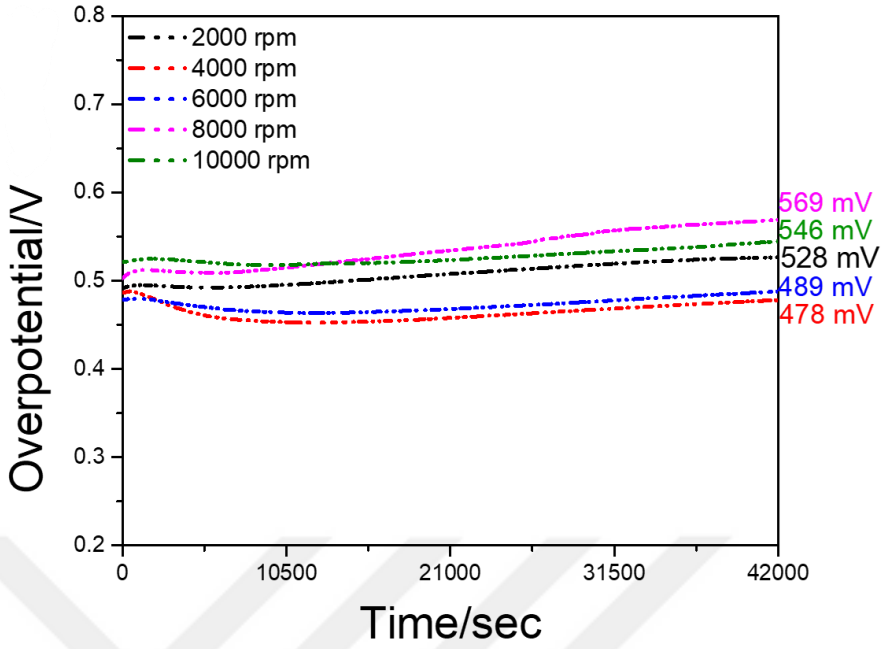

Figure 3.83. 12 hours 10 mA CP of the m-NiO electrodes, prepared at different spin rates and calcined at 350 ºC.

Table 3.13. Series resistance of the m-NiO electrodes, prepared at different spin rates and calcined at 350 ºC before and after 12 hours 10 mA CP.

Coating Rate	Resistance (ohm) Before CP	Resistance (ohm) After CP
2000 rpm	11.75	11.91
4000 rpm	12.30	12.53
6000 rpm	11.38	11.75
8000 rpm	11.53	13.02
1000 rpm	11.75	12.30

The 4000- and 6000-rpm electrodes show the lowest overpotential around 480 mV while the thinnest 10000-rpm electrode has an overpotential of 550 mV. As for the resistance values, all of the numbers are comparable and are around 11-12 ohms. As a

general trend, the resistance increases after the catalytic use due to decomposition of electrode on the FTO surface.

SEM images representing thickness of the m-NiO prepared at different spin rates are shown in the Figure 3.84.

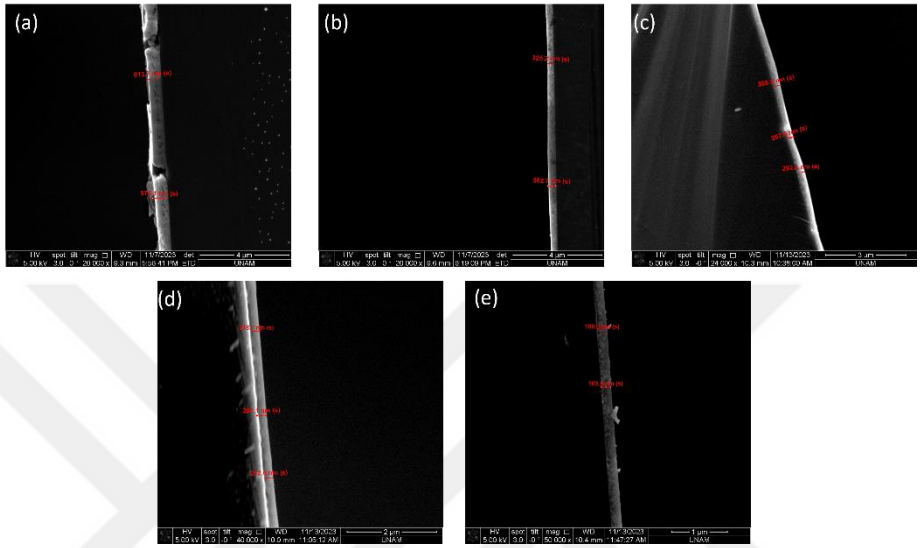

Figure 3.84. SEM images of the m-NiO electrodes, prepared at different spin rates and calcined at 350 ^{o}C (a) 2000 rpm (4 µm), (b) 4000 rpm (4 µm), (c) 6000 rpm (3 µm), (d) 8000 rpm (2 µm), (e) 10000 rpm (1 µm).

The thickness of the nickel oxide electrodes, prepared at 2000, 4000, 6000, 8000 and 10000 rpm spin rates are approximately 600, 350, 300, 200, and 150 nm, respectively. However, thickness of the electrode does not dictate the electrochemical performance as only very top surface of particular thickness is involved in catalytic use. As shown in schematics below (Figure 3.86), the active surface is more or the less the same for all spin rates and it is reflected in the cyclic voltammograms, also provided below. Note that the dark green color represents the active surface of the electrodes.

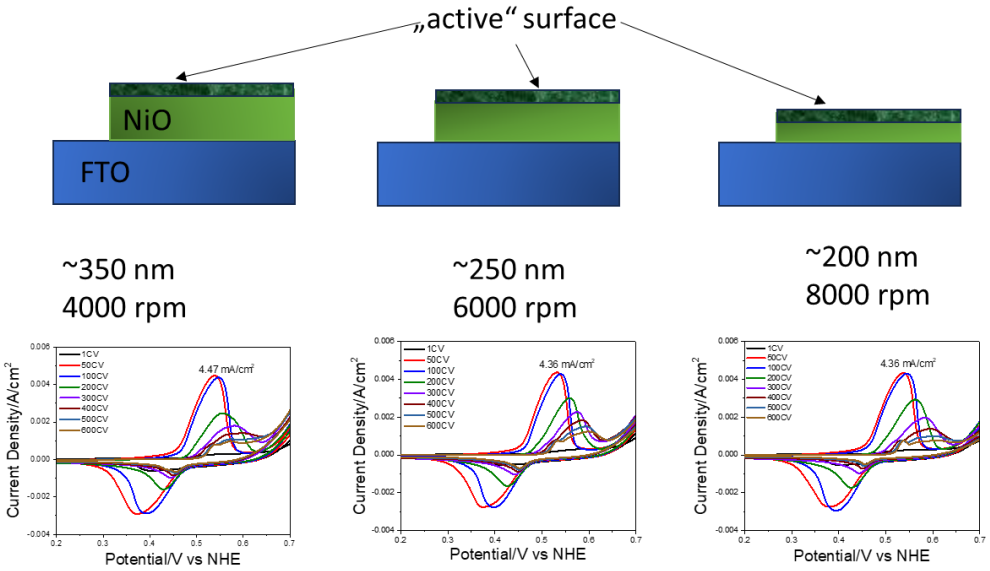

Figure 3.85. Schematic representations of the active surface of the electrodes, used in electrochemical process (top) and corresponding cyclic voltammograms showing the same current density of the m-NiO electrodes, prepared at different spin rates and calcined at 350 ^{o}C.

Note that manganese is a quite abundant and not toxic transition metal. Introducing Mn to NiO may have many advantages. First of all, the NiO content will be reduced, and manganese along with nickelis more active (due to the synergic effect) in the water oxidation process. Ni is more electronegative than Mn, so bringing together, the manganese sites become more electropositive, which helps to attract hydroxide ions from the electrolyte and makes water oxidation more efficient. From the mechanism suggested below (see Figure 3.86), nucleophilic hydroxide ion attacks to the electrochemically produced metal-oxygen double bond (M=O, metal oxo bond) to form oxygen-oxygen bond [44]. In steps 2, 3, 6 and 8 H_3O^+ is produced [44]. Oxidation of the metal sides produces the electrons in steps 2, 4, 6, and 7. The metal oxo bond is formed in step 1, superoxide in step 5, and oxygen in step 8 [44]. That mechanism was suggested for spinel metal cobaltites, but it as well applicable for the nickel manganese binary oxides [44].

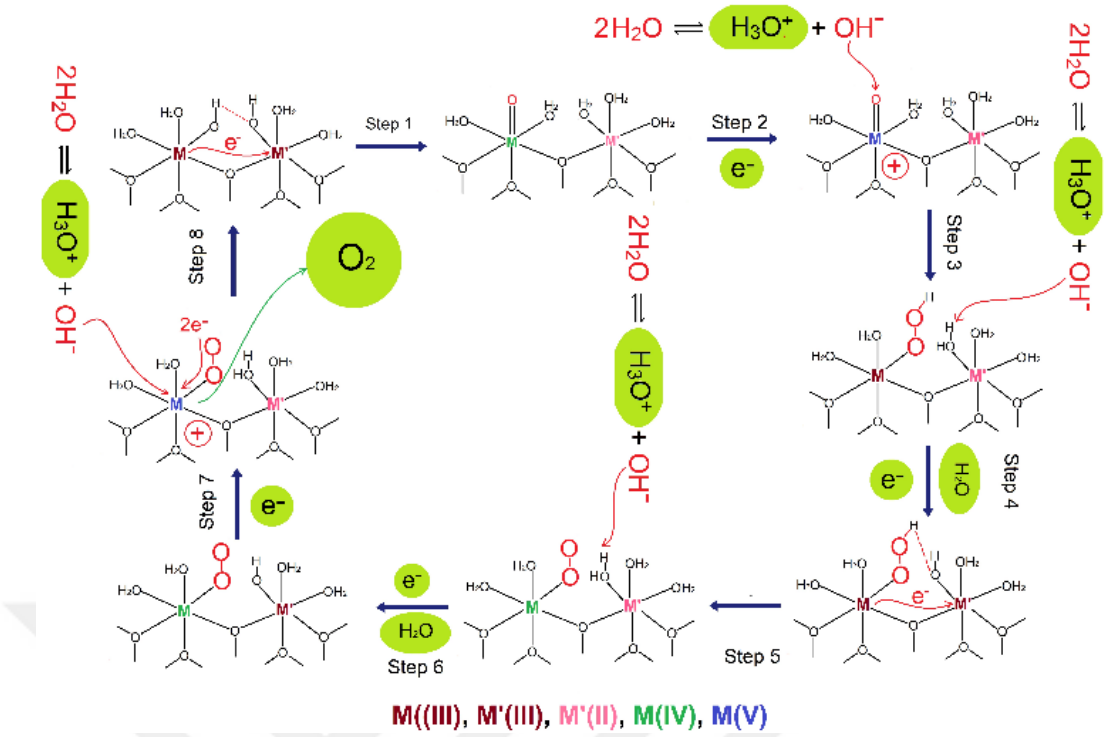

Figure 3.86. Suggested eight-step OER mechanism for binary transition metal oxide electrodes[44]. *Reprinted (adapted) with permission from [44] Copyright 2021 American Chemical Society.*

All the electrodes were prepared at 2000 rpm and the GCD and XPS analysis have been carried. The GCD data of these electrodes are shown in Figures 3.87 and 3.88.

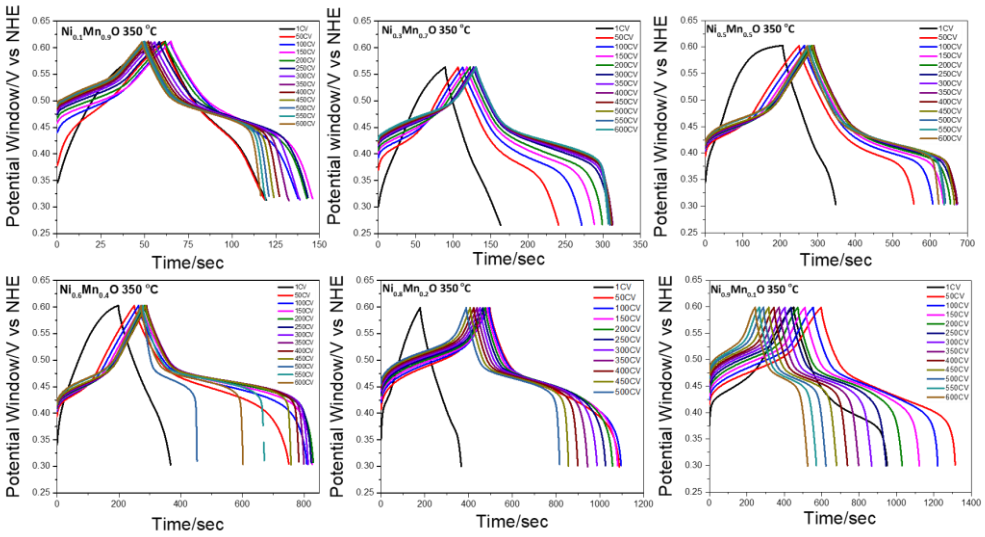

Figure 3.87. GCDs after each 50 cycles (from 1st to 600th CVs) at 0.1 mA/cm^2 current density of the $Ni_{1-x}Mn_xO$ binary electrodes, calcined at 350 °C (compositions are given in each panel).

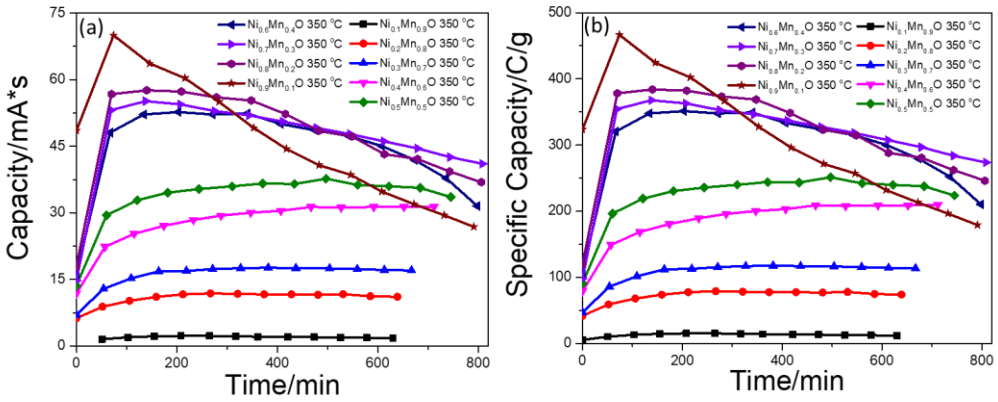

Figure 3.88. (a) Capacity vs time and (b) specific capacity vs time plots of the $Ni_{1-x}Mn_xO$ binary electrodes, calcined at 350 ^oC (compositions are given in each panel).

Capacity and specific capacity values of the binary oxides are very different and depends on the Ni to Mn ratio. In general, the Ni-rich oxides show the highest capacity values, but those electrodes are unstable and lose their charge storage capacities. On the other hand, Mn rich electrodes show low-capacity values, but they are more stable within consecutive cycling and do not lose their charge storage capacity quickly. For instance, the $Ni_{0.9}Mn_{0.1}O$ electrode, after 50th (about 60 mins) cycle shows the highest capacity of 70 mA*s then it drops to 29 mA*s after 800 mins. It should be noted that these values are higher than pure NiO (see Figure 3.53), so introducing manganese is improving the capacitive properties of the NiO based electrodes. For the $Ni_{0.5}Mn_{0.5}O$ electrode, initial capacity is quite low, and provides 12 mA*s but after 700 minutes the capacity reaches 35 mA* s that is higher compared to the $Ni_{0.9}Mn_{0.1}O$ electrode. Also, the capacity values remain stable for almost the whole time in the case of $Ni_{0.5}Mn_{0.5}O$. Since the catalytic load is 0.15 mg, the capacity values are converted into specific capacity values, following the same trend as capacity values.

Every charge-discharge scan was followed by cyclic voltammetry measurements, similar to the NiO electrodes. The CVs from -0.1 to 1.15 V and from 0.2 – 0.7 V (at a scan rate of 5 mV/s) are shown in Figures 3.89 and 3.90, respectively.

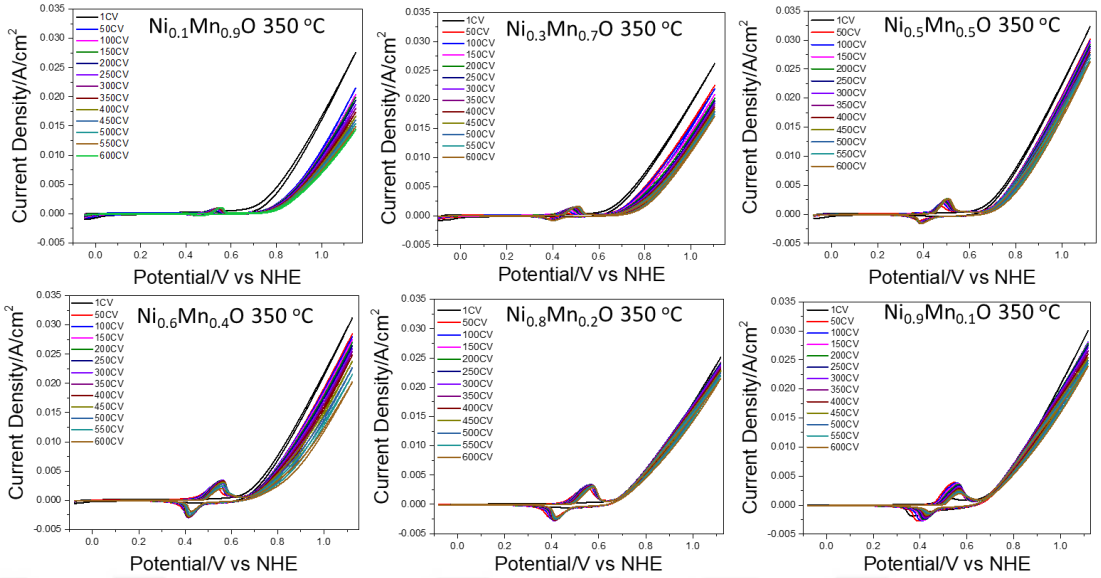

Figure 3.89. CV curves (from 1st to 600th CVs each 50 cycles) at 5 mV/s scan rate of the $Ni_{1-x}Mn_xO$ binary electrodes, calcined at 350 °C (compositions are given in each panel).

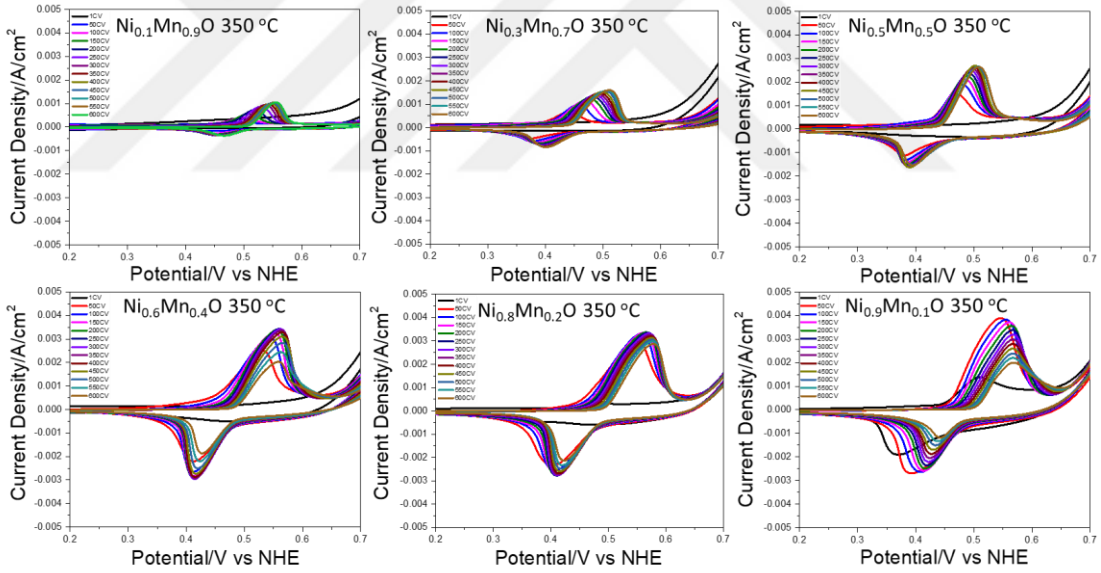

Figure 3.90. CV curves (in the 0.2 – 0.7 V window) of each 50 cycles (from 1st to 600th CVs) at 5 mV/s scan rate of the $Ni_{1-x}Mn_xO$ binary electrodes, calcined at 350 °C.

Initially, all the electrodes show reasonable water oxidation, but after 50 cycles, the picture starts to change as they all lose their OER performance. The $Ni_{0.9}Mn_{0.1}O$ electrode, at 1.15 V potential, in the 1st CV has a 27 mA/cm^2 current density, but drops to half after 600th CV. The $Ni_{0.5}Mn_{0.5}O$ is better in term of water oxidation and it has a current density of 32 and 26 mA/cm^2 in the 1st and 600th cycles, respectively. The

manganese-rich $Ni_{0.1}Mn_{0.9}O$ electrode also shows good electrocatalytic performance with a peak current density of 30 mA/cm^2 that drops slightly at the end of the cycles.

In the low manganese content, the $Ni_{1-x}Mn_xO$ electrode does not show any oxidation or reduction peaks in their first CVs, meaning that the surface is covered by metal oxide ($Ni_{1-x}Mn_xO$) species, after cycling, the typical $Ni(OH)_2$ oxidation and reduction peaks appear and enhance with each cycle. This process occurs due to the manganese disproportionation reaction. Electrochemically, manganese oxide eventually is removed to some extent from the electrode surface exposing NiO rich surface that transforms to $Ni(OH)_2$ and makes the oxidation and reduction peaks more prominent. Higher the oxidation and reduction peak current densities, higher the capacity of the electrodes. The oxidation peak current follows the same trend in the capacity values.

For further analysis, the XPS spectra were recorded using these electrodes before and after GCD experiment. Ni 2p and Mn 2p spectra are shown in Figure 3.91.

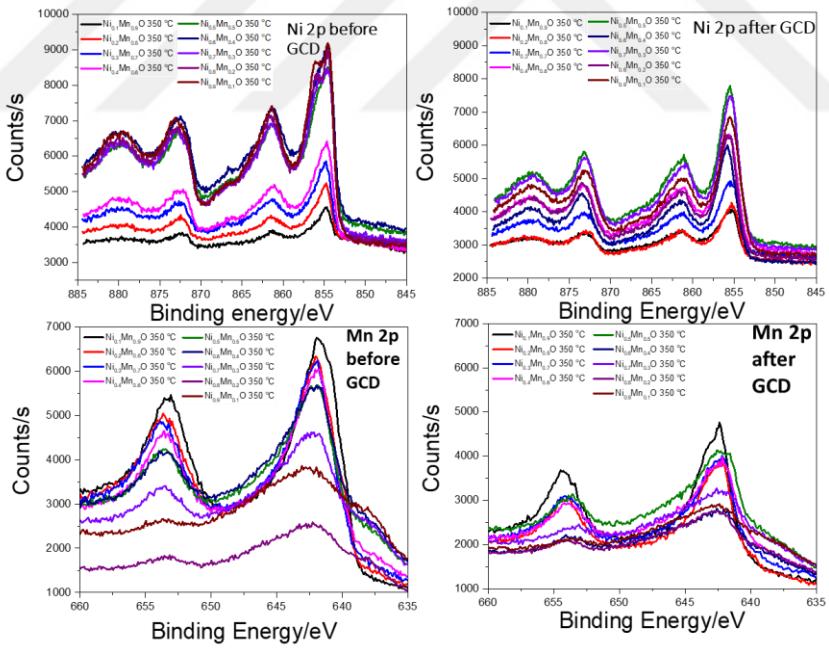

Figure 3.91. Ni 2p (top) and Mn 2p (bottom) regions of the $Ni_{1-x}Mn_xO$ electrodes, calcined at 350 ^oC, before and after GCD experiment.

The Ni 2p region, before the GCD experiment, shows a typical NiO spectrum, where the high energy peak belongs to hydroxides and oxyhydroxides, while the low energy peaks belong to core NiO. After the GCD experiment, surface of the electrode changes, as low energy peak disappears completely in all samples, and new peak at high

energy appears, that could be assigned to $Ni(OH)_2$ and NiOOH. Intensity of the peaks is related to the concentration of Ni species in the sample, and it follows the same trend after the GCD experiment. In the Mn 2p region, before GCD, the peaks have high intensity and wide shoulders, especially when the concentration of manganese is low. That is due to different oxidation states of manganese species. After the usage, the amount of manganese significantly drops, supporting the CV data, and some shoulders disappear that probably due to manganese disproportionation reaction and remaining surface manganese species change their oxidation state. A clearer picture is shown in the Mn 3s region in Figure 3.92.

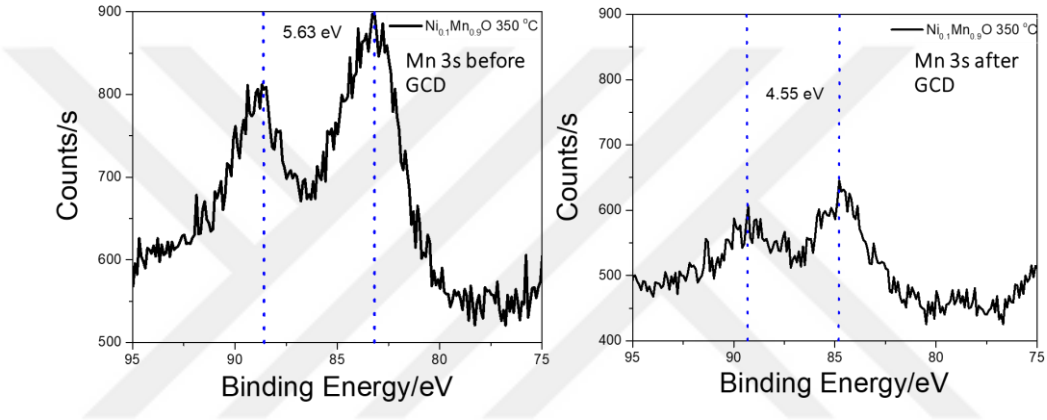

Figure 3.92. Mn 3s scan of the $Ni_{0.1}Mn_{0.9}O$ 350 ºC electrode before and after GCD.

The Mn 3s splitting is very useful in determining the oxidation state of the manganese oxide species. That is similar to the electrochemical analysis that has been discussed in previous sections. Before GCD experiment, manganese is in +3 oxidation state as peak separation is around 5.63 eV. After GCD, this value drops to 4.55 eV and indicates that the surface Mn species change their oxidation state to +4. That once more confirms the disproportionation reaction of the manganese; the Mn(III) disproportionate into Mn(II) and Mn(IV) and Mn(VI) to Mn(IV) and Mn(VII)[72].

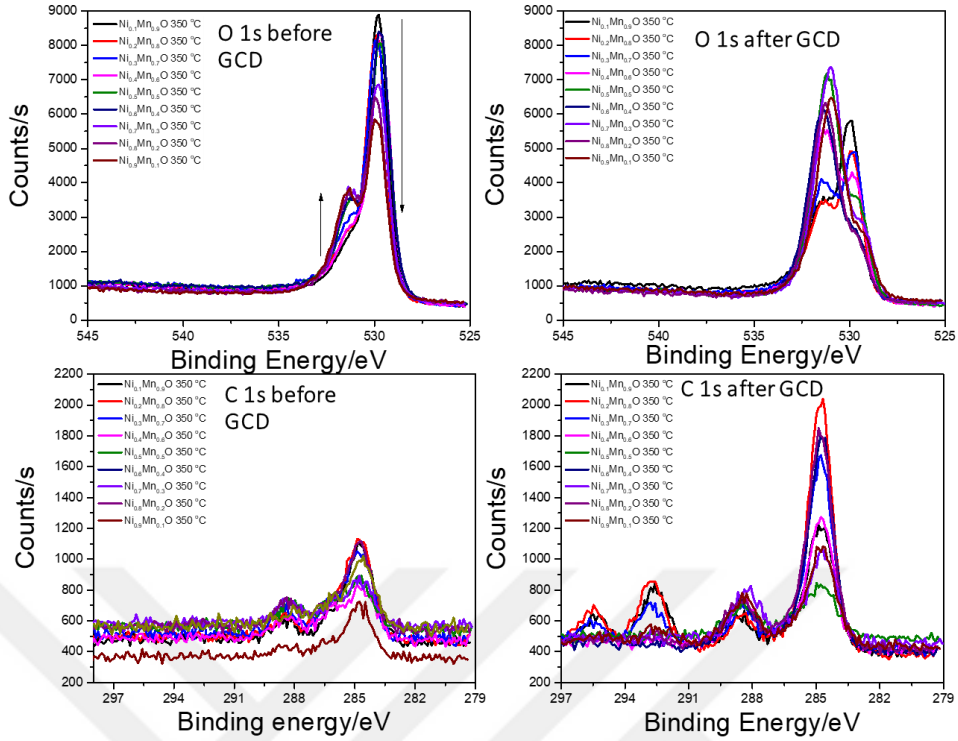

Figure 3.93. O 1s (top) and C 1s (bottom, also shows the K 2p region) spectra of the $Ni_{1-x}Mn_xO$ electrodes, calcined at 350 ^oC before and after GCD.

O 1s spectra are also valuable, as it provides more details regarding the transformation on top of the electrode surface. Before electrode were exposed to electrolysis, the O 1s region around 530 eV splits into two peaks. The higher the manganese concentration, the less intense the shoulder peaks at higher binding energies. If the oxide is Nickel-rich, the splitting is more visible. After GCD experiments, the high energy peak enhances in intensity in the Ni-rich sample, but it remains weaker in the Mn-rich oxides. The low energy peak is weak in the case of Ni-rich oxides, while in the case of Mn-rich oxides they are quite intense. Again, this observation supports the CV data. With increasing Ni concentration, the amount of $Ni(OH)_2$ species also increase that is reflected in the oxidation peaks in the CVs and high energy peaks in the XPS spectra. Also, addition of manganese inhibits the formation of $Ni(OH)_2$/NiOOH species.

As shown in the C 1s spectra, the carbonate peak enhances after the GCD experiment. We did not observe the same behavior in the pure NiO spectrum. In the presence of more Mn in the sample, more carbonates are produced. There are some

additional peaks in the C1 s region and do not belong to any carbon species, so those peaks are assigned to potassium species. K 2 p scan is shown in Figure 3.94.

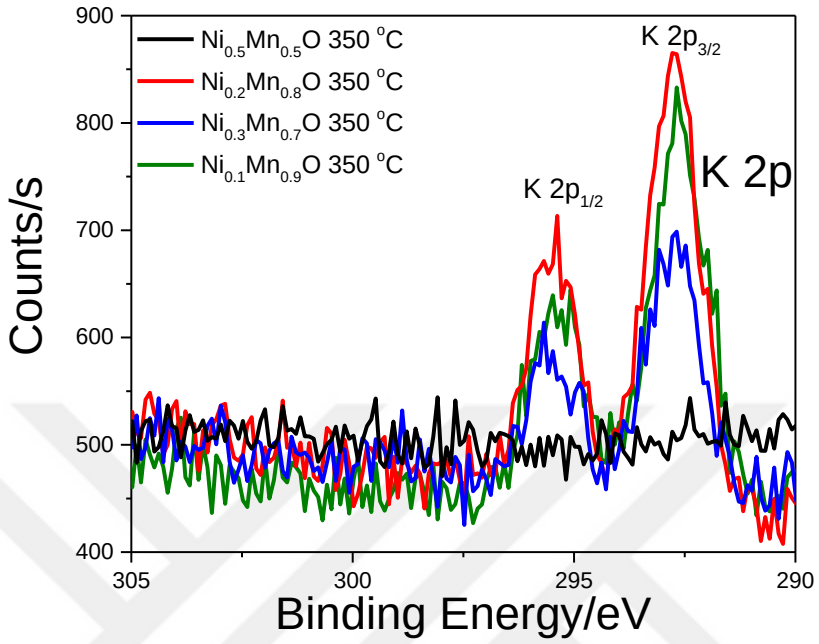

Figure 3.94. K 2p region of the m-$Ni_{1-x}Mn_xO$ electrodes, calcined 350 °C after GCD.

No matter how long the electrode is washed after the usage, it is hard to get rid of the potassium ions in the samples. More manganese is present in the electrode, more potassium contaminates the surface. There must be a good reason for that; no potassium (very little) is observed in the pure NiO sample. It must be again related with the manganese disproportionation reaction. Oxidation of Mn_3O_4 may produce KMn_2O_4, species on the surface of the electrode. All the compositions are annealed at 500 °C and analyzed in an identical way. The reason of choosing 500 °C is that a phase separation occurs, and the binary phase is no longer stable, it is rather a mixture of different phases like NiO, Mn_3O_4 and $NiMnO_3$ (see XRD patterns in the previous chapters).

The GCD curves at 0.1 mA/cm^2 current density, capacity and specific capacity versus time plots are shown in Figures 3.95 and 3.96.

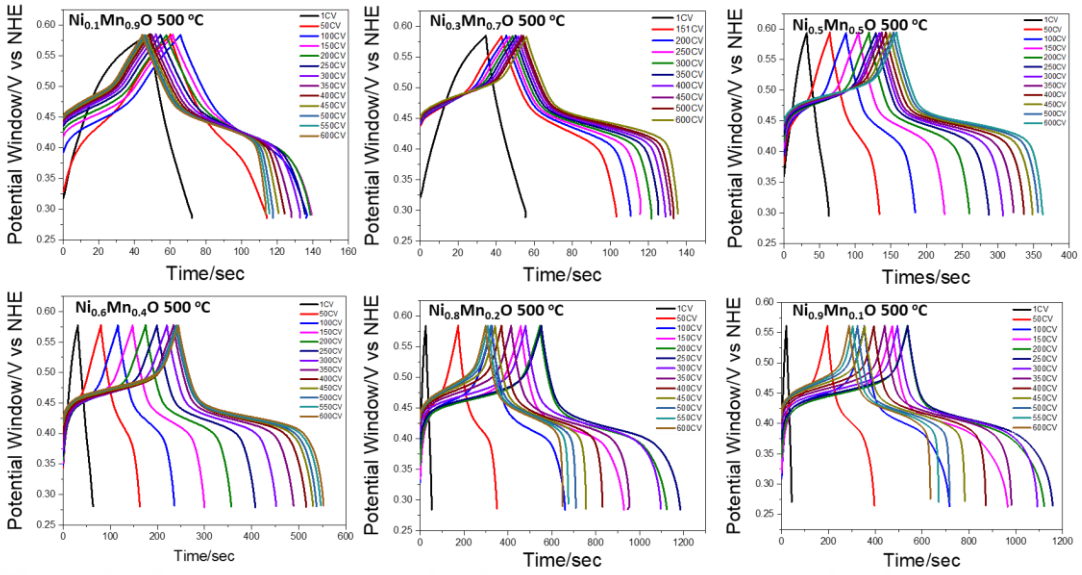

Figure 3.95. GCD curves after each 50 CV cycles (from 1st to 600th CVs) at 0.1 mA/cm^2 current density of the $Ni_{1-x}Mn_xO$ binary electrodes, calcined at 500 °C.

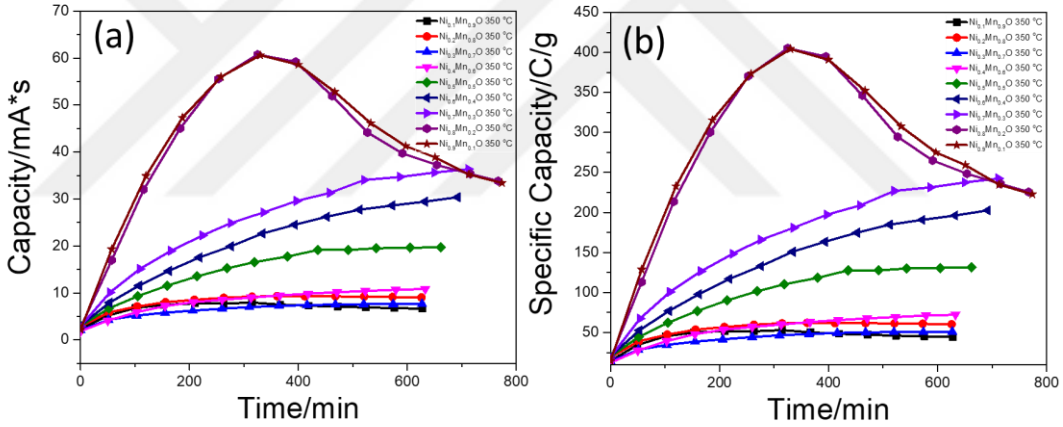

Figure 3.96. (a) Capacity vs time and (b) specific capacity vs time plots of the $Ni_{1-x}Mn_xO$ binary electrodes, calcined at 500 °C.

Initially, the capacity is very low compared to the 350 °C calcined electrodes, due to low surface area and high crystallinity of the samples. The $Ni_{0.1}Mn_{0.9}O$ and $Ni_{0.2}Mn_{0.8}O$ electrodes reach their maximum capacity of 62 mC after 300 minutes, then it drops to 35 mC after 800 minutes. The other electrodes follow the same trend, higher the nickel in the electrodes higher the capacity values, but more manganese brings more stability. The specific capacity (C/g) assuming catalytic load of 0.15 mg follow the same trend as of the capacity plot.

The CVs (Figure 3.97) show that the water oxidation region stays constant compared to electrodes calcined at 350 °C, though the peak current densities are not

high at 1.15 V. That can be attributed to a better crystallinity of the 500 ^{o}C annealed electrodes. The values in the 1st and 600th cycles at 1.15 V are as follow: current density of the 350 and 500 ^{o}C annealed electrodes of $Ni_{0.1}Mn_{0.9}O$ are 30 and 21 mA/cm^2, respectively. Those are 21 and 19 mA/cm^2 for the $Ni_{0.5}Mn_{0.5}O$ electrodes, and 23 and 21 mA/cm^2 for the $Ni_{0.9}Mn_{0.1}O$ electrodes, respectively. Interestingly, all values are silimar in electrodes calcined at 500 ^{o}C. Moreover, these electrodes are more robust and do not decompose easily during electrochemical experiment.

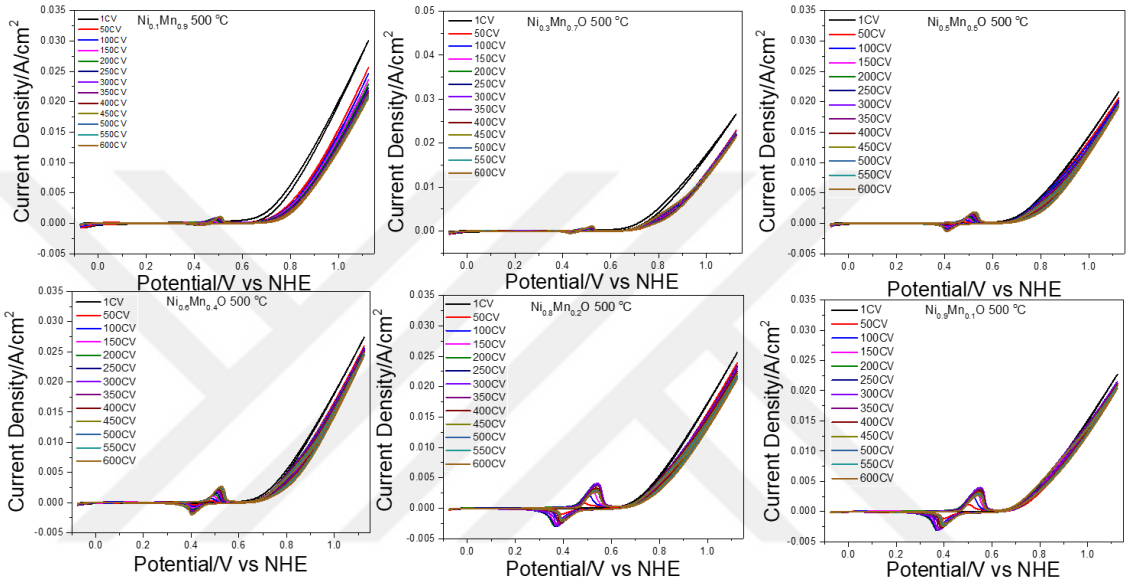

Figure 3.97. CV curves (each 50 cycles from 1st to 600th CVs) at 5 mV/s scan rate of the $Ni_{1-x}Mn_xO$ binary electrodes, calcined at 500 ^{o}C.

Figure 3.97 shows the cyclic voltammograms, but between 0.2 and 0.6 V potential window. The peak currents do mimic the capacity values, higher the peak current density, higher the capacity of the electrode. The intense oxidation peak around 0.5 V splits into two broad peaks.

The XPS analysis before and after GCD experiment has been done and the Ni 2p and Mn 2p spectra are shown in Figure 3.99.

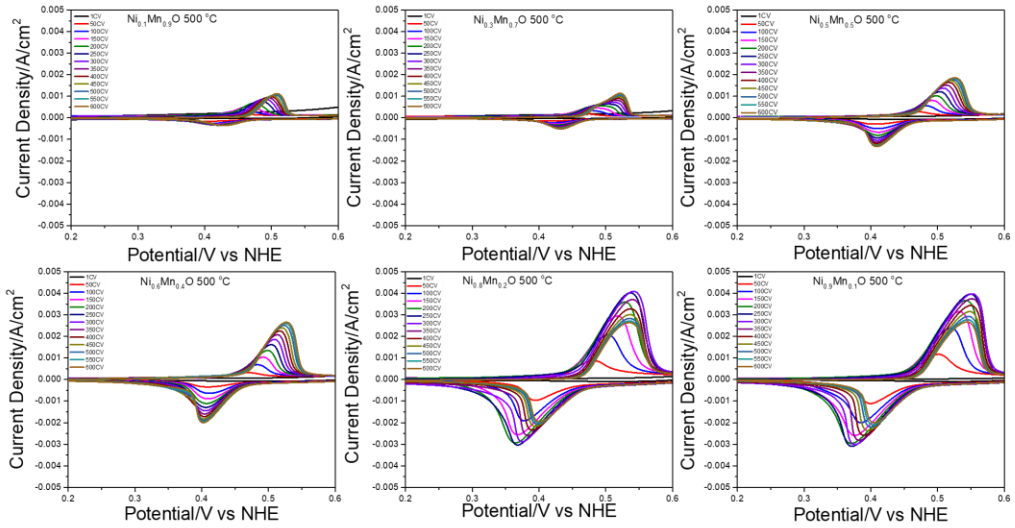

Figure 3.98. CV curves (each 50 cycles from 1st to 600th CVs, 0.2 to 0.6 V) at 5 mV/s scan rate of the $Ni_{1-x}Mn_xO$ binary electrodes, calcined at 500 °C.

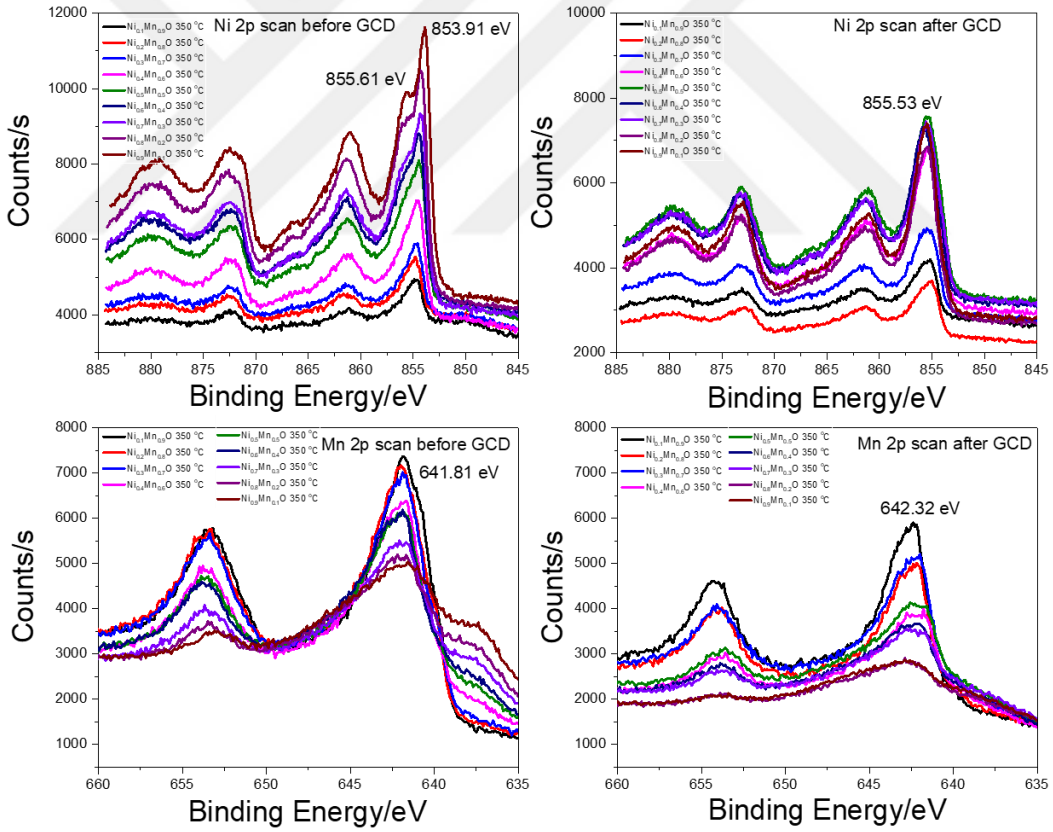

Figure 3.99. Ni 2p (top) and Mn 2p (bottom) spectra of the $Ni_{1-x}Mn_xO$ electrodes, calcined at 500 °C, before and after GCD experiment.

Ni 2p spectra of the $Ni_{1-x}Mn_xO$ electrodes, calcined at 500 °C, before and after GCD are very similar to the electrodes, calcined at 350 °C. Again, the $^2P_{3/2}$ region splits

before the usage and the 855.61 eV peak becomes more dominant after GCD experiment indicating that the surface of the NiO based electrode is covered with nickel hydroxide and nickel oxyhydroxides species. The intensity of the peaks is related with the amount of nickel present in the sample both before and after electrode usage.

In the case of manganese 2p spectra, the amount of manganese is significantly reduced after the usage and the main peak shifts from 641.81 eV to 642.3e eV after GCD experiment, showing the change in oxidation state of Mn^{3+} to Mn^{4+}. Also, the peaks get narrower that also can be due to manganese disproportionation reaction.

Manganese 3s spectra are shown in Figure 3.100. The spectra show the same trend as in the case of 1Ni9Mn 350 ºC sample. Splitting energy of the peaks changes from 5.61 to 4.83 eV, meaning that the Mn^{3+} is oxidized to Mn^{4+}. Amount of manganese is significantly reduced due to disproportionation reaction.

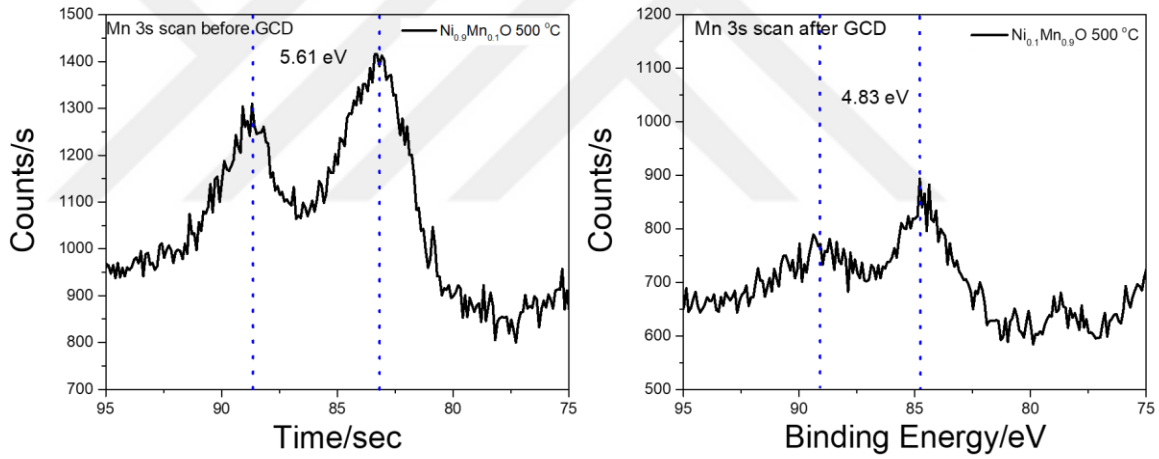

Figure 3.100. Mn 3s spectra of the 1Ni9Mn electrode, calcined at 500 ºC before and after GCD.

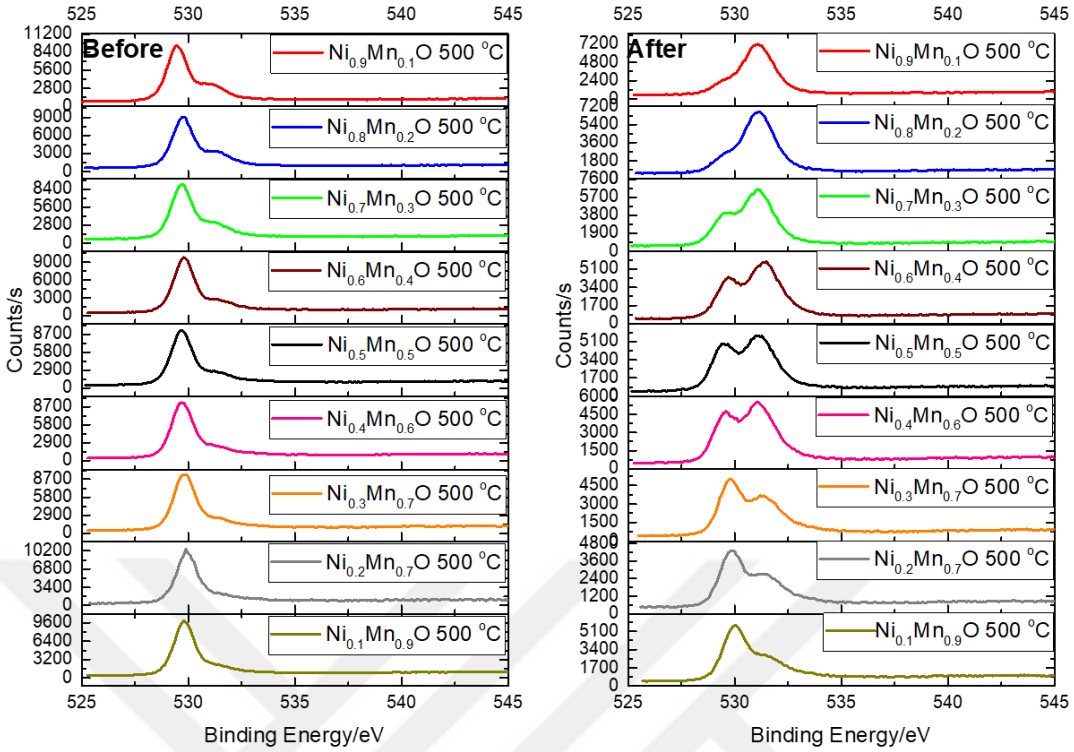

Figure 3.101. O 1s spectra of the $Ni_{1-x}Mn_xO$ electrodes, calcined at 500 °C (a) before and (b) after GCD.

Figure 3.101 shows O 1s spectra of the same electrodes before and after GCD experiment. The amount of manganese in the sample does affect the nickel oxide to nickel hydroxide conversion similarly to the electrodes calcined at 350 °C. In the Ni-rich samples, the high energy peak is more dominant due to presence of the $Ni(OH)_2$/NiOOH species on the surface while the Mn-rich oxides show a peak with a very low intensity in the higher energy side, meaning not much hydroxides are formed on the surface of the electrode.

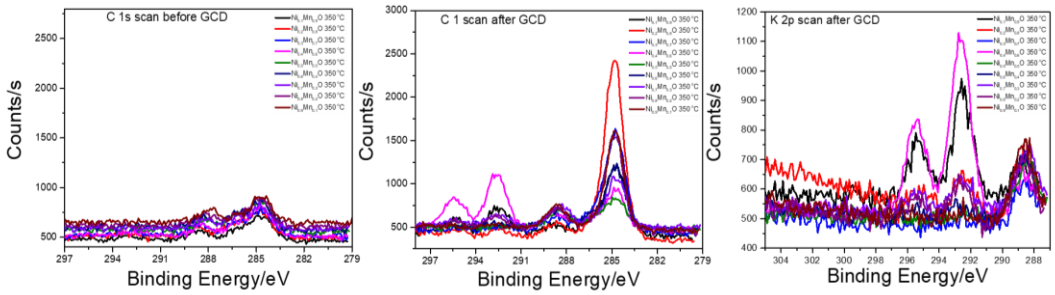

Figure 3.102. C 1s and K 2p spectra of the $Ni_{1-x}Mn_xO$ electrodes, calcined at 500 °C before and after GCD.

The C 1s spectra before and after GCD and K 2p spectra after GCD are shown in Figure 3.102. From the carbon scan, the amount of carbon increases after the GCD experiment. That is probably happening due to CO2 dissolved in the electrolyte solution that ends up as carbonate species on the surface of the electrode.

3.9 Capacitive properties of NiO-based thin film electrodes on Graphite Substrate.

After the charge capacity of the $Ni_{1-x}Mn_xO$ electrodes on FTO was thoroughly analyzed, the three optimized and previously analyzed electrodes, namely G-NiO, G-$Ni_{0.9}Mn_{0.1}O$, and G-$Ni_{0.5}Mn_{0.5}O$, calcined at 350 and 500 ^oC, were also tested for their charge capacities.

Prior to the experiment, the NiO electrode, calcined at 350 ^oC, was exposed to a long GCD experiment without cycling before the measurement. Capacity values are quite low compared to previously reported data, as the electrode needs activation before the GCD measurement. The data is provided in Figure 3.103.

A potential window was determined from the first CV cycle, which does not change the composition of the surface much as the current density is still quite low. Potential window of 0.16 to 0.46 V was chosen to make sure that the water oxidation site is not involved in the capacity measurement. The charge capacity values are tabulated in the Table 3.14.

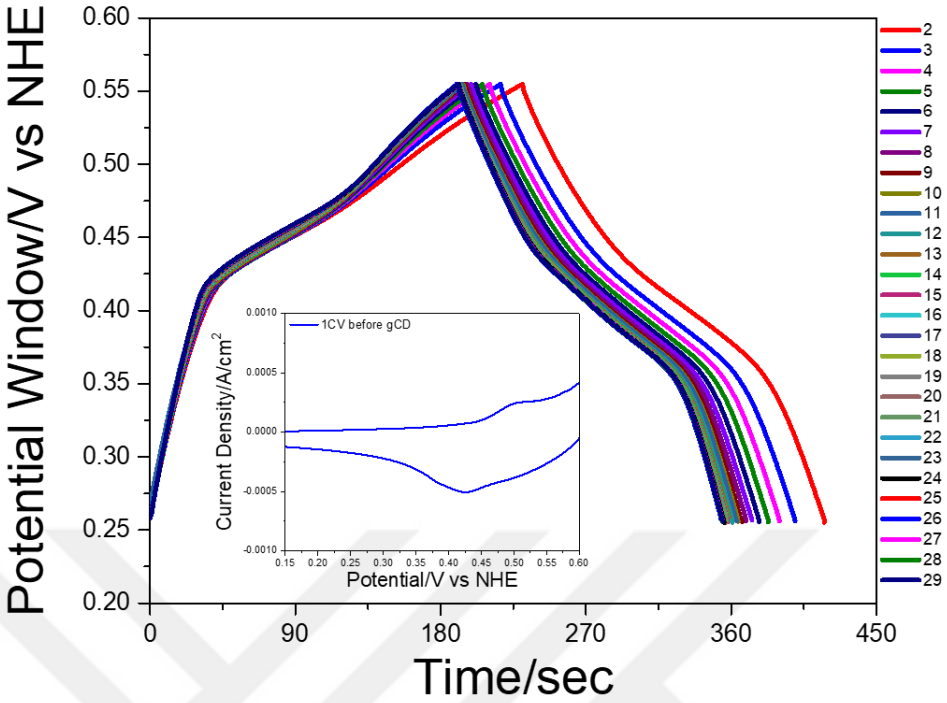

Figure 3.103. GCD curves of the G-NiO (calcined at350 ^{o}C, without "activation") electrode, at a potential window of 0.16-0.46 V and 0.1 mA/cm^2 current density. In inset CV is the 1st CV, given for determination potential window.

Table 3.14. Capacity values of the G-NiO-350 electrode.

Discharge №	NiO 350 ^{o}C Graphite Capacity (mC)	Discharge №	NiO 350 ^{o}C Graphite Capacity (mC)	Discharge №	NiO 350 ^{o}C Graphite Capacity (mC)
1	18.5	11	16.1	21	15.7
2	17.7	12	16.1	22	15.7
3	17.3	13	15.9	23	15.6
4	17.1	14	15.9	24	15.6
5	16.9	15	15.8	25	15.6
6	16.7	16	15.8	26	15.6
7	16.5	17	15.8	27	15.6
8	16.4	18	15.7	28	15.6
9	16.3	19	15.6	29	15.6
10	16.7	20	15.7	30	15.6

As shown in Table 3.14, the charge-capacity values decrease after each GCD cycle, which contradicts with the CV data as, after each cycle, the capacity is supposed

to increase. The reason for that is the cyclic voltammograms are recorded in a wider potential window from -0.2 to 1 V that also includes water oxidation. Water Oxidation enhances the formation of an "active" surface, namely $Ni(OH)_2$/NiOOH, contributing to higher charge capacity values. From now on, the initial cycling is going to be performed on optimized electrodes, 200 CVs, and then charge capacity is going to be measured. 200 CV prior to the GCD experiment of the G-NiO, G- $Ni_{0.9}Mn_{0.1}O$, and G-$Ni_{0.5}Mn_{0.5}O$ electrodes, calcined/annealed at 350 and 500 ^oC, are given in Figure 3.104.

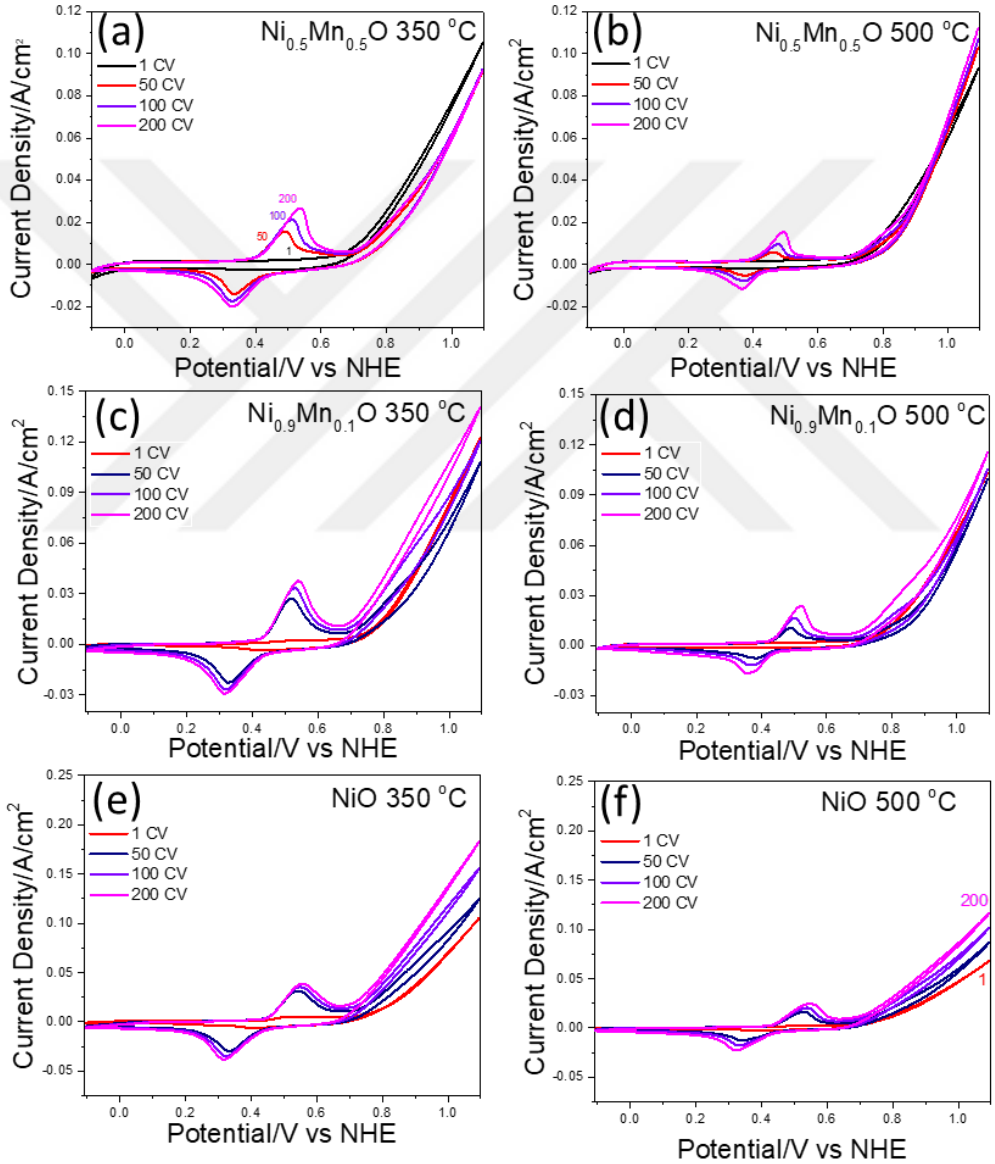

Figure 3.104. Cyclic voltammograms at 50 mV/s scan rate of the (a) G-$Ni_{0.5}Mn_{0.5}O$ 350 ^oC, (b) G-$Ni_{0.5}Mn_{0.5}O$ 500 ^oC, (c) G-$Ni_{0.9}Mn_{0.1}O$ 350 ^oC, (d) G-$Ni_{0.9}Mn_{0.1}O$ 500 ^{o}, (e) G-NiO 350 ^oC and (f) G-NiO 500 ^oC electrodes.

The potential of each electrode was chosen by recording CV at the slow scan of the same electrodes after 200 CVs to make sure that includes the Faradaic reaction ($(Ni(OH)_2 + OH^- \rightarrow NiOOH + H_2O + e^-$). The CVs are shown in the Figure 3.105. Potential window is kept 300 mV for each electrode for the GCD measurements.

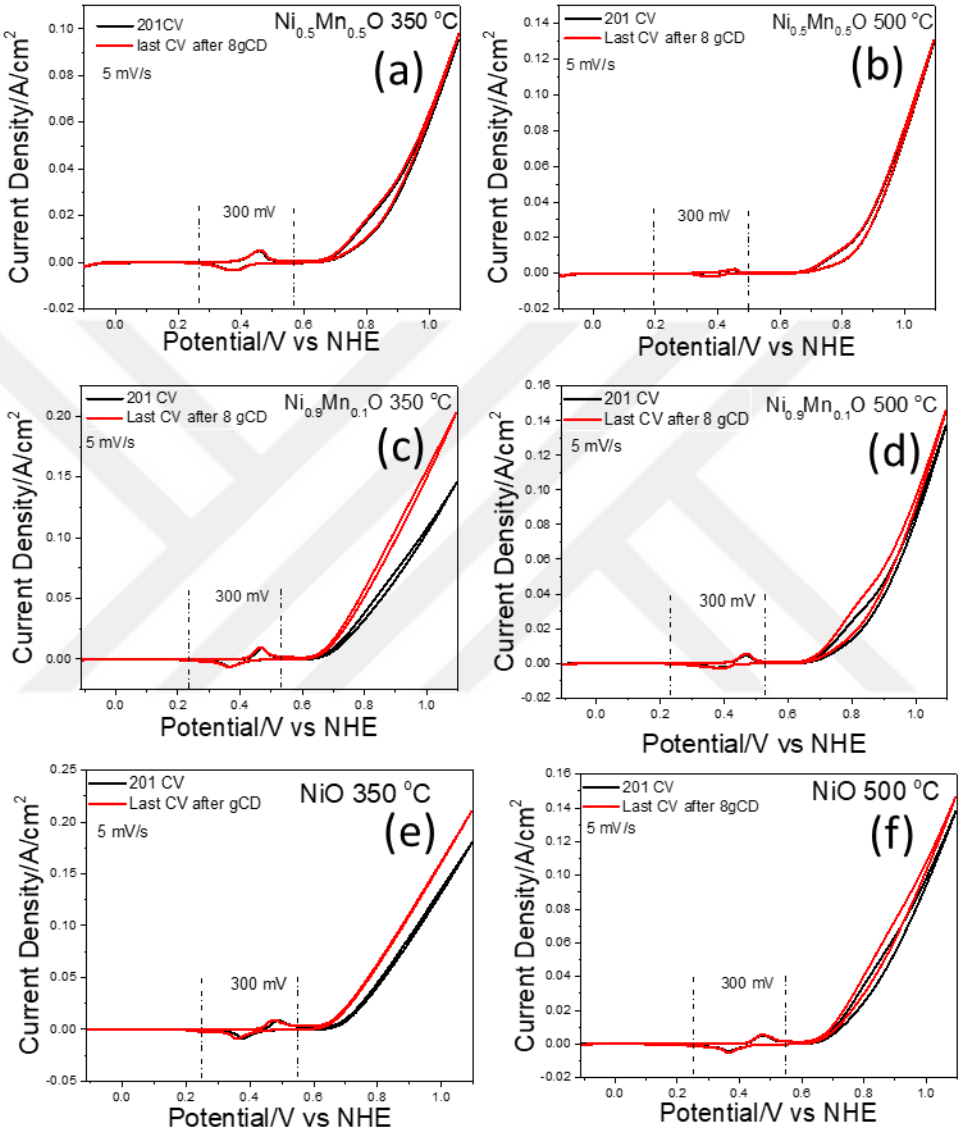

Figure 3.105. Cyclic voltammograms at 5 mV/s scan rate of the (a) G-$Ni_{0.5}Mn_{0.5}O$ 350 °C, (b) G-$Ni_{0.5}Mn_{0.5}O$ 500 °C, (c) G-$Ni_{0.9}Mn_{0.1}O$ 350 °C, (d) G-$Ni_{0.9}Mn_{0.1}O$ 500 °, (e) G-NiO 350 °C and (f) G-NiO 500 °C electrodes with potential window shown in dash for the GCD experiment.

The potential range shown with dashed lines for the G-$Ni_{0.5}Mn_{0.5}O$-350, G-$Ni_{0.9}Mn_{0.1}O$-350, and G-NiO-350 electrodes are, 0.195-0.495, 0.235-0.535, and 0.255-

0.55 V, respectively. It is chosen in a way it does not include high potential water oxidation site that results in overcharging.

Four charge-discharge curves were collected after activation of the surface of the electrode at a current density 0.1 mA/cm^2. The GCD profiles are given in Figure 3.106.

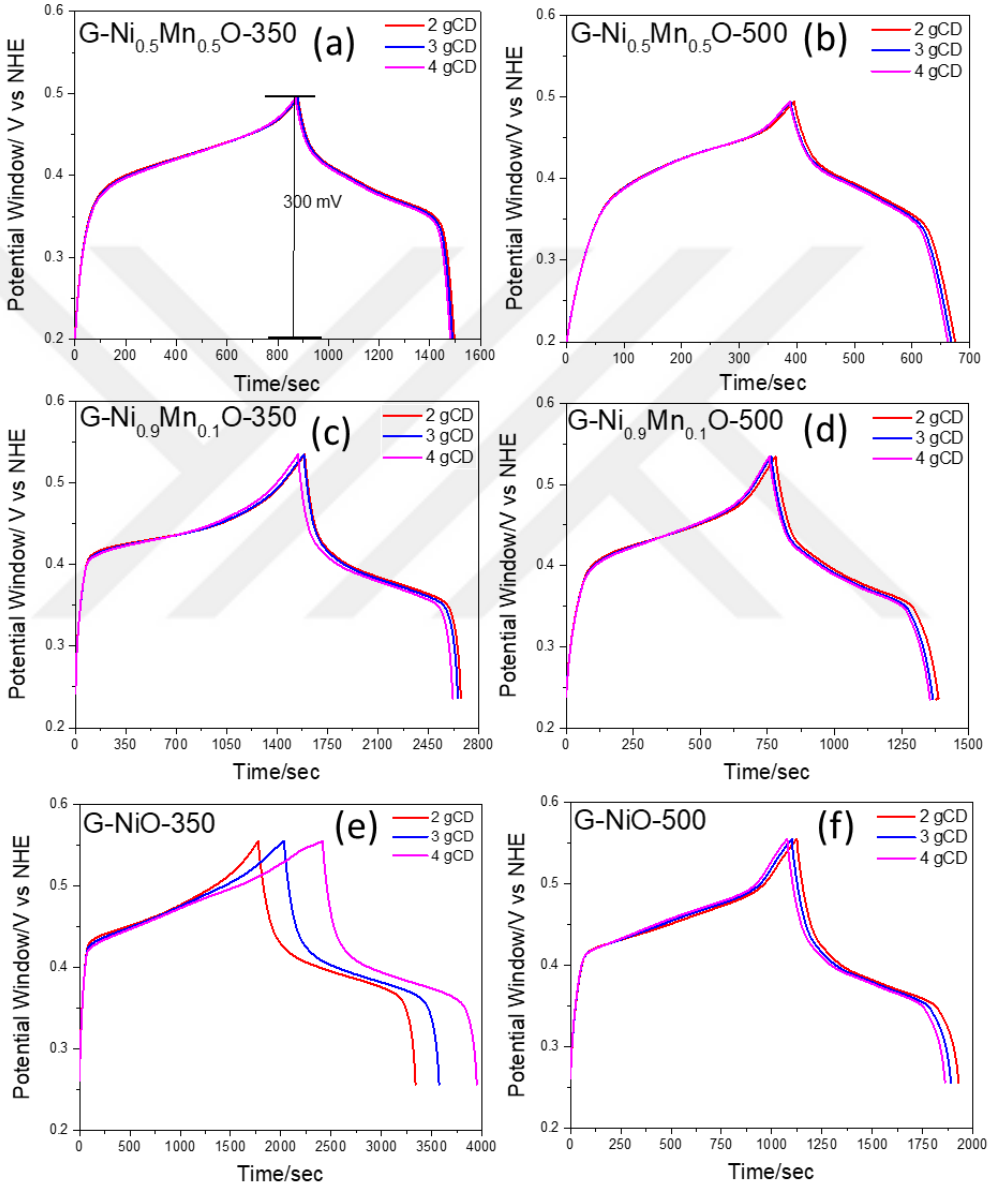

Figure 3.106. The GCD curves in 1M KOH in a 300-mV potential window at a 0.1 mA/cm^2 current density after 200 CVs of the (a) G-$Ni_{0.5}Mn_{0.5}O$-350, (b) G-$Ni_{0.5}Mn_{0.5}O$-500, (c) G-$Ni_{0.9}Mn_{0.1}O$-350, (d) G-$Ni_{0.9}Mn_{0.1}O$-500, (e) G-NiO 350, and (f) G-NiO-500 electrodes.

The GCD curves show that the charge capacity does not change much. There is a plateau around 0.38 V, which is the Faradaic process of converting nickel hydroxide to nickel oxyhydroxides, and it supports cyclic voltammogram data. The capacity values are tabulated in Table 3.15.

Table 3.15. Capacity Values of the G-$Ni_{1-x}Mn_xO$ Binary Electrodes, Calcined at 350 and 500 ºC Collected from the Discharge Curves and Cyclic Voltammograms (MC, Maximum Capacity; SP Specific Capacity; NSC, Normalized Specific Capacity; C, Capacity; *data from GCD; and **from CVs).

Electrode	MC* (mC)	SC* (mC/mg)	NSC (mC/mg)	C** (mC)
G-NiO-350	153.3	948.1	948.1	177.9
G-$Ni_{0.9}Mn_{0.1}O$-350	103.8	648.8	720.8	141.9
G-$Ni_{0.5}Mn_{0.5}O$-350	59.3	370.6	741.3	86.8
G-NiO-500	82.1	513.1	513.1	107.6
G-$Ni_{0.9}Mn_{0.1}O$-500	58.3	364.4	404.9	79.4
G-$Ni_{0.5}Mn_{0.5}O$-500	26.7	166.9	258.8	41.2

Capacity values do not correlate with the CV data because the G-NiO-350 has the highest capacity of 153 mC, while the G-$Ni_{0.9}Mn_{0.1}O$-350 electrode exhibits 103.4 mC. In the CV data, G-$Ni_{0.9}Mn_{0.1}O$-350 shows higher oxidation current density than NiO. That can be explained by the fact that the capacity value is dependent on the area under the CV curve, e.g., charge value, but the oxidation current also depends on the resistance; the lower the resistance, the sharper/higher the oxidation peak current density.

Specific capacity was also determined by dividing the first capacity value by the catalytic load of the electrode. The catalytic load was determined to be 0.16 mg (see experimental section). There is a general trend of decreasing specific capacity with increasing manganese content. Specific capacities of the G-NiO-350. G-$Ni_{0.9}Mn_{0.1}O$-350 and G-$Ni_{0.5}Mn_{0.5}O$-350 electrodes are 948.1, 648.8, and 370.6 mC/mg,

respectively. This is related to $Ni(OH)_2$ surfaces that is formed during the “activation” of the electrode. More nickel hydroxide-rich surface has higher capacity, because the $Ni(OH)_2$ species are layered and ultra-small nanoflakes, where most nickel ions are oxidized and reduced during cycling and therefore have higher charge capacity.

In Table 3.15, there is a charge capacity that is calculated from cycle voltammogram data. The data from the charge capacity calculation collected from CVs are shown in Figure 3.107. This data is higher than collected from GCD data because in GCD experiment, particular potential was set while in CV, all available area under CV curve is included into calculation of the charge-capacity of the G-$Ni_{0.5}Mn_{0.5}$O-500or G-NiO-350, G-$Ni_{0.9}Mn_{0.1}$O-350, G-$Ni_{0.5}Mn_{0.5}$O-350, G-NiO-500 and G-$Ni_{0.9}Mn_{0.1}$O-500 electrodes; the charge capacities collected from CVs are 177.9, 141.9, 86.8, 107.6, 79.4 and 41.2 mC, respectively.

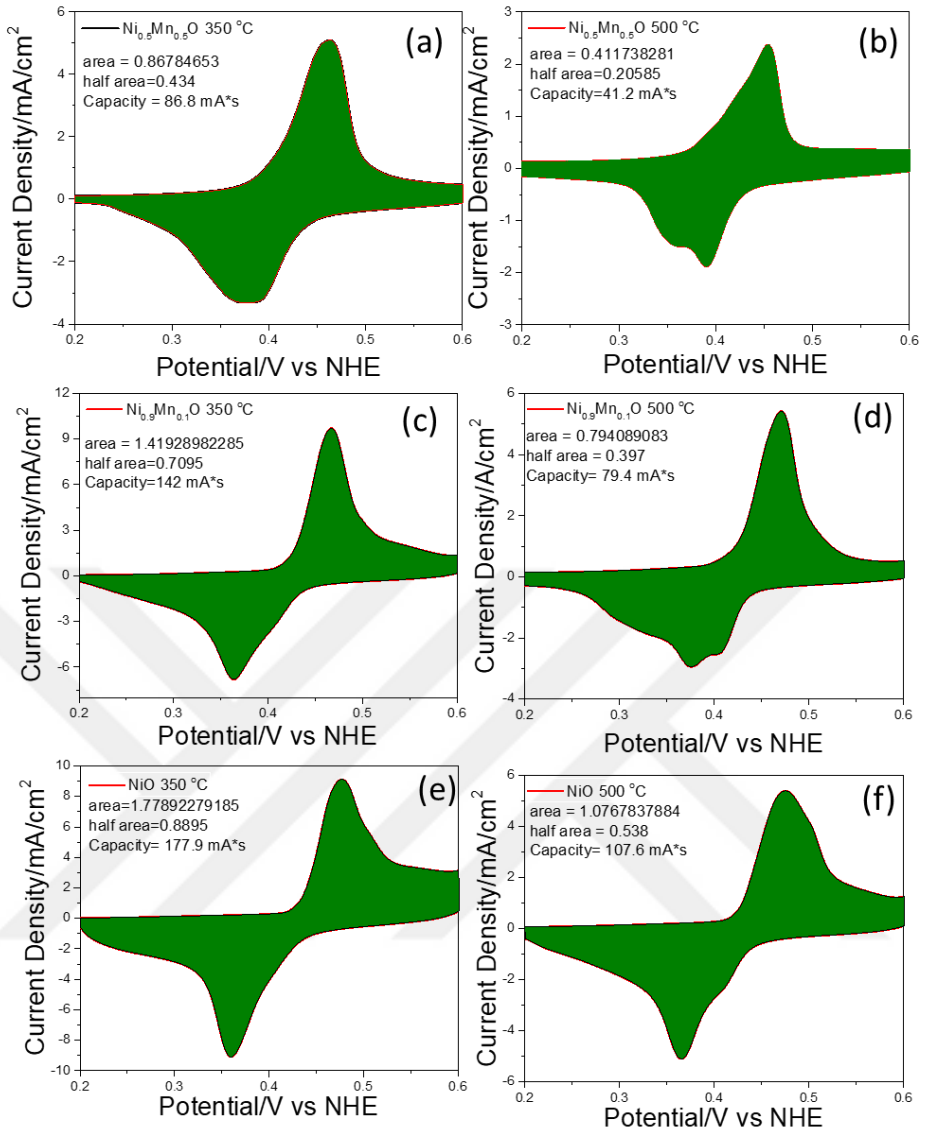

Figure 3.107. 200th cyclic voltammograms at 5 mV/s scan rate of the (a) G-$Ni_{0.5}Mn_{0.5}O$-350, (b) G-$Ni_{0.5}Mn_{0.5}O$-500 , (c) G-$Ni_{0.9}Mn_{0.1}O$-350 , (d) G-$Ni_{0.9}Mn_{0.1}O$-500, (e) G-NiO-350 and (f) G-NiO-500 electrodes between 0.2 to 0.6 V for charge capacity calculation.

Figure 3.107 shows the slow scan CVs (at 5 mV/s) of the G-$Ni_{0.5}Mn_{0.5}O$-500, G-NiO-350, G-$Ni_{0.9}Mn_{0.1}O$-350, G-$Ni_{0.5}Mn_{0.5}O$-350, G-NiO-500 and G-$Ni_{0.9}Mn_{0.1}O$-500 electrodes. The area of the CV curves was calculated using a potential window between 0.2 to 0.6 V. Assuming that the Faradaic reaction mechanism is 1 electron process, the charge capacity was calculated from the area under the CV curves and divided by 2. Charge under the curve was obtained in Coulomb units and that value was converted to mol of the active sites; Data is shown in Table 3.15 above.

Also, from the curves above, we can calculate what percent of the NiO core is converted into $Ni(OH)_2$. The conversion of nickel oxide into nickel hydroxide becomes 45 and 21% in the NiO, calcined at 350 and 500 ^oC, respectively.

The electrodes, calcined at 500 ^oC are more crystalline and possess a lower surface area. However, their capacity values are comparable with the electrodes that are calcined at 350 ^oC. If we consider pure NiO, the surface area at 350 ^oC is 164 m^2/g, while at 500 ^oC, it is only 21 m^2/g, and particle sizes are 4.4 and 27.2 nm, respectively[15], [20]. Charge capacity, however, just decrease from around 153.1 to 82.1 mC/cm^2, see Figure 3.108. Assuming that the NiO particle is spherical and all nickel in nickel hydroxide is accessible for one-electron oxidation, the particle with size 4.4 nm at 350 ^oC forms a 2.4 nm core of nickel oxide with a 2 nm of hydroxide shell. The calculated thickness of $Ni(OH)_2$ shell provides the above-mentioned capacity. It should be noted that the particle size increases from 4.4 nm to 27.2 nm by annealing the NiO from 350 to 500 ^oC, respectively.

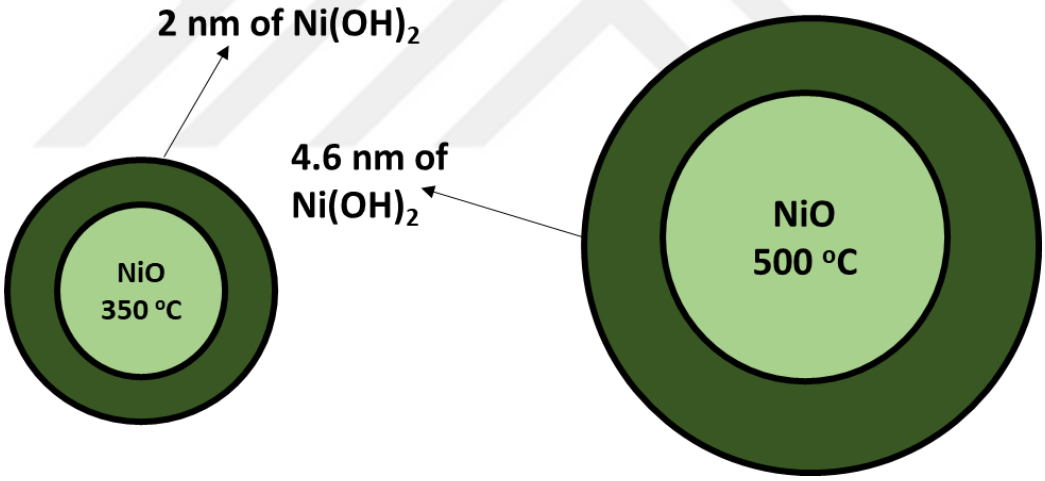

Figure 3.108. Schematic representation of nickel oxide to nickel hydroxide transformation after 600 CVs (NiO core with a $Ni(OH)_2$ shell).

By using the following equation 3.1

$$D' = (1-SC_N/C_T)^{1/3}D \quad \textbf{Equation 3.1}$$

where D' is the core size of the core, D is the nanoparticle size before transformation, SC_N is the normalized specific capacity, C_T is the theoretical specific capacity

The number of nickel hydroxides in the shell is calculated by dividing shell thickness by the unit cell parameter of nickel hydroxide. So, for the electrode calcined at 500 ºC, the core of NiO is 21.6 nm, and the shell of hydroxide is 4.6 nm. So, it can be concluded that the thickness of $Ni(OH)_2$ on top of the NiO core increases with increasing particle size, e.g., calcination temperature.

In the XPS analysis of the graphite electrodes, the post and pre-treatment spectra are similar to FTO electrodes (see previous chapter). In Figure 3.109, Mn 3s and Mn 2p spectra before and after the GCD analysis of the G-$Ni_{0.5}Mn_{0.5}$O-350 electrode are shown.

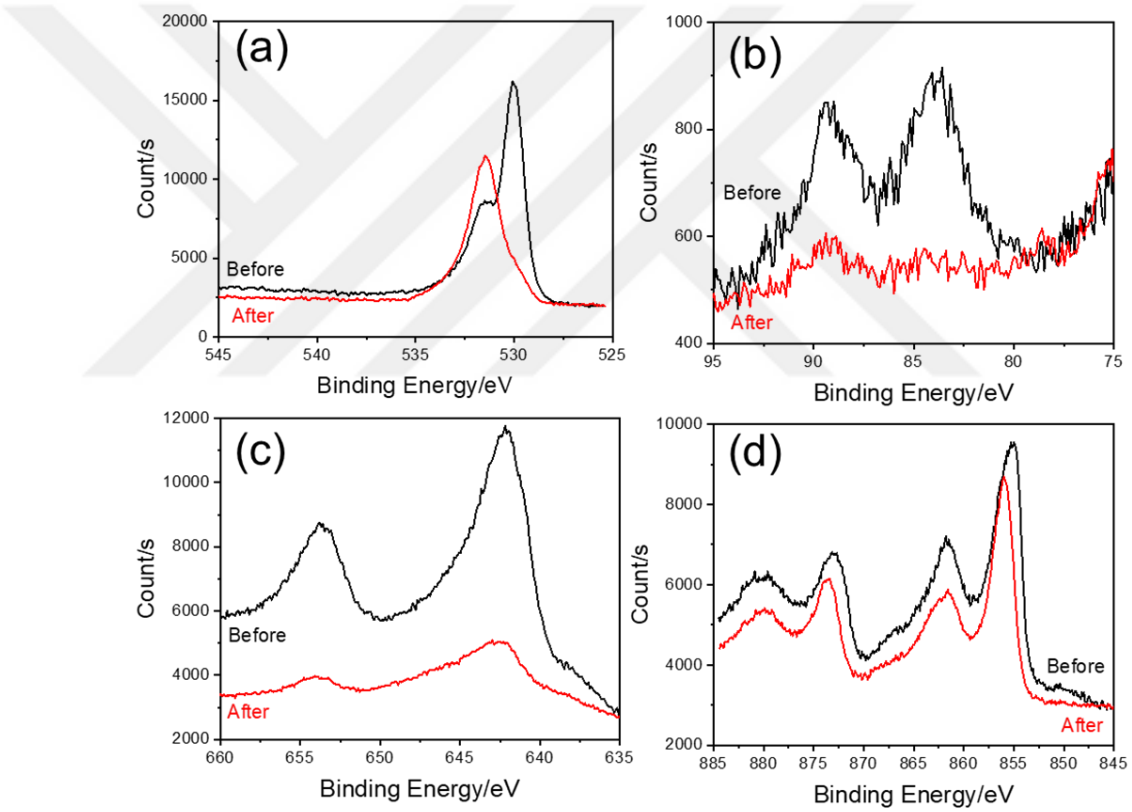

Figure 3.109. XPS spectra (a) O 1s, (b) Mn 3s, (c) Mn 2p, and (d) Ni 2p scans of the G-$Ni_{0.5}Mn_{0.5}$O-350 before and after GCD experiments.

Enhanced O 1s peak (531.2 ev) is a strong indication of the formation $Ni(OH)_2$ species on the surface of the electrode. After the GCD experiment, the amount of Mn is significantly reduced as shown in the Mn 3s and Mn 2p spectra; the Ni 2p scan after

GCD and shift in the binding energy are also consistent with the formation of $Ni(OH)_2$/NiOOH species.

3.10 Structural Characterization of Silica-supported Mesoporous Nickel Oxide Electrodes

As was mentioned in the experimental part, the mesopores silica (m-SiO_2) has been synthesized using nickel nitrate hexahydrate as a catalyst. The m-SiO_2 powder displays diffraction line in the small angle XRD pattern before and after calcination at 450 ^oC, indicating an ordered and porous structure of the silica network. The high angle XRD pattern displays a pattern typical for amorphous silica. Both diffraction patterns are shown in Figure 3.110.

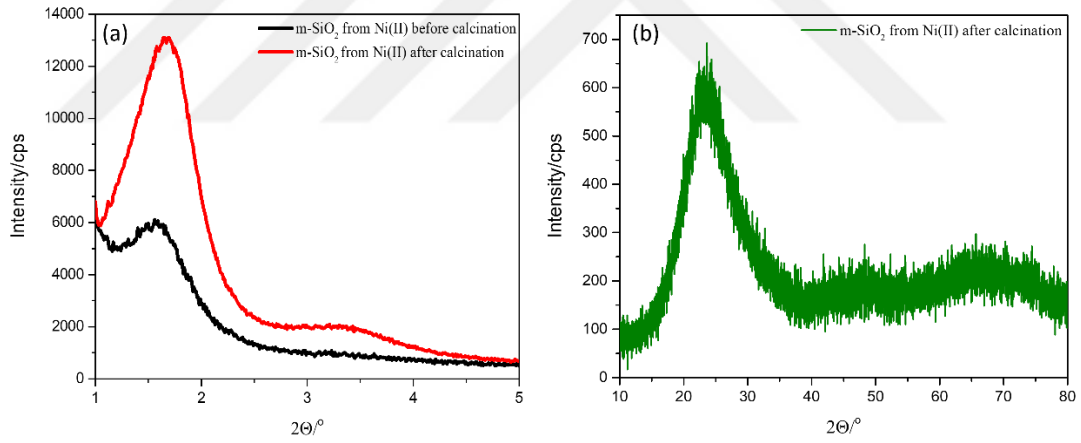

Figure 3.110. (a) Small angle X-ray diffraction patterns of the m-SiO_2 as-prepared (red), and calcined at 450 ^oC (black) and (b) high angle x-ray diffraction pattern of the m-SiO_2 calcined at 450 ^oC.

As prepared samples can be thoroughly washed with ethanol to remove extra surfactant from the pores. The N_2 adsorption-desorption isotherms and pore size distribution plot are given in Figure 3.111. The air-dried mesoporous silica has a high surface area without calcination as depicted from the N_2 adsorption-desorption isotherms.

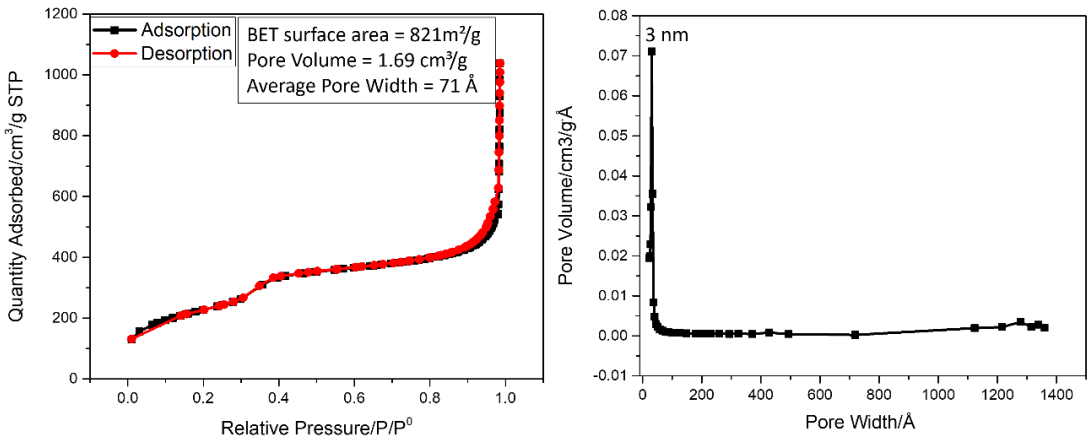

Figure 3.111. N_2(77 K) adsorption-desorption isotherms (left) and pore size distribution plot (right) (obtained from desorption branches) of the as-prepared m-SiO_2.

BET surface area is 821 m^2/g that is almost the same as the calcined samples. So, the calcination temperature does not affect the pore size and pore size distribution in the case of pure silica; pores are quite uniform. Barrett-Joyner-Halenda (BJH) pore-size distribution plot displays a 3 nm wide pore-size.

The mesoporous silica particles can be synthesized by reusing the same filtrate to test its reusability[139]. The filtrates have been reused three times upon filtering the silica and adding only surfactants and silica source. The N_2 adsorption-desorption isotherms and pore size distribution plots of the consecutive use of the filtrate are shown in Figure 3.98. The related data are tabulated in Table 3.112.

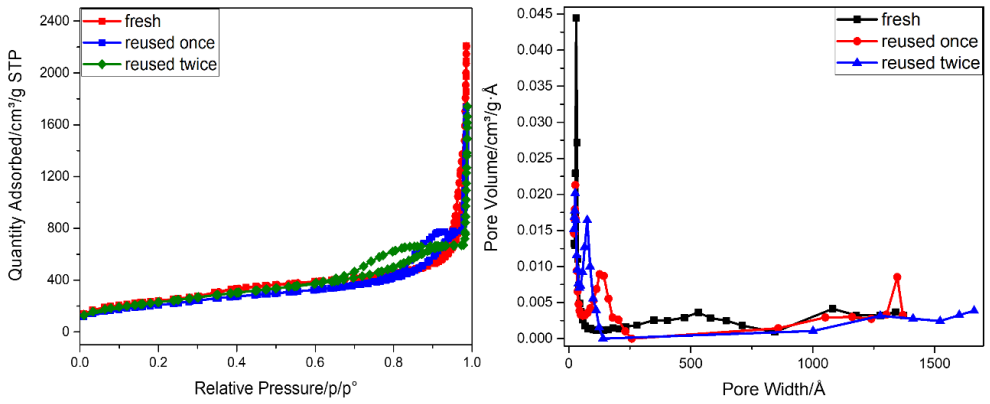

Figure 3.112. N_2(77 K) adsorption-desorption isotherms (left) and pore size distribution plot (right) (obtained from desorption branches) of the m-SiO_2, calcined at 450 °C from fresh and reused filtrates.

Table 3.16. N_2 (77K) adsorption-desorption data of the m-SiO_2, calcined at 450 °C from fresh and reused filtrates.

	BET Surface Area m^2/g	**BJH Desorption cumulative volume of pores cm^3/g**
Fresh	871	3.48
Reused 1	753	2.73
Reused 2	835	2.75

The surface area of the three calcined samples is very similar with similar pore volumes. The only difference is in the pore size distribution plots. They display secondary larger pores that become smaller and more uniform with second and third use. This is due to increasing surfactant amount in the solution; in each reusage, extra surfactant was added into the filtrate. The large pores are due to the pores created by packing ultra-small silica particles. So, it can be concluded that reusing the filtrate by adding more surfactant leads to a more uniform and ordered mesoporous silica particles.

Later, these particles will be used as a hard template for the synthesis of mesopores NiO on graphite and denoted as m-NiO-SiO_2. 5 ml of precursor solution with TMOS was introduced into the nickel nitrate hexahydrate surfactant solution, so the mole ratios of salt to surfactant is adjusted to 10 to 1. This is the original solution, used in all previously synthesized NiO, except in place of ethanol as the solvent, water

was used. Figure 3.113 shows the N_2 adsorption-desorption isotherms (left) and pore size distribution plots (right) (obtained from desorption branches) of the m-NiO-SiO_2 samples, calcined at 450 ^oC. The related data are tabulated in Table 3.14. Three samples were prepared and analyzed. When 5 ml of TMOS containing solution is added to Ni(II) precursor, the electrode was dip coated and calcined at 350 ^oC, so this electrode is denoted as 5 ml as prepared. Another sample was prepared using the same solution by ageing for 1 week to ensure a full polymerization of silica. And the last electrode, NiO electrode was prepared without silica. Along with the electrodes, powder samples were also prepared and their surface area were measured.

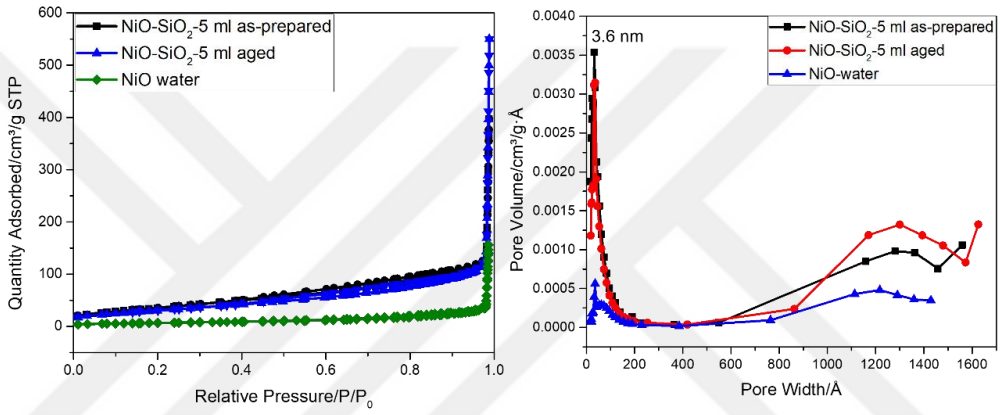

Figure 3.113. N_2(77 K) adsorption-desorption isotherms (left) and pore size distribution plots (right) (obtained from desorption branches) of the m-NiO-SiO_2 (from aged and as-prepared precursor) and m-NiO (prepared from water precursor) samples, calcined at 350 ^oC.

There is no difference in term of surface area of the aged and fresh samples, though it is significantly lower, compared with the pure silica. Note also that the mesoporous NiO, prepared without silica, has a very low surface area and pore volume. However, in all cases, the pore size distribution is quite narrow and varies from 2.6 to 3.3 nm, indicating the pre-formed mesoporous silica remains porous in the m-NiO-SiO_2 samples; the small and uniform pores originate from the m-SiO_2 domains.

Table 3.17. N_2 (77K) adsorption-desorption data of the m-NiO-SiO_2 (from aged and as-prepared precursor solutions) and m-NiO (prepared from water precursor) samples, calcined at 350 ºC.

Sample	BET Surface Area (m^2/g)	BJH Pore Volume (cm^3/g)	BJH Pore Size (nm)
m-NiO-SiO_2 from Fresh Solution	130	0.621	3.6/15
m-NiO-SiO_2 from Aged solution	111	0.855	3.6/24
m-NiO from Water solution	24	0.242	3.5/33

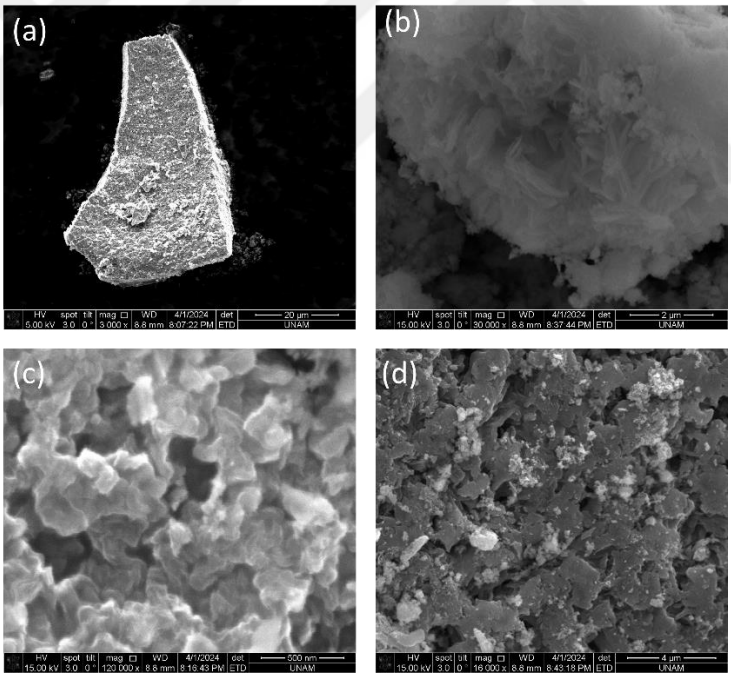

Figure 3.114. SEM images of the drop-casted m-NiO-SiO_2 (prepared from fresh precursor) calcined at 350 ºC. Scale bars are (a) 20 µm, (b) 2 µm, (c) 500 nm, and (d) 4 µm.

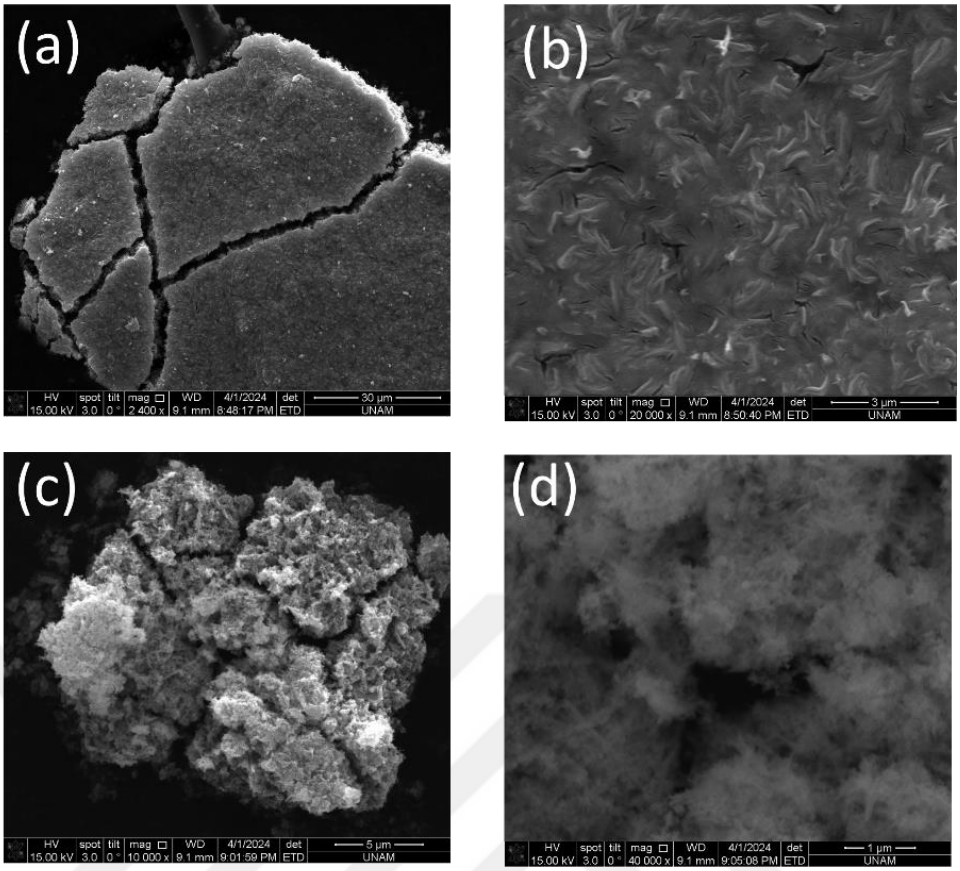

Figure 3.115. SEM images of the drop-casted m-NiO-SiO_2 (prepared from aged precursor) calcined at 350 ºC. Scale bars are (a) 30 µm, (b) 3 µm, (c) 5 µm, and (d) 1 µm magnifications.

Figures 3.114 and 3.115 show the SEM images of the same samples. It is shown in the images that the m-NiO-SiO_2 samples form thick films with a lot of cracks due to high thickness. In the high magnification images, the film consists of small silica nickel oxide particles that look like a porous sponge. Even at higher magnification, it is obvious that the film consists of macropores that can be advantageous for electrochemistry applications as it allows easy infiltration of the electrolyte.

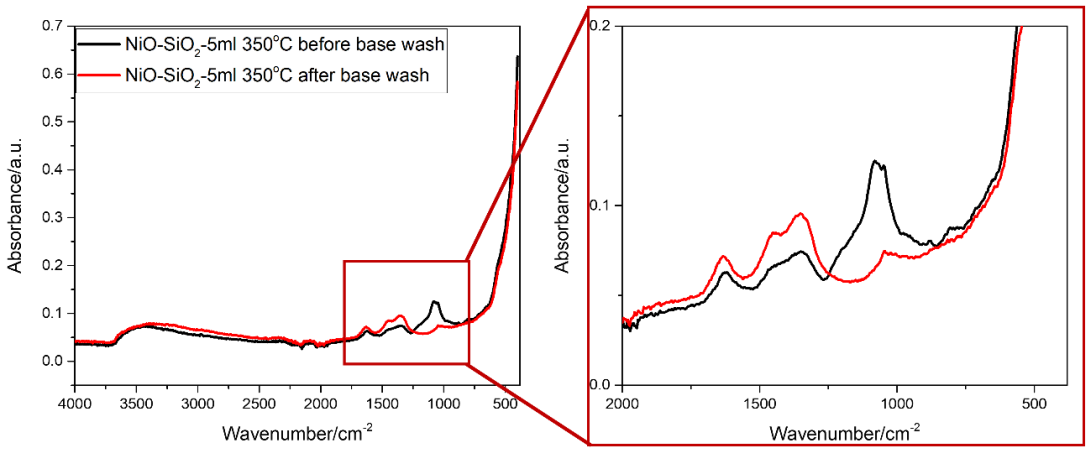

Figure 3.116. ATR-FTIR spectra of m-NiO-SiO_2 powder before and after 1 M KOH treatment.

Since the electrodes will be used in a basic media, silica will be etched out, leaving secondary pores in m-NiO. To show that, some m-NiO-SiO_2 powder was kept in 1 M KOH overnight and its ATR-FTIR spectrum was recorded. Figure 3.116 shows the ATR-FTIR spectra of m-NiO-SiO_2 before and after base treatment.

The silica related peak (Q**4** or TO mode, O_4Si) around 1050 cm^{-1} mostly disappears after base treatment, indicating etching of the silica. However, the water regions (3500 and 1640 cm^{-1} regions) and NiO peaks remain unchanged after base-treatment, indicating that the m-NiO domains remain porous.

3.11. Electrochemical Characterization of Mesoporous Nickel Oxide Electrode with Silica Support.

Four graphite electrodes, were prepared using different amount of TMOS containing solution (5 ml, 10 ml, 15 ml, and 20 ml) and analyzed using collecting their CVs (see Figure 3.117).

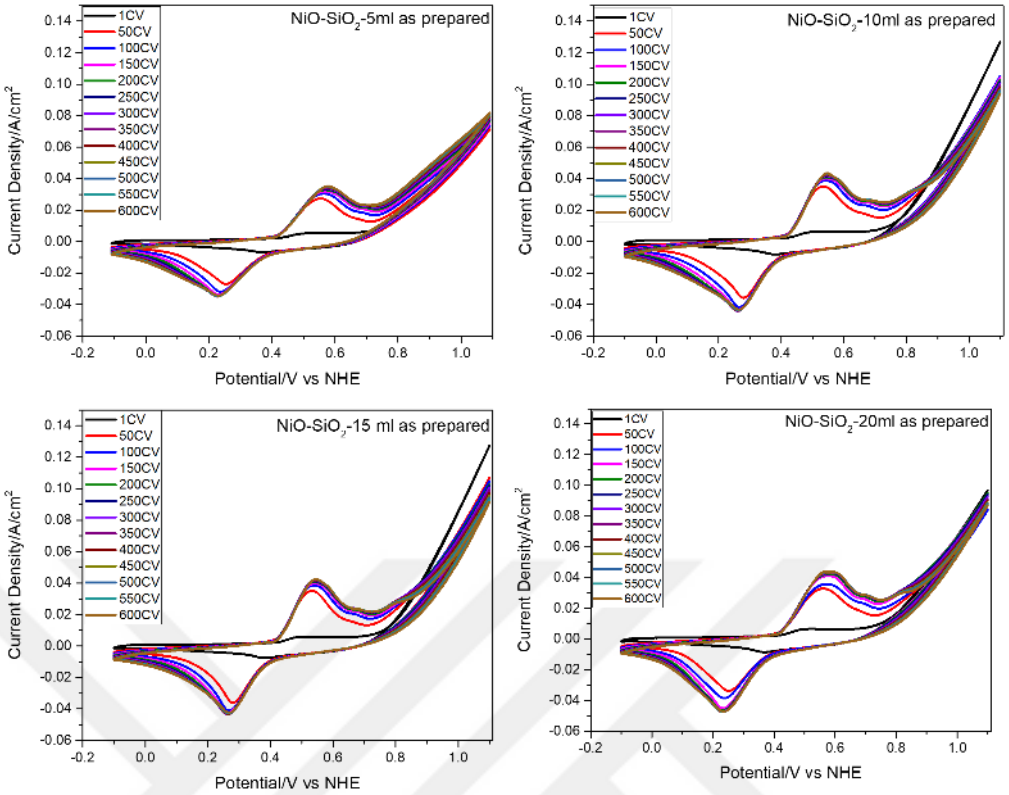

Figure 3.117. 600 cyclic voltammograms (every 50th cycle) of the m-NiO-SiO_2 electrodes, prepared at different TMOS amounts and calcined at 350 ^oC.

With cycling, the peak current increases, indicating etching of the silica in basic electrolyte and formation of nickel hydroxide and oxyhydroxide species on the surface. Current density reaches to 45 mA/cm^2 in the 20 ml sample and higher than pure m-NiO electrode. In case of 5 ml sample, it is a bit lower and around 35 mA/cm^2. Increasing silica amount increases the accessible surface area and provides a higher current density.

12 hours 10 mA CP experiment has been carried using the same electrodes. The CP curves display low overpotential at the end of the catalytic usage (see Figure 3.118.) The overpotential values are around 380-390 mV. There is not much difference among all the electrodes, investigated so far.

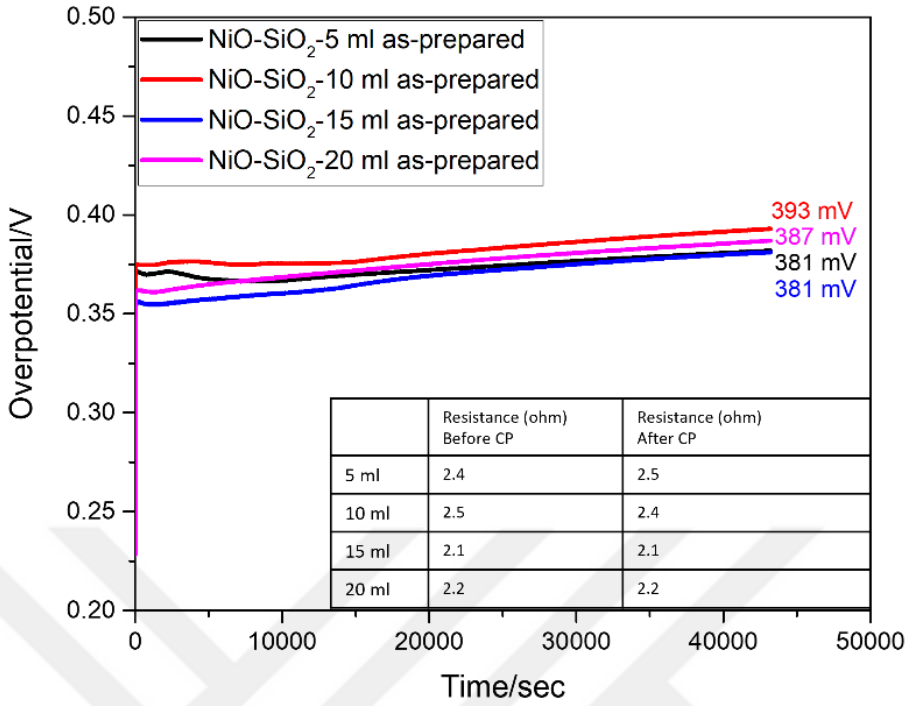

	Resistance (ohm) Before CP	Resistance (ohm) After CP
5 ml	2.4	2.5
10 ml	2.5	2.4
15 ml	2.1	2.1
20 ml	2.2	2.2

Figure 3.118. 12 hours 10 mA CP of the m-NiO-SiO_2 electrodes, prepared at different TMOS amounts and calcined at 350 ^oC. The series resistance values are given in the inset.

Series resistance that is given in the inset is very low and around 2 ohm and it does not change much after CP experiments.

The previously discussed aged and fresh sample of 5 ml TMOS containing solution has also been tested in electrochemistry experiments (see Figure 3.119).

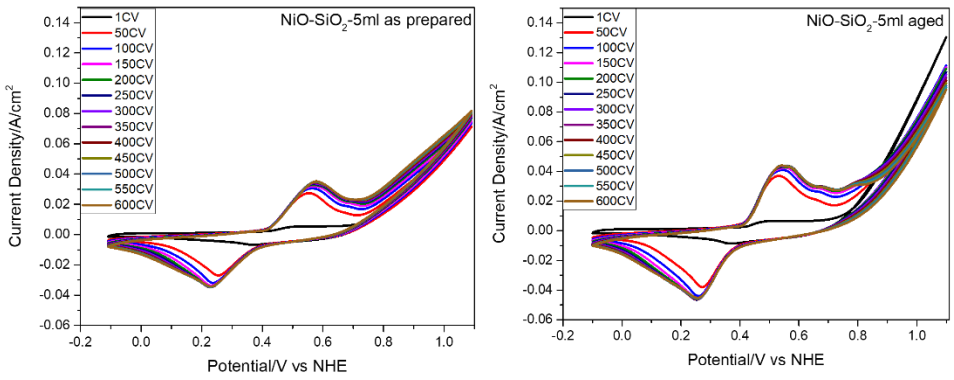

Figure 3.119. 600 cyclic voltammograms (every 50th cycle) of the m-NiO-SiO_2 electrodes, calcined at 350 ^oC, (left) from the as-prepared and (right) from the aged precursor solutions.

The only difference is that the aged sample has slightly higher current density of 43 and 130 mA/cm^2 at 0.5 and 1 V, respectively, while the fresh electrode has 35 and 80 mA/cm^2 current density at the same potentials.

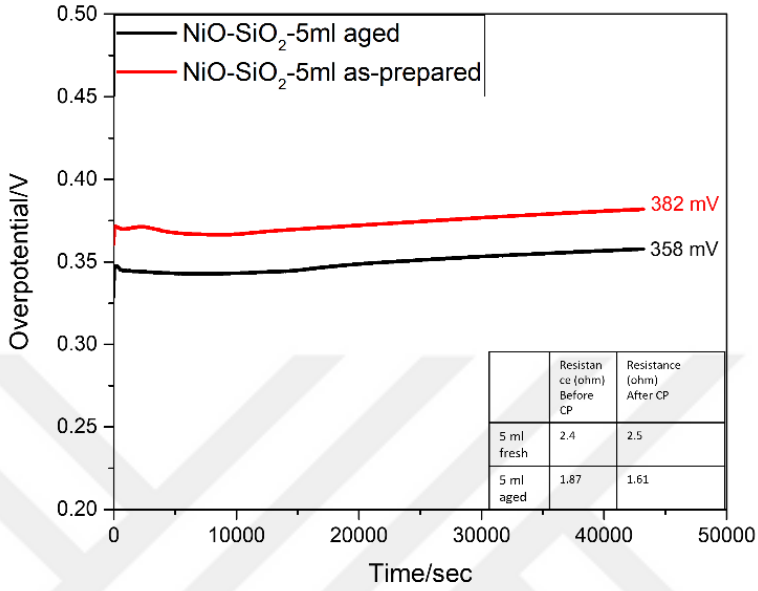

Figure 3.120. 12 hours 10 mA CP of the m-NiO-SiO$_2$ electrodes, calcined at 350 ^{o}C, prepared from the as-prepared (red) and from the aged (black) precursor solutions, the series resistance values are given in the inset.

In the 12 hours 10 mA CP measurement (Figure 3.1120), 5 ml aged sample show the lowest overpotential value of 358 mV and supports the CV data, where the current density in the water oxidation side is higher compared to the electrode, prepared from the fresh sample. This may be due to further polymerization of silica domains that somehow improves the structure and results in a better catalytic behavior. Series resistance is also quite low (1.8 ohm); it is the lowest resistance observed so far.

Considering that the solvent of the Ni(II) precursor solution was switched from ethanol to water, it would be useful to test the electrodes, prepared from both solvents. The initial solution was diluted 10 times and used to prepare the graphite electrodes. 600 CVs are given in Figure 3.121.

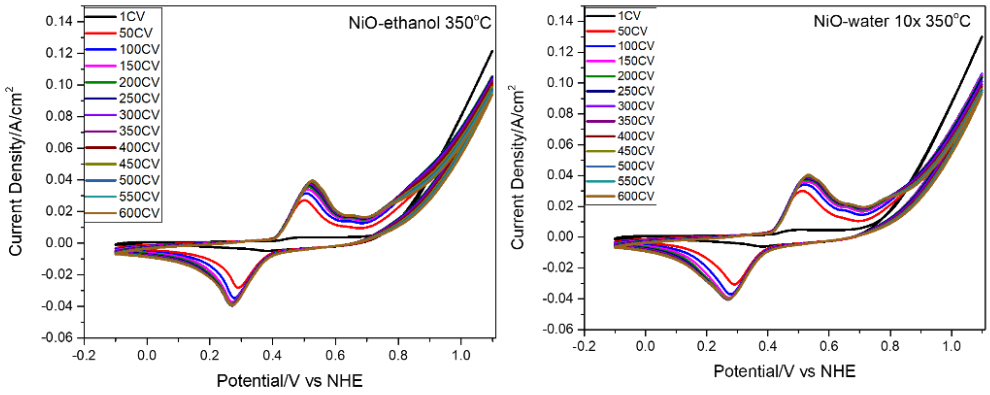

Figure 3.121. 600 cyclic voltammograms (every 50th cycle) of the m-NiO electrodes, prepared from two different solvent precursors ((left) ethanol, (right) water) and calcined at 350 ^{o}C.

Both electrodes, from ethanol and water, display almost identical cyclic voltammograms with the same stability with cycling and same current densities along the potential range. They are also comparable with the electrodes, prepared with silica. Considering that water sample has a lower surface area (24 cm^2/g) compared to the ethanol sample (200 cm^2/g), it can be concluded that the internal surface is not accessible and have no contribution to the observed current density of the electrodes, only the very top surface is used in the catalytic process.

The m-NiO electrode, prepared from the aqueous solution, shows a better water oxidation with low and steady overpotential of 393 mV after 12 hours 10 mA CP experiment. Initially overpotential are very similar for both electrodes. However, the electrode, prepared from ethanol solution, displays a 480 mV overpotential at the end of the same experiment and it is not stable and kept increasing showing that the electrode surface is getting deactivated. Therefore, water in general is a better solvent for the fabrication of the mesoporous nickel oxide electrodes.

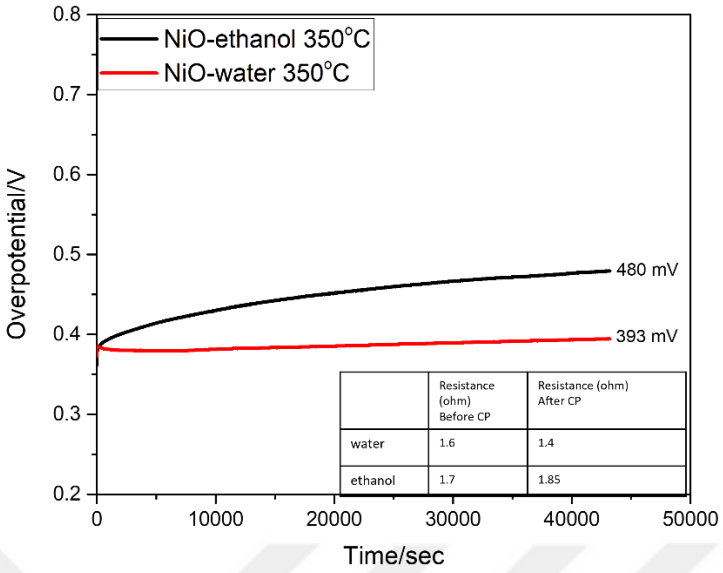

Figure 3.122. 12 hours 10 mA CP of the m-NiO calcined at 350 °C, prepared from the water (red) and ethanol (black) precursor solutions, the series resistance values are given in the inset.

3.12 Fabrication of Ordered Mesoporous Nickel Oxide and α-, β - $Ni(OH)_2$.

As mentioned in the discussion above, the electrodeposition from dilute surfactant solution was utilized to produce mesoporous nickel oxide electrodes via electrodeposition of nickel hydroxide on the FTO surface and calcined at 350 °C and characterized accordingly. Compositions of the solution, used for electrodeposition, are given in the Table 3.18.

Table 3.18. Composition that has been used for electrodeposition.

Ni(II)/Mn(II)/$C_{12}E_{10}$ Mole Ratio	Mn Salt (g)	Ni Salt (g)	CTAB (g)	$C_{12}E_{10}$ (g)	Ethanol (ml)
10:0:1	0	2.321	0.291	0.500	5

The original solution, prepared in ethanol was diluted till the concentration of nickel nitrate is 0.05M. For the dilution both ethanol and water have been used to test, whether the electrodeposition is more efficient in the water or ethanol. The electrodeposition set up is still three electrodes system, where the reference electrode

is Ag/AgCl, counter electrode is Pt wire and working electrode, where the electrodeposition occurs. Electrodeposition has been conducted by using chronoamperometry experiment by applying -1 V negative potential for 5 and 10 mins. Since negative potential is applied, the water is reduced to produce H_2 and hydroxide ions that are produced is used to deposit $Ni(OH)_2$. Then, the electrode is removed from the solution and immediately characterized by monitoring the deposition using small-angle XRD over time. Initially, the electrodes are transparent and look like a gel, and upon drying, it turns to nickel hydroxide green opaque color. As expected, the electrodes, prepared in ethanol, did not give any diffraction, so the samples, obtained from water precursor solution, are used for further characterization. The small-angle XRD patterns of the freshly deposited electrodes are given in Figure 3.123.

To test the time, required for the electrodeposition experiment, the electrodeposition was conducted for 5 and 10 minutes. Both samples display diffraction line(s) at small-angle and over time and the diffraction lines get sharper, indication of an ordered mesostructure.

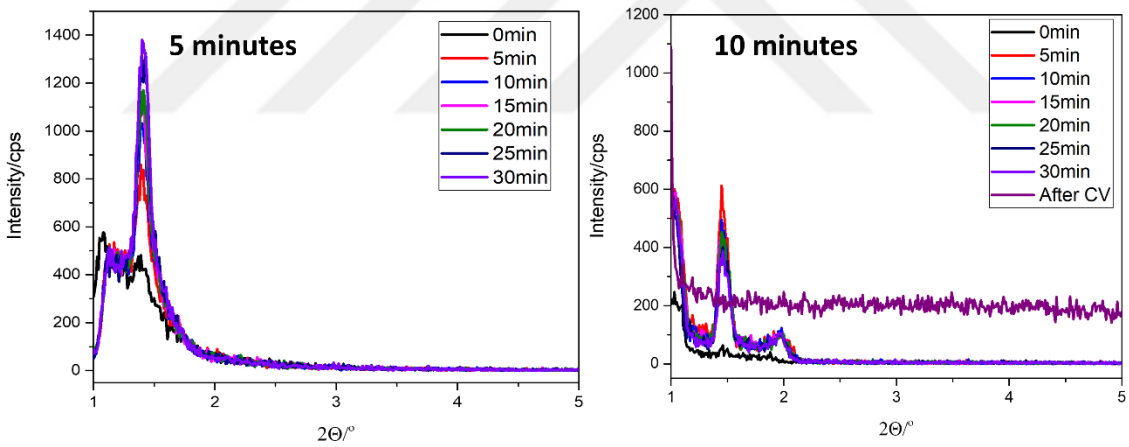

Figure 3.123. Small-angle XRD patterns of the freshly deposited electrodes at different CA times.

Right after small-angle XRD analysis, the CVs were also recorded using the 5- and 10-minutes electrodeposited electrodes (see Figure 3.124).

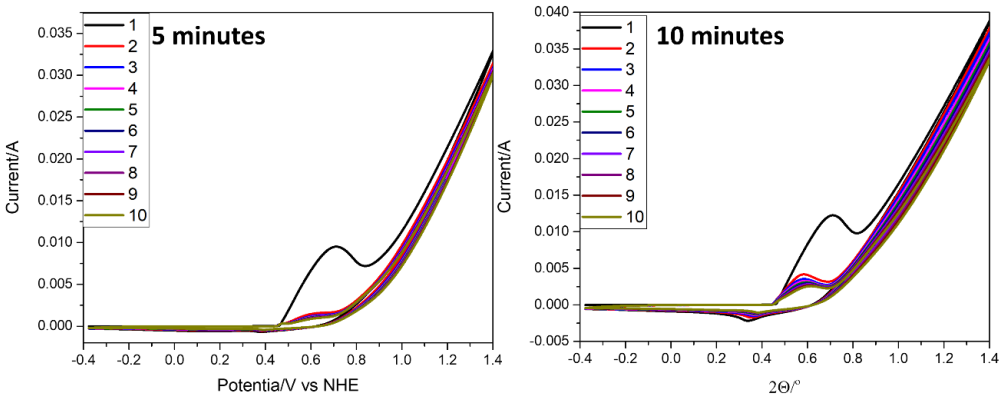

Figure 3.124. 10 CVs of the electrodeposited $Ni(OH)_2$ at different deposition times, 5 and 10 minutes.

If the electrodes are not washed after electrodeposition, the first CV has a high current density, because of a lot of nitrate species on top of the nickel hydroxide. Other cycles show typical nickel hydroxide electrode cyclic voltammogram. Longer the deposition time, higher the current density, because more sample is deposited. However, to optimize the deposition time, these electrodes are calcined at 350 ^{o}C, and their CVs are similarly recorded (see Figure 3.125).

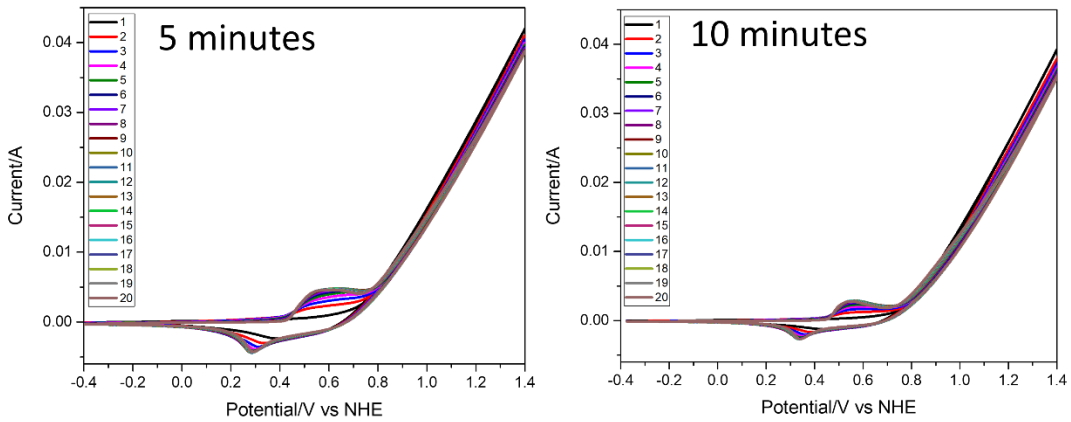

Figure 3.125. CVs of electrodeposited electrodes, calcined at 350 ^{o}C, deposition time of 5 and 10 minutes.

From the CVs, given above, typical behavior of NiO electrodes has been observed. With cycling, the current density gradually increases because of $Ni(OH)_2$ formation on the surface of NiO core. 5 minutes deposition time gave a higher current density, so the deposition time is optimized to be 5 minutes at -1V CA.

A new $Ni(OH)_2$ electrode is prepared, at -1V CA, 5 minutes electrodeposition. After electrode preparation, it is washed several times by dipping it to a deionized water. Then, this electrode is characterized by small-angle XRD and electrochemical methods (see Figure 3.126).

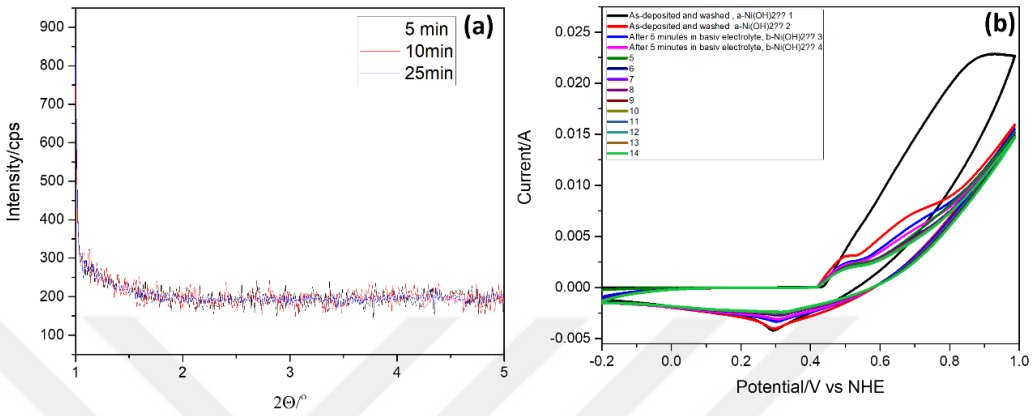

Figure 3.126. (a) Small-angle XRD patterns and (b) CVs of the as deposited and washed $Ni(OH)_2$ electrode.

After washing the electrodeposited electrode, there is no diffraction line at small angles, probably due to the fact that all surfactant molecules are removed, and there is no ordered mesophase/mesostructure on the surface of the electrode. Therefore, without washing, there must be a Ni salt-surfactant mesophase on the surface of the electrode. As shown in the CVs, the first cycle displays a high current density, and the CV line shape is also different. There is a structural difference between the two phases, namely α- and β-phases. The α-phase is directly formed during the electrodeposition (see Figure 3.127), while the β phase is formed in the basic media. So, the freshly synthesized electrode is always α-$Ni(OH)_2$, and with cycling in the basic media it transforms to β-$Ni(OH)_2$. That is why the line shape of CV curve and current densities are different. The α-$Ni(OH)_2$ has a higher surface coverage and consists of $Ni(OH)_2$ layers that are connected by water molecules with a higher current density and larger layer-layer separation. It was discussed before that, in the base alpha phase is dehydrated and transforms to beta phase having a lower surface coverage, that results in low current density. We will try to use that discussion in the NiO electrode transformation during electrochemical process. Since the electrochemical analysis is performed in a basic media, we may assume that the hydroxide that was building up on top of NiO is β –

$Ni(OH)_2$. Increase in current density is not due to α-$Ni(OH)_2$ (α-$Ni(OH)_2$ does not exist in basic media), but due to accumulation of beta phase.

The powder XRD patterns and ATR-FTIR spectra of freshly deposited nickel hydroxide (α-$Ni(OH)_2$) and the same sample after base treatment (β – $Ni(OH)_2$) are shown in Figure 3.127.

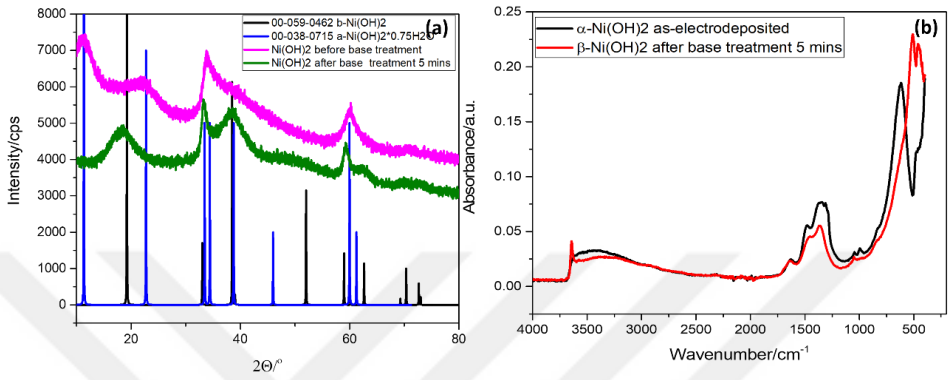

Figure 3.127. (a) XRD patterns of α- and β-$Ni(OH)_2$ before and after base treatment and corresponding PDF cards for α-$Ni(OH)_2$- 00-038-0715, and β – $Ni(OH)_2$ - 00-059-0462 and (b) ATR-FTIR spectra of α and β – $Ni(OH)_2$.

The XRD patterns clearly show that upon aging the α-$Ni(OH)_2$ in a basic media, it transforms to β – $Ni(OH)_2$. This transition occurs in 5 minutes of keeping the sample in the 1M KOH solution. This datum is supported by ATR-FTIR spectra of the same samples. A narrow strong band at 3646 cm^{-1} is observed due to Ni-OH) stretching vibration of β – $Ni(OH)_2$ and the broad peak at 3445 cm^{-1} is due to water stretching mode in both hydroxides. The sharp peak at 3646 cm^{-1} does not exist in the case of α-$Ni(OH)_2$. The bands around 1034, 1341 and 1480 cm^{-1} belong to carbonate species. They get more intense after base treatment because of adsorbing atmospheric CO_2 and KOH tends to capture CO_2 more efficiently. There is no change in the water bending mode at 1660 cm^{-1}. It should be also noted that the carbonates are not observed in the XRD patterns, so amount of CO_2 adsorbed is negligible or the carbonate species are amorphous.

The NiO electrodes were also characterized using ATR-FTIR to check if one can observe band at 3646 cm^{-1} typical for pure β-$Ni(OH)_2$, after electrochemical use. This was not detected by XRD as only surface transformed into a hydroxide. The ATR-

FTIR spectra of NiO electrode, calcined at 350 °C, before and after electrochemical tests are shown in Figure 3.128.

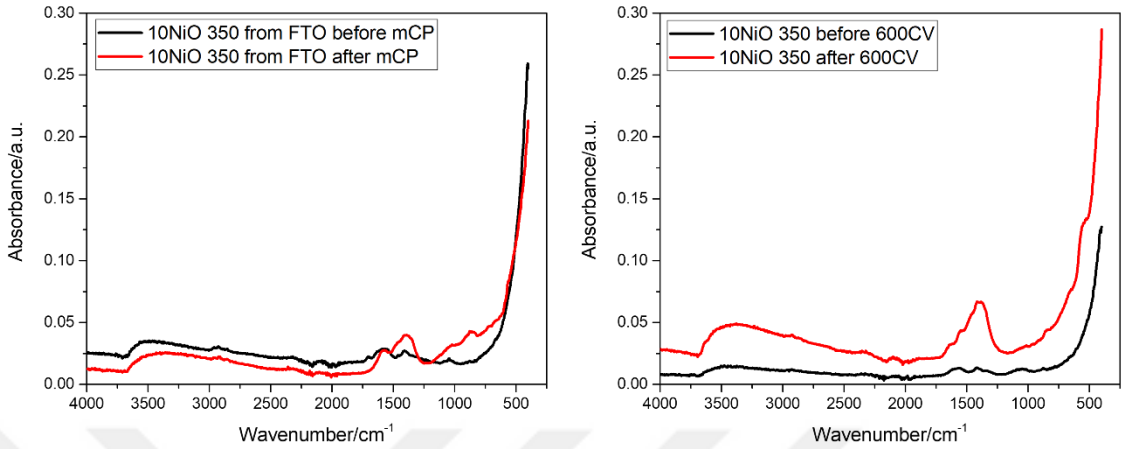

Figure 3.128. ATR-FTIR spectra of NiO electrode, calcined at 350 °C, before and after (left) m-CP experiment, (right) before and after 600 CVs.

Although the electrodes are exposed to harsh electrochemical conditions for quite a long time, the only difference is the carbonate region, which is enhanced after usage, meaning absorbance of carbon dioxide from the atmosphere after base treatment. Since it could not be determined from the ATR-FTIR spectrum, which phase is forming on top of NiO electrode after electrochemical use, the XPS spectra of α- and β-$Ni(OH)_2$ and NiO 500 °C electrodes before and after 600 CVs are collected and compared (see Figure 3.129).

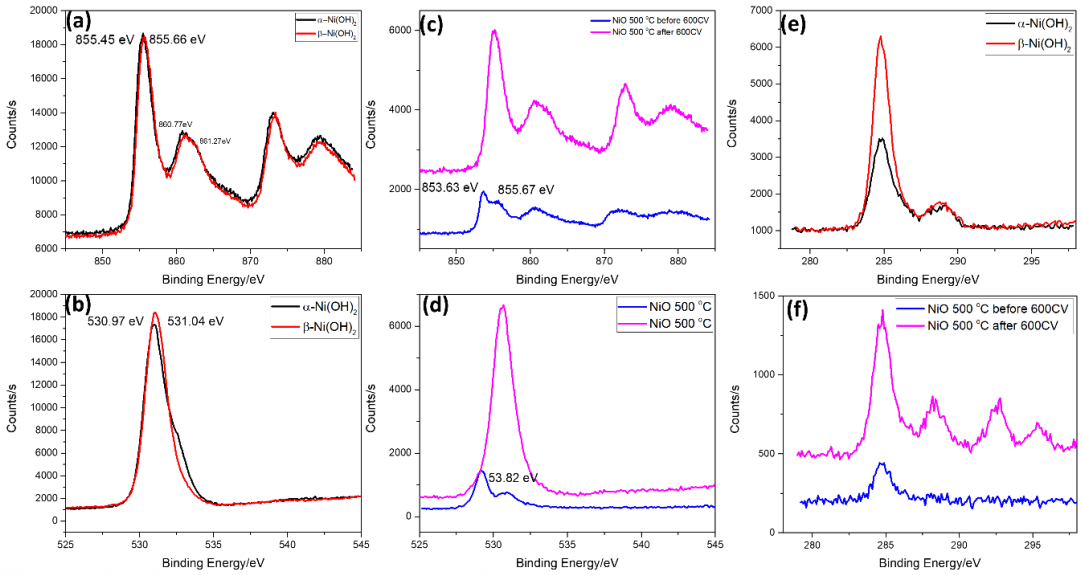

Figure 3.129. XPS spectra in the (a), (c) Ni 2p , (b), (d) O 1s , (e), (f) C 1s regions of the α- and β – $Ni(OH)_2$ and NiO, calcined at 500°C before and after 600 CVs, respectively.

From Ni 2p spectra of the α- and β – $Ni(OH)_2$, the $^2P_{3/2}$ peak is shifted in case of β hydroxide (855,66 eV), while in the case of α-$Ni(OH)_2$ the same peak is observed at a slightly lower binding energy, 855.45 eV. Satellite peaks are also shifted and comprise 860.77 eV and 861.27 eV for α- $Ni(OH)_2$ and β – $Ni(OH)_2$, respectively. In the case of pure NiO, before catalytic use, only one peak is observed that belongs to NiO, as surface is dominated mostly by NiO. After cycling, that peak splits and higher energy one is observed at 855.67 eV that belongs to hydroxide species on top of the NiO core. It has the same value as pure beta phase, so it can be assumed that β–$Ni(OH)_2$ forms during electrochemical process. In the O1s region, single peak of pure NiO before use becomes two after 600 CVs and the new peak that appears after catalytic use is not similar to β–$Ni(OH)_2$, however, those peaks may also belong to oxygen that originate from carbonate species as confirmed by ATR-FTIR spectroscopy. If one looks at C 1s region, the amount of carbonate increases after catalytic use, that is in good agreement with ATR-FTIR data.

This chapter begins with the characterization of electrodeposited $Ni(OH)_2$. After deposition, the washed sample was calcined at 350 °C and analyzed using XRD, electrochemical techniques and SEM imaging. Powder XRD, cyclic voltammograms and multi-step chronopotentiometry are illustrated in Figure 3.130.

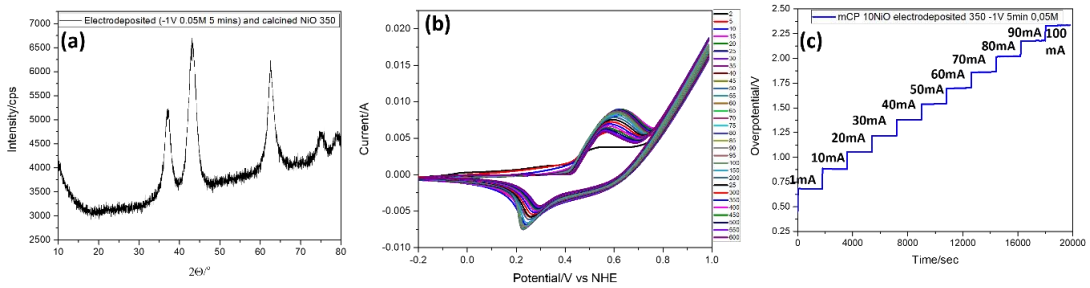

Figure 3.130. (a) XRD, (b) 600 CVs and (c) m-CP plot of NiO electrode, calcined at 350 ^{o}C and obtained via electrodeposition.

The XRD lines belong to cubic rock salt NiO. The lines are broad but not as broad as in the NiO, synthesized from MASA method, indicating that the particles are larger in the electrodeposited samples. Current densities in the cyclic voltammograms are relatively high, meaning that that sample has a large surface area, yet N_2-adsorbtion desorption analysis is needed to check whether the electrodeposited electrode is mesoporous. Overpotentials are constant at each current densities and comparable with sample synthesized by MASA method. SEM images, obtained directly from FTO and from carbon tape, are shown in Figure 3.131.

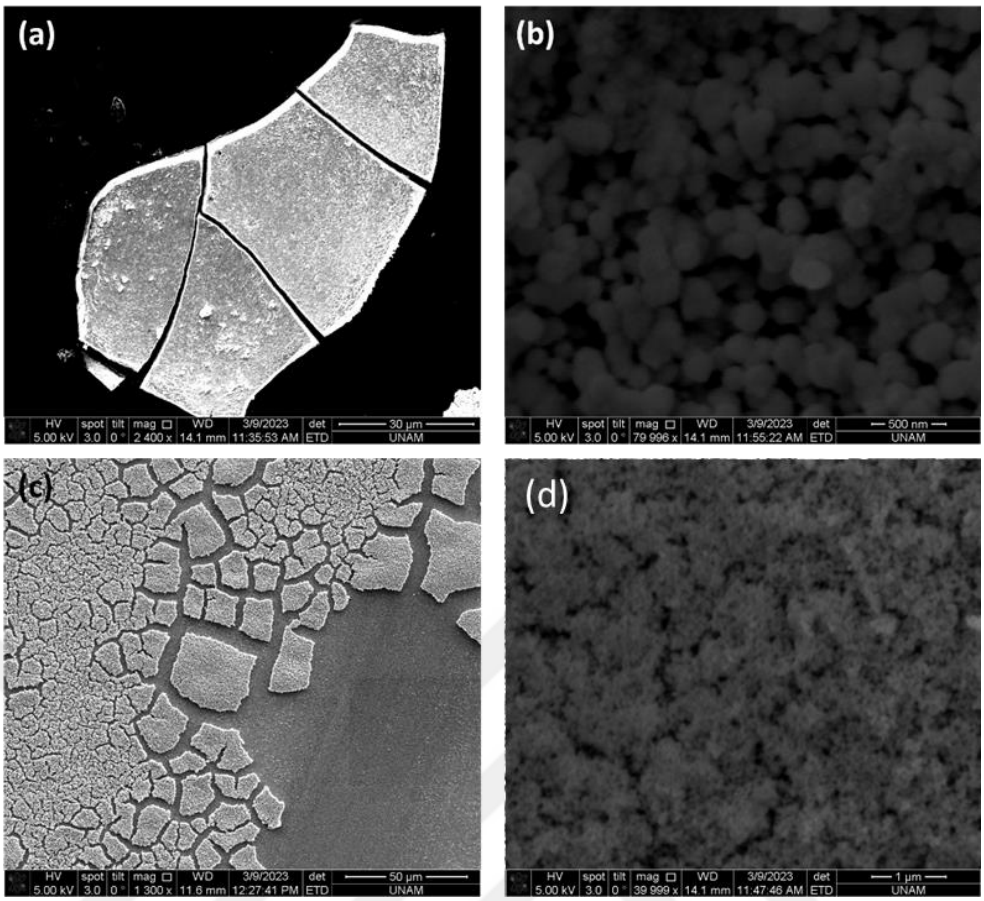

Figure 3.131. SEM images of NiO electrode at 350 ºC obtained from electrodeposition. Imaged from (a) carbon tape (scale bar is 30 µm), (b) carbon tape (scale bar is 500 nm), (c) FTO surface (scale bar is 50 µm) and (d) FTO surface (scale bar is 1 µm).

Electrodeposited NiO forms as a film on top of the FTO substrate, which is quite uniform but more rough structure with larger pores that are observable even at lower magnification. Also, the film is quite thick meaning that spin coating produces much thinner NiO films. To reduce the thickness of the oxide, the applied electrodeposition potential, electrodeposition time or even concentration of the precursor solution needs to be optimized.

Chapter 4

4 CONCLUSION

Mesoporous $Ni_{1-x}Mn_xO$ has been synthesized at different Ni to Mn mole ratios, from pure m-NiO up to $Ni_{0.1}Mn_{0.9}O$ using molten salt-assisted self-assembly method using CTAB and $C_{12}E_{10}$ surfactants. The mesophase forms immediately after spin coating as it ensures immediate ethanol evaporation or drop-casting, whereas the mesophase forms after 15 minutes when the solvent evaporates. The LLC films can be obtained at different thicknesses by simply changing the spin rate of the coating and diluting the precursor solution. Calcination of the mesophase on FTO and Graphite substrate produces the thin film electrodes. The materials were characterized using XRD, SEM, XPS, N_2 adsorption-desorption, and electrochemical techniques.

Nickel-rich oxides contain a small amount of Mn_3O_4 phase that forms due to Mn^{2+} oxidation in the gel phase. The rest of the nickel and manganese, being in a +2 oxidation state in the mesophase, produce cubic rock salt $Ni_{1-x}Mn_xO$ phase upon calcination at 350 ^oC and higher temperatures. In the Mn-rich side, the Mn_3O_4 phase is more dominant. At 350 ^oC, the particle size of the obtained oxides (pore-wall thickness) is around 4 nm up to x of 0.7. Above 0.7, with increasing manganese ratio, particles sizes get significantly larger. Particle size grow with increasing annealing temperature and become 27 nm in pure NiO at 500 ^oC. However, addition of Mn to $Ni_{1-x}Mn_xO$ hinders the growth. The typical pore-wall thickness is around 12 nm in the homogeneously mixed $Ni_{1-x}Mn_xO$ at 500 ^oC. The growth is also enhanced in the manganese rich end member with a pore wall thickness of around 20 nm even at low calcination temperatures. Homogeneous mixing of these two metals in the gel-phase and also in the solid solution determines the pore-wall growth as a well as phase separation in the calcined samples.

All samples display typical type IV isotherms that are characteristic of mesoporous materials with narrow pore size distribution, except manganese-rich oxides. The surface

area is reduced significantly with calcination or annealing at higher temperatures in all samples, but the pore-size expands as a benefit in electrocatalysis.

The thin film electrodes prepared on FTO, namely NiO-350, $Ni_{0.9}Mn_{0.1}O$, and $Ni_{0.5}Mn_{0.5}O$, were analyzed using CV, GCD, m-CP, and m-CA techniques. Due to the high resistance of the FTO substrate, the compositions are not stable enough for long-term experiments. For this reason, graphite electrodes are chosen to characterize the above-mentioned oxides due to its low resistance. In the OER reactions and GCD experiments, graphite-coated electrodes show much better performance compared to FTO.

Thickness-dependent analysis has been shown that series resistance have an effect on overpotential of the electrode. The lower the series resistance, the more conductive is material that lowers the overpotential of the electrode. Therefore, it is very important to reduce resistance by properly connecting the electrodes to the cell. Dilution and spin rates are optimized for the efficient NiO and $Ni_{1-x}Mn_xO$ electrodes.

During the electrocatalytic process, the surface of nickel manganese oxide is always covered with $Ni(OH)_2$ species due to the transformation of the NiO to $Ni(OH)_2$/NiOOH and manganese disproportionation reactions in the manganese containing electrodes. The electrochemically produced hydroxide surface is about 2 nm thick at 350 ^oC in the pure NiO electrode. the $Ni(OH)_2$ thickness increases with increasing annealing temperature up to 4.5 nm (500 ^oC). However, addition of Mn in to $Ni_{1-x}Mn_xO$ reduces the shell-thick and hinders the $Ni(OH)_2$ transformation. Calcination at high temperatures produces larger pores and pore-wall thickness that enhances the $Ni(OH)_2$ transformation and $Ni(OH)_2$ shell-thickness. The $Ni(OH)_2$ is the active species in the water oxidation process.

Increasing the calcination temperature decreases the charge capacity values. The surface becomes rougher, which improves OER, but the relatively capacitive nickel hydroxide to nickel oxide ratio at high temperatures is reduced, leading to a drop in charge capacity. This study concludes that a higher surface area with an accessible pore structure is necessary for a high charge capacity and water oxidation efficiency. Producing stable, accessible, and thicker $Ni(OH)_2$ shells enable efficient OER.

Chapter 5

5 FUTURE OUTLOOK

Electrochromic Properties of Mesoporous Nickel Oxide Electrode.

Mesoporous Nickel Oxide, due to its unique optical properties, can be used as electrochromic material[20]. In our previous work, the electrochromic behavior was monitored in liquid electrolyte (1M KOH solution) using three electrodes system, where Ag/AgCl is a reference electrode, Pt wire is counter electrode and NiO coated on FTO substrate is working electrode. The purpose of this chapter is to show that the electrochromic properties can be shown when gel electrolytes are used. Two types of gel electrolytes have been prepared. One is a basic-electrolyte, containing LiCl, LiOH, and 10 lauryl-ether in water. Another electrolyte to test is acidic electrolyte, LiH_2PO_4, H_3PO_4, and 10 lauryl ether without addition of water but gel kept in a humidity chamber. The gel-electrolyte was spin coated or spread between NiO electrode and bare FTO (2 electrode system). The color change with cycling during CV has been observed. Data from the acidic-electrolyte is shown in Figure 4.1. Acidic-electrolyte provides a good contrast between dark and bleached state of the m-NiO electrodes, however, with time the electrode dissolves due to the high acidity of the electrolyte, for that reason basic electrolyte has been chosen for the further analysis (Figure 3.133).

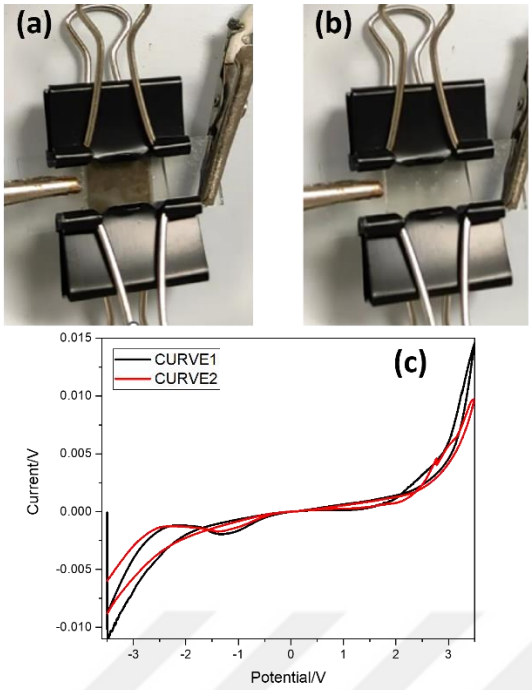

Figure 5.1. (a) The dark and (b) bleached states of NiO electrode, (c) CV of NiO electrode, prepared at 350 ^{o}C in the basic electrolyte.

In the basic gel-electrolyte, the contrast is preserved as in the case with acidic electrolyte, however though electrode does not dissolve, the second CV displays a lower current density, indicating that electrode for some reason loses its activity. Small pore sizes as the sample calcined at 350 ^{o}C and pores are not accessible or lack of water in the gel media could be the reasons of losing the contrast. To overcome this issue, electrodes prepared at higher temperature (500 ^{o}C) need to be tested due to larger pores that ensure easier infiltration of the gel- electrolyte, or improving the order of the porous material (discussed earlier) can help to achieve reproducibility of the electrochromic switching. Furthermore, the effect of humidity can be checked to ensure presence of necessary water that is needed for electrochromic processes. This could be achieved by prepared gel-electrolytes with higher water amounts or performing the electrochromic tests in a humidity chamber with a high humidity. Role of water and humidity has been investigated in a similar cell (2 electrode system), namely a dye sensitized solar cell, where the cell performance enhances with increasing water in the gel-electrolyte[140].

Electrochromic “device” needs more optimization. Larger pore size or regular pore size-electrode needs to be tested, efficient infiltration of gel-electrolytes, and humidity control needs to be established to obtain better contrast and reproducibility on the NiO based electrochromic device. These studies may open up new era to use gel-

electrolytes for electrochromic devices and the gel-electrolytes, specifically the lithium salt-surfactant mesophases, need to be further investigated in the near future.

Ordered mesoporous NiO.

For the formation of ordered mesoporous NiO, the electrochemical deposition of $Ni(OH)_2$ from surfactant precursor solution can be established and with further calcination to obtain nickel oxide. Originally, cetyltrimethylammonium bromide as a charged surfactant, 10 lauryl ether as neutral surfactant and nickel nitrate hexahydrate as a nickel precursor were used, the electrochemical deposition can be carried using the same original solution. Further analysis and characterization may be performed according to the procedure mentioned earlier. The electrodeposition parameters like precursor concentration, applied potential, applied time of electrodeposition need to be optimized to obtain electrode with better order and thinner film thickness. More structural characterization is needed for both electrodeposited $Ni(OH)_2$ and NiO, like surface area analysis and temperature dependent XRD to judge whether this method may be more applicable then MASA method. Electrochromic properties of these electrodes also need to be checked.

Mesoporous NiO-SiO_2 electrodes.

Mesoporous silica was synthesized using transition metal salts and diluted surfactant solution. New set of electrodes on graphite using synthesized mesoporous silica were fabricated (m-NiO-SiO_2) and their electrochemical properties were investigated and found that there is no significant improvement in their catalytic performance. More controlled synthesis method needs to be introduced to produce homogeneous m-SiO_2 distribution in the ordered m-NiO-SiO_2 electrodes. Maybe secondary pores can be created using polystyrene sphere (SPS) that is commercially available with different sizes. The embedded SPS can be burned out during calcination to open larger pores in the electrodes for effective diffusion of the electrolyte and better electrode-electrolyte contact. This work has shown that internal surface is not effective in electrocatalysis during OER. Above suggestions can be introduce to improve the OER and electrochromic performance of the Ni-based porous electrodes.

6 REFERENCES

[1] Q. Zhang, E. Uchaker, S. L. Candelaria, and G. Cao, "Nanomaterials for energy conversion and storage," *Chem. Soc. Rev.*, vol. 42, pp. 3127–3171, 2013, doi: 10.1039/c3cs00009e.

[2] A. Venter and J. R. Botha, "Optical and electrical properties of NiO for possible dielectric applicatons," *S. Afr. J. Sci.*, vol. 107, no. 1–2, pp. 1–6, 2011, doi: 10.4102/sajs.v107i1/2.268.

[3] S. D. Dhas, P. S. Maldar, M. D. Patil, A. B. Nagare, M. R. Waikar, R. G. Sonkawade, A. V. Moholkar, "Synthesis of NiO nanoparticles for supercapacitor application as an efficient electrode material," *Vacuum*, vol. 181, Nov. 2020, doi: 10.1016/j.vacuum.2020.109646.

[4] L. Wang, Y. Hao, Y. Zhao, Q. Lai, and X. Xu, "Hydrothermal synthesis and electrochemical performance of NiO microspheres with different nanoscale building blocks," *J. Solid St. Chem.*, vol. 183, no. 11, pp. 2576–2581, 2010, doi: 10.1016/j.jssc.2010.09.006.

[5] Y. E. Chen, Z. N. Yu, Y. G. Chen, L. Q. Luo, and X. Wang, "Preparation of NiO nanoparticles as supercapacitor electrode by precipitation using carbon black powder," in *ICMREE2011 - Proceedings 2011 International Conference on Materials for Renewable Energy and Environment*, 2011, pp. 640–643. doi: 10.1109/ICMREE.2011.5930892.

[6] G. S. Gund, C. D. Lokhande, and H. S. Park, "Controlled synthesis of hierarchical nanoflake structure of NiO thin film for supercapacitor application," *J. Alloys Comp.*, vol. 741, pp. 549–556, Apr. 2018, doi: 10.1016/j.jallcom.2018.01.166.

[7] J. P. Kumar, S. D. Giri, and A. Sarkar, "Mesoporous NiO with different morphology: Synthesis, characterization and their evaluation for oxygen evolution reaction," *Int. J. Hydrogen Energy*, vol. 43, no. 33, pp. 15639–15649, Aug. 2018, doi: 10.1016/J.IJHYDENE.2018.06.097.

[8] X. Lai *et al.*, "Ordered mesoporous NiO with thin pore walls and its enhanced sensing performance for formaldehyde," *Nanoscale*, vol. 7, no. 9, pp. 4005–4012, Mar. 2015, doi: 10.1039/c4nr05772d.

[9] A. Renaud *et al.*, "Origin of the black color of NiO used as photocathode in p-type dye-sensitized solar cells," *J. Phys. Chem. C*, vol. 117, no. 44, pp. 22478–22483, Nov. 2013, doi: 10.1021/jp4055457.

[10] A. K. Singh, D. Sarkar, G. G. Khan, and K. Mandal, "Hydrogenated NiO Nanoblock Architecture for High Performance Pseudocapacitor," *ACS Appl. Mater. Interfaces*, vol. 6, no. 7, pp. 4684–4692, Apr. 2014, doi: 10.1021/am404995h.

[11] Y. Wang, J. Zhu, X. Yang, L. Lu, and X. Wang, "Preparation of NiO nanoparticles and their catalytic activity in the thermal decomposition of ammonium perchlorate,"

Thermochim. Acta, vol. 437, no. 1–2, pp. 106–109, 2005, doi: 10.1016/j.tca.2005.06.027.

[12] H. Zhou, B. Lv, Y. Xu, and D. Wu, "Synthesis and electrochemical properties of NiO nanospindles," *Mater. Res. Bull.*, vol. 50, pp. 399–404, 2014, doi: https://doi.org/10.1016/j.materresbull.2013.11.004.

[13] A. Venter and J. R. Botha, "Optical and electrical properties of NiO for possible dielectric applicatons," *S. Afr. J. Sci.*, vol. 107, no. 1–2, pp. 1–6, 2011, doi: 10.4102/sajs.v107i1/2.268.

[14] M. P. Browne, H. Nolan, N. C. Berner, G. S. Duesberg, P. E. Colavita, and M. E. G. Lyons, "Electrochromic nickel oxide films for smart window applications," *Int. J. Electrochem. Sci.*, vol. 11, 2016, doi: 10.20964/2016.08.38.

[15] A. Amirzhanova, "Synthesis and Characterization Mesoporous Nickel Oxide and Nickel Cobaltite Thin Films," Sep. 2019.

[16] T. Nathan, A. Aziz, A. F. Noor, and S. R. S. Prabaharan, "Nanostructured NiO for electrochemical capacitors: Synthesis and electrochemical properties," *J. Solid State Electrochem.*, Springer Science and Business Media, LLC, 2008, pp. 1003–1009. doi: 10.1007/s10008-007-0465-3.

[17] F. F. Ferreira and E. Avendaño, "Reversible electronic charge transfer between Au nanoparticles and electrochromic NiO matrices upon electrochemical cycling," *J. Phys. Chem. C*, vol. 111, no. 44, pp. 16608–16612, 2007, doi: 10.1021/jp0758162.

[18] M. K. Carpenter, R. S. Conell, and D. A. Corrigan, "The electrochromic properties of hydrous nickel oxide," *Sol. Energy Mater.*, vol. 16, no. 4, pp. 333–346, 1987, doi: 10.1016/0165-1633(87)90082-7.

[19] J. L. Garcia-Miquel *et al.*, "Nickel oxide sol-gel films from nickel diacetate for electrochromic applications," *Thin Solid Films*, vol. 424, no. 2, pp. 165–170, 2003, doi: 10.1016/S0040-6090(02)01041-6.

[20] A. Amirzhanova, Irmak Karakaya, Can Berk Uzundal, Gözde Karaoğlu, Ömer Dag, Burak Ülgüt, Ferdi Karadas, "Synthesis and water oxidation electrocatalytic and electrochromic behaviors of mesoporous nickel oxide thin film electrodes," *J. Mater. Chem. A*, vol. 7, no. 38, pp. 22012–22020, 2019, doi: 10.1039/c9ta07693j.

[21] K. Wang, L. Li, and T. Zhang, "Synthesis of nickel hydroxide and its electrochemical performances," *Int. J. Electrochem. Sci.*, vol. 8, pp. 6252–6257, 2013, doi: 10.1016/S1452-3981(23)14758-4.

[22] P. Jeevanandam and V. R. R. Pulimi, "Synthesis of nanocrystalline NiO by sol-gel and homogeneous precipitation methods," *Indian J. Chem. - Section A Inorganic, Physical, Theoretical and Analytical Chemistry*, vol. 51A, pp. 586–590, 2012.

[23] L. Wang, Y. Hao, Y. Zhao, Q. Lai, and X. Xu, "Hydrothermal synthesis and electrochemical performance of NiO microspheres with different nanoscale building blocks," *J. Solid. State Chem.*, vol. 183, no. 11, pp. 2576–2581, 2010, doi: 10.1016/j.jssc.2010.09.006.

[24] S. K. Meher, P. Justin, and G. R. Rao, “Microwave-mediated synthesis for improved morphology and pseudocapacitance performance of nickel oxide,” *ACS Appl. Mater. Interfaces*, vol. 3, no. 6, pp. 2063–2073, 2011, doi: 10.1021/am200294k.

[25] Y. Ren, Z. Ma, and P. G. Bruce, “Ordered mesoporous metal oxides: Synthesis and applications,” 2012. doi: 10.1039/c2cs35086f.

[26] P. Yang, D. Zhao, D. I. Margolese, B. F. Chmelka, and G. D. Stucky, “Block copolymer templating syntheses of mesoporous metal oxides with large ordering lengths and semicrystalline framework,” *Chem. Mater.*, vol. 11, no. 10, pp. 2813–2826, 1999, doi: 10.1021/cm990185c.

[27] L. Guo, H. Arafune, and N. Teramae, “Synthesis of mesoporous metal oxide by the thermal decomposition of oxalate precursor,” *Langmuir*, vol. 29, no. 13, pp. 4404–4412, 2013, doi: 10.1021/la400323f.

[28] A. DM, A. Nakahira, and Y. JY, “Ligand-assisted liquid crystal templating in mesoporous niobium oxide molecular sieves,” *Inorg. Chem.*, vol. 35, no. 11, pp. 3126–3136, 1996, doi: 10.1021/ic951533p.

[29] D. M. Antonelli and J. Y. Ying, “Synthesis of Hexagonally Packed Mesoporous TiO_2 by a Modified Sol–Gel Method,” *Angew. Chem., In. Ed. Engl.*, vol. 34, no. 18, pp. 2014–2017, 1995, doi: 10.1002/anie.199520141.

[30] R. Muñoz-Espí, Y. Mastai, S. Gross, and K. Landfester, “Colloidal systems for crystallization processes from liquid phase,” in *Cryst. Eng. Comm.*, Mar. 2013, pp. 2175–2191. doi: 10.1039/c3ce26657e.

[31] Y. Deng *et al.*, “Ordered mesoporous silicas and carbons with large accessible pores templated from amphiphilic diblock copolymer poly(ethylene oxide)-b-polystyrene,” *J. Am. Chem. Soc.*, vol. 129, no. 6, pp. 1690–1697, 2007, doi: 10.1021/ja067379v.

[32] H. Yang and D. Zhao, “Synthesis of replica mesostructures by the nanocasting strategy,” *J. Mater. Chem.*, vol. 15, pp. 1217– 1231, 2005, doi: 10.1039/b414402c.

[33] A. H. Lu and F. Schüth, “Nanocasting: A versatile strategy for creating nanostructured porous materials,” *Adv. Mater.*, vol. 18, pp. 1793-1805, 2006, doi: 10.1002/adma.200600148.

[34] K. Zhu, B. Yue, W. Zhou, and H. He, “Preparation of three-dimensional chromium oxide porous single crystals templated by SBA-15,” *Chem. Comm.*, vol. 8, no. 1, pp. 98–99, 2003, doi: 10.1039/b210065g.

[35] W. C. Li, A. H. Lu, C. Weidenthaler, and F. Schüth, “Hard-templating pathway to create mesoporous magnesium oxide,” *Chem. Mater.*, vol. 16, no. 26, pp. 5676–5681, 2004, doi: 10.1021/cm048759n.

[36] A. Rumplecker, F. Kleitz, E. L. Salabas, and F. Schüth, “Hard templating pathways for the synthesis of nanostructured porous Co_3O_4,” *Chem. Mater.*, vol. 19, no. 3, pp. 485–496, 2007, doi: 10.1021/cm0610635.

[37] C. Karakaya, Y. Türker, C. Albayrak, and Ö. Dag, "Assembly of molten transition metal salt-surfactant in a confined space for the synthesis of mesoporous metal oxide-rich metal oxide-silica thin films," *Chem. Mater.*, vol. 23, no. 12, pp. 3062–3071, 2011, doi: 10.1021/cm200932k.

[38] S. Chandrasekhar and G. S. Ranganath, "Discotic liquid crystals," *Rep. Prog. Phys.*, vol. 116, no. 3, pp. 1139–1241, 1990, doi: 10.1088/0034-4885/53/1/002.

[39] Q. Liang, P. Liu, C. Liu, X. Jian, D. Hong, and Y. Li, "Synthesis and properties of lyotropic liquid crystalline copolyamides containing phthalazinone moiety and ether linkages," *Polymer (Guildf)*, vol. 46, no. 16, pp. 6258–6265, 2005, doi: 10.1016/j.polymer.2005.05.059.

[40] Ö. Çelik and Ö. Dag, "A New Lyotropic Liquid Crystalline System: Oligo(ethylene oxide) Surfactants with [M(H_2O)n]Xm Transition Metal Complexes," *Angew. Chem., In. Ed. Engl.*, vol. 40, no. 20, pp. 3799–3803, 2002, doi: 10.1002/1521-3773(20011015)40:20<3799::aid-anie3799>3.0.co;2-i.

[41] G. J. T. Tiddy, "Surfactant-water liquid crystal phases," *Phys. Rep.*, vol. 57, no. 1, pp. 1–46, 1980, doi: 10.1016/0370-1573(80)90041-1.

[42] Ö. Dag, C. Albayrak and A. M. Soylu, "Lyotropic Liquid-Crystalline Mesophases of [$Zn(H_2O)_6$](NO_3)$_2$)-$C_{12}EO_{10}$-CTAB-H_2O and [$Zn(H_2O)_6$](NO_3)$_2$-$C_{12}EO_{10}$-SDS-H," *Langmuir*, vol. 110, no. 18, pp. 9039–9047, 2004, doi: 10.1021/la8022453

[43] C. Karakaya, Y. Türker, and Ö. Dag, "Molten-salt-assisted self-assembly (MASA)-synthesis of mesoporous metal titanate-titania, metal sulfide-titania, and metal selenide-titania thin films," *Adv. Funct. Mater.*, vol. 23, no. 32, pp. 4002–4010, 2013, doi: 10.1002/adfm.201202716.

[44] A. Amirzhanova, N. Akmanşen, I. Karakaya, and Ö. Dag, "Mesoporous $MnCo_2O_4$, $NiCo_2O_4$, and $ZnCo_2O_4$Thin-Film Electrodes as Electrocatalysts for the Oxygen Evolution Reaction in Alkaline Solutions," *ACS Appl. Energy Mater.*, vol. 4, no. 3, pp. 2769–2785, Mar. 2021, doi: 10.1021/acsaem.1c00064.

[45] F. M. Balci, I. Karakaya, E. P. Alsaç, M. Y. Yaman, G. Saat, F. Karadas, B. Ülgüt, Ö. Dag, "Synthesis of mesoporous $LiMn_2O_4$ and $LiMn_2$-xCo_xO_4 thin films using the MASA approach as efficient water oxidation electrocatalysts," *J. Mater. Chem. A*, vol. 6, no. 28, pp. 13925–13933, 2018, doi: 10.1039/c8ta04138e.

[46] A. Faik Demirörs, B. E. Eser, and Ö. Dag, "Liquid crystalline mesophases of pluronics (L64, P65, and P123) and transition metal nitrate salts ([M(H_2O)$_6$](NO_3)$_2$)," *Langmuir*, vol. 21, no. 9, pp. 4156–4162, 2005, doi: 10.1021/la047136l.

[47] J. Ran, J. Yu, and M. Jaroniec, "$Ni(OH)_2$ modified CdS nanorods for highly efficient visible-light-driven photocatalytic H_2 generation," *Green Chemistry*, vol. 13, no. 10, pp. 2708–2713, Jan. 2011, doi: 10.1039/c1gc15465f.

[48] M. Gao *et al.*, "Efficient water oxidation using nanostructured α-nickel-hydroxide as an electrocatalyst," *J. Am. Chem. Soc.*, vol. 136, no. 19, pp. 7077–7084, May 2014, doi: 10.1021/ja502128j.

[49] W. Yang *et al.*, "Rapid room-temperature fabrication of ultrathin $Ni(OH)_2$ nanoflakes with abundant edge sites for efficient urea oxidation," *Appl. Catal. B*, vol. 259, p. 118020, 2019, doi: 10.1016/j.apcatb.2019.118020.

[50] M. Aghazadeh, M. Ghaemi, B. Sabour, and S. Dalvand, "Electrochemical preparation of α-$Ni(OH)_2$ ultrafine nanoparticles for high-performance supercapacitors," *J. Solid State Electrochem.*, vol. 18, no. 6, pp. 1569–1584, 2014, doi: 10.1007/s10008-014-2381-7.

[51] X. Xiong *et al.*, "Three-dimensional ultrathin $Ni(OH)_2$ nanosheets grown on nickel foam for high-performance supercapacitors," *Nano Energy*, vol. 11, pp. 154-161, 2015, doi: 10.1016/j.nanoen.2014.10.029

[52] Y. Tang *et al.*, "Highly Oxidized Graphene Anchored $Ni(OH)_2$ Nanoflakes as Pseudocapacitor Materials for Ultrahigh Loading Electrode with High Areal Specific Capacitance," *J. Phys. Chem. C*, vol. 118, no. 43, pp. 24866–24876, Oct. 2014, doi: 10.1021/jp5075779.

[53] D. U. Lee, J. Fu, M. G. Park, H. Liu, A. Ghorbani Kashkooli, and Z. Chen, "Self-Assembled NiO/$Ni(OH)_2$ Nanoflakes as Active Material for High-Power and High-Energy Hybrid Rechargeable Battery," *Nano Letters*, vol. 16, no. 3, pp. 1794–1802, Mar. 2016, doi: 10.1021/acs.nanolett.5b04788.

[54] M. Vidotti, R. Torresi, and S. I. C. de Torresi, "Nickel hydroxide modified electrodes: A review study concerning its structural and electrochemical properties aiming the application in electrocatalysis, electrochromism and secondary batteries," 2010, *Soc. Bras. Quim.*, doi: 10.1590/s0100-40422010001000030.

[55] P. Oliva et al., "Review of the Structure and the Electrochemistry of Nickel Hydroxides and Oxy-Hydroxides," *J. Power Sources*, vol. 8, no. 2, pp. 229−255, 1982, doi: 10.1016/0378-7753(82)80057-8.

[56] D. S. Hall, D. J. Lockwood, C. Bock, and B. R. MacDougall, "Nickel hydroxides and related materials: A review of their structures, synthesis and properties," *Proc. Roy. Soc. A Math. Phys. Eng. Sci.*, vol. 471, 20140792, 2015, doi: 10.1098/rspa.2014.0792.

[57] D. Wang, C. Song, Z. Hu, and X. Fu, "Fabrication of hollow spheres and thin films of nickel hydroxide and nickel oxide with hierarchical structures," *J. Phys. Chem. B*, vol. 109, no. 3, pp. 1125–1129, Jan. 2005, doi: 10.1021/jp046797o.

[58] M. Yao, Z. Hu, Z. Xu, Y. Liu, P. Liu, and Q. Zhang, "High-performance electrode materials of hierarchical mesoporous nickel oxide ultrathin nanosheets derived from self-assembled scroll-like α-nickel hydroxide," *J. Power Sources*, vol. 273, pp. 914–922, Jan. 2015, doi: 10.1016/j.jpowsour.2014.09.175.

[59] R. S. Mcewen and R. S. Mcewen1, "Crystallographic Studies on Nickel Hydroxide and the Higher Nickel Oxides.", *J. Phys. Chem.*, vol. 75, pp. 1782– 1789, 1971 doi: 10.1021/j100681a004

[60] R.-Shi. Liu, Electrochemical technologies for energy storage and conversion. [Volume 1 & 2]. *John Wiley & Sons*, 2012.

[61] J. Luo *et al.*, "Water photolysis at 12.3% efficiency via perovskite photovoltaics and Earth-abundant catalysts," *Science*, vol. 345, no. 6204, p. 1593—1596, Sep. 2014, doi: 10.1126/science.1258307.

[62] P. W. Menezes *et al.*, "Using nickel manganese oxide catalysts for efficient water oxidation," *Chem. Comm.*, vol. 51, no. 24, pp. 5005–5008, 2015, doi: 10.1039/c4cc09671a.

[63] Y. Zhang, H. Zhang, L. Fang, J. Deng, and Y. Wang, "Facile Synthesis of Nickel Manganese Composite Oxide Nanomesh for Efficient Oxygen Evolution Reaction and Supercapacitors," *Electrochim. Acta*, vol. 245, pp. 32–40, 2017, doi: https://doi.org/10.1016/j.electacta.2017.05.119.

[64] V. Vij *et al.*, "Nickel-based electrocatalysts for energy-related applications: Oxygen reduction, oxygen evolution, and hydrogen evolution reactions," *ACS Catalysis*, vol. 7, no. 10, pp. 7196–7225, Oct. 2017, doi: 10.1021/acscatal.7b01800.

[65] C.-H. Wu, J.-S. Ma, and C.-H. Lu, "Synthesis and characterization of nickel–manganese oxide via the hydrothermal route for electrochemical capacitors," *Curr. Appl. Phys.*, vol. 12, no. 4, pp. 1190–1194, 2012, doi: https://doi.org/10.1016/j.cap.2012.02.056.

[66] A. Kumar *et al.*, "Solid-State Reaction Synthesis of Nanoscale Materials: Strategies and Applications," *Chem. Rev.*, vol. 122, no. 15, pp. 12748–12863, Aug. 2022, doi: 10.1021/acs.chemrev.1c00637.

[67] D. Hong, Y. Yamada, A. Nomura, and S. Fukuzumi, "Catalytic activity of $NiMnO_3$ for visible light-driven and electrochemical water oxidation," *Phys. Chem. Chem. Phys.*, vol. 15, no. 44, pp. 19125–19128, 2013, doi: 10.1039/C3CP53518E.

[68] J. Yu, Q. Yan, W. Chen, A. Jain, J. B. Neaton, and K. A. Persson, "First-principles study of electronic structure and photocatalytic properties of $MnNiO_3$ as an alkaline oxygen-evolution photocatalyst," *Chem. Comm.*, vol. 51, no. 14, pp. 2867–2870, Feb. 2015, doi: 10.1039/c4cc08111k.

[69] S. Periyasamy, P. Subramanian, E. Levi, D. Aurbach, A. Gedanken, and A. Schechter, "Exceptionally Active and Stable Spinel Nickel Manganese Oxide Electrocatalysts for Urea Oxidation Reaction," *ACS Appl. Mater. Interfaces.*, vol. 8, no. 19, pp. 12176–12185, May 2016, doi: 10.1021/acsami.6b02491.

[70] X. Niu, H. Wei, K. Tang, W. Liu, G. Zhao, and Y. Yang, "Solvothermal synthesis of 1D nanostructured Mn_2O_3: effect of Ni^{2+} and Co^{2+} substitution on the catalytic activity of nanowires," *RSC Adv.*, vol. 5, no. 81, pp. 66271–66277, Jul. 2015, doi: 10.1039/c5ra14618f.

[71] R. Wang and J. Wu, "Structure and basic properties of ternary metal oxides and their prospects for application in supercapacitors," *in Metal Oxides in Supercapacitors, Elsevier Inc.*, pp. 99–132, 2017, doi: 10.1016/B978-0-12-810464-4.00005-X.

[72] I. K. Durukan, I. Ulu, and Ö. Dag, "Manganese oxide-based mesoporous thin-film electrodes: manganese disproportionation reaction in alkaline media," *J. Mater. Chem. A*, vol. 12, no. 11, pp. 6359–6375, Feb. 2024, doi: 10.1039/d3ta07973b.

[73] Y. Meng, W. Song, H. Huang, Z. Ren, S. Y. Chen, and S. L. Suib, “Structure-property relationship of bifunctional MnO_2 nanostructures: Highly efficient, ultra-stable electrochemical water oxidation and oxygen reduction reaction catalysts identified in alkaline media,” *J. Am. Chem. Soc.*, vol. 136, no. 32, pp. 11452–11464, Aug. 2014, doi: 10.1021/ja505186m.

[74] J. S. Hong *et al.*, “Nickel-Doping Effect on Mn_3O_4 Nanoparticles for Electrochemical Water Oxidation under Neutral Condition,” *Small Methods*, vol. 4, no. 3, p. 1900733, 2020, doi: doi.org/10.1002/smtd.201900733.

[75] M. Duraivel, S. Nagappan, J. Reddy, K. H. Park, and K. Prabakar, “Engineering the active sites by tuning the Ni and Mn composition in hierarchical heterostructured composites for electrocatalytic water splitting,” *Electrochim. Acta*, vol. 472, Dec. 2023, doi: 10.1016/j.electacta.2023.143372.

[76] R. Rajendiran *et al.*, “Nickel self-doped iron oxide/manganese carbonate hierarchical 2D/3D structures for electrochemical energy storage,” *Electrochim. Acta*, vol. 297, pp. 77–86, Feb. 2019, doi: 10.1016/j.electacta.2018.11.177.

[77] M. Duraivel, S. Nagappan, K. H. Park, and K. Prabakar, “Optimised Ni^{+3}/Ni^{2+} and Mn^{3+}/Mn^{2+} Ratios in Nickel Manganese Layered Double Hydroxide for Boosting Oxygen and Hydrogen Evolution Reactions,” *ChemElectroChem.*, vol. 9, no. 19, p. e202200822, 2022, doi: 10.1002/celc.202200822.

[78] W. Wei, X. Cui, W. Chen, and D. G. Ivey, “Manganese oxide-based materials as electrochemical supercapacitor electrodes,” *Chem. Soc. Rev.*, vol. 40, no. 3, pp. 1697–1721, Feb. 2011, doi: 10.1039/c0cs00127a.

[79] M. Lee, Y. Jang, G. Yoon, S. Lee, and G. H. Ryu, “Synthesis and electrochemical evaluation of nickel hydroxide nanosheets with phase transition to nickel oxide,” *RSC Adv.*, vol. 14, no. 15, pp. 10172–10181, 2024, doi: 10.1039/d4ra01120a.

[80] A. Seghiouer, J. Chevalet, A. Barhoun, and F. Lantelme, “Electrochemical oxidation of nickel in alkaline solutions: a voltammetric study and modelling,” *J. Electroanal. Chem.*, vol. 442, p. 1131998, 1998, doi: 10.1016/S0022-0728(97)00498-1

[81] M. H. Ubeda, H. T. Mishima, B. A. Lopez, and D. E. Mishima, “The Electrochemical Response of Manganese Hydroxide-Oxide Films in Slightly Alkaline Solutions. The Redox Couple,” *Electrochim. Acta*, vol. 36, p. 1013, 1991, doi: 10.1016/0013-4686(91)85309-U.

[82] J. Y. Park *et al.*, “Chemical and electrochemical synthesis of cobalt hydroxides: selective phase transformation and application to distinct electrocatalytic reactions,” *J. Mater. Chem. A*, vol. 10, no. 22, pp. 12047–12054, May 2022, doi: 10.1039/d2ta02166h.

[83] C. Qin *et al.*, “Light-Mediated Electrochemical Synthesis of Manganese Oxide Enhances Its Stability for Water Oxidation,” *ACS Nanoscience Au*, vol. 3, no. 4, pp. 310–322, Aug. 2023, doi: 10.1021/acsnanoscienceau.3c00002.

[84] A. L. Yan, X. C. Wang, and J. P. Cheng, “Research progress of NiMn layered double hydroxides for supercapacitors: A review,” *Nanomaterials*, vol. *8, no.* 10, p. 747, 2018, doi: 10.3390/nano8100747.

[85] E. Conterosito, V. Gianotti, L. Palin, E. Boccaleri, D. Viterbo, and M. Milanesio, “Facile preparation methods of hydrotalcite layered materials and their structural characterization by combined techniques,” *Inorganica Chim. Acta*, vol. 470, pp. 36–50, 2018, doi: 0.1016/j.ica.2017.08.007.

[86] A. N. Ay, B. Zümreoglu-Karan, and L. Mafra, “A Simple Mechanochemical Route to Layered Double Hydroxides: Synthesis of Hydrotalcite-Like Mg-Al-NO3-LDH by Manual Grinding in a Mortar,” *Z Anorg. Allg. Chem.*, vol. 635, no. 9–10, pp. 1470–1475, 2009, doi: 10.1002/zaac.200801287.

[87] M. Latorre-Sanchez *et al.*, “The synthesis of a hybrid graphene–nickel/manganese mixed oxide and its performance in lithium-ion batteries,” *Carbon N Y*, vol. 50, no. 2, pp. 518–525, 2012, doi: 10.1016/j.carbon.2011.09.007.

[88] M. Li, P. W. Yuan, S. H. Guo, F. Liu, and J. P. Cheng, “Design and synthesis of Ni-Co and Ni-Mn layered double hydroxides hollow microspheres for supercapacitor,” *Int. J. Hydrogen Energy*, vol. 42, no. 48, pp. 28797–28806, Nov. 2017, doi: 10.1016/j.ijhydene.2017.10.019.

[89] X. Li *et al.*, “Bifuntional petaloid nickel manganese layered double hydroxides decorated on a freestanding carbon foam for flexible asymmetric supercapacitor and oxygen evolution,” *Electrochim. Acta*, vol. 252, pp. 275–285, 2017, doi: 10.1016/j.electacta.2017.08.028.

[90] S. Fritsch and A. Navrotsky, “Thermodynamic Properties of Manganese Oxides,” *J. Am. Ceram. Soc.* vol. 79, no. 7, pp. 1761–1768, 1996, doi:10.1111/j.1151-2916.1996.tb07993.x.

[91] A. A. Dakhel, “Correlated structural and electrical properties of thin manganese oxide films,” *Thin Solid Films*, vol. 496, no. 2, pp. 353–359, 2006, doi: 10.1016/j.tsf.2005.09.024.

[92] Yu. V. Golikov and V. F. Balakirev, “Phase equilibrium diagram of the system—Ni-Mn-O,” *J. Phys. Chem. Solids*, vol. 49, no. 4, pp. 329–332, 1988, doi: 10.1016/0022-3697(88)90087-X.

[93] H. Chen *et al.*, “Carbon-coated Hierarchical Ni–Mn Layered Double Hydroxide Nanoarrays on Ni Foam for Flexible High-capacitance Supercapacitors,” *Electrochim. Acta*, vol. 213, pp. 55–65, 2016, doi: 10.1016/j.electacta.2016.06.038.

[94] X. Li, D. Du, Y. Zhang, W. Xing, Q. Xue, and Z. Yan, “Layered double hydroxides toward high-performance supercapacitors,” *J. Mater. Chem. A*, vol. 5, no. 30, pp. 15460–15485, 2017, doi: 10.1039/C7TA04001F.

[95] K. Ma, W. Zhao, J. P. Cheng, F. Liu, and X. Zhang, “Free-standing α-$Co(OH)_2$/graphene oxide thin films fabricated through delamination and reassembling of acetate anions intercalated α-$Co(OH)_2$ and graphene oxide in water,” *J. Colloid. Interface Sci.*, vol. 468, pp. 238–246, 2016, doi: 10.1016/j.jcis.2016.01.058.

[96] F. Kovanda, T. Grygar, and V. Dorničák, “Thermal behaviour of Ni–Mn layered double hydroxide and characterization of formed oxides,” *Solid State Sci.*, vol. 5, no. 7, pp. 1019–1026, 2003, doi: 0.1016/S1293-2558(03)00129-8.

[97] R. S. Jayashree and P. Vishnu Kamath, “Layered double hydroxides of Ni with Cr and Mn as candidate electrode materials for alkaline secondary cells,” *J. Power Sources*, vol. 107, no. 1, pp. 120–124, 2002, doi: 10.1016/S0378-7753(01)00994-6.

[98] L. Guerlou-Demourgues, C. Denage, and C. Delmas, “New manganese-substituted nickel hydroxides: Part 1. Crystal chemistry and physical characterization,” *J. Power Sources*, vol. 52, no. 2, pp. 269–274, 1994, doi: 10.1016/0378-7753(94)02023-X.

[99] P. Vialat, F. Leroux, and C. Mousty, “Electrochemical properties of layered double hydroxides containing 3d metal cations,” *J. Solid State Electrochem.*, vol. 19, no. 7, pp. 1975–1983, Jul. 2015, doi: 10.1007/s10008-014-2671-0.

[100] B. Zhang, P. Dong, S. Yuan, Y. Zhang, Y. Zhang, and Y. Wang, “Manganese-Based Oxide Cathode Materials for Aqueous Zinc-Ion Batteries: Materials, Mechanism, Challenges, and Strategies,” *Chem & Bio Engineering*, vol. 1, no. 2, pp. 113–132, Mar. 2024, doi: 10.1021/cbe.3c00120.

[101] H. Y. Lee and J. B. Goodenough, “Supercapacitor Behavior with KCl Electrolyte,” *J. Solid State Chem.*, vol. 144, no. 1, pp. 220–223, 1999, doi: 10.1006/jssc.1998.8128.

[102] C. Toro and J. M. Buriak, “Materials + Energy + International Collaboration = Fundamental Insights,” *ACS Chem. Mater.*, vol. 28, no. 9, pp. 2883–2885, 2016, doi: 10.1021/acs.chemmater.6b01645.

[103] A. Ray *et al.*, “Electrochemical energy storage properties of Ni-Mn-oxide electrodes for advance asymmetric supercapacitor application,” *Langmuir*, vol. 35, no. 25, pp. 8257–8267, Jun. 2019, doi: 10.1021/acs.langmuir.9b00955.

[104] Y.-A. Sun, L.-T. Chen, S.-Y. Hsu, C.-C. Hu, and D.-H. Tsai, “Silver Nanoparticles-Decorating Manganese Oxide Hybrid Nanostructures for Supercapacitor Applications,” *Langmuir*, vol. 35, no. 44, pp. 14203–14212, Nov. 2019, doi: 10.1021/acs.langmuir.9b02409.

[105] P. Dhandapani, P. K. Nayak, and A. Maruthapillai, “Improved electrochemical performance and charge storage mechanism of $NiMnCoO_4$ by XPS study,” *Mater Chem Phys*, vol. 297, p. 127287, 2023, doi: 10.1016/j.matchemphys.2022.127287.

[106] P. R. P. R. Shalom, V. Sreekala Kumari Gopakumar, A. M. Aravind, and X. T. Suryabai, “Microwave assisted synthesis of $NiMn_2O_4$ as electrode material for supercapacitor applications,” *Zastita Materijala*, vol. 65, no. 3, pp. 501- 509, 2024, doi: 10.62638/zasmat1059.

[107] I. S. Ezhov *et al.*, “Use of Equivalent Reactant Feeding in Deposition of Ni–Mn–O Coatings by Molecular Layering,” *Russ. J. Appl. Chem.*, vol. 95, no. 3, pp. 352–356, Mar. 2022, doi: 10.1134/S107042722203003X.

[108] I. M. Hezam, A. M. Al-Syadi, A. Foul, A. Alshamrani, and J. Gwak, “Evaluation of nanostructured electrode materials for high-performance supercapacitors using

multiple-criteria decision-making approach," *Electron. Res. Arch.*, vol. 31, no. 4, pp. 2286–2314, 2023, doi: 10.3934/era.2023117.

[109] N. S. Kumar, R. P. Suvarna, K. C. Babu Naidu, and B. V. S. Reddy, "19 - Magnetic nanoparticles for high energy storage applications," in *Fundamentals and Industrial Applications of Magnetic Nanoparticles*, C. M. Hussain and K. K. Patankar, Eds., in Woodhead Publishing Series in Electronic and Optical Materials. , Woodhead Publishing, 2022, pp. 601–618. doi: 10.1016/B978-0-12-822819-7.00006-5.

[110] G. S. Attard, J. C. Glyde, and C. G. Göltner, "Liquid-crystalline phases as templates for the synthesis of mesoporous silica," *Nature*, vol. 378, pp. 366–368, 1995, doi: 10.1038/378366a0.

[111] N. R. B. Coleman and G. S. Attard, "Ordered mesoporous silicas prepared from both micellar solutions and liquid crystal phases," *Micro. Meso. Mater.*, vol. 44–45, pp. 73–80, 2001, doi: 10.1016/S1387-1811(01)00170-6.

[112] G. H. Bogush and C. F. Zukoski IV, "Studies of the kinetics of the precipitation of uniform silica particles through the hydrolysis and condensation of silicon alkoxides," *J. Colloid. Interface Sci.*, vol. 142, no. 1, pp. 1–18, 1991, doi: 10.1016/0021-9797(91)90029-8.

[113] P. T. Tanev and T. J. Pinnavaia, "Mesoporous silica molecular sieves prepared by ionic and neutral surfactant templating: A comparison of physical properties," *Chem. Mater.* vol. 8, no. 8, pp. 2068–2079, 1996, doi: 10.1021/cm950549a.

[114] X. Liu, C. M. Chun, I. A. Aksay, and W. H. Shih, "Synthesis of mesostructured nickel oxide with silica," *Ind. Eng. Chem. Res.*, vol. 39, no. 3, pp. 684–692, 2000, doi: 10.1021/ie990129l.

[115] H.-S. Kim, C. S. Kim, and S.-G. Kim, "Preparation of nickel oxide– and nickel–silica nanocomposites by spray pyrolysis," *J. Non Cryst. Solids*, vol. 352, no. 21, pp. 2204–2212, 2006, doi: 10.1016/j.jnoncrysol.2006.02.040.

[116] M. A. Wahab and F. Darain, "Nano-hard template synthesis of pure mesoporous NiO and its application for streptavidin protein immobilization," *Nanotechnology*, vol. 25, no. 16, Apr. 2014, doi: 10.1088/0957-4484/25/16/165701.

[117] M. Mihaly, A. F. Comanescu, A. E. Rogozea, E. Vasile, and A. Meghea, "NiO–silica based nanostructured materials obtained by microemulsion assisted sol–gel procedure," *Mater. Res. Bull.*, vol. 46, no. 10, pp. 1746–1753, 2011, doi: 10.1016/j.materresbull.2011.05.031.

[118] C. Avci, A. Aydın, Z. Tuna, Z. Yavuz, Y, Yamauchi, N. Suzuki and Ö. Dag, "Molten salt assisted self-assembly (MASA): Synthesis of mesoporous metal titanate ($CoTiO_3$, $MnTiO_3$, and $Li_4Ti_5O_{12}$) thin films and monoliths," *Chem. Mater.* vol. 26, no. 20, pp. 6050–6057, 2014, doi: 10.1021/cm503020y.

[119] C. Avci, Y. Liu, J. A. Pariente, A. Blanco, C. Lopez, I. Imaz, and D. Maspoch, "Template-Free, Surfactant-Mediated Orientation of Self-Assembled Supercrystals of Metal–Organic Framework Particles," *Small*, vol. 15, no. 31, p. 1902520, 2019, doi: 10.1002/smll.201902520.

[120] K. Nama Manjunatha and S. Paul, “Investigation of optical properties of nickel oxide thin films deposited on different substrates,” *Appl. Surf. Sci.*, vol. 352, pp. 10–15, 2015, doi: 10.1016/j.apsusc.2015.03.092.

[121] Q. Huo, “Chapter 16 - Synthetic Chemistry of the Inorganic Ordered Porous Materials,” in *Modern Inorganic Synthetic Chemistry*, R. Xu, W. Pang, and Q. Huo, Eds., Amsterdam: Elsevier, 2011, pp. 339–373. doi: 10.1016/B978-0-444-53599-3.10016-2.

[122] Y. Tan, S. Srinivasan, and K. S. Choi, “Electrochemical deposition of mesoporous nickel hydroxide films from dilute surfactant solutions,” *J. Am. Chem. Soc.*, vol. 127, no. 10, pp. 3596–3604, Mar. 2005, doi: 10.1021/ja0434329.

[123] D. D. Macdonald, “Chronopotentiometry,” in *Transient Techniques in Electrochemistry*, 1977, pp. 119–184. doi: 10.1007/978-1-4613-4145-1_5.

[124] F. Licht, M. A. Davis, and H. A. Andreas, “Charge redistribution and electrode history impact galvanostatic charging/discharging and associated figures of merit,” *J. Power Sources*, vol. 446, p. 227354, 2020, doi:10.1016/j.jpowsour.2019.227354.

[125] N. Elgrishi, K. J. Rountree, B. D. McCarthy, E. S. Rountree, T. T. Eisenhart, and J. L. Dempsey, “A Practical Beginner’s Guide to Cyclic Voltammetry,” *J. Chem. Educ.*, vol. 95, no. 2, pp. 197–206, Feb. 2018, doi: 10.1021/acs.jchemed.7b00361.

[126] T. Shinagawa, A. T. Garcia-Esparza, and K. Takanabe, “Insight on Tafel slopes from a microkinetic analysis of aqueous electrocatalysis for energy conversion,” *Sci. Rep.*, vol. 5, no. August, pp. 1–21, 2015, doi: 10.1038/srep13801.

[127] Q. Abbas *et al.*, “Engineering of nickel, cobalt oxides and nickel/cobalt binary oxides by electrodeposition and application as binder free electrodes in supercapacitors,” *Sci. Rep.*, vol. 13, no. 1, Dec. 2023, doi: 10.1038/s41598-023-42647-4.

[128] G. A. Niklasson, Z. Qiu, I. Bayrak Pehlivan, and T. Edvinsson, “Impedance spectroscopy of water splitting reactions on nanostructured metal-based catalysts,” in *IOP Conference Series: Materials Science and Engineering*, Institute of Physics Publishing, Mar. 2019. doi: 10.1088/1757-899X/503/1/012005.

[129] O. Kanoun, “Impedance spectroscopy advances and future trends: A comprehensive review,” in *Advanced Applications: Battery Research, Bioimpedance, System Design*, 2019, pp. 1–22. doi: doi:10.1515/9783110558920-001.

[130] M. Zeng Gengsheng Lawrence and Zeng, “Ohm’s Law,” *Electric Circuits: A Concise, Conceptual Tutorial, Cham.: Springer International Publishing*, 2021, pp. 17–21. doi: 10.1007/978-3-030-60515-5_3.

[131] J. R. H. Ross, “Catalyst Characterization,” *Contemporary Catalysis, Elsevier*, 2019, pp. 121–132. doi: 10.1016/b978-0-444-63474-0.00005-9.

[132] C. G. Sonwane and S. K. Bhatia, “Characterization of Pore Size Distributions of Mesoporous Materials from Adsorption Isotherms,” *J. Phys. Chem. B*, vol. 104, no. 39, pp. 9099–9110, Oct. 2000, doi: 10.1021/jp000907j.

[133] Š. Trafela, J. Zavašnik, S. Šturm, and K. Ž. Rožman, "Formation of a $Ni(OH)_2$/NiOOH active redox couple on nickel nanowires for formaldehyde detection in alkaline media," *Electrochim. Acta*, vol. 309, pp. 346–353, 2019, doi: 10.1016/j.electacta.2019.04.060.

[134] M. C. Biesinger, B. P. Payne, A. P. Grosvenor, L. W. M. Lau, A. R. Gerson, and R. St. C. Smart, "Resolving surface chemical states in XPS analysis of first row transition metals, oxides and hydroxides: Cr, Mn, Fe, Co and Ni," *Appl. Surf. Sci.*, vol. 257, no. 7, pp. 2717–2730, 2011, doi: 10.1016/j.apsusc.2010.10.051.

[135] E. S. Ilton, J. E. Post, P. J. Heaney, F. T. Ling, and S. N. Kerisit, "XPS determination of Mn oxidation states in Mn (hydr)oxides," *Appl. Surf. Sci.*, vol. 366, pp. 475–485, Mar. 2016, doi: 10.1016/j.apsusc.2015.12.159.

[136] M. C. Biesinger, L. W. M. Lau, A. R. Gerson, and R. S. C. Smart, "Resolving surface chemical states in XPS analysis of first row transition metals, oxides and hydroxides: Sc, Ti, V, Cu and Zn," *Appl. Surf. Sci.*, vol. 257, no. 3, pp. 887–898, Nov. 2010, doi: 10.1016/j.apsusc.2010.07.086.

[137] I. Karakaya Durukan and Ö. Dag, "Electronic Synergistic Effects on the Stability and Oxygen Evolution Reaction Efficiency of the Mesoporous $LiMn_{2-x}M_xO_4$ (M = Mn, Fe, Co, Ni, and Cu) Electrodes," *Inorg. Chem.*, vol. 63, no. 46, pp. 22239–22257, Nov. 2024, doi: 10.1021/acs.inorgchem.4c03885.

[138] A. Amirzhanova, N. Ullah, and Ö. Dag, "Transition metal salt catalysed green synthesis of mesoporous silica nanoparticles," *Micropor. Mesopor. Mat.*, vol. 378 p. 113233, 2024, doi: 10.1016/j.micromeso.2024.113233.

[139] E. Y. Topuzlu, B. Ulgut, and Ö. Dag, "Role of Water in the Lyotropic Liquid Crystalline Lithium Iodide-Iodine-Water-$C_{12}E_{10}$ Mesophase as a Gel Electrolyte in a Dye-Sensitized Solar Cell," *Langmuir*, vol. 37, no. 27, pp. 8305–8313, Jul. 2021, doi: 10.1021/acs.langmuir.1c01094.

Mesoporous $MnCo_2O_4$, $NiCo_2O_4$, and $ZnCo_2O_4$ Thin-Film Electrodes as Electrocatalysts for the Oxygen Evolution Reaction in Alkaline Solutions

Author: Assel Amirzhanova, Nesibe Akmanşen, Irmak Karakaya, et al
Publication: ACS Applied Energy Materials
Publisher: American Chemical Society
Date: Mar 1, 2021